

GEOCHEMISTRY OF THE NEOGENE LOS FRAILES IGNIMBRITE COMPLEX
ON THE CENTRAL ANDEAN ALTIPLANO PLATEAU

A Thesis

Presented to the Faculty of the Graduate School

of Cornell University

In Partial Fulfillment of the Requirements for the Degree of

Master of Science

by

Joseph John Kato

August 2013

© 2013 Joseph John Kato

ABSTRACT

The Los Frailes Ignimbrite Complex sits in the backarc of the Andean Central Volcanic Zone (CVZ) and is the most easterly of the large Altiplano volcanic centers. Despite its large size (2000 km³) and substantial mineralization in its satellite units, the majority of the Los Frailes Complex remains poorly described with conflicting age assessments of the main Los Frailes ignimbrite. Processes related to its emplacement include: variable crustal thickening and uplift over a steepening subducted slab, episodes of delamination of the mantle-lithosphere and lower crust and deep crustal flow.

Based on 25 new analyses and the works of previous sub-regional studies, a three tier crustal magma evolution is proposed for the Los Frailes Complex, similar to models suggested for Puna ignimbrites. The crust-to-mantle mixing ratio of the erupted mass is put near 50:50 based on new fractionation corrected $\delta^{18}\text{O}_{\text{Quartz}}$ analyses (+9.43-10.79‰). AFC models incorporating new $^{87}\text{Sr}/^{86}\text{Sr}$ (0.710-0.713) and $^{143}\text{Nd}/^{144}\text{Nd}$ (0.5121-0.5123) ϵ_{Nd} (-9 to -6) ratios and the strongly peraluminous character of the complex support a metapelitic crustal end-member and silicic crustal base. Melting and mixing near the Moho is established based on steep HREE patterns (Sm/Yb=4-12) and very high Sr content (400-650 ppm Sr) while middle crustal plagioclase removal creates negative Eu anomalies (Eu/Eu*=0.6-0.9). High crystal content and reported cordierite are the results of low pressure crystallization in upper crustal magma chambers prior to eruption.

Coherent temporal trends of REE and HFSE ratios display the effects of crustal thickening and delamination on Moho-depth AFC processes. Two distinct ratio changes at 10-12 Ma and 2-4 Ma are proposed to correlate with two discreet delamination events below the Los Frailes Complex. The 10-12 Ma event is

supported by corresponding shifts in regional brittle deformation and isotopic character as well as proposed rapid uplift at that time. Major eruptions of the Livicucho and Condor Nasa ignimbrites and emplacement of the large main Los Frailes ignimbrite mark the volcanic expression. The age of the main Los Frailes ignimbrite is established at 1.5-3.5 Ma, in agreement with Barke et al. (2007), based on two new $^{40}\text{Ar}/^{39}\text{Ar}$ sanidine ages ~ 1.521 Ma. In addition, seismic tomographic studies show missing lithosphere directly below the complex which corresponds with a $^3\text{He}/^4\text{He}$ emissions study suggesting recent mantle melting. These findings demonstrate that delamination in the southern Altiplano is episodic with the results of the 2-4 Ma event still observable today.

BIOGRAPHICAL SKETCH

Joseph Kato was born March 28, 1977, in Middletown, New York, son of John and Ruth Kato. His early years were spent in Central and Southeast Alaska where his father worked as a geologist for the Federal Government. He graduated from Juneau-Douglas High School in 1995 and spent a year at Northwestern Preparatory School in Malibu, California as well as the University of Alaska Fairbanks before entering the U.S. Naval Academy with the class of 2000. At Annapolis, he earned a Bachelor of Science in Honors Oceanography and was ordered to flight training to become a Naval Flight Officer following graduation. In Pensacola, Florida, he earned his “Wings of Gold” and was assigned to EA-6B Prowlers in Whidbey Island, Washington as an Electronic Countermeasures Officer. His junior officer tours included VAQ-136 in Atsugi, Japan and the Royal Air Force 12 Bomber Squadron in Lossiemouth, Scotland. In 2010, he was assigned to Cornell University Naval Reserve Officers Training Unit (NROTC) as a Naval Science Instructor and Visiting Lecturer. It was then that, under the guidance of Professor Suzanne Kay, this project and thesis took shape.

Dedicated to Snes, whose time and support made this possible.

ACKNOWLEDGMENTS

I acknowledge, first and foremost, my advisor, Professor Suzanne M. Kay for her time and patience while teaching me most of what I know about geochemistry and South American geology, and William M. White and Robert W. Kay for the remainder. I would also like to acknowledge the Cornell Earth and Atmospheric Department staff for their time and help, especially Savannah Sawyer.

This thesis and the work it describes was made possible by the 2009 and 2010 reconnaissance trip and field work done by Beatriz Coira, Suzanne Kay, Nestor Jiménez, Brenhin Keller, Pablo Caffè, Luis Galvan and Chelsea Allison. In the early stage of development of this thesis, extensive input was borrowed from Brenhin Keller's (now at Princeton) 2010 Senior Thesis. In the later stages of this project, Brian Jicha (University of Wisconsin-Madison), Chris Harris (University of Cape Town, South Africa) and Brenhin Keller contributed valuable Ar/Ar ages, oxygen isotopic data and zircon analyses.

I would like to thank Louis A. Derry and George Hade for their assistance with a temperamental TIMS, as well as John Hunt for his instruction on the use of the microprobe. In addition, my fellow graduate students deserve thanks for endless questions I have directed their way, particularly Ashley Tibbetts, Nicolas Consentino and Sander Hunter. Finally, thank you to my father for reading this about a dozen times during the editing process.

TABLE OF CONTENTS

Biographical Sketch	iii
Dedication.....	iv
Acknowledgments.....	v
Table of Contents.....	vi
List of Figures.....	viii
List of Tables.....	xi
List of Abbreviations.....	xii
List of Symbols.....	xiv
Chapter 1: Introduction and Geologic Setting.....	1
Introduction to the Los Frailes Ignimbrite Complex.....	1
Geological Setting of the Los Frailes Ignimbrite Complex.....	7
Volcanic History of the Los Frailes Ignimbrite Complex.....	15
Comparison to Cerro Galán, selected APVC and Morococala Ignimbrites	18
Chapter 2: Analytical Methods.....	22
Major Elements Analyses.....	22
Trace Elements Analyses	22
Mineral Analyses	23
Strontium and Neodymium Isotopic Analyses.....	23
Oxygen Isotopic Analyses	25
Zircon Isotopic Analyses.....	26
⁴⁰ Ar- ³⁹ Ar Age Analyses.....	27
Geothermometry and Geobarometry Analyses	28
Chapter 3: Analytical Results.....	29

Major Elements.....	30
Trace Elements.....	30
Mineral Compositions.....	60
Isotopic Results.....	65
Zircon Age Analysis.....	71
⁴⁰ Ar- ³⁹ Ar Age Analysis.....	72
Geothermometry and Geobarometry.....	72
Chapter 4: Discussion of Analytical Results.....	75
Major Elements.....	75
Trace Elements.....	78
Isotopic Compositions.....	89
Mineralogy.....	99
Geochronology.....	99
Geothermometry and Geobarometry.....	102
Chapter 5: Modeling.....	104
AFC Models.....	104
Magma Evolution and Ignimbrite Genesis Model.....	127
Chapter 6: Conclusions.....	132
Appendix A: Neodymium Separation Procedure.....	136
Appendix B: Major and Trace Element Data.....	139
Appendix C: Strontium and Neodymium Isotopic Data and Error Analysis.....	144
Appendix D: Oxygen Isotopic Data and Error Analysis.....	146
Appendix E: Zircon Isotopic Data and Error Analysis.....	147
Appendix F: Microprobe Data and Error Analysis.....	149
Appendix G: ⁴⁰ Ar- ³⁹ Ar Data and Error Analysis.....	159
References.....	161

LIST OF FIGURES

Figure 1.1:	Map of South America showing major tectonic features.....	2
Figure 1.2:	Map of Central Andean Altiplano-Puna ignimbrites.....	3
Figure 1.3:	Modified composite map of the Los Frailes Complex.....	5
Figure 1.4:	Lithospheric cross-section for evolution of the southern Altiplano.	9
Figure 1.5:	Lithospheric scale cross-section near 21°S.....	10
Figure 1.6:	Schematic cross-section cartoon of seismic low velocity zones in the mantle.....	12
Figure 1.7:	A compilation of seismic P-wave tomographic images and figures depicting ongoing delamination of the northern Puna lithosphere...	14
Figure 3.1:	Plot of SiO ₂ versus Al/(K+Na+Ca) depicting the highly peraluminous nature of Los Frailes Complex.....	31
Figure 3.2:	Plot of K ₂ O versus Na ₂ O displaying the aluminosity variability of the ignimbrites reflected in their Na ₂ O and K ₂ O concentrations.....	33
Figure 3.3:	Plot of SiO ₂ versus K ₂ O displaying high K ₂ O content.....	34
Figure 3.4:	Primitive mantle normalized plots of trace element concentrations.	35
Figure 3.5:	Plot of Sm/Yb ppm ratio versus La/Sm ppm ratio which illustrates variable REE depletion.....	37
Figure 3.6:	Plot of La ppm versus La/Yb ppm ratio shows no discernible effect of La concentration on the La/Yb ppm ratio.....	39
Figure 3.7:	Plot of SiO ₂ versus La/Yb ppm ratio which shows the REE ratios changes are not SiO ₂ driven.....	40
Figure 3.8:	Plot of SiO ₂ versus La ppm showing no trend of La concentration decrease with SiO ₂ increase.....	42
Figure 3.9:	Plot of La/Ta ppm ratio versus Ba/Ta ppm ratio as well as Ba/La ppm ratios showing systematic variation in the HFSE (La and Ta) and LILE (Ba) ratios with time.....	43

Figure 3.10:	Plot of Ta ppm versus Nb ppm depicting the unit variability of HFSE elements Nb and Ta concentrations.....	45
Figure 3.11:	Plot of SiO ₂ versus Eu/Eu* ratios showing highest values in low silica units and lowest values in high silica units.....	49
Figure 3.12:	Plot of Sm/Yb versus Eu/Eu* ratios showing Eu/Eu* values are slightly more negative at higher Sm/Yb ratios; indicating greater plagioclase fractionation.....	51
Figure 3.13:	Plot of SiO ₂ versus Sr ppm showing the Sr ppm range has remained nearly constant over 25 My and through variable SiO ₂ content.....	53
Figure 3.14:	Plot of Eu/Eu* ratio versus Sr ppm showing the Sr ppm range has remained nearly constant over 25 My and variable Eu/Eu*.....	54
Figure 3.15:	Plot of Sm/Yb ppm ratio versus Sr ppm showing the Sr ppm range has remained nearly constant over 25 My and variable Sm/Yb.....	55
Figure 3.16:	Plot of SiO ₂ versus Nd ppm showing the Nd ppm range has remained generally constant over 25 My and through variable SiO ₂ content...	56
Figure 3.17:	Plot of Sr ppm versus Nd ppm and resulting Sr/Nd ratio showing most Los Frailes Complex samples maintain a Sr/Nd ratio of 6-11.....	57
Figure 3.18:	Plot of SiO ₂ versus Rb ppm showing the Rb ppm range has remained generally constant over 25 My and through variable SiO ₂ content..	58
Figure 3.19:	Plot of Sr ppm versus Rb ppm and resulting Rb/Sr ratios showing most Los Frailes Complex samples maintain an Rb/Sr ratio of 0.33-0.5..	59
Figure 3.20:	Feldspar ternary diagram with plotted Los Frailes Complex plagioclase data.....	62
Figure 3.21:	(a) Plot of ⁸⁷ Sr/ ⁸⁶ Sr versus ¹⁴³ Nd/ ¹⁴⁴ Nd (ε _{Nd}) for Los Frailes Complex data showing two distinct fields with pre-12 Ma samples having less enriched character, and the post-12 Ma samples with more enriched character. (b) Plot of ⁸⁷ Sr/ ⁸⁶ Sr versus ¹⁴³ Nd/ ¹⁴⁴ Nd (ε _{Nd}) for comparative Altiplano-Puna backarc ignimbrites with assumed mantle and calculated crustal end-members.....	67
Figure 3.22:	Plots of SiO ₂ versus ⁸⁷ Sr/ ⁸⁶ Sr and of Sr ppm versus ⁸⁷ Sr/ ⁸⁶ Sr. Shows large variation in ⁸⁷ Sr/ ⁸⁶ Sr between varying units at near equal SiO ₂ and Sr ppm, but little change in ⁸⁷ Sr/ ⁸⁶ Sr within individual units with variable SiO ₂ and Sr ppm (flat fields).....	69

Figure 4.1:	Graph of ignimbrite age (Ma) versus individual unit average La/Sm, (Sm/Yb)/2, (La/Ta)/10 and (Ba/Ta)/100 ratios.....	82
Figure 4.2:	Plots of $^{206}\text{Pb}/^{204}\text{Pb}$ versus $^{207}\text{Pb}/^{204}\text{Pb}$ and of $^{206}\text{Pb}/^{204}\text{Pb}$ versus $^{208}\text{Pb}/^{204}\text{Pb}$. Shows Los Frailes Complex basement similarities to the northern Puna centers as compared with the southern Puna centers.	97
Figure 5.1:	Plots of $^{87}\text{Sr}/^{86}\text{Sr}$ ratios versus (a) ppm Sr and (b) $\delta^{18}\text{O}_{\text{magma}}$ in ‰ for representative measured values of the Kari Kari and Los Frailes ignimbrites.....	119
Figure 5.2:	Plots of $^{87}\text{Sr}/^{86}\text{Sr}$ ratios versus (a) ppm Sr and (b) $\delta^{18}\text{O}_{\text{magma}}$ in ‰ with mixing curves for various Los Frailes ignimbrite crustal end-member compositions.....	121
Figure 5.3:	Plots of $^{87}\text{Sr}/^{86}\text{Sr}$ ratios versus (a) ppm Sr and (b) $\delta^{18}\text{O}_{\text{magma}}$ in ‰ with mixing curves for various Los Frailes ignimbrite crustal end-member compositions.....	125
Figure 5.4:	Model of the Los Frailes Complex magmatic system at 19° to 20°S with evolution at three crustal levels based on geochemical and geophysical evidence.....	128

LIST OF TABLES

Table 1.1:	Los Frailes Complex pertinent units, mineralogy, volumes and references.....	4
Table 1.2:	Sr, Nd and O isotopic and concentrations values of selected Altiplano-Puna ignimbrites.....	19
Table 3.1:	Representative plagioclase electron microprobe analyses (cores and rims).....	62
Table 3.2:	Representative sanidine electron microprobe analyses.....	63
Table 3.3:	Representative biotite electron microprobe analyses.....	64
Table 3.4:	Sr, Nd and O isotopic analyses of Los Frailes Complex samples....	66
Table 3.5:	$^{40}\text{Ar}/^{39}\text{Ar}$ sanidine age analyses.....	73
Table 3.6:	Zircon saturation and two-feldspar geothermometry temperatures..	74
Table 4.1:	Whole rock Sr and Pb isotopic data from Schneider (1985).....	90
Table 4.2:	$\delta^{18}\text{O}$ isotopic analyses of Los Frailes Complex samples.....	90
Table 4.3:	25 Samples collected on 2009 and 2010 reconnaissance trips and assigned ages.....	100
Table 5.1:	Selected Altiplano volcanic samples for mafic end-members.....	108
Table 5.2:	Aitchison and Forrest (1994) AFC equations derived from DePaolo (1981) equations.....	112
Table 5.3:	AFC models using $^{87}\text{Sr}/^{86}\text{Sr}$, Sr ppm, $^{143}\text{Nd}/^{144}\text{Nd}$, Nd ppm and $\delta^{18}\text{O}$	116

LIST OF ABBREVIATIONS

- Ab – Albite, plagioclase Na end-member
- AFC – Assimilation, fractionation and crystallization
- ALVC- Altiplano low velocity zone
- An – Anorthite, plagioclase Ca end-member
- APVC – Altiplano-Puna volcanic center
- CHUR – Chondritic uniform reservoir
- CL - Cathodoluminescence
- CVZ – Central volcanic zone (Andean)
- DRE – Dense rock equivalent
- EC-AFC - Energy constrained assimilation, fractionation and crystallization
- FCs – Fish Canyon tuff sanidine
- fO₂ – Oxygen fugacity
- Ga - Giga annum (billions of years ago from present)
- GPS - Global positioning system
- JDF - Juan de Fuca
- JEOL - Japan Electron Optics Laboratory Company
- Ka – Kilo annum (thousands of years ago from present)
- HFSE – High field strength elements (Nb, Ta, Hf, Zr)
- HREE – Heavy rare earth elements (Ho to Lu)
- ID-TIMS - Isotope dilution thermal ionization mass spectrometry
- INAA - Instrumental neutron activation analysis
- Kd – Elemental partition (distribution) coefficient
- LCP – Lake City plagioclase
- LILE – Large ion lithophile elements (K, Rb, Cs, Sr, Ba)

LREE – Light rare earth elements (La to Nd)
Ma – Mega annum (millions of years ago from present)
MORB – Mid ocean ridge basalt
MREE – Middle rare earth elements (Sm to Dy)
MSWD – Mean square of weighted deviates
My – Million years
NASC – North American shale composite
NCKFMASHTO - Na₂O, CaO, K₂O, FeO, MgO, Al₂O₃, SiO₂, H₂O, TiO₂ and O
OIB – Ocean island basalt
Or - Orthoclase, K-feldspar end-member
ICP-MS – Inductively coupled plasma mass spectrometer
QBBs- Quebrada Blanca Bright spot
REE – Rare earth elements (La to Lu)
SCLM - Subcontinental lithospheric mantle
SMOW- Standard mean ocean water
TIMS – Thermal ionization mass spectrometer
WDS – Wavelength dispersive
XRF - X-ray fluorescence

LIST OF SYMBOLS

$$\text{Eu}/\text{Eu}^* = [\text{Eu}/(0.5(\text{Sm}+\text{Gd}))]$$

Deviation of measured Eu concentration from predicted Eu* concentration assuming chondrite-normalization and similar compatibility to other REE

$$\delta^{18}\text{O} (\text{‰}) = [({}^{18}\text{O}/{}^{16}\text{O}_{\text{Sample}}/{}^{18}\text{O}/{}^{16}\text{O}_{\text{SMOW}})-1] \times 10^3$$

$$\epsilon_{\text{Nd}} = [({}^{143}\text{Nd}/{}^{144}\text{Nd}_{\text{Sample}}/{}^{143}\text{Nd}/{}^{144}\text{Nd}_{\text{CHUR}})-1] \times 10^4$$

$$\sigma = \text{Standard Deviation (1}\sigma \text{ or 2}\sigma)$$

CHAPTER 1

INTRODUCTION AND GEOLOGIC SETTING

Introduction to the Los Frailes Ignimbrite Complex

The Los Frailes Ignimbrite Complex of Bolivia is situated in the backarc of the Andean Central Volcanic Zone (CVZ) near the center of the South American convergent margin (see Figure 1.1). Bounded to the west by the active arc (Western Cordillera) and to the east by the west-verging thin-skinned fold-and-thrust belt (Eastern Cordillera), the ~200-450 km wide Altiplano-Puna plateau stretches 1800 km along the length of the CVZ (Isacks, 1988; Allmendinger et al., 1997) (see Figure 1.2). The Los Frailes Complex straddles the boundary of the eastern margin of the Bolivian Altiplano plateau and the Eastern Cordillera of the Central Andes between 19°S and 20°S longitude, and is the most easterly of the large Altiplano volcanic structures. With more than 2000 km³ of total erupted volume, a ~100 km diameter, and covering an area of ~7500-8500 km² (Schneider, 1985), it is one of the largest ignimbrite complexes on the Altiplano-Puna plateau (see review of Kay and Coira, 2009). At an average elevation of nearly 4,000 meters and a maximum of 4,800 meters, the complex sits atop 60-65 km thick crust (Beck et al., 1996; Yuan et al., 2000; McGlashan et al., 2008).

The Los Frailes Complex ignimbrites are composed of andesitic to rhyodacitic welded ash units of late Oligocene to recent age (25 to <1 Ma) which have been produced by eruptions every 2-5 My over that period. The southern Altiplano on which it sits is an internally drained, sediment-filled basin of Ordovician shales, Cretaceous syn-rift sandstones and Tertiary redbeds and volcanics (e.g., Schneider, 1985; Kennen et al., 1995), with a basement composed largely of Paleozoic

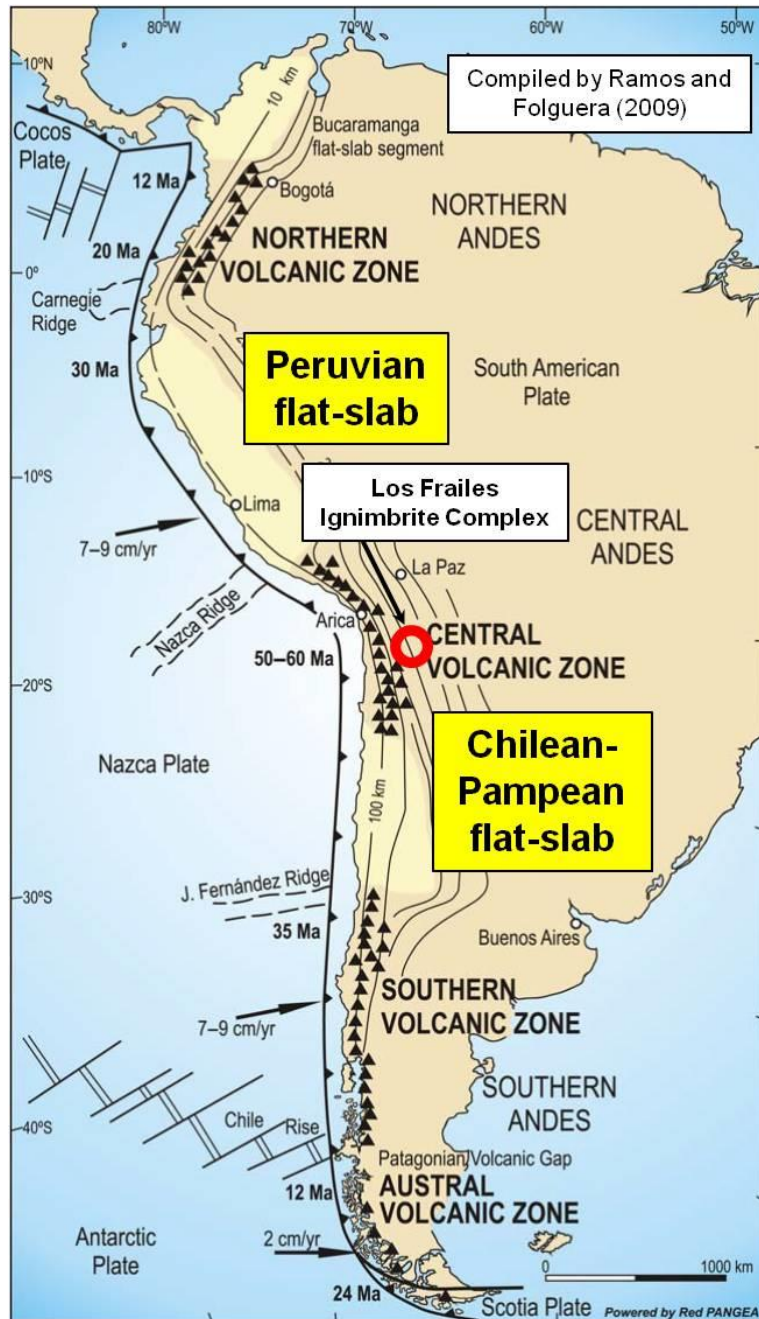


Figure 1.1

Map of South America showing major tectonic features from Ramos and Folguera (2009). The location of the Los Frailes Complex (red circle) is in the backarc of the Andean Central Volcanic Zone (CVZ) near the center of the South American convergent margin. The CVZ is bracketed by two non-volcanic gaps associated with the subduction of aseismic bathymetric oceanic ridges. The Nazca Ridge is subducted to the north (Peruvian flatslab) and the Juan Fernandez Ridge is subducted to the south (Chilean-Pampean flatslab) (e.g., Barzangi and Isacks, 1976; Pilger, 1981; Nur and Ben-Avraham, 1981).

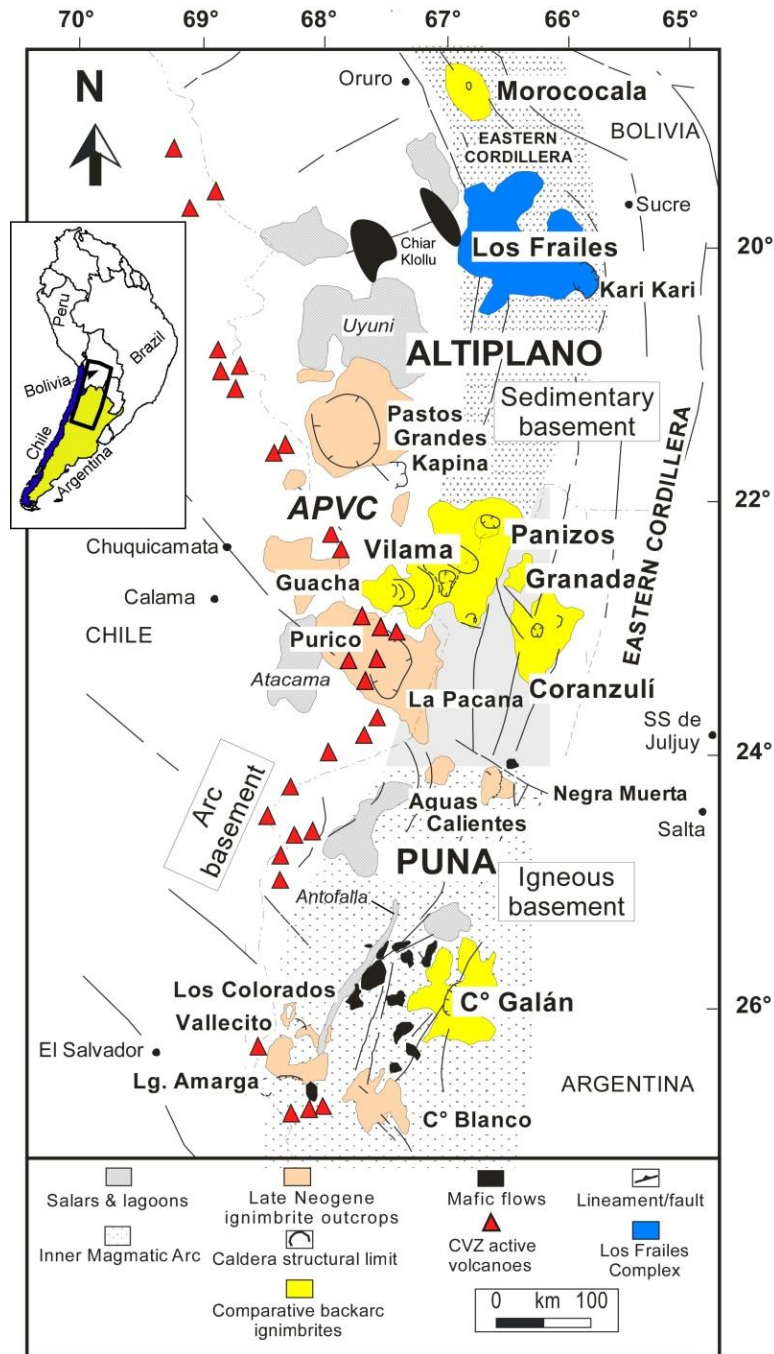


Figure 1.2

Map of Central Andean Altiplano-Puna backarc ignimbrites (blue, yellow & beige) and mafic flows (black) from Kay et al. (2010). Depicts the location of the Los Frailes Ignimbrite Complex (blue) relative to the southern Puna Cerro Galán, the central Altiplano-Puna Volcanic Complexes (APVC) and the central Altiplano Morococala ignimbrites (yellow). Central Volcanic Zone (CVZ) active arc volcanoes are shown as red triangles.

sedimentary rocks over Proterozoic and Archean crust (see reviews in Lucassen et al., 2001; Ramos, 2008). The Los Frailes Complex contains significant mineralization, though this is concentrated in volumetrically minor pre-12 Ma units. Mineral deposits of silver, tin and zinc are economically important, and include the world's largest silver mine in the late-middle Miocene Cerro Rico de Potosi. Despite its large size and its economically important ore deposits, the majority of the Los Frailes Complex has not been extensively studied, primarily due to the lack of economic mineralization.

Table 1.1

Los Frailes Complex pertinent units, mineralogy, volumes and references					
Unit	Mineral Assemblage	Volume (km ³ in DRE)	Age (Ma)	SiO ₂ (wt. %)	Major Reference Sources
Kumurana	Plag-San-Qtz-Bio- Hbl	Very Small	~25	58-69	Schneider and Halls, 1985; Keller, 2010
Kari Kari	Plag-Bio-San-Qtz-Gar-Cor	~550 ^a	20-22	58-65	Evernden et al., 1977; Grant et al., 1979; Francis et al., 1981; McBride et al., 1983; Schneider and Halls, 1985; Schneider, 1985, 1987; Keller, 2010
Porco	Plag-San-Qtz-Bio-Ilm	Small	12-14	66-72	Schneider and Halls, 1985; Schneider, 1985, 1987; Cunningham et al. 1996; Kennan et al., 1995; Luedke et al., 1997; Keller, 2010
Sevaruyo	Qtz-Plag-San-Bio	Small	9-10? ^b	65-72	Schneider, 1985; Barke et al., 2007; Keller, 2010
Livicucho	Plag-San-Qtz-Bio-Orth-Cor	~500-1000 ^a	7-8	59-65	Evernden et al, 1977; Grant et al. 1979; Schneider and Halls, 1985; Schneider, 1985, 1987; Kennan et al. 1995; Jiménez et. al. 1997; Barke et al., 2007; Keller, 2010
Condor Nasa	Plag-San-Qtz-Bio-Orth-Cor	~500 ^a	7-8	59-65	Evernden et al, 1977; Grant et al. 1979; McBride, et. al. 1983; Schneider and Halls, 1985; Schneider, 1985, 1987; Kennan et al. 1995; Jiménez et. al. 1997; Keller, 2010
Los Frailes	Plag-San-Qtz-Bio-Cor-Ilm	~1200-2000 ^a	1.5-3.5	64-69	Barker and Francis, 1978; Schneider and Halls, 1985; Schneider, 1985, 1987; Luedke et al., 1997; Rice et. al., 2005; Barke et. al., 2007; Keller, 2010
Nuevo Mundo	Bio-San-Plag-Qtz-Cor-Apt-Ilm	Small	<1.0	66-67	de Silva and Francis, 1991; Luedke et al., 1997; Jiménez et al., 2005

Plag=Plagioclase, San=Sanidine, Qtz=Quartz, Bio=Biotite, Hbl=Hornblende, Cor=Cordierite, Orth=Orthopyroxene, Gar=Garnet, Ilm=Ilmenite, Apt = Apatite

^a From Schneider (1985).

^b See Chapter 4 for a discussion of Sevaruyo region age uncertainty.

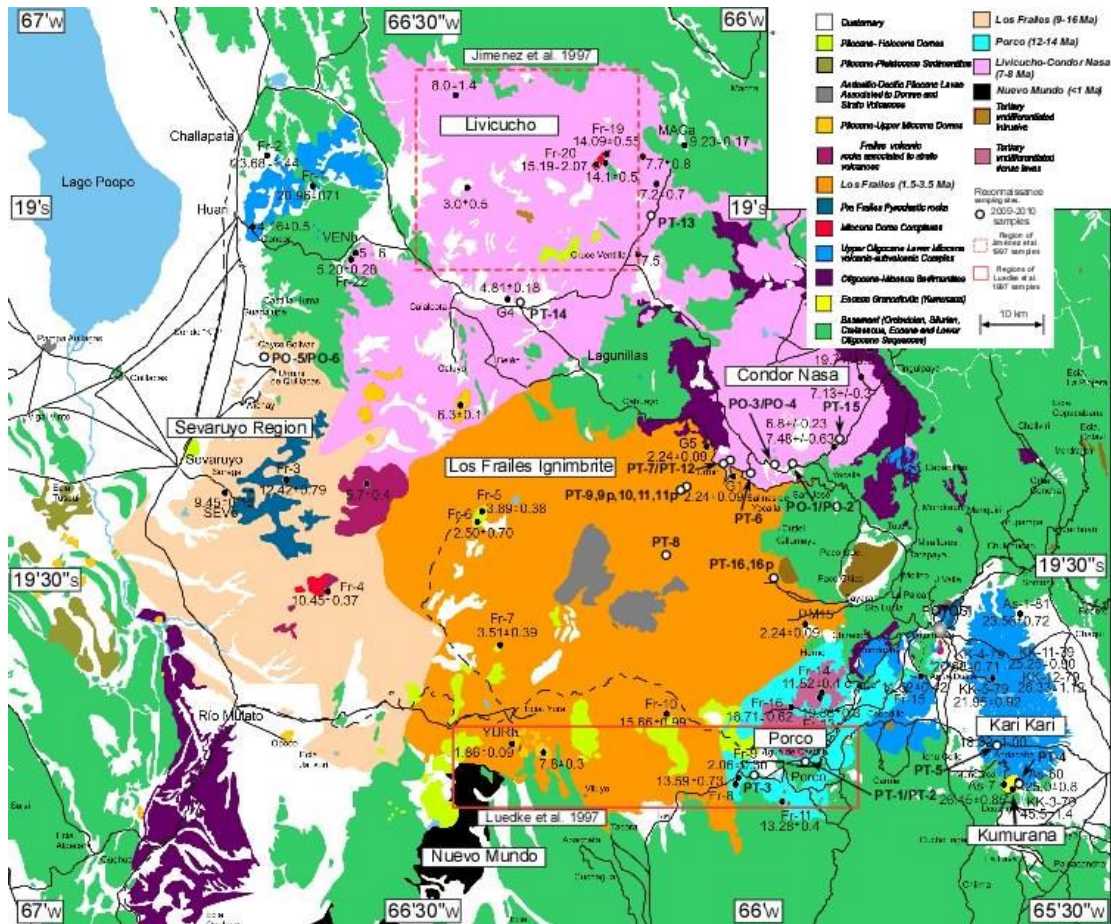


Figure 1.3

Modified composite map of the Los Frailes Complex compiled by Beatriz Coira from Bolivian maps showing the 25 (PT and PO series) sample localities (white dots). The study regions of Jimenez et al. (1997) (red dashed box) and Luedke et al. (1997) (red solid box) are also shown. $^{40}\text{K}/^{39}\text{Ar}$ biotite ages are from Bolivian survey, Schneider (1985), Evernden et al. (1977), Grant et al. (1979), and Kennen et al. (1995) as well as $^{40}\text{Ar}/^{39}\text{Ar}$ biotite ages from Barke et al. (2007) are in black. The Los Frailes ignimbrite ages and units have been modified here.

Table 1.1 and Figure 1.3 show the major and minor Los Frailes Volcanic Complex units. For the purpose of this paper, the term Los Frailes Complex is used to refer to the entire 8500 km² area and 25 My history, while the term Los Frailes ignimbrite refers only to the central 1.5-3.5 Ma massif without the associated satellite mesetas or smaller units. It should be noted that this is a departure from the terminology in Schneider (1985), who placed the Livicucho and Condor Nasa mesetas coeval with the Los Frailes ignimbrite and treated them largely as part of the same

volcanic episode. This study will look at the entire 25 My geochemical history of the Los Frailes Complex in order to determine what the geochemical data can contribute to the current understanding of the evolution of the Altiplano plateau during that period. Tectonic shortening, crustal thickening, delamination, plateau uplift and a steepening slab subduction angle are all thought to have occurred in the southern Altiplano during the Los Frailes Complex history, (see review in Kay and Coira, 2009) and are expected to have imparted geochemical signals in the regular backarc eruptions, which now serve as the record of these changes.

Previous investigations of the Los Frailes Complex have been sporadic and directed dominantly towards the mineralized units (Kumurana, Kari Kari and Porco), part of its pre-12 Ma history. Only four geochemical studies exist of the volumetrically dominant, but economically unimportant post-12 Ma ignimbrites; Jiménez et al. (1997), Luedke et al. (1997) and the theses of Schneider (1985) and Keller (2010). This study will add the results of 25 new samples from reconnaissance trips in 2009 and 2010. Those trips, by Beatriz Coira, Suzanne Kay, Nestor Jiménez, Brenhin Keller, Pablo Caffè, Luis Galvan and Chelsea Allison, were directed at describing the geochemistry of the main post-12 Ma ignimbrites. The data includes 25 whole rock major and trace element analyses, 16 whole rock $^{87}\text{Sr}/^{86}\text{Sr}$ measurements, 13 whole rock $^{143}\text{Nd}/^{144}\text{Nd}$ (ϵ_{Nd}) measurements, 10 quartz phenocryst $^{18}\text{O}/^{16}\text{O}$ ($\delta^{18}\text{O}\text{‰}$) measurements and electron microprobe and optical microscopy results. The $^{143}\text{Nd}/^{144}\text{Nd}$ (ϵ_{Nd}) and $\delta^{18}\text{O}_{\text{Quartz}}$ are the first reported from the Los Frailes Complex. In order to determine the age of the main Los Frailes ignimbrite, two new $^{40}\text{Ar}/^{39}\text{Ar}$ sanidine ages and two zircon age analyses are presented.

Geochemical information is used to investigate the crust-to-mantle mixing ratio in the erupted magmas, the location of crustal assimilation fractionation and crystallization (AFC), as well as the nature of hybrid magma storage sites and their

locations. Finally, this paper will compare the Los Frailes Complex to other researchers' findings of selected similar and contrasting Altiplano-Puna backarc ignimbrites. To accomplish this, new Sr, Nd and O isotopic and concentration data will be used to estimate the crust-to-mantle mixing ratio which will be then applied to the AFC model equations of Aitchison and Forrest (1994) to assess the crustal end-member composition. New and reported geochemical data are compiled and compared to existing geophysical studies to decipher volcanic plumbing and temporal changes in the southern Altiplano. From the integrated data, a working model of the current Los Frailes Complex magmatic system will be presented.

Geological Setting of the Los Frailes Ignimbrite Complex

Since the Jurassic Period, the western margin of, what is now, South America has hosted a convergent margin with Pacific oceanic plate subduction (see review of Allmendinger et al., 1997). Currently, the Nazca plate converges with the South American plate at a near perpendicular direction to the Peru-Chile trench at a rate of ~63 mm a year for the central Andes (DeMets et al., 1990). This convergence is accommodated by the subduction of the Nazca plate beneath South America and has resulted in four main volcanic zones along the western Andean margin (see Figure 1.1). These include the CVZ, which is bracketed by non-volcanic gaps associated with the subduction of aseismic bathymetric oceanic ridges including the Nazca ridge to the north (Peruvian flatslab 5° to 15°S latitude) and the Juan Fernandez ridge to the south (Chilean-Pampean flatslab 27° to 33°S latitude) (e.g., Barazangi and Isacks, 1976; Pilger, 1981; Nur and Ben-Avraham, 1981). These non-volcanic gaps are thought to be caused by a flattening in slab subduction angle which results in a flatslab geometry as seen in the seismic contours (Cahill and Isacks 1992; Barazangi and Isacks, 1976). Contouring of the Wadati-Benioff zone of the subducting Nazca plate has revealed the seismic outline of the subducted Juan Fernandez ridge in Chile (e.g.,

Pardo et al., 2002; Gans et al., 2011) supporting the role of the ridge buoyancy in the resulting flatslab geometry. A decrease in the already relatively shallow ($\leq 30^\circ$) Nazca plate subduction angle leaves insufficient space between the slab and the South American lithosphere for normal asthenospheric circulation and results in a cessation of volcanic activity in that segment of the arc (e.g., Barazangi and Isacks, 1976).

As the Juan Fernandez ridge is not aligned parallel to the subduction direction (see Figure 1.1), the intersection of the ridge with the trench and subduction zone has progressed south and moved the resultant flatslab and non-volcanic gap with it (e.g., Yáñez et al., 2001; Kay and Coira, 2009). The re-initiation of CVZ volcanism at 19°S to 20°S latitude corresponds to the southward passage of the subducted Juan Fernandez ridge and the gradual steepening of a previous flatslab configuration at the end of the Oligocene (Paleogene) which marks the beginning of $\sim 25\text{-}28$ Ma of current volcanism at the Los Frailes Complex (James and Sacks, 1999). Figure 1.4 depicts the stages of slab steepening at 20°S latitude and the lithospheric changes proposed by this paper since 25 Ma.

Coeval with regional changes in the subducted slab geometry, the western margin of South America has undergone substantial crustal shortening with an estimate of >300 km since 40 Ma (e.g., McQuarrie, 2002; McQuarrie et al., 2005) at 20°S latitude. This shortening has been accommodated in the upper crust of the Altiplano and northern Puna by the east-vergent fold-and-thrust belt of the Eastern Cordillera (Cordillera Oriental) which is bounded to the east by the thin-skinned Subandean fold-and-thrust belt. Deeper crustal accommodation is facilitated by extensive associated crustal thickening (e.g., Isacks, 1988). Elger et al. (2005) argue that the west-central Altiplano and the Eastern Cordillera thrust systems are independent and only merge in the ductile lower crust (see Figure 1.5). A combined

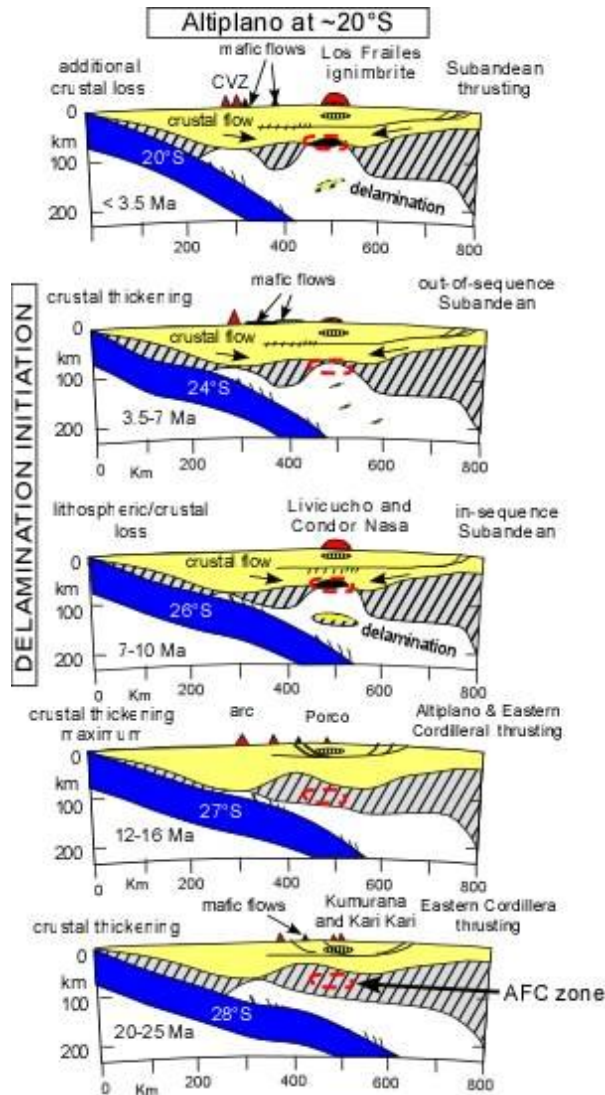


Figure 1.4

Lithospheric cross-section modified from Kay and Coira (2009) for evolution of the southern Altiplano. It reconciles the magmatic history of the Los Frailes Complex and slab geometries based on models for the current southern Puna region. This model shows eruption of large ignimbrites in response to lithospheric delamination and in association with steepening of the subduction zone (e.g., Kay et al., 1994; Kay and Coira, 2009). The importance of changing slab geometry models for the Altiplano was pointed out by James and Sacks (1999) and in the Puna by Kay et al. (1999). The white numbers on the slab profile are the latitudes at which the current Nazca slab corresponds to the geometry depicted in the cartoon. The red dashed circles show the proposed location of the AFC zone during each period.

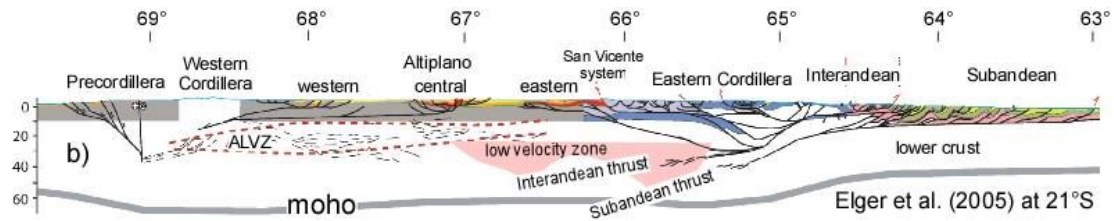


Figure 1.5

Lithospheric scale cross-section from Elger et al. (2005) and modified by Kay and Coira (2009) near 21°S latitude along the ANCORP Working Group (2003) and Re-Fu-Ca geophysical profiles (Heit et al., 2008) showing major structures merging into the ductile lower crust (discussed in text). Region labeled “low velocity zone” has the lowest velocity P-wave tomographic image of Heit et al. (2008) and was added by Kay and Coira (2009).

total shortening of 65 km has been suggested in the Altiplano from 27-33 Ma and 8-19 Ma, with deformation occurring in the Eastern Cordillera during the middle interval.

Three primary thrust systems; east-verging western, doubly-verging central and west-verging eastern, are thought to have accommodated the shortening in the Altiplano.

All three systems moved at a maximum combined rate of 4.7 mm/yr between 8 and 11 Ma at the time a delamination event proposed here is thought to have occurred and when the large Livicucho, Condor Nasa and Morococala ignimbrites were emplaced.

There is general agreement that deformation in the Altiplano and Eastern Cordillera shifted to the east after 10 Ma at the time the Subandean fold-and-thrust belt became active (e.g., Gubbels et al., 1993; Elger et al., 2005; McQuarrie et al., 2005).

McQuarrie et al. (2005) suggests that Cenozoic deformation within the mantle lithosphere was focused at the Eastern Cordillera- Altiplano boundary, beneath the Los Frailes Complex, which is the site of continued piecemeal delamination.

Altiplano crustal thickening is accompanied by proposed deep crustal flow (e.g., Isacks, 1988; Husson and Sempere, 2003; Gerbault et al., 2005) and the underthrusting of the Archean Brazilian Shield craton from the east (e.g., Isacks, 1988; Polet et al., 2000; Beck and Zandt, 2002). Oncken et al. (2006) place the regional

deformation rate at 8 mm/yr by the end of the Oligocene (~23 Ma) then maintained that average until 7-8 Ma when thrusting shifted into the Subandean belt and the rate increased to ~8-16 mm/yr. Current rates are put at 9.0 ± 1.5 mm/yr by Bevis et al. (2001) which is based on global positioning system (GPS) data.

Proposed models of Altiplano uplift are varied and include: crustal shortening (e.g., Isacks, 1988) and periodic upper-plate lithosphere loss (e.g., Hoke and Lamb, 2007), deep crustal flow (Husson and Sempere, 2003; Gerbault et al., 2005) and wholesale removal of a dense eclogitic lower crust and lithospheric-mantle by delamination with resulting isostatic rebound (Molnar and Garzzone, 2007). Estimates of plateau uplift rates range from a rapid 2000-3000 m rise between 6.8 and 10.3 Ma based on $\delta^{18}\text{O}$ of carbonate as well as paleobotany data (Ghosh et al., 2006; Garzzone et al., 2006), which necessitates a massive delamination (Molnar and Garzzone, 2007), to a more gradual increase driven by crustal shortening (Barnes and Ehlers, 2009).

The role of delamination has been proposed to play a role in both the uplift and magmatic histories of the Altiplano and Puna (see review of Kay and Coira, 2009). Magmatism in response to discrete delamination events at times of large ignimbrite eruptions is supported by Kay and Kay (1993), Kay et al. (1994, 1999) and Kay and Coira (2009) while McQuarrie et al. (2005), de Silva and Gosnold (2007) and Hoke and Lamb (2007) argue for a gradual, more piecemeal, loss of mantle through delamination. Following delamination, rebound of the remaining light silicic crust and thermally driven uplift from an influx of asthenospheric heat are argued to cause uplift (e.g., Molnar and Garzzone, 2007).

Figure 1.6 is a regional lithospheric cross-section interpretation from Beck and Zandt (2002) which shows a seismic low velocity (V_p and V_s) region interpreted as a gap in the lithosphere (shown in red) below the Los Frailes Complex with direct

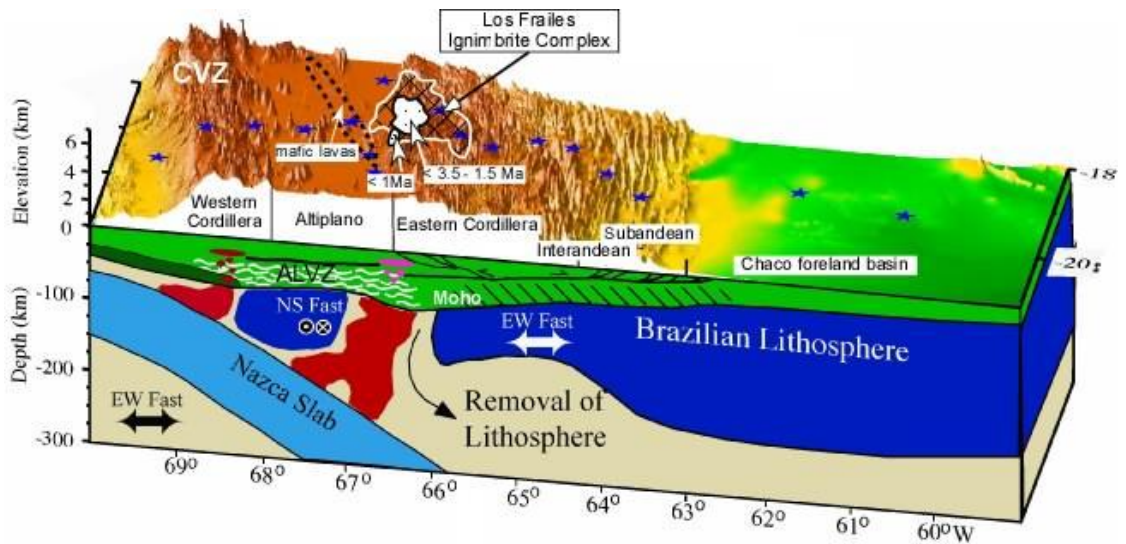


Figure 1.6

Schematic cross-section cartoon modified from Beck and Zandt (2002) by Kay and Coira (2009) showing the position of the Los Frailes Complex over seismic low velocity zones in the mantle (red) (Myers et al., 1998; Polet et al., 2000). Within the crust, the Altiplano low velocity zone (ALVZ) (Yuan et al., 2000) (white wavy lines) and middle-upper crust regions (red and pink) are interpreted as zones of partial melt (e.g., Zandt et al., 2003). Stars are locations of seismic stations (see Beck and Zandt, 2002). See text for full discussion.

contact between a felsic crust and the intruded high temperature asthenosphere (Myers et al., 1998; Polet et al., 2000; Beck and Zandt, 2002). Hoke and Lamb (2007) used a regional isotopic study of $^3\text{He}/^4\text{He}$ emissions to suggest recent mantle melting in a wide zone behind the arc at 20°S latitude, which is substantiated by seismic tomographic images of the same location. The central and western Altiplano has an intact lithosphere with a base at 125-150 km (Myers et al., 1998) with another low velocity region to the west below the Western Cordillera (Cordillera Occidental) and active arc (Myers et al., 1998; Polet et al., 2000; Beck and Zandt, 2002). A widespread low velocity anomaly has also been identified within the middle crust of the Altiplano and Eastern Cordillera by Yuan et al., (2000) who established the term Altiplano low velocity zone (ALVZ) to describe the broad area interpreted to contain

partial melt (white wavy lines in Figure 1.6). The receiver function study of Beck and Zandt (2002) found an additional low velocity Lg-wave (high frequency love waves) high attenuation anomaly directly beneath the Los Frailes Complex as well as to the west beneath the CVZ at depths of 14 to 20 km, which are also interpreted as partial melt zones (pink area in Figure 1.6). Under the Eastern Cordillera, just to the east of the Los Frailes Complex, a low velocity zone is shown at ~30 km by Beck and Zandt (2002). Convincing tomographic evidence for delamination as an ongoing mechanism in the Altiplano-Puna is provided by Schurr et al. (2006) and Asch et al. (2006) beneath the Altiplano-Puna Volcanic Complex (APVC) at the latitude of 23°-24°S and beneath the southern Puna at 25°-28°S by Bianchi et al. (2013). The southern Puna is a region of ongoing research in this area with the completion of a two-year-long deployment of a 74-station passive seismic array in October 2009. Figure 1.7 from Schurr et al. (2006), Asch et al. (2006) and Heit et al. (2008) shows what is interpreted as a block of detached cold continental lithosphere resting atop the subducted Nazca plate. This evidence of the descent of large blocks of delaminated lithosphere leads to the possibility that a comparable recent event generated the similar lithospheric hole beneath the Los Frailes Complex.

Composition of the Altiplano crust is distinctly siliceous, based on P-wave velocities of 5.8-6.25 km/s through the 59-64 km thick crust (Beck and Zandt, 2002). There could be no associated mafic base, suggesting it was also lost, though this is disputed by Yuan et al. (2002) who interpret a thin mafic layer at the crustal base. Thicker Altiplano crust of 73-75 km is reported to the south near 21°S latitude by McGlashan et al. (2008) and a variable thickness of ~60-80 km with eastward-thinning below the Eastern Cordillera (Yuan et al., 2002; McGlashan et al., 2008). Farther to the east, the Subandean zone is given a thickness of ~40 km and the Chaco foreland basin ~32 km by Beck and Zandt (2002).

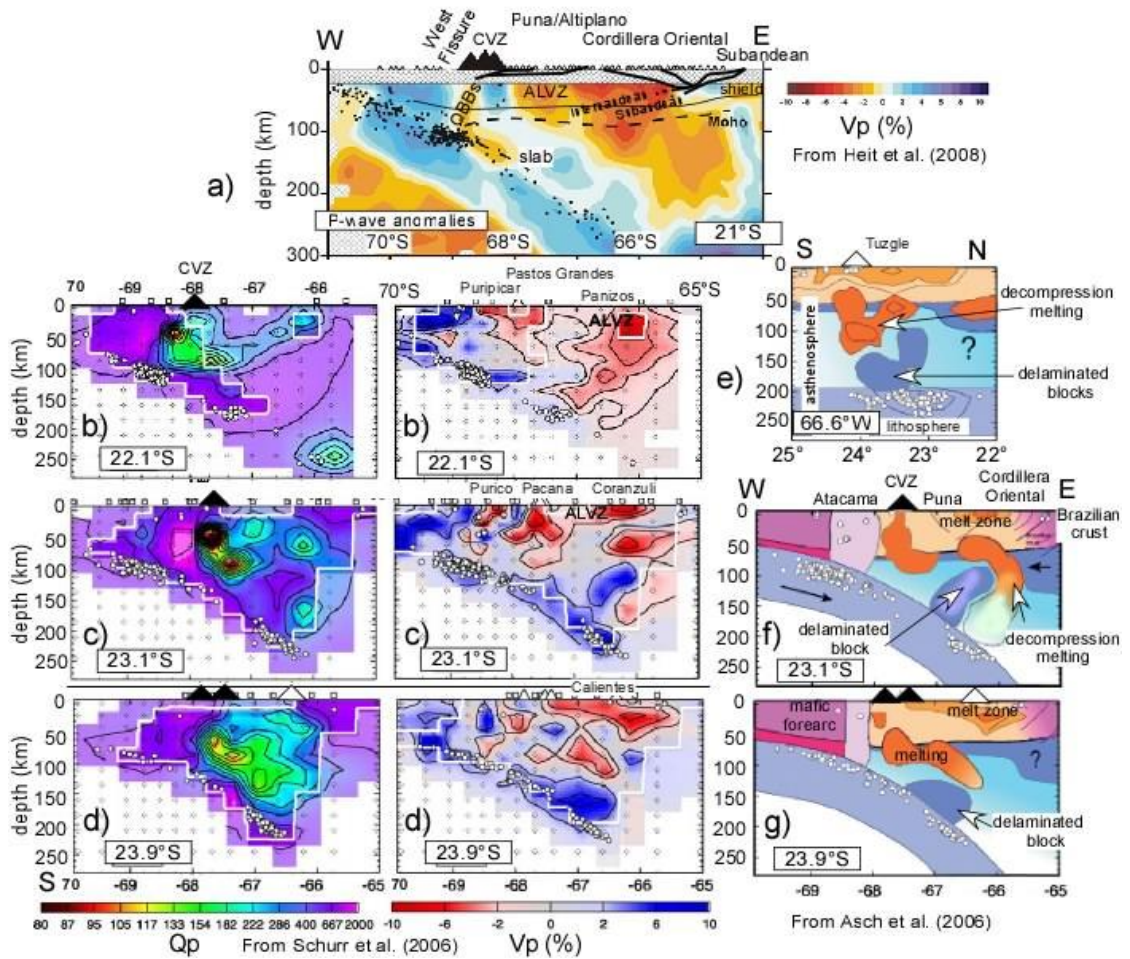


Figure 1.7

A compilation of seismic P-wave tomographic images and figures by Kay and Coira (2009) depicting ongoing delamination of the northern Puna lithosphere. A similar process is proposed to be ongoing in the central Altiplano with delamination occurring directly beneath the Los Frailes Complex. Images are arranged north to south at equal scale along with selected Qp (attenuation generally correlates with temperature; low values are highest temperatures) and interpreted images. Dots are earthquake hypocenter locations. (a) P-wave tomographic images of Heit et al. (2008). The solid black line is the Moho on the Elger et al. (2005) section in Figure 1.5. The dashed lines are the receiver function Moho of Heit et al. (2008). (b, c and d) Qp and Vp tomographic sections at 22.1°S, 23.1°S and 23.9°S latitudes from Schurr et al. (2006) with the position of some of the major ignimbrites from Figure 1.2. The white lines outline regions where the images are most robust. (e, f and g) Interpreted east-west and north-south sections of the northern Puna region modified from Asch et al. (2006). QBBs- Quebrada Blanca Bright spot.

Andean-type subduction zones have been argued to be sites of considerable continental crustal growth through magmatic addition. While magmatic addition has largely been excluded as the primary mechanism for plateau uplift (Francis and Hawkesworth, 1994; Allmendinger et al., 1997; Kay et al., 2011), determining the input sources and ratios is essential to understanding the relative volumes of new mantle-derived material versus recycled and assimilated continental material. This is done in order to quantify the true crustal volumetric growth by magmatism.

Arguments have been made for a near total crustal source for the CVZ ignimbrites by Francis et al. (1989) and Babeyko et al. (2002) as well as much lower estimates of near 50% by Ort et al. (1996), Caffè et al. (2002) and Kay et al. (2010, 2011).

Volcanic History of the Los Frailes Ignimbrite Complex

The Schneider (1985) thesis, which was published in part as Schneider and Halls (1985) and Schneider (1987) was the first comprehensive description of the Los Frailes Complex with a concentration of the study on the mineralized Kari Kari and Porco units. That study set the framework for further geochemical work. The Jiménez et al. (1997) study was centered on the Livicucho satellite meseta and caldera to the northeast of the main Los Frailes ignimbrite while the Luedke et al. (1997) study was to the south along the southern rim of the plateau from the Nuevo Mundo to Porco units (see Figure 1.3). The Keller (2010) thesis, using the same PT and PO series samples in this study, concentrated on the Condor Nasa meseta region and the northern Los Frailes unit.

Schneider (1985) divided the late-Oligocene to Quaternary volcanic history of the Los Frailes Complex into five main episodes, which are useful given some adjustment in the post-12 Ma time frame. The first episode near ~25 Ma includes the small volume metaluminous Kumurana granodiorite pluton intrusion in the extreme southeast of the Los Frailes Complex, which marks the beginning of magmatism in

south-central Bolivia following the postulated flatslab stage and its volcanic gap (James and Sacks, 1999) (see Figure 1.3). The Kumurana intrusion occupies $\sim 10 \text{ km}^2$ on the southern edge of the much larger Kari Kari unit and contains high temperature Sn-W ores associated with its dike system. The Azanaques ignimbrite deposits on the northwest edge of the Los Frailes Complex with Pb, Ag and Sn sulfide mineralization and the mineralization in the Santa Barbara Mining District 8 km to the southeast were also emplaced near this time. No unaltered samples of the Azanaques unit have been described geochemically.

The second episode lasted from $\sim 20\text{-}23 \text{ Ma}$ and consists of the Agua Dulce volcanics and later peraluminous Kari Kari trapdoor caldera deposits (Francis et al., 1981). While field differences exist, the Agua Dulce and Kari Kari samples are geochemically indistinguishable and are combined as the Kari Kari group in this study. The $30 \times 30 \text{ km}$ Kari Kari unit is assessed to have had an original volume of 550 km^3 of ejected ashflow material (Schneider, 1985).

The third stage is named the Cebadillas episode which occurred at $9\text{-}17 \text{ Ma}$. The primary activity during this time was the emplacement of the Porco volcanic group in the area between the cities of Potosi and Porco (see Figure 1.3). Important vein mineralization of Sn, Ag, Zn, Bi and U ores as well as the world's largest Ag deposit at Cerro Rico de Potosi dome (Zartman and Cunningham, 1995; Cunningham et al., 1996; Rice et al., 2005) occurred during this time. In addition to the main Porco unit, smaller volume Cebadillas episode volcanic units are also exposed beneath the Livicucho and western Los Frailes ignimbrites and given the labels pre-Livicucho and pre-Los Frailes in this study. Associated with these widespread eruptions are younger deposits, as recent as $\sim 9 \text{ Ma}$, which make up the western edge of the Los Frailes meseta. A Sevaruyo region sample in this study from southwest of Livicucho is thought to be within this temporal group.

The fourth episode was originally termed the Los Frailes Cover by Schneider (1985) when the Los Frailes unit was thought to be late Miocene in age. This was based on a $^{40}\text{K}/^{39}\text{Ar}$ age of 7.8 Ma for an ash-flow tuff within the main Los Frailes unit formation about 5 km southeast of Estacion Yura (Baker and Francis, 1978). That age is within the 5-9 Ma age window given the tuffs in the northwestern part of the Los Frailes ignimbrite field (Evernden et al., 1977; Baker and Francis, 1978; Grant et al., 1979; Schneider and Halls, 1985; Kennan et al., 1995). In this study, it is called the Livicucho-Condor Nasa episode and given an age range of 5 to 8 Ma and includes the large Livicucho and Condor Nasa volcanic units. The Livicucho center is 40 km in diameter and erupted up to 1000 km^3 of material (Schneider, 1985; Jiménez et al., 1997). The Condor Nasa unit to the southeast of Livicucho is slightly smaller with an estimated erupted volume of greater than 500 km^3 (Schneider, 1985). Additionally, this episode includes the previously mentioned volcanic rocks on the northwestern portion of the Los Frailes meseta nearest Livicucho where ages are ~5-6 Ma.

The fifth and final episode is appropriately termed here the Los Frailes Cover as it includes the main 1.5-3.5 Ma Los Frailes ignimbrite and spans the period from 3.5 Ma to the present (see Chapter 4 for discussion of ages). These units consist of moderately welded ash flow tuff sheets with typical thicknesses of 250-300 m and a total volume as great as 2000 km^3 , which likely covers earlier, potentially mineralized units under its nearly 8500 km^2 span (Schneider, 1985). Multiple eruptive centers are thought to have participated in the episode and were preceded by the development of large domes in the central portion of the meseta, some of which were sampled and dated by Schneider (1985). The Nuevo Mundo volcanic center to the south is the youngest unit within the Los Frailes Complex with flows as recent as <1.0 Ma consisting of block and ash and dacitic coulees (Luedke et al, 1997; Jiménez et al., 2005). Lava flows are seen over <11000 year old glacial moraines and are similar in

composition and mineralogy to the dacitic tuffs of the Los Frailes unit (Luedke et al., 1997). Cordierite is reported in the capping flows by these authors. This center may also be the source of a white air fall ash, with a sanidine $^{40}\text{Ar}/^{39}\text{Ar}$ age of 0.374 ± 0.22 Ma (Rice et al., 2005), which is seen along much of the southern margin of the main Los Frailes ignimbrite. The Nuevo Mundo center is located directly over the seismic low velocity anomalies in the crust indicating an intimate and recent association (see Figure 1.6).

Comparison to Cerro Galán, selected APVC and Morococala Ignimbrites

The Cerro Galán ignimbrite center is one of the most studied and well understood in the Altiplano-Puna backarc. It has a nearly equivalent erupted volume to the Los Frailes Complex and is situated south of the APVC in the southern Puna (see Figure 1.2 and Table 1.2). The Galán (2.0-2.8 Ma) and multiple Toconquis (3.8-6.4 Ma) ignimbrites are the major units which are underlain by late Precambrian and Paleozoic crystalline and sedimentary rocks. Studies by Sparks et al. (1985), Francis et al. (1989) and Kay et al. (2011) include dates as well as whole rock major and trace element data, microprobe analyses on mineral phases and Sr, Nd, Pb and O isotopic analyses. A well-defined three tier model of magma evolution is described by Kay et al. (2010) and is the basis for a similar system proposed for the Los Frailes Complex in this paper. Based on Sr AFC modeling and $\delta^{18}\text{O}$ values from quartz phenocrysts, Kay et al. (2010, 2011) concluded that the Cerro Galán ignimbrites consist of a near 50:50 mixture of enriched mantle and crustal melts. The same methodology will be used in this paper with the Nd system added to the AFC calculations.

Table 1.2

Sr, Nd and O isotopic and concentrations values of selected Altiplano-Puna ignimbrites									
Sample	SiO ₂ (wt. %)	Age (Ma)	⁸⁷ Sr/ ⁸⁶ Sr*	Sr ppm	¹⁴³ Nd/ ¹⁴⁴ Nd	ε _{Nd}	Nd ppm	δ ¹⁸ O _{Quartz} ‰ Measured	δ ¹⁸ O _{Magma} ‰ Calculated
<u>APVC Large Volume</u>									
Coranzuli ^a	65-69	6.4-8.4	0.71221	340	-	-	35	+9.8-9.9	+9.5-9.6
Panizos ^a	61-66	6.7-10	0.71478	300	0.512129	-9.9	42	+10.0-10.2	+9.7-9.9
Vilama ^a	63-68	8.4-8.5	0.71505	280	0.512158	-9.4	33	+9.2-9.5	+8.9-9.2
<u>APVC Small Volume</u>									
Granda ^a	63-68	9.5-10.5	0.71595	300	0.512148	-9.6	38	+9.0-10.0	+8.7-9.7
<u>Puna Large Volume</u>									
Cerro Galán ^b	67-70	2.1-6.4	0.71150	270	0.512240	-7.8	39	+8.3-9.2	+8.0-8.9
<u>Altiplano Large Volume</u>									
Morococala ^c	69-76	6.4-8.4	-	300	-	-	33	-	-

Greater than 500 km³ of DRE erupted material is considered large volume. Following Chang (2007), the fractionation correction for quartz is about 0.3‰ for Δqtz-melt and therefore 0.3‰ was subtracted from δ¹⁸O_{quartz} to produce δ¹⁸O_{magma}.

^a Kay et al. (2010).

^b Kay et al. (2011).

^c Morgan et al. (1998).

* Initial ratios.

The Kay et al. (2011) three tier crustal evolution model at Cerro Galán calls for processes at lower crustal, middle crustal and upper crustal levels. In the lower crust, amphibolite partial melts mix with mantle basalts and produce hybrid melts. These melts evolve under high pressure conditions imparting steep heavy rare earth element (HREE) patterns and very low Nb/Ta ratios in the melt. As the melts rise, they leave a gravitationally unstable garnet-bearing residue (restite) which sets the stage for delamination of the upper mantle and lower crust as originally argued by Kay et al. (1994). Middle crustal level processes involve storage in zones of crystalline mush at temperature near 800°-850°C. Here, plagioclase stability and fractionation increases, which creates negative Eu anomalies and variable trace element enrichment. Repeated magma recharge and evacuation into the upper crust is thought to occur during times of regional contraction. Once in the upper crust, temperatures drop to as low as 680°C and crystallization increases. Ignimbrite chemical variability is attributed to differences in near-eutectic crystallization prior to eruption. Kay et al. (2011) also argues that

episodic delamination of gravitationally unstable lithosphere and lower crust is directly related to crustal heating and thereby to the eruption history of Cerro Galán.

The APVC is one of the largest ignimbrite provinces on Earth and is the dominant feature on the central part of the Altiplano-Puna plateau (e.g., de Silva, 1989; Coira et al. 1993). The APVC is located on the northern Puna at the margin of the Puna and Altiplano and straddles the change from a more sedimentary basement in the north to a more igneous basement to the south (see Figure 1.2). It has been the center of much of the work on the structure and chemistry of the Altiplano-Puna ignimbrites and both major and trace element geochemistry and Sr, Nd, Pb and O isotopic data are available (e.g., Kay et al., 1999, 2010; Trumbull et al., 2006). The four APVC centers most geochemically similar to the Los Frailes Complex, and used for comparison here, are the large volume Coranzuli ($>650 \text{ km}^3$), Panizos ($>650 \text{ km}^3$) and Vilama ($\sim 1400 \text{ km}^3$) ignimbrites as well as the small volume Granda ignimbrite (Table 1.2). The best studied are the Panizos (e.g., Ort et al., 1996) and Vilama ignimbrites (e.g., Soler, 2005; Soler et al., 2007). All four centers are moderately to strongly peraluminous and are the northernmost units in the APVC (see Figure 1.2). Kay et al. (2010) used a methodology like that applied to Cerro Galán ignimbrites in using fractionation corrected $\delta^{18}\text{O}$ values from quartz and Sr AFC solutions to model the APVC ignimbrites as a near 50:50 hybrid mixture of mantle and crustal melt.

The last comparative volcanic unit is the 6.4 to 8.4 Ma Morococala ignimbrite located about 75 km to the northwest of the Los Frailes Complex (see Figure 1.2 and Table 1.2) and best described by Morgan et al. (1998). The Morococala center consists of three primary ash-flow units erupted at three localities from 6.4 to 8.4 Ma. The oldest unit is made of andalusite-bearing two-mica rhyolitic tuffs, the middle unit is a cordierite-biotite bearing rhyolitic tuff while the youngest capping unit consists of biotite-quartz latitic tuffs and domes (Koeppen et al., 1987). While the Morococala

center is more silicic (69-76% SiO₂) and volumetrically smaller, it is the closest major ignimbrite to the Los Frailes Complex and shares its sedimentary basement, highly peraluminous character and association with the Bolivian tin belt. Whole-rock major and trace element data as well as mineral analyses are included in Morgan et al. (1998), however, no isotopic data has been reported for Morococala.

CHAPTER 2

ANALYTICAL METHODS

Major Element Analyses

Whole-rock major element and Rb, Nb, Y, and Zr concentrations were determined by X-ray fluorescence (XRF) at the University of Jujuy in Argentina, following analytical methodology delineated in Caffè et al. (2002). Samples were selected and trimmed in the field to minimize the effect of weathering. In order to avoid contamination and minimize systematic error between techniques in the chemical analyses, all whole rock analyses were conducted on the same bulk-rock powders mechanically pulverized in an alumina shatter-box.

Trace Element Analyses

Whole-rock trace element analyses by instrumental neutron activation analysis (INAA) were conducted at Cornell University after sample irradiation at the North Carolina State University PULSTAR research reactor. Prior to neutron irradiation, samples and standards were prepared by sealing bulk rock powder of known mass (~0.5 g) in high-purity silica glass ampoules. Following irradiation, ampoules were individually placed in front of a Pb brick shielded ORTEC GEM-20170-S solid-state gamma-ray spectrometer and counted for 3-10 hours each to determine each sample's gamma-energy spectrum, which was then interpreted by comparison to three in-house standards, correcting for decay and interferences (standard analyses shown in Appendix B). In order to obtain a more complete set of analyses of elements with both short and long half-life radioisotopes, samples were counted twice: first for ~3 hours each, beginning seven days after irradiation; and second for ~10 hours each, starting at least 30 days after irradiation.

Mineral Analyses

In situ mineral analyses were completed at the Cornell University Center for Materials Research Electron Microprobe Laboratory. Nine specimens (PT-1, PT-3, PT-8, PT-9, PT-10, PT-11p, PT-12, PT-14 and PT-16) were cut and polished to 30 μm and examined by petrographic microscope in order to describe mineral assemblages and to identify individual crystal phenocrysts for electron microprobe analysis. Seven samples (PT-1, PT-3, PT-8, PT-11p, PT-12, PT-14 and PT-16) were coated with sputtered graphite carbon for microprobe analysis to determine the elemental compositions of major minerals, as well as to identify minerals too small to be detected or identified petrographically. Individual mineral grains were analyzed by a JEOL 8900 in wavelength dispersive (WDS) mode with a beam diameter of 10 μm , accelerating voltage of 15 kV and an incident current of 2.00×10^{-8} amps. The oxides analyzed were SiO_2 , TiO_2 , Al_2O_3 , FeO , MnO , MgO , CaO , Na_2O , and K_2O . Three or more measurements were regularly made at each analysis point and an average of valid measurements used. When possible, measurements were made at both the core and rim of a grain to determine if zoning was present that was not identified petrographically. Smithsonian volcanic glass standards A-99, Juan de Fuca (JDF) and rhyolite glass (RG) along with natural mineral standards Lake City plagioclase (LCP), PX-1 clinopyroxene and Kakanui hornblende (KH) were measured three times each at the beginning and end of each daily session. The deviation from known values was then used to produce a daily correction value for each oxide. Analyses with low total weight were removed. Standards and data are presented in Appendix F.

Strontium and Neodymium Isotopic Analyses

Isotopes of Sr and Nd were analyzed in the W.M. Keck Foundation Isotope Laboratory at Cornell University using a Fisons Instruments VG Sector 54 Thermal Ionization Mass Spectrometer (TIMS). Samples were prepared and analyzed

following the method described by White and Duncan (1996). Procedures were carried out in a clean environment using Teflon containers and chemicals purified through sub-boiling distillation. Rock specimens were powdered and 0.05 gram sample portions dissolved in 1.0 ml 6.0N QD HCl and then dried. 2.0 ml of HF and 0.1 ml of HClO₄ were added to the samples which were dried and then heated to evolve SiOF₄ and HClO₄ gasses. The samples were dissolved in 3.0 ml of 6.0N QD HCl then dried before again being dissolved in 1.2 ml of 2.5N QD HCl. The solutions were loaded in a centrifuge for 15 minutes at 5000 rpm after which the top 1.0 ml of each sample was pipetted off and loaded in a cation exchange column with Dowex 50WX8 (400 mesh) resin (columns were prepared and calibrated by Ashley Tibbetts at Cornell University). Sr and rare earth elements (REE) fractions were then extracted and collected by elution with 2.5N and 6.0N QD HCl. A second extraction of Nd from the REE fraction was done using Eichrom LN Resin 100-150 micron columns with 0.23N QD HCL. See Appendix A for detailed Nd column calibration and separation procedures.

Sr and Nd fractions were then loaded on tungsten and rhenium filaments respectively and analyzed by TIMS using a dynamic multicollection technique. ⁸⁶Sr/⁸⁸Sr ratio is normalized to 0.11940 to correct for mass fractionation and the measured ⁸⁷Sr/⁸⁶Sr ratio mean for the NBS 987 Sr standard is 0.71023 (n=27, from 10/2011 to 8/2012). The ⁸⁷Sr/⁸⁶Sr ratio analytical uncertainty is estimated at ±0.00003 (2σ error). The ⁸⁷Sr/⁸⁶Sr measured ratios are corrected to ⁸⁷Sr/⁸⁶Sr initial ratios using the assigned ages and the ⁸⁷Rb→⁸⁷Sr β- decay constant of λ=1.396x10⁻¹¹y⁻¹ (Rotenberg et al., 2012). In the cases of PT-14 and PT-16 which have Sr concentrations but no associated Rb concentrations, a value of 230 ppm Rb was used. All ⁸⁷Sr/⁸⁶Sr ratio values reported and used in this study are calculated initial ratios. The ¹⁴⁶Nd/¹⁴⁴Nd ratio is normalized to 0.72190 to correct for mass fractionation and

the measured $^{143}\text{Nd}/^{144}\text{Nd}$ ratio mean for the Ames Nd standard is 0.512167 (-9.19 ϵ_{Nd}) (n=13, from 2/2012 to 5/2012). The $^{143}\text{Nd}/^{144}\text{Nd}$ ratio analytical uncertainty is estimated at ± 0.000040 (2σ error). Reported $^{143}\text{Nd}/^{144}\text{Nd}$ ratio values are normalized to $^{143}\text{Nd}/^{144}\text{Nd}_{\text{Ames}} = 0.512131$ ($\epsilon_{\text{Nd Ames}} = -9.89$) which resulted in a correction factor of -0.000036 ($\epsilon_{\text{Nd}} = -0.70$) that is applied to the reported values. Where reported in ϵ_{Nd} , a value of $^{143}\text{Nd}/^{144}\text{Nd}_{\text{CHUR}} = 0.512638$ is used. Data, standards and errors are presented in Appendix C.

Oxygen Isotopic Analyses

Oxygen isotopes were analyzed by laser fluorination on select quartz mineral grains following the procedure of Harris and Vogeli (2010). Ten samples were disaggregated and 1-4 mg quartz grains selected using a binocular microscope and tweezers at Cornell University and then sent to the University of Cape Town Department of Geological Sciences. Analyses were conducted on individually hand-selected quartz phenocrysts. Quartz is thought to be the least altered major mineral, and was used in order to avoid matrix alteration of tuff which was seen to be a problem with some whole rock oxygen values in the APVC (e.g., Kay et al. 2010). The individual mineral grains were then analyzed using a 20 W New Wave CO₂ laser mounted on a moveable stage. Measured values for unknowns were corrected to the average measured value for the internal standard of Monastery Garnet (MONGT, $\delta^{18}\text{O} = 5.38\text{‰}$ assuming a value of 5.80‰ for UWG-2). SMOW ($^{18}\text{O}/^{16}\text{O} = 3.990 \times 10^{-4}$) was used to calculate $\delta^{18}\text{O}$ values. In run error (2σ) is estimated at $\pm 0.10\text{‰}$ (n=6, from 1/11/2013 to 1/18/2013). A quartz-melt fractionation correction value is calculated following Chang (2007). The fractionation correction for quartz is about 0.3‰ for $\Delta_{\text{qtz-melt}}$ and therefore 0.3‰ is subtracted from $\delta^{18}\text{O}_{\text{quartz}}$ to produce $\delta^{18}\text{O}_{\text{magma}}$. Data, standards and errors are presented in Appendix D.

Fractionation-corrected $\delta^{18}\text{O}_{\text{Magma}}$ values are used to calculate the $\delta^{18}\text{O}$ of the crustal end-member with various crust-to-mantle source ratios and assuming the mantle, crust and cumulates all have the same oxygen concentrations. The $\delta^{18}\text{O}$ of the mantle is set at +5.8‰ (e.g., Bindeman, 2008; Kay et al., 2010, 2011) and crust-to-mantle mixing ratios of 40:60, 50:50 and 60:40 are used. The Kari Kari and Kumurana centers were not measured as quartz is not present in the available samples.

Zircon Isotopic Analyses

Zircons were analyzed for U and Pb isotopes by Brenhin Keller at Princeton University using an Isotopx Phoenix62 thermal ionization mass spectrometer (Pb by peak-hopping on a Daly detector; U on Faraday cups). All the steps after taking the zircons out of epoxy were conducted in class 10 (<10 particles >5microns in size per cubic foot of air) laminar flow clean hoods in a class 1000 clean room, and all reagents were sub-boiling distilled with <.15 picograms/gram Pb. NBS 981 and SynZirc 100Ma standards were used for U and Pb. The procedures follow Parrish and Noble (2003) which also contains a thorough review of isotope dilution – thermal ionization mass spectrometry (ID-TIMS).

Each sample was ground to a ~300 micron powder with a disc mill, zircons were then isolated by magnetic susceptibility with a Frantz isodynamic magnetic separator and density with methylene iodide. The isolated zircons were then annealed for 48 hours at 900°C and relatively inclusion-free grains were picked by hand and mounted in epoxy. They were then ground and polished halfway through before being carbon coated with ~20 nanometers sputtered graphite. Imaging was conducted by cathodoluminescence (CL) with a Gatan Mini CL detector in a Quanta XL30 SEM. The zircons were then removed from epoxy and cleaned in acetone for 24 hours, chemically abraded in concentrated HF for 12 hours at 185 C in Teflon microcapsules and finally rinsed with 6N HCL, H2O and concentrated HF. They were then spiked

with ~0.006 g EarthTime 535 spike, dissolved in concentrated HF for 24 hours at 210 C before being evaporated to dryness on hot plate. The samples were then redissolved in 6N HCl at 185 C for 12 hours before using Eichrom anion exchange resin (chloride form) to isolate U and Pb. Isolated U and Pb were dried down together with one microdrop 0.0015 M H₃PO₄ and then loaded on degassed rhenium filaments with silica gel. Data standards and errors are presented in Appendix E.

⁴⁰Ar-³⁹Ar Age Analyses

Sanidine crystals from samples PT-8 and PT-11 along with the 28.201 Ma Fish Canyon tuff sanidine (FCs) standards (Kuiper et al., 2008) were irradiated for 5 hours at the Oregon State University TRIGA-type reactor in the Cadmium-Lined In-Core Irradiation Tube. Analyses at University of Wisconsin-Madison Rare Gas Geochronology Laboratory were done by Brian Jicha. Single sanidine grains were fused using a 25 Watt CO₂ laser followed by an additional 5 minutes for gas cleanup. The gas was cleaned during and after the heating period with two SAES C50 getters, one of which was operated at ~450°C and the other at room temperature. Blanks were analyzed after every second laser fusion, and were less than 4×10^{-17} , 3×10^{-19} , 6×10^{-20} , and 2×10^{-19} moles for ⁴⁰Ar, ³⁹Ar, ³⁷Ar, ³⁶Ar, respectively. Ten to twenty mass discrimination measurements via automated analysis of air pipettes were made prior to, and following each incremental heating experiment and encompass the range of ⁴⁰Ar observed for the samples. Measured ⁴⁰Ar/³⁶Ar ratios of atmospheric argon were normalized to ⁴⁰Ar/³⁶Ar = 295.5 (Steiger and Jäger, 1977) and the discrimination was calculated using a linear law relationship.

Argon isotope analyses were done using a MAP 215–50, and the isotope data was reduced using ArArCalc software version 2.5 <<http://earthref.org/ArArCALC/>>. Ages were calculated from the blank-, discrimination- and decay-corrected Ar isotope data after correction for interfering isotopes produced from K and Ca during neutron

irradiation in the nuclear reactor. The age uncertainties reported in Appendix G reflect analytical contributions only at the 2σ level; the decay constants used are those of Min et al. (2000). Data, standards and errors are detailed in Appendix G.

Geothermometry and Geobarometry Analyses

Zircon saturation thermometry is applied to all samples with appropriate Zr concentration data using the major and trace element data reported here and the equations of Watson and Harrison (1983). The six samples of the PO series were calculated previously by Keller (2010) and only reconfirmed here. Two-feldspar thermometry of plagioclase-sanidine pairs is done by using the mineral data collected by microprobe analysis and calculations using the SOLVCALC program (Wen and Nekvasil, 1994), which uses the thermodynamic models of Nekvasil and Burnham (1987). Separate calculations were performed for plagioclase cores and rims for each sample at pressures between 200 and 1200 MPa and reported at 400 and 1000 MPa. Optical microscopy and microprobe analysis were used to look for the presence of cordierite. The presence of cordierite indicates low pressure equilibrium at ≤ 450 MPa which is equivalent to a crustal depth of ~ 15 km or less.

CHAPTER 3

ANALYTICAL RESULTS

While most of the 25 analyzed samples had major and trace element data and isotopic values that fell within a restricted analytical range for a respective unit, there were three samples that did not. The first is Kumurana sample PT-4, which is significantly different than the four Kumurana samples with reported major and trace element data in Schneider (1985). In all cases, PT-4 shares chemical values with the Schneider (1985) Kari Kari samples and only plots in the Kumurana field where it overlaps the Kari Kari field. Based on its chemical distinctness from Schneider (1985) Kumurana values, PT-4 will be labeled as a Kumurana sample, but will not be used to expand the Kumurana field. This has implications when discussing $^{143}\text{Nd}/^{144}\text{Nd}$ (ϵ_{Nd}) data as PT-4 is the only Kumurana sample which has been analyzed.

The other two samples are PO-5 and PO-6 from the Sevaruyo region. As these two samples are the only Sevaruyo region samples yet studied, no comparison can be made to existing data. PO-6, with an intermediate 66% SiO_2 , has extensive similarities to the main Los Frailes ignimbrite chemistry. PO-5 has a unique chemistry with the highest SiO_2 seen in the Los Frailes Complex (72% SiO_2) and concentration and isotopic values that do not resemble any other unit. PO-6 was collected from a stone fence next to a quebrada and may be transported fill material from a main Los Frailes meseta type source to the east. Both samples will be displayed with Sevaruyo symbology on plots, but should not be relied upon for extensive interpretation. PO-5 is assumed to be the most representative of the chemistry of the Sevaruyo region unit and will be denoted on plots.

PT-14 from Livicucho is the only sample that does not have a complete major elemental data set. PT-14, PT-10, PT-16 and PT-16p from Livicucho and the Los

Frailes unit are missing some trace element concentration data as well. Full analytical results for major and minor elements are found in Appendix B.

Major Elements

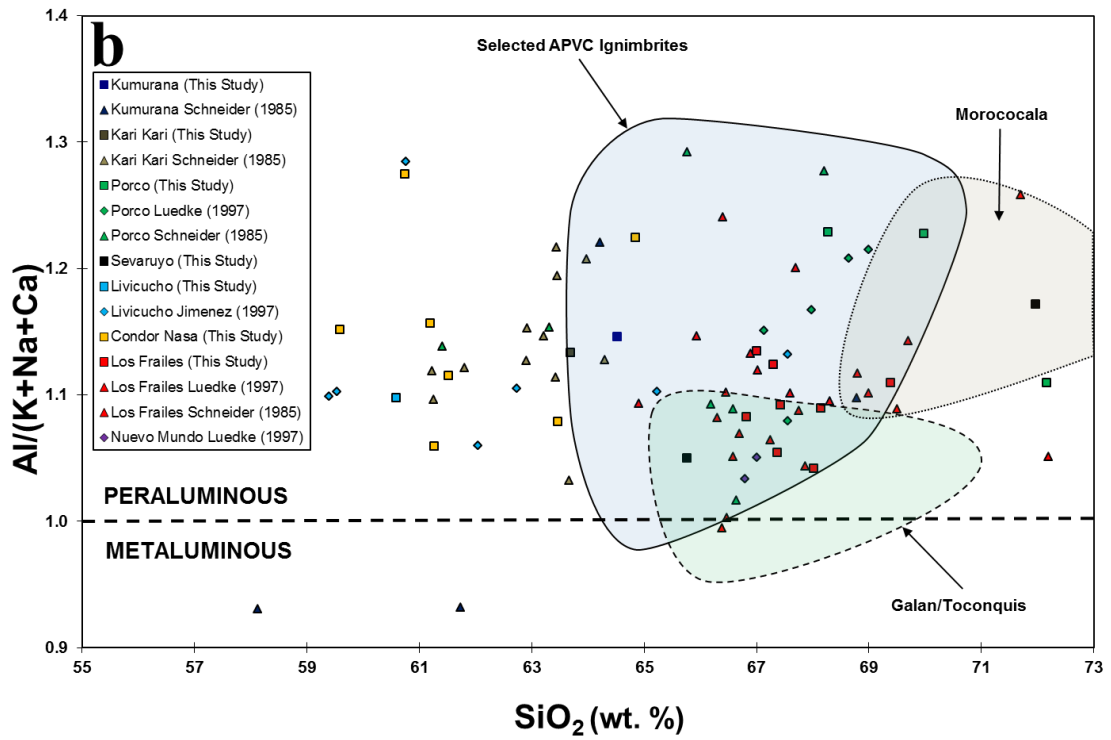
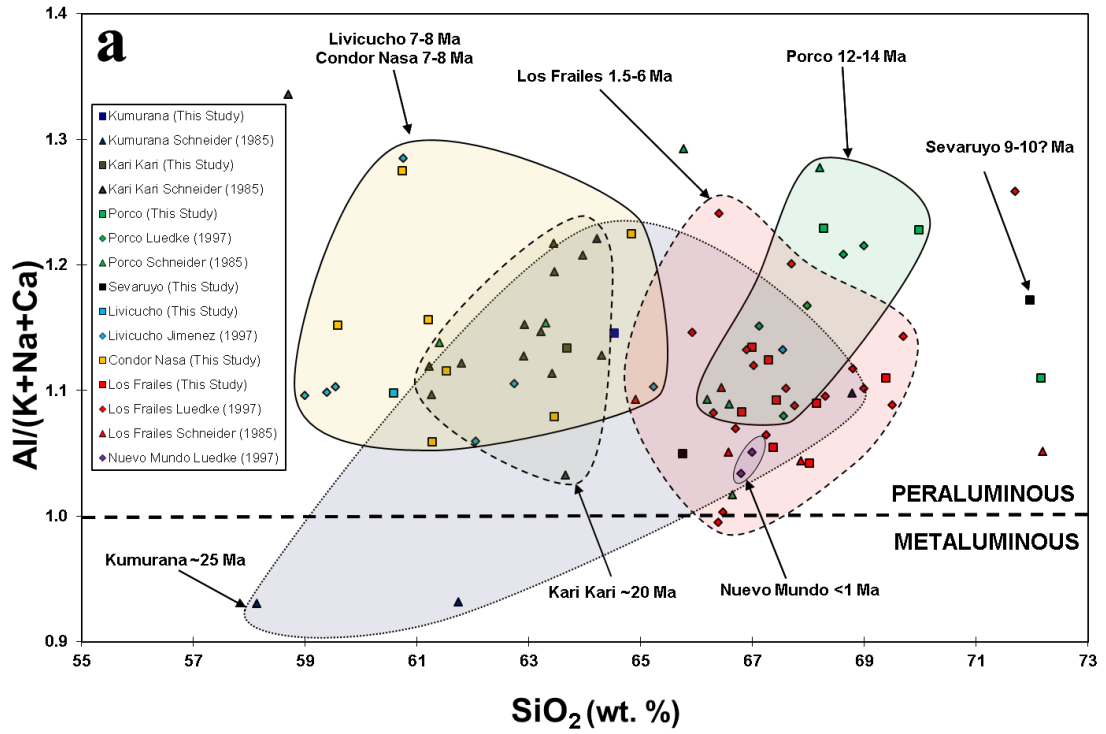
All samples from this study exhibit a clear peraluminous nature with Al/(K+Na+Ca) values between 1.04-1.28 (Figure 3.1a). All units have Al/(K+Na+Ca) ratios close to 1.2 with the exception of the Los Frailes ignimbrite which has a lower average of near 1.1. In Figure 3.2, all but one silica-rich (>64% SiO₂) samples plot in the S-type (*sedimentary*) granitoid field of the sedimentary-igneous-anorogenic-mantle (S-I-A-M) classification (Chappell and White, 1974; Loiselle and Wones, 1979; White, 1979). Silica-poor (<64% SiO₂) Livicucho and Condor Nasa have lower, more S-type, values. Figure 3.3 depicts wt. % K₂O set against wt. % SiO₂ and shows the high K₂O content of the Los Frailes Complex with all samples plotting in or near the shoshonitic field. Only three samples, which are all >68% SiO₂, from Porco, the Sevaruyo region and the Los Frailes ignimbrite are in the upper high-K field.

Trace Elements

Figure 3.4a is a primitive mantle normalized plot of trace element concentrations, using the normalization values of Sun and McDonough (1989), depicted on a logarithmic scale of representative samples from the various Los Frailes Complex units. The negative slope of the REE portion reflects light rare earth element (LREE) enrichment and variable HREE depletion and will be discussed further using La/Sm, Sm/Yb and La/Yb ratios. HFSE element depletion is also clearly seen with Nb, Ta and Ti exhibiting marked variation between units. Low Ba/La and Ta/Nb ratios are also present.

Figure 3.1

Plot of $Al/(K+Na+Ca)$ versus weight percent SiO_2 depicting the highly peraluminous nature of Los Frailes Complex. (a) There may be a slight temporal decreasing peraluminous trend in <10 Ma samples, as the Livicucho-Condor Nasa values average is ~ 1.2 , the Los Frailes ignimbrite values are between 1.1-1.2 and the youngest <1 Ma Nuevo Mundo values are ~ 1.1 . (b) The large APVC centers; Coranzuli, Panizos and Vilama as well as the smaller Granada, are the most peraluminous ignimbrites found on the Puna plateau with other volcanic centers showing generally intermediate to metaluminous values as represented by Cerro Galán. The central Altiplano ignimbrite Morococala has similar peraluminosity to the Los Frailes Complex of 1.1-1.3. Symbols: (a and b) Los Frailes Complex: squares- This study and Keller (2010), diamonds - Jiménez et al. (1997) and Luedke et al. (1997), triangles – Schneider (1985); (b) Cerro Galán and APVC fields as compiled in Kay et al. (2010, 2011); Morococala field as compiled by Morgan et al. (1998).



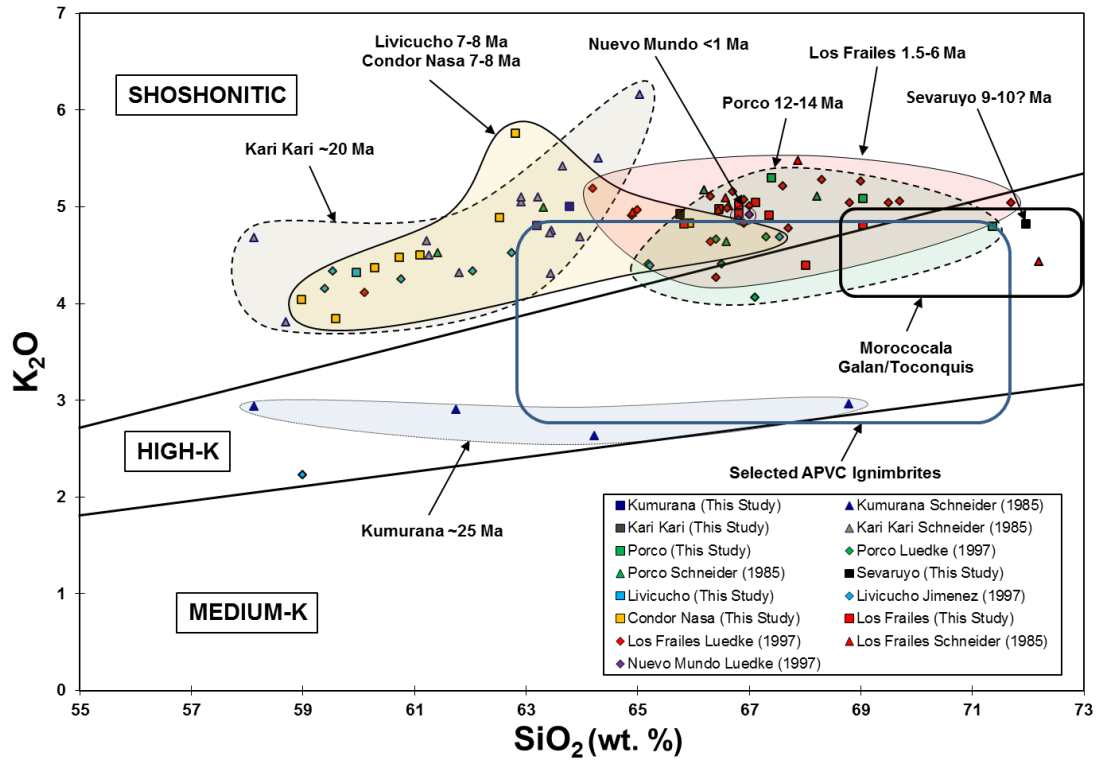


Figure 3.3

Plot of weight percent K_2O versus weight percent SiO_2 displaying the high K_2O content of the <20 Ma units in the shoshonitic field while the older ~25 Ma Kumurana unit has distinctly lower K_2O values in the high-K field. The Los Frailes Complex (except Kumurana) K_2O values are higher than those seen in the four APVC ignimbrites (blue box) or at Morococala and Cerro Galán (black box). Symbols: Los Frailes Complex: squares- This study and Keller (2010), diamonds - Jiménez et al. (1997) and Luedke et al. (1997), triangles – Schneider (1985); Cerro Galán and APVC fields as compiled in Kay et al. (2010, 2011); Morococala field as compiled by Morgan et al. (1998).

Figure 3.4

Primitive mantle normalized plots of trace element concentrations on a logarithmic scale from (a) the various Los Frailes Complex units and (b) representative samples from the peraluminous APVC ignimbrites, Cerro Galán and Morococala centers with Kari Kari, Porco and the main Los Frailes units of the Los Frailes Complex for comparison. (a) The negative slope of the REE portion reflects LREE enrichment (high La/Sm ratios) and variable HREE depletion (Sm/Yb ratios). HFSE element depletion is also clearly seen with Nb, Ta and Ti exhibiting marked variation between units. (b) All share similarly negative REE trends reflecting LREE enrichment and HREE depletion but with reduced slopes compared to those seen at the Los Frailes Complex. Depletion of HFSE elements Nb, Ta and Ti is also seen but with lower Nb/Ta and extreme Ti depletion in Morococala.

Los Frailes Complex concentrations: This study and Keller (2010); Cerro Galán and APVC concentrations: as reported by Kay et al. (2010, 2011); Morococala concentrations: as reported by Morgan et al. (1998).

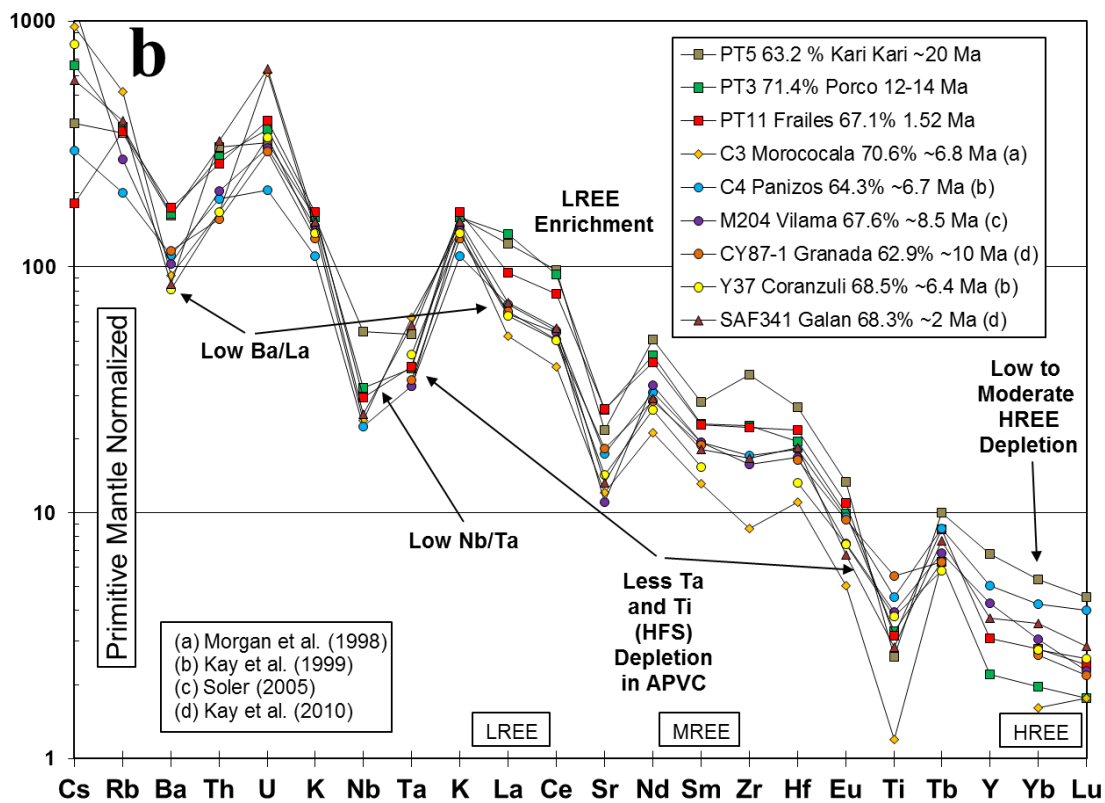
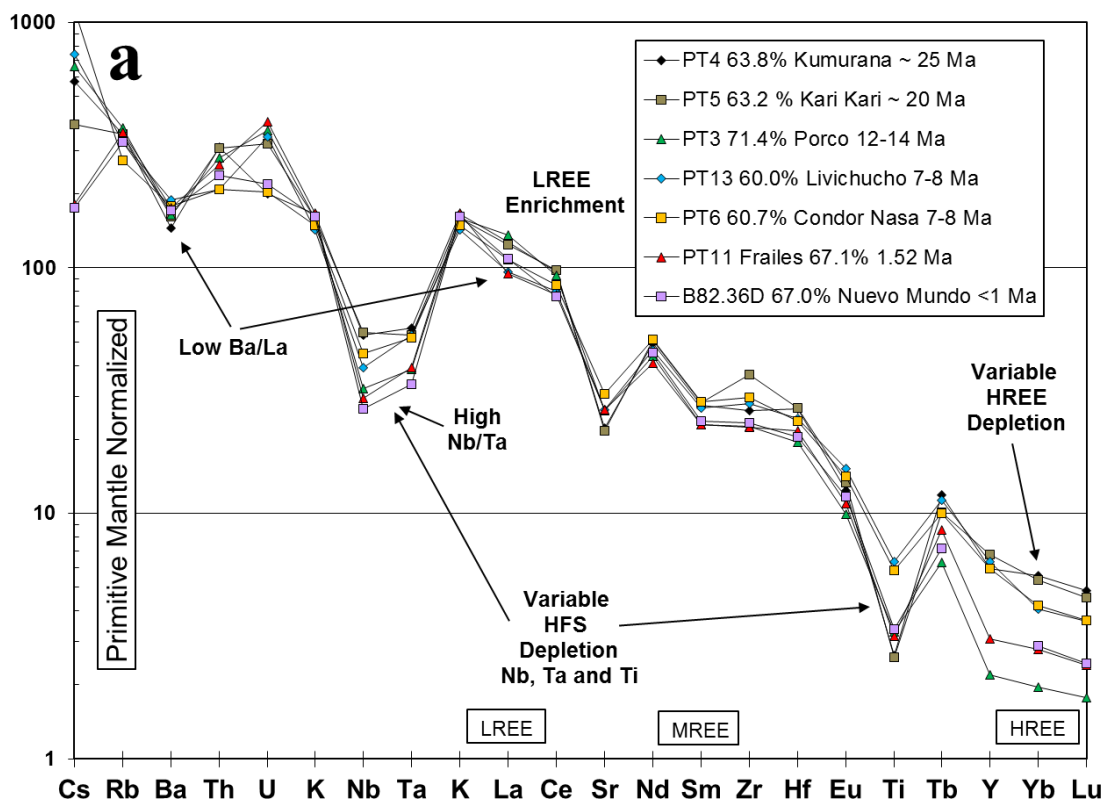
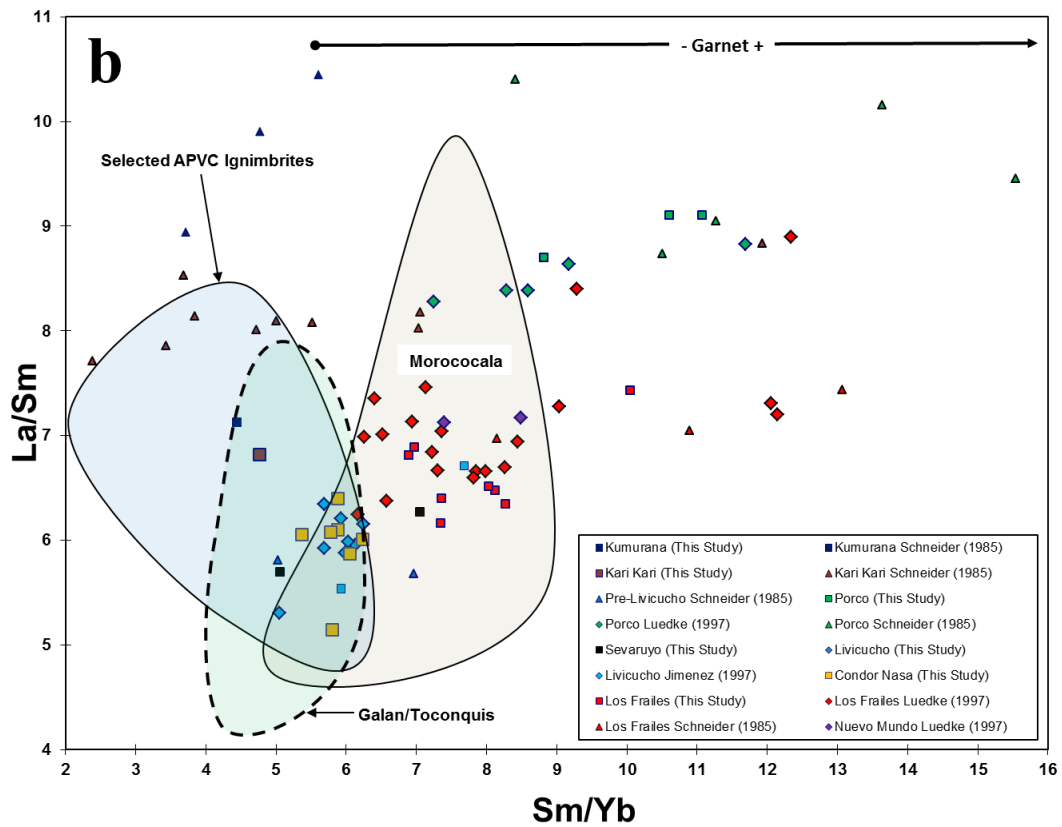
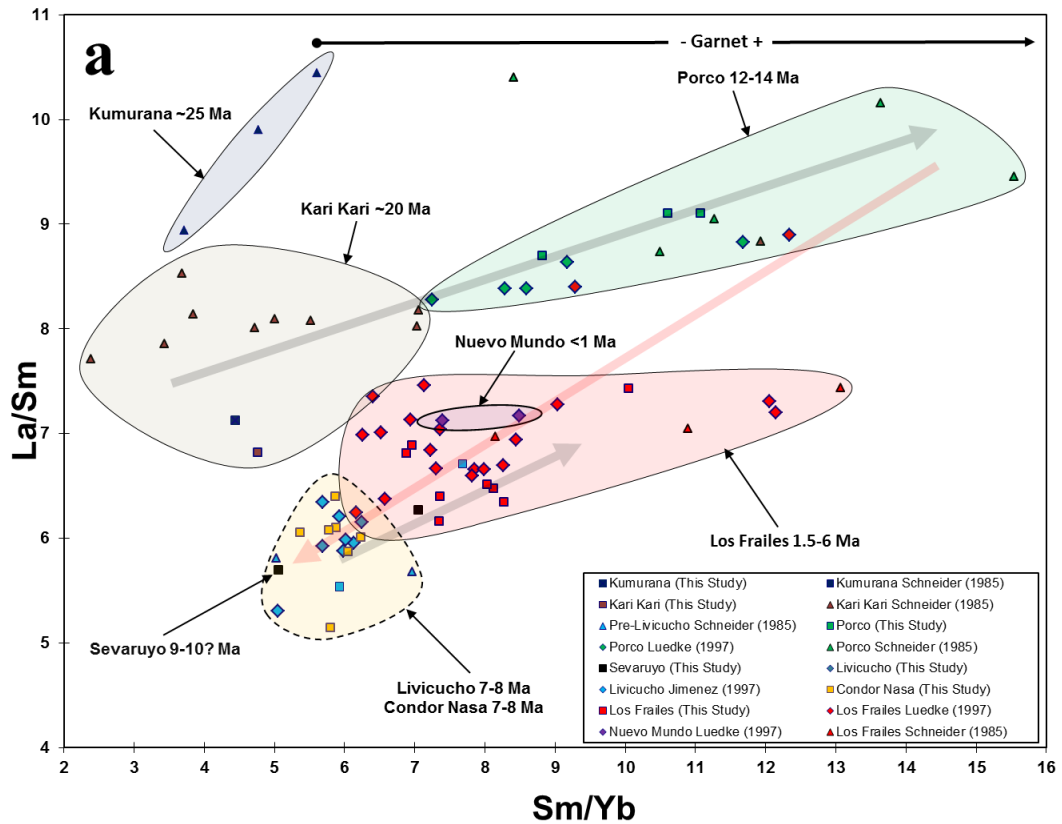


Figure 3.5

Plot of La/Sm ppm ratio versus Sm/Yb ppm ratio which illustrates variable REE depletion. HREE depletion is quantified by an increased Sm/Yb ratio while LREE enrichment is characterized by an increased La/Sm ratio. In general, Sm/Yb <2 indicates magma that equilibrated with pyroxenes, Sm/Yb of 2-5 indicates amphiboles, and Sm/Yb >5 is a garnet-induced signature which requires exceptionally thick crust of >45-55 km with a pressure of ~15 kbar (1.5 GPa). (a) The pattern of the Los Frailes Complex samples indicates that the Altiplano crust underwent two thickening episodes with a dramatic thinning event between them (see text for detailed discussion). The rapid decrease in La/Sm and Sm/Yb at 10-12 Ma, following the high values seen in the Porco data, is interpreted as the detachment of the lithosphere and lower crust in response to the crustal thickening and high-pressure driven lower crustal phase changes. A second, less dramatic, decrease occurs at 2-4 Ma prior to the main 1.5-3.5 Ma Los Frailes ignimbrite eruption. Arrows pointing to the upper-right (black) represent crustal thickening trends while the arrow pointing to the lower-left (red) depicts rapid thinning. The second, 2-4 Ma, delamination event is not depicted in order to avoid excessive clutter of the plot. (b) No temporal pattern is seen in the comparative ignimbrites. The Cerro Galán field and the APVC have low Sm/Yb and low to moderate La/Sm, while Morococala has moderate Sm/Yb and mostly moderate La/Sm with a few high samples, but without correspondingly high Sm/Yb ratios. Symbols: (a and b) Los Frailes Complex: squares- This study and Keller (2010), diamonds - Jiménez et al. (1997) and Luedke et al. (1997), triangles – Schneider (1985); (b) Cerro Galán and APVC fields as compiled in Kay et al. (2010, 2011); Morococala field as compiled by Morgan et al. (1998).



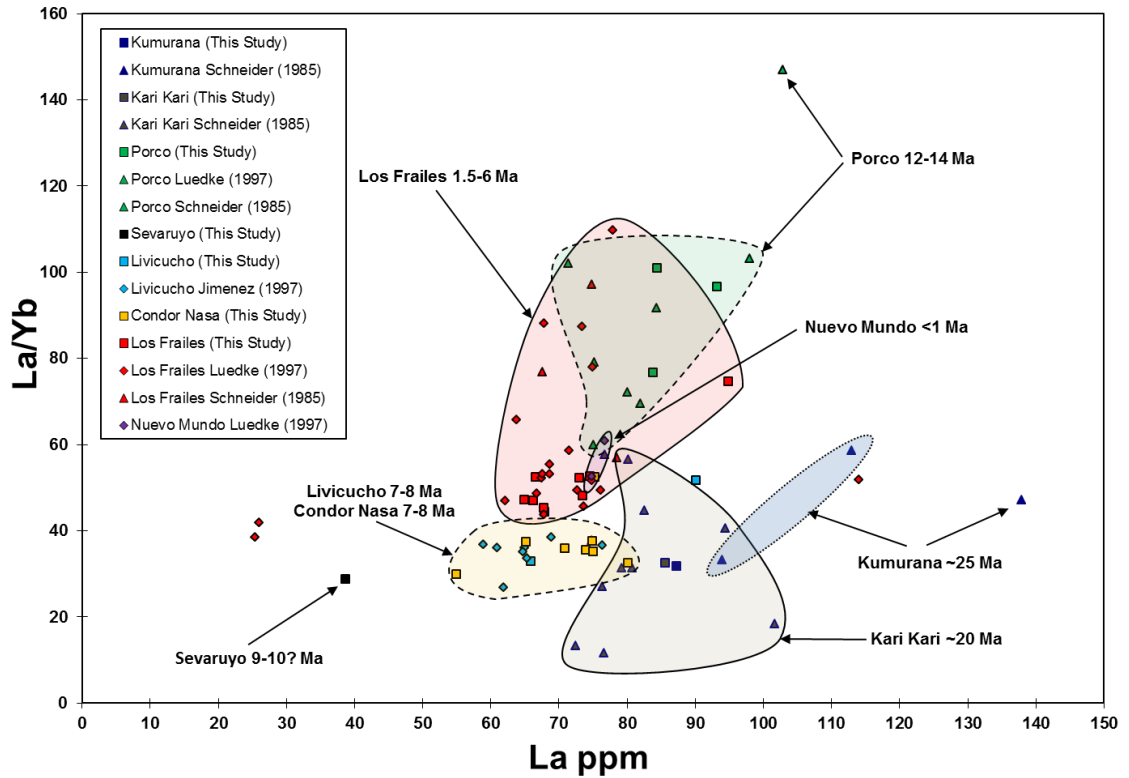


Figure 3.6

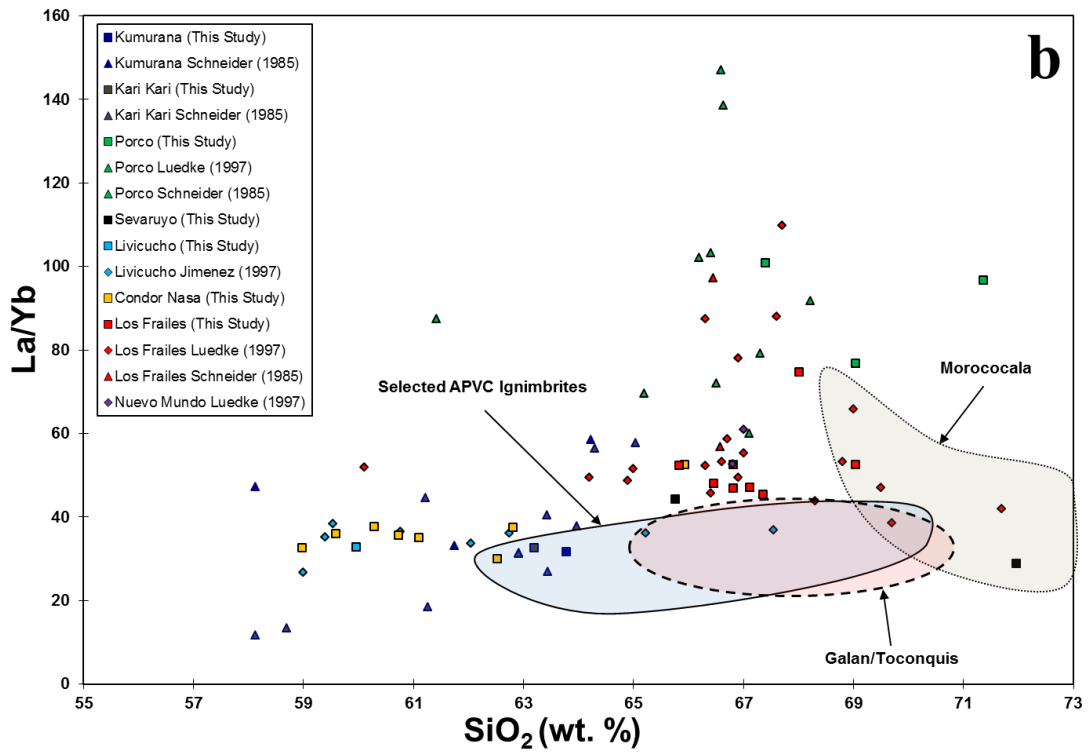
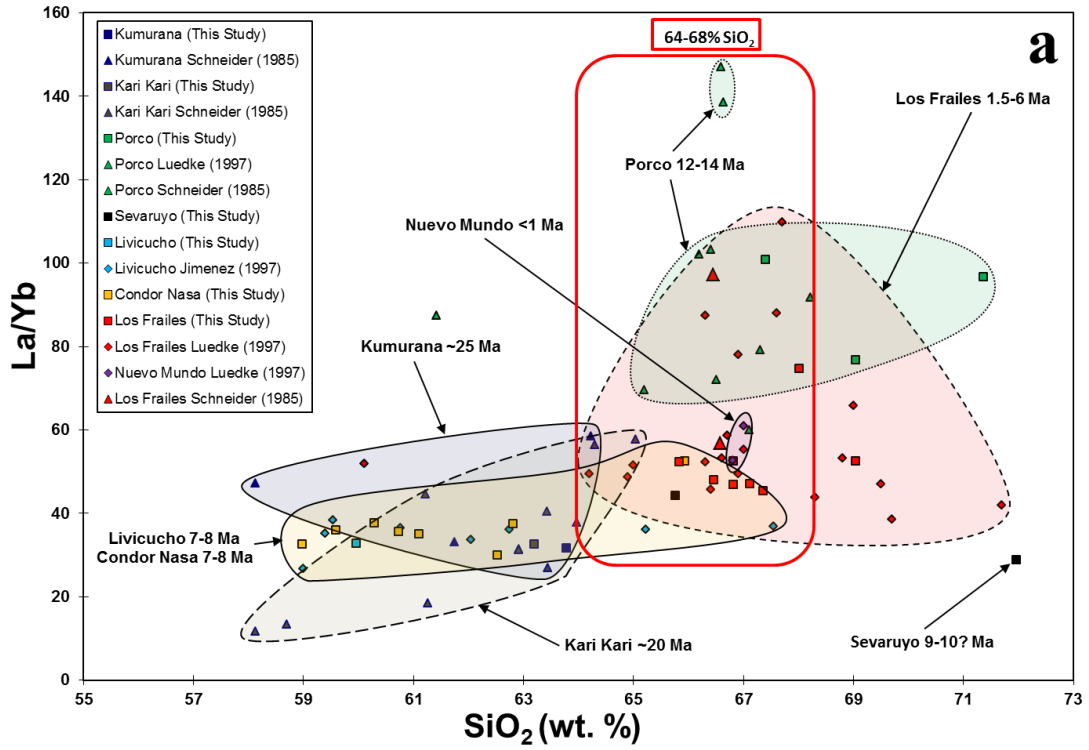
Plot of La/Yb ppm ratio versus La ppm which shows no discernible effect of La concentration on the La/Yb ppm ratio. The lack of La concentration influence indicates that the ratio is being controlled by variations in HREE (Yb) which are preferentially incorporated in garnet under high pressure conditions which raises the La/Yb ratio of the remaining melt. This is interpreted to occur during periods of thickened continental crust below the Los Frailes Complex.

Symbols: (a and b) Los Frailes Complex: squares- This study and Keller (2010), diamonds - Jiménez et al. (1997) and Luedke et al. (1997), triangles – Schneider (1985).

Figure 3.7

Plot of La/Yb ppm ratio versus weight percent SiO₂ which shows REE ratio changes are not SiO₂ driven. (a) Moderate silica (64-68% SiO₂) Kukurana, Kari Kari, Livicucho and Condor Nasa samples (red box) have similarly low Sm/Yb ratios as lower silica (<64% SiO₂) samples from the same units. In addition, several of the highest silica Los Frailes and Sevaruyo samples (>69% SiO₂) have low La/Yb. When samples of similar silica content are considered (64-68% SiO₂), the La/Yb ratio ranges are nearly unchanged which indicates that REE ratios changes are not SiO₂ driven. (b) Patterns of near horizontal La/Yb ratios with variable SiO₂ are also seen in the APVC, Cerro Galán and Morococala fields. La/Yb ratios seen in the Porco, Los Frailes and Nuevo Mundo ignimbrites are far above those reported in the APVC, Cerro Galán or at Morococala.

Symbols: (a and b) Los Frailes Complex: squares- This study and Keller (2010), diamonds - Jiménez et al. (1997) and Luedke et al. (1997), triangles – Schneider (1985); (b) Cerro Galán and APVC fields as compiled in Kay et al. (2010, 2011); Morococala field as compiled by Morgan et al. (1998).



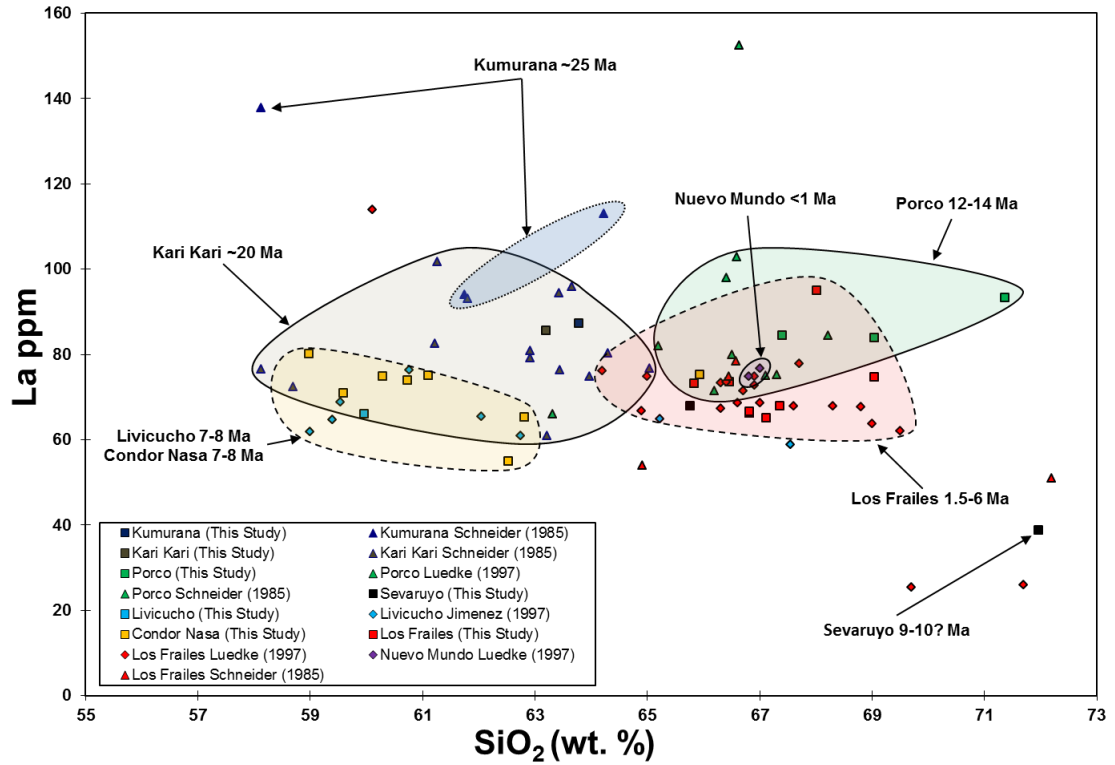


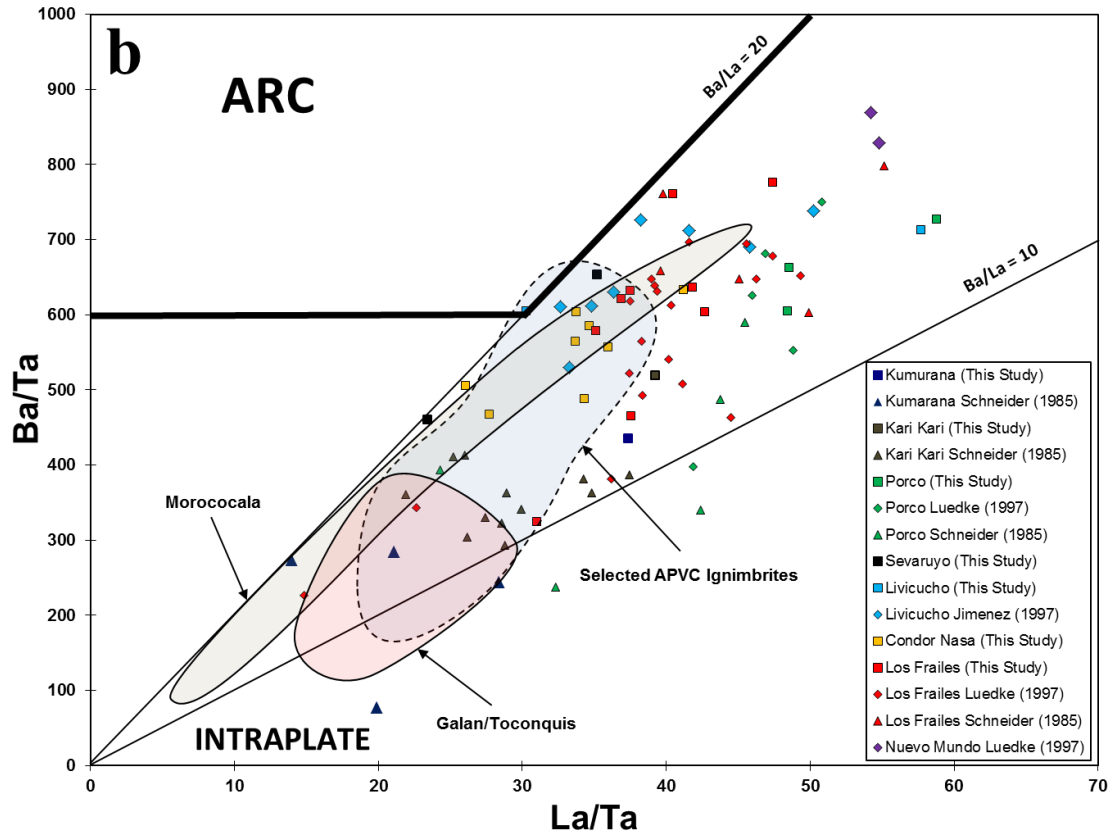
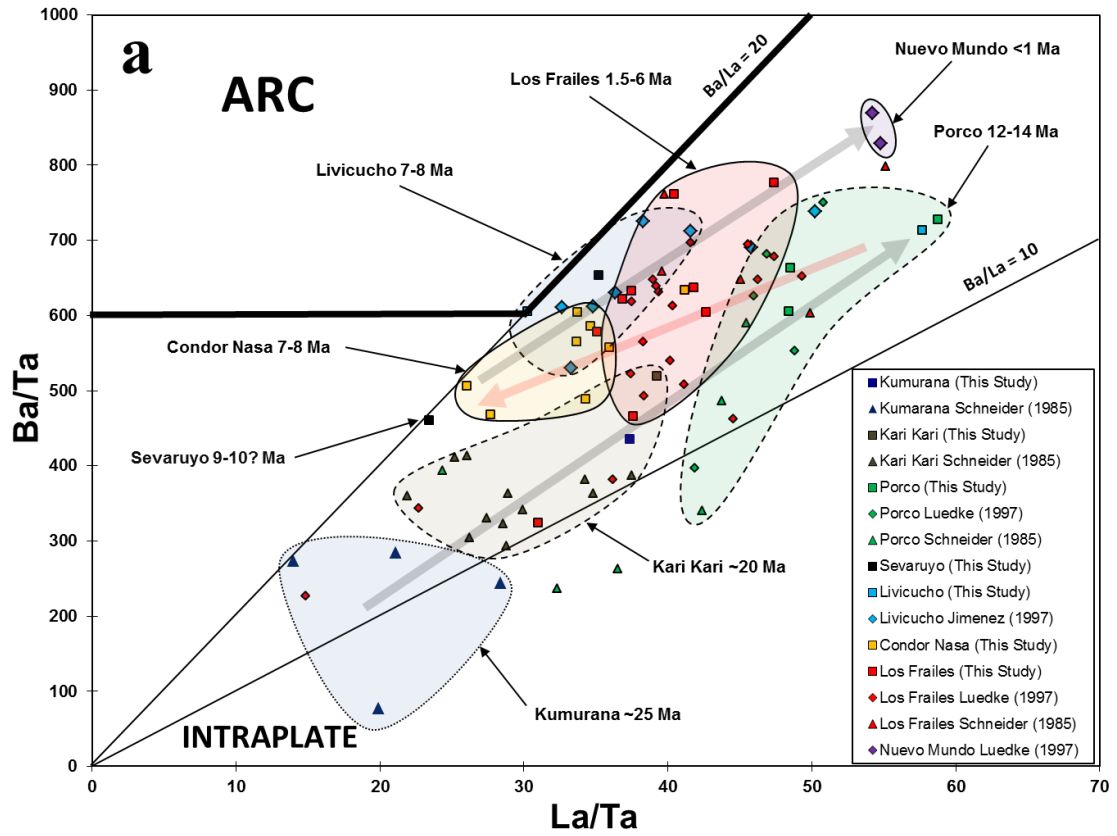
Figure 3.8

Plot of La ppm versus weight percent SiO₂ showing a slight decreasing trend of La concentration with increased SiO₂ in the Los Frailes Complex data. This indicates that silica sensitive phases only minimally affect the La concentration of the magma. Symbols: Los Frailes Complex: squares- This study and Keller (2010), diamonds - Jiménez et al. (1997) and Luedke et al. (1997), triangles – Schneider (1985).

Figure 3.9

Plot of Ba/Ta ppm ratio versus La/Ta ppm ratio as well as Ba/La ppm ratio showing systematic variation in the HFSE (La and Ta) and LILE (Ba) ratios with time. (a) The Los Frailes Complex Ba/Ta and La/Ta ratio pattern of increases and decreases mirrors the temporal pattern seen in La/Sm versus Sm/Yb plot (Figure 3.5a) which indicates a pressure-driven mechanism. Increasing ratios (black arrows) coincide with times believed to represent thickening crust and decreases (red arrow) occur following proposed delamination events at 10-12 Ma and 2-4 Ma when lithospheric-mantle and basal crustal materials are proposed to have been lost. The increase in Ba/La ratio seen at ~10-12 Ma is interpreted as enrichment of the mafic end-member melts or an increase in crustal fertility following the initiation of delamination at that time. See the text for a detailed discussion. The second delamination event is not depicted by the arrows to avoid cluttering the plot. (b) Illustrates that the APVC has a similar Ba/La but with much reduced La/Ta compared to the Los Frailes Complex which places them in the field of ratios occupied by Livicucho and Condor Nasa. The Cerro Galán field has even lower ratios putting it in the Kukurana and lower Kari Kari fields. Morococala has a wide range of moderate to extremely low Ba/Ta and La/Ta ratios caused by both low La and Ba and elevated Ta concentrations as compared to the Los Frailes Complex. In contrast, Ba/La ratios are steadily 15-20 which is in the same range as post-12 Ma units of the Los Frailes Complex.

Symbols: (a and b) Los Frailes Complex: squares- This study and Keller (2010), diamonds - Jiménez et al. (1997) and Luedke et al. (1997), triangles – Schneider (1985); (b) Cerro Galán and APVC fields as compiled in Kay et al. (2010, 2011); Morococala field as compiled by Morgan et al. (1998). The Ta concentrations used for the Schneider (1985) and Jiménez et al. (1997) are calculated values (Nb ppm/14).



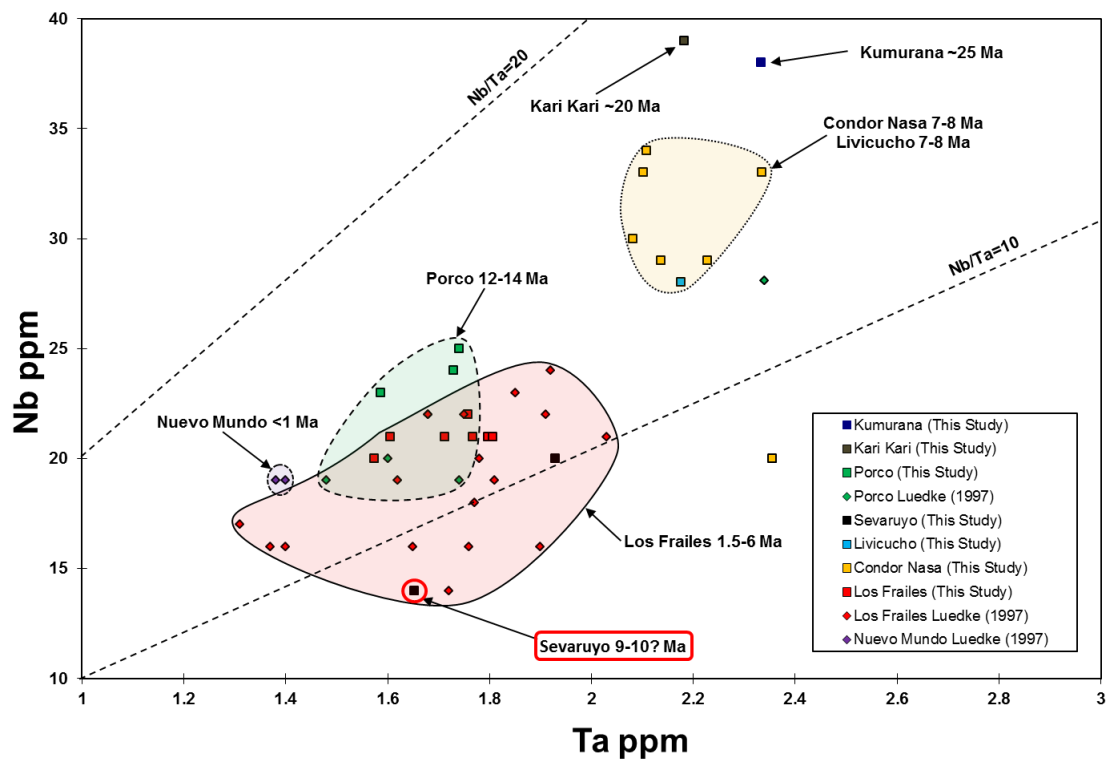


Figure 3.10

Plot of Nb ppm versus Ta ppm depicting the unit variability of HFSE elements Nb and Ta concentrations. High concentrations, and near chondritic (19.9 ± 0.6) Nb/Ta ratios, are found at Kumurana and Kari Kari while Livicucho and Condor Nasa also have high concentrations, but intermediate Nb/Ta ratios. The lowest concentrations of both Nb and Ta as well as the lowest Nb/Ta ratios occur in the Porco, Sevaruyo, Los Frailes and Nuevo Mundo ignimbrites which are also the most silicic units. The high-silica (72% SiO_2) Sevaruyo sample (red box and circle) plots with the other high-silica units and not with the low-silica, but temporally coeval, Livicucho and Condor Nasa as it does with La/Sm versus Sm/Yb plot and La/Ta versus Ba/Ta plot (Figures 3.5a and 3.9a). This indicates that Nb and, to a lesser extent, Ta concentrations are controlled by accessory phases in siliceous melts and not pressure driven accessory phases as Ba and La concentrations indicate. See text for full discussion.

Symbols: Los Frailes Complex: squares- This study and Keller (2010), diamonds - Luedke et al. (1997). The Ta concentrations used for the Schneider (1985) and Jiménez et al. (1997) are calculated values ($\text{Nb ppm}/14$) and so are omitted here. Kumurana, Kari Kari and Livicucho centers are represented by a single sample each (PT-4, PT-5, and PT-13 respectively).

Rare Earth Elements

Figure 3.5a demonstrates that the lowest Sm/Yb values are found in the samples from the ~20-25 Ma Kumurana and Kari Kari centers, which have Sm/Yb = 4.4 and 4.8 and relatively high La/Sm values of 6.8 and 7.1. These are followed chronologically by the 12-14 Ma Porco group samples with a range of high to extremely high values of Sm/Yb = 8.8-11.1, accompanied by high La/Sm = 8.7-9.1. The ratios then retreat with marked decreases in both Sm/Yb and La/Sm in the 7-10 Ma Sevaruyo, Condor Nasa and Livicucho samples that have a collective range of Sm/Yb = 4.5-7.7 and La/Sm = 5.1-6.7. The 1.5-3.5 Ma main Los Frailes ignimbrite samples have a generally intermediate range of ratios with Sm/Yb = 6-10 and La/Sm = 6-7.5.

Figure 3.6 shows that La concentration variations are not controlling the resulting La/Yb ratio. This can also be seen in Figure 3.4a which shows that although LREE enrichment has occurred, the La concentrations are relatively constant compared to the Yb concentrations which have undergone variable HREE depletion. Figure 3.7a plots La/Yb ppm ratio versus wt. % SiO₂ which shows that although the upper range of the La/Yb ratio increases at >65% SiO₂, the lower range remains the same which indicates that silica content is not the driving factor in La/Yb ratio creation. Figure 3.8 plots La ppm versus wt. % SiO₂ and shows only a slight possible decreasing trend in the La concentration range (60-90 ppm) with variable SiO₂.

High Field Strength and Large-Ion Lithophile Elements

As seen in Figure 3.9a, the samples from the Los Frailes Complex plot in the Ba/La ratio range of 10-20 with a pre-12 Ma mean of 12 and a shift to a post-12 Ma mean of 17-18. The ~25 Ma PT-4 Kumurana sample exhibits low Ba/Ta = 435 and La/Ta = 37 while the ~20 Ma PT-5 Kari Kari sample has slightly higher values of Ba/Ta = 520 and La/Ta = 39. The 12-14 Ma Porco samples exhibit a range of very

high values of $Ba/Ta = 605-727$ and $La/Ta = 48-59$. The La/Ta values then decrease back to low-moderate values for the 7-8 Ma Livicucho and Condor Nasa samples (26-41) with higher $Ba/Ta = 470-605$ which also effectively increases the corresponding Ba/La ratio to 17-18. The 9-10 Ma Sevaruyo region PO-5 sample has the highest Ba/La which is near 20 with $Ba/Ta = 460$ and $La/Ta = 23$. The 1.5-3.5 Ma Los Frailes ignimbrite samples show a large scatter but generally occupy a high, nearly Porco-like, field of $Ba/Ta = 466-777$ and $La/Ta = 37-47$.

Figure 3.10 depicts the variability of HFSE elements Nb and Ta concentrations between individual units. Kumurana and Kari Kari have the highest Nb concentrations of 38-39 ppm and high Ta values of 2.2-2.3 ppm. The Livicucho sample plots with the closely related Condor Nasa field (Nb = 28-34 ppm, Ta = 2.1-2.35 ppm), as it does with most other major and trace elements. The high silica (66% SiO_2) Condor Nasa sample PT-12 is an extreme outlier with much lower Nb concentration. The higher silica (66-72% SiO_2) Porco, Sevaruyo, Los Frailes and Nuevo Mundo ignimbrite samples all have significantly lower concentrations of both Nb and Ta (Nb = 20-25 ppm, Ta = 1.6-2.8 ppm).

Europium Anomaly

The plot of Eu/Eu^* ratio versus SiO_2 in Figure 3.11a shows that the Los Frailes Complex units have variable Eu/Eu^* ratio values which range from 0.7-0.9 in the low silica samples (<64% SiO_2) to a maximum negativity of 0.6-0.75 in the more silicic samples (>64% SiO_2). Both the Kumurana PT-4 and Kari Kari PT-5 have relatively low Eu/Eu^* values (greater negative Eu anomaly) of 0.61 and 0.68. The low silica Livicucho and Condor Nasa samples plot together and overlay each other with a range of $Eu/Eu^* = 0.68-0.91$. The Porco samples values have an intermediate range of $Eu/Eu^* = 0.66-0.74$ and the Los Frailes ignimbrite samples have $Eu/Eu^* = 0.61-0.68$. The Sevaruyo region samples follows the expected pattern of increasing Eu/Eu^*

negativity with increased silica, however, PO-6 at 66% SiO₂ and a high Eu/Eu* = 0.86 is the only time in which its chemistry plots distinctly outside of the main Los Frailes ignimbrite field. Figure 3.12a depicts the Eu/Eu* ratios plotted against Sm/Yb ppm ratios. The individual unit fields show no distinct trend of Eu/Eu* ratio change with highly variable Sm/Yb ratios.

Strontium, Rubidium and Neodymium

Figures 3.13, 3.14 and 3.15 confirm that Sr ppm has remained in the range of 400-650 ppm over the 25 My history of the Los Frailes Complex despite extremely variable Sm/Yb and Eu/Eu* ratios as well as SiO₂ content. The Kumurana PT-4 and Kari Kari PT-5 samples have a relatively low Sr concentration of ~465 ppm with moderate silica of ~63%, a negative Eu/Eu* anomaly of ~0.65 and low Sm/Yb of 0.45. The Porco samples have an average Sr ppm of 550 but with high SiO₂ of ~70% and high Sm/Yb of 10.6-11.1. The SiO₂-poor Livicucho and Condor Nasa samples have a large combined range of 410-670 ppm Sr with Condor Nasa exhibiting higher upper-end values. The high silica (72% SiO₂) PO-5 Sevaruyo sample exhibits the overall lowest value of 270 ppm Sr for the Los Frailes Complex. The main Los Frailes ignimbrite samples contain 405-625 ppm Sr which represents the Complex's average.

Figure 3.16 depicts the Nd concentration against wt. % SiO₂ and remains relatively steady over time with all but two values between 55 and 70 ppm Nd. Again, Kumurana and Kari Kari samples have similar concentrations of ~68 ppm Nd. The three Porco samples have a tight range of 68-70 ppm Nd, while the high-silica (72% SiO₂) Sevaruyo sample PO-5 exhibits a lower value of 33 ppm Nd. Livicucho and Condor Nasa samples share a field of 58-69 ppm Nd with the main Los Frailes ignimbrite having the widest, but intermediate range of 50-71 ppm Nd. Figure 3.17 indicates that most Los Frailes Complex samples maintain an average Sr/Nd ratio of near 8-9 with a total range of 6-12.

Figure 3.11

Plot of Eu/Eu^* ratios versus weight percent SiO_2 . (a) Shows the Los Frailes Complex has variable Eu/Eu^* with the highest values in low silica units and lowest values in high silica units. This indicates magma evolution and plagioclase removal are driving the Eu/Eu^* value. (b) Shows the trend of decreasing Eu/Eu^* with increased silica content is present in other Altiplano-Puna ignimbrites at higher silica contents than the Los Frailes Complex. This suggests that the volume of plagioclase removal is greater at APVC and Morococala centers and helps to explain the higher Sr concentration in Los Frailes Complex units. The outlier near $\text{Eu}/\text{Eu}^* = 0.45$ is Luedke et al. (1997) sample P60, which has SiO_2 near 70% and also contains low FeO and MgO which indicates a more evolved character.

Symbols: Los Frailes Complex - squares: This study with Keller (2010); diamonds - Jiménez et al. (1997) and Luedke et al. (1997); triangles – Schneider (1985); Cerro Galán and APVC fields as compiled in Kay et al. (2010 and 2011); Morococala field as compiled by Morgan et al. (1998).

Symbols: (a and b) Los Frailes Complex: squares- This study and Keller (2010), diamonds - Jiménez et al. (1997) and Luedke et al. (1997), triangles – Schneider (1985); (b) Cerro Galán and APVC fields as compiled in Kay et al. (2010, 2011); Morococala field as compiled by Morgan et al. (1998).

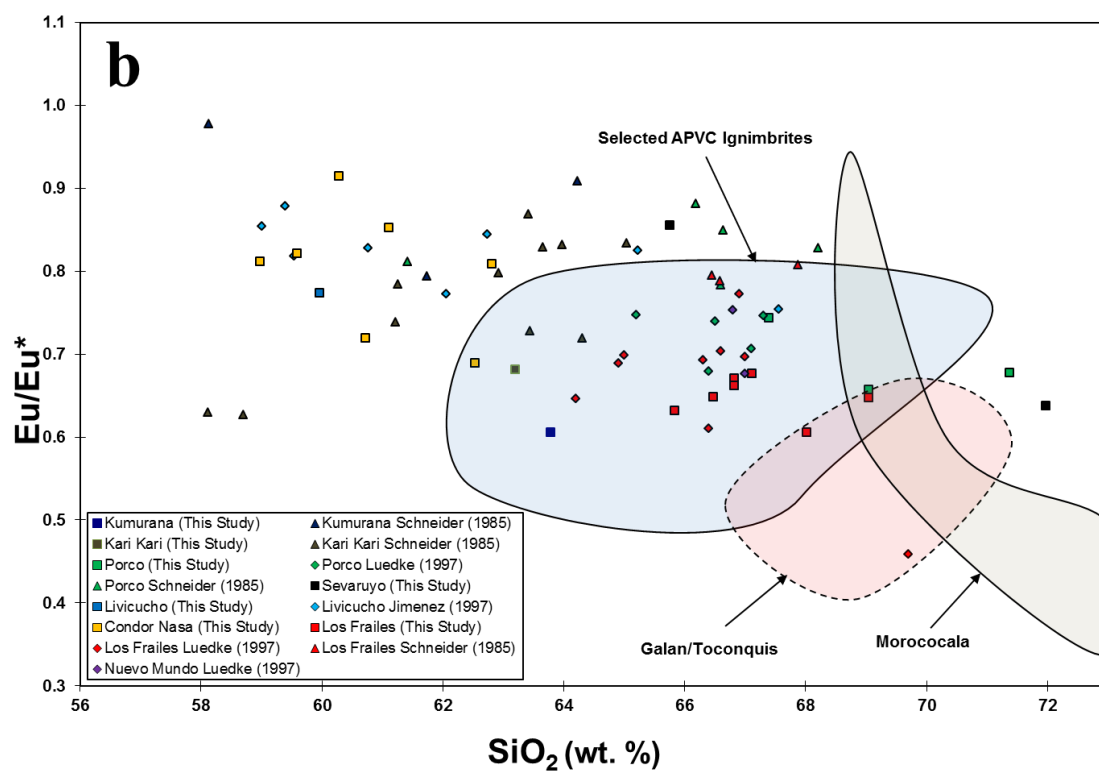
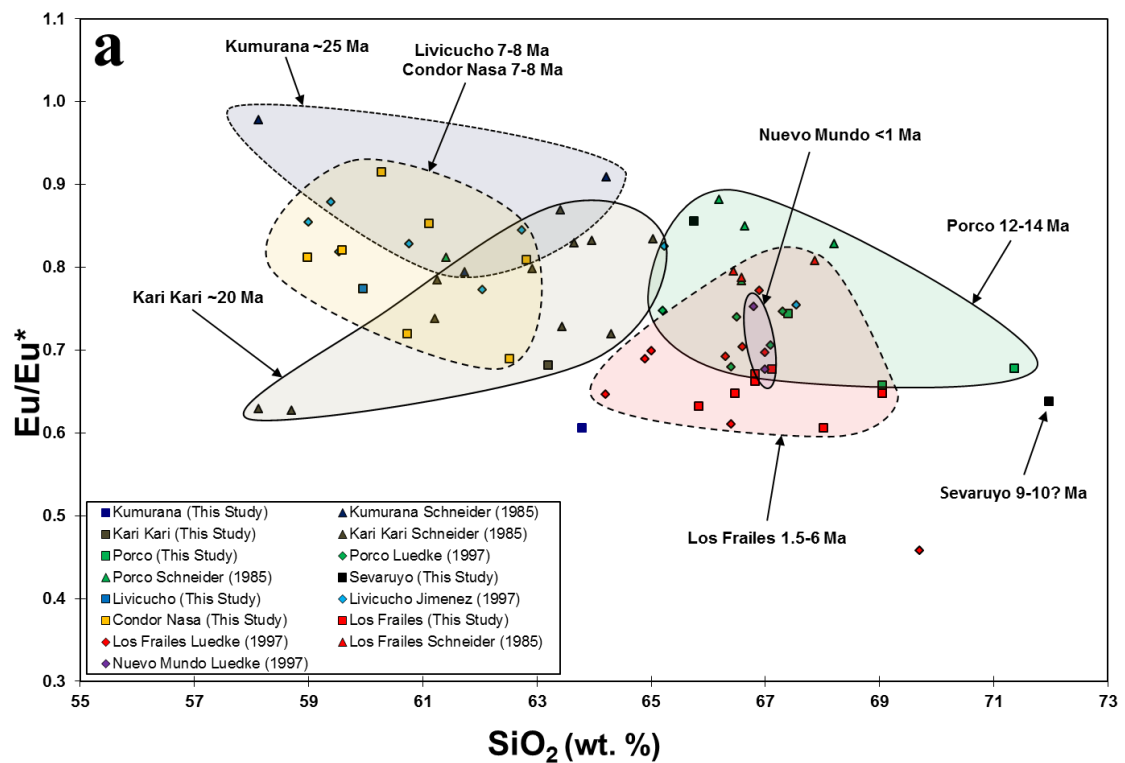
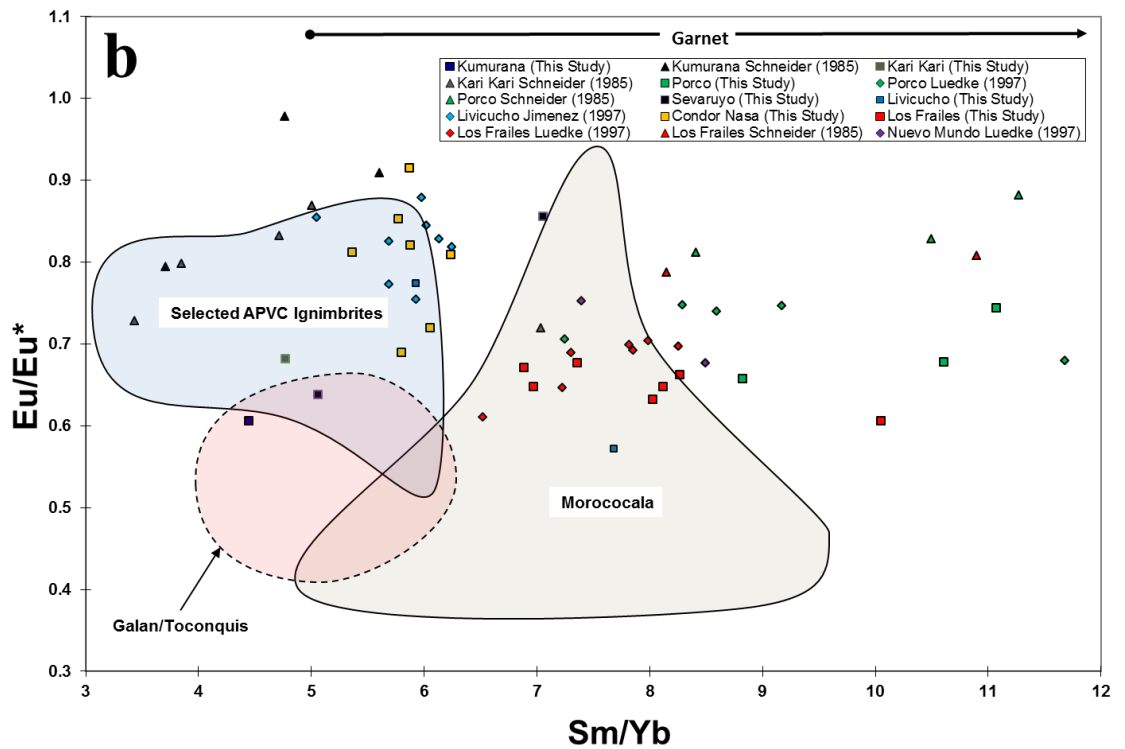
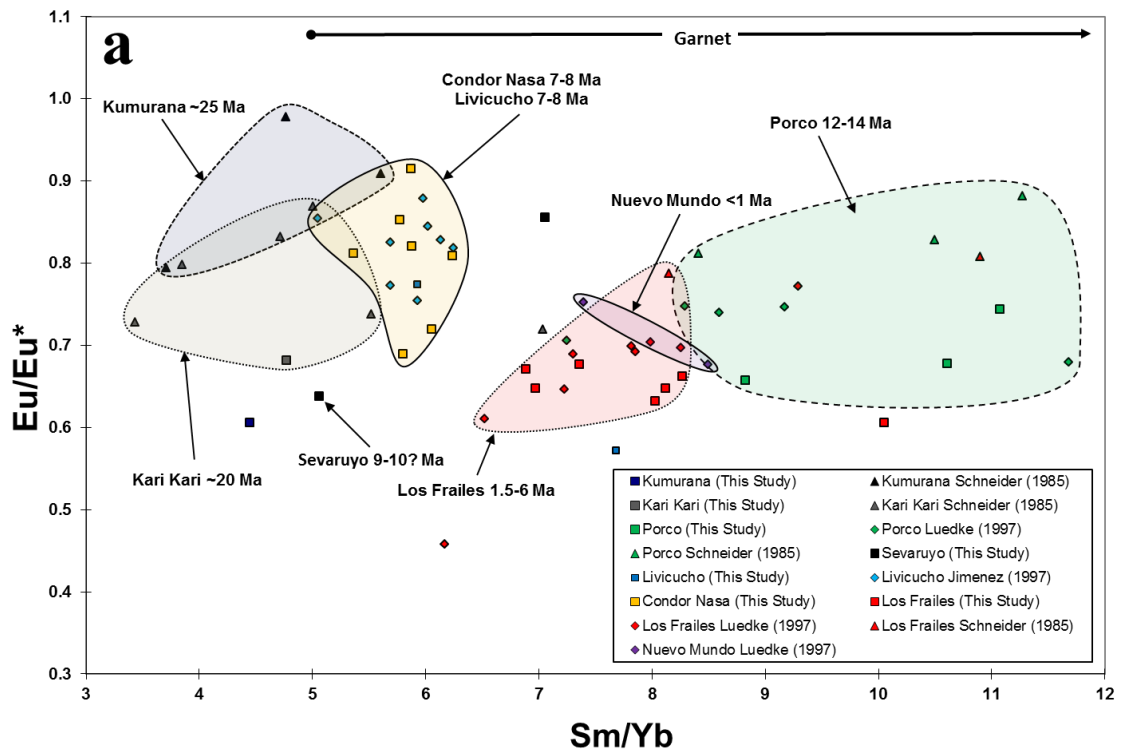


Figure 3.12

Plot of Eu/Eu^* ratio versus Sm/Yb ppm ratio which (a) shows that Los Frailes Complex Eu/Eu^* values are slightly more negative at higher Sm/Yb ratios; indicating greater plagioclase fractionation. This indicates that Eu/Eu^* character is not being set in the assimilation region, but is being generated at lower pressure during magmatic ascent to the surface. A thinner crust leads to decreased plagioclase loss during magma transit while a thicker crust has greater plagioclase loss. (b) No correlation between Sm/Yb ratios and Eu/Eu^* exists which indicates that the Eu/Eu^* values are not being set at the time of assimilation and mixing.

Symbols: (a and b) Los Frailes Complex: squares- This study and Keller (2010), diamonds - Jiménez et al. (1997) and Luedke et al. (1997), triangles – Schneider (1985); (b) Cerro Galán and APVC fields as compiled in Kay et al. (2010, 2011); Morococala field as compiled by Morgan et al. (1998).



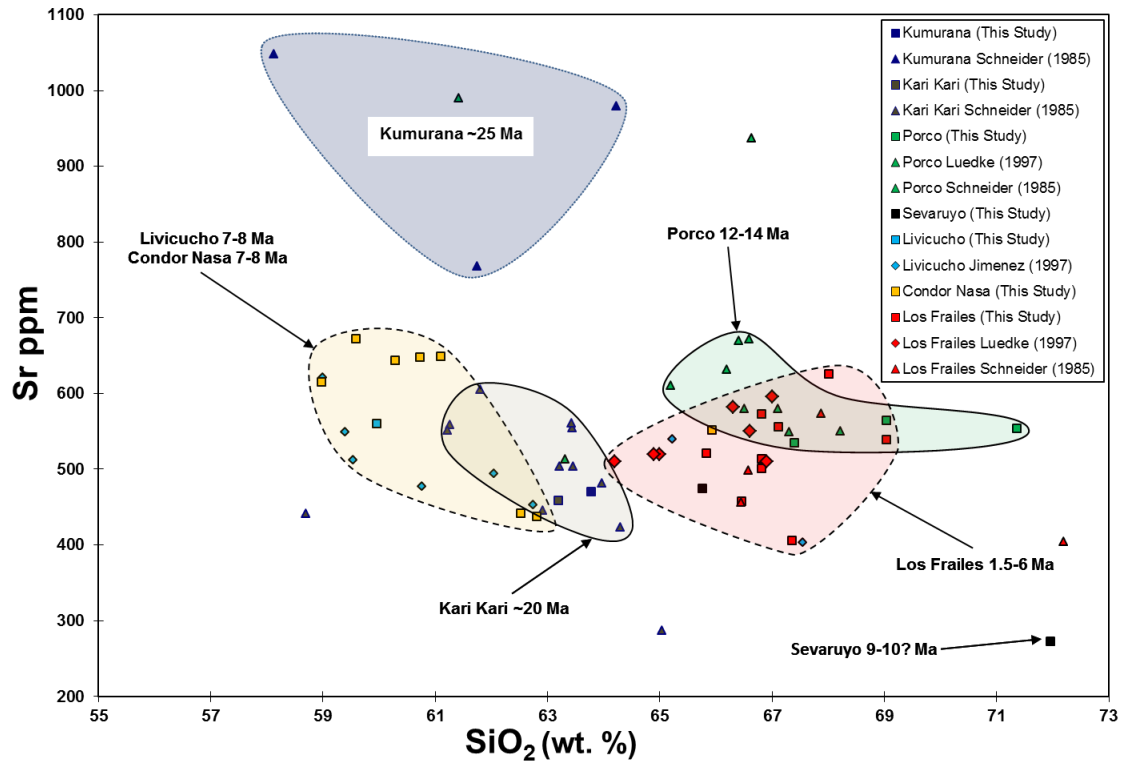


Figure 3.13

Plot of Sr ppm versus weight percent SiO₂ showing the Sr ppm range has remained nearly constant over the 25 My history of the Los Frailes Complex and through variable SiO₂ content. The 65% SiO₂ Kari Kari outlier with 290 ppm Sr also has low FeO and low MgO compared to other Kari Kari samples indicating more evolved character.

Symbols: Los Frailes Complex: squares- This study and Keller (2010), diamonds - Jiménez et al. (1997) and Luedke et al. (1997), triangles – Schneider (1985).

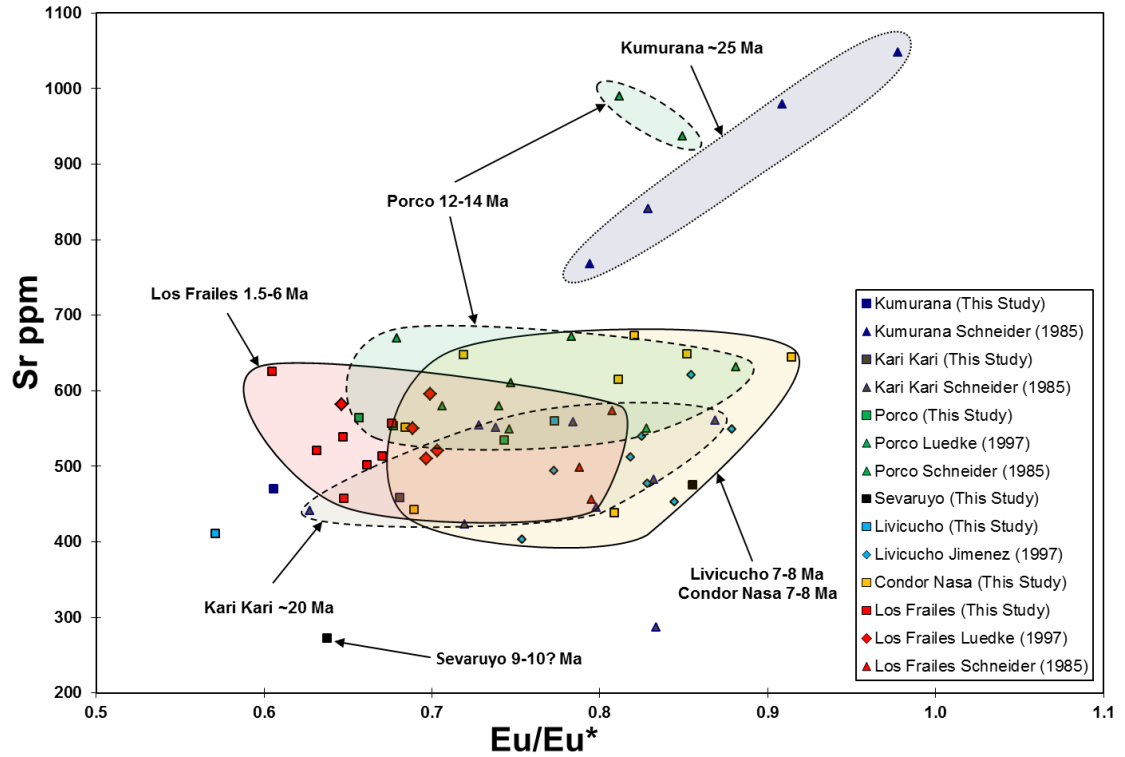


Figure 3.14

Plot of Sr ppm versus Eu/Eu^* ratio showing the Sr ppm range has remained nearly constant over the 25 My history of the Los Frailes Complex through variable Eu/Eu^* . Variable Eu/Eu^* indicates variable plagioclase removal has had minimal impact on the Sr ppm of the resulting ignimbrites. The Kari Kari outlier at 290 ppm Sr also has low FeO and low MgO compared to other Kari Kari samples indicating more evolved character.

Symbols: Los Frailes Complex: squares- This study and Keller (2010), diamonds - Jiménez et al. (1997) and Luedke et al. (1997), triangles – Schneider (1985).

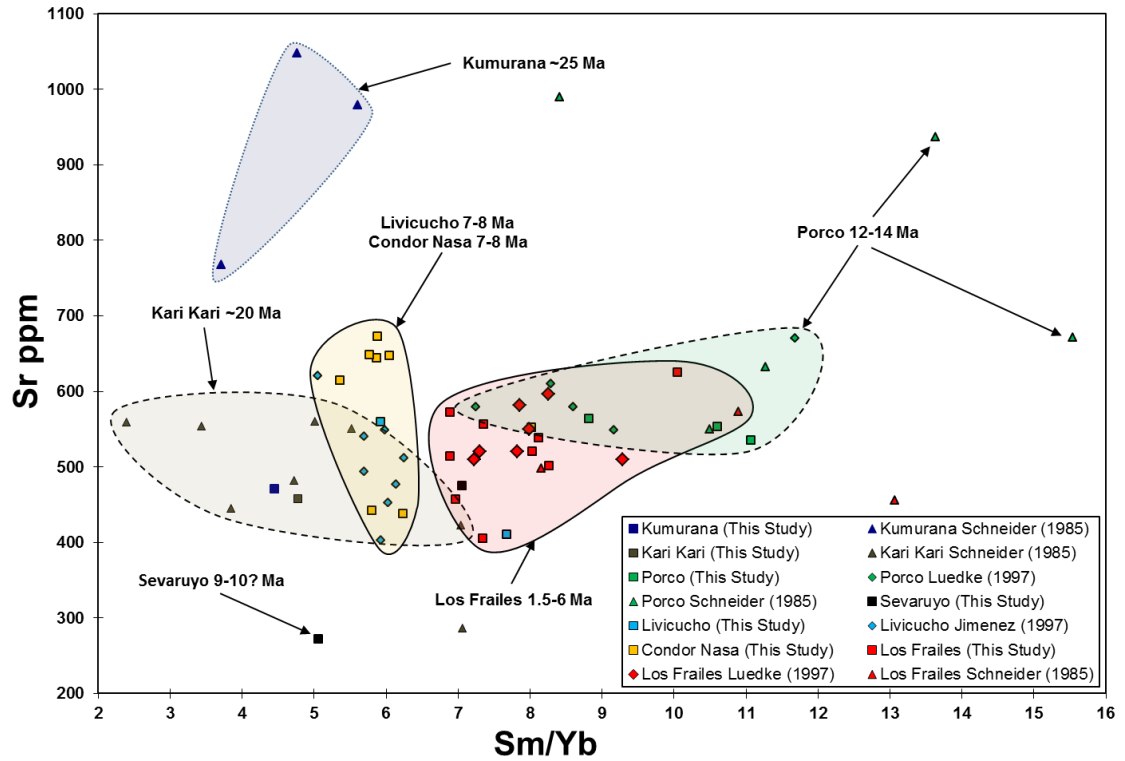


Figure 3.15

Plot of Sr ppm versus Sm/Yb ppm ratio showing the Sr ppm range has remained nearly constant over the 25 My history of the Los Frailes Complex through variable Sm/Yb. Variable Sm/Yb indicates variable AFC zone depth has had minimal impact on the Sr ppm of the resulting ignimbrites. The Kari Kari outlier with 290 ppm Sr also has low FeO and low MgO compared to other Kari Kari samples indicating more evolved character

Symbols: Los Frailes Complex: squares- This study and Keller (2010), diamonds - Jiménez et al. (1997) and Luedke et al. (1997), triangles – Schneider (1985).

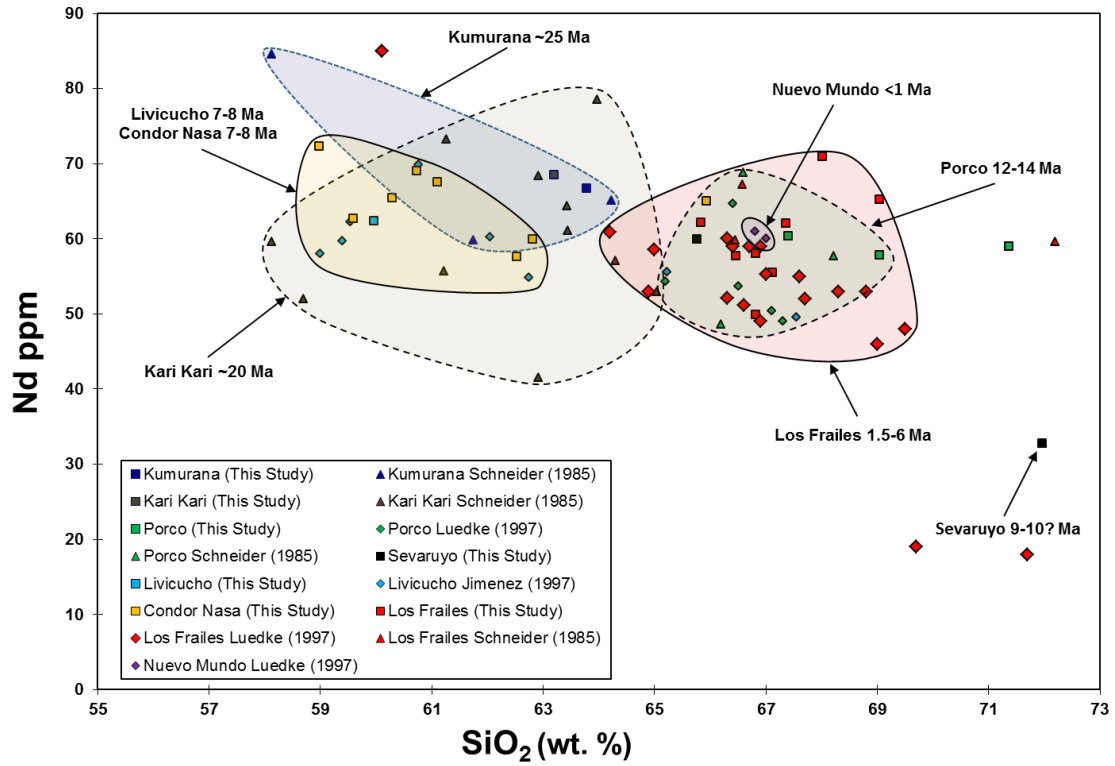


Figure 3.16

Plot of Nd ppm versus weight percent SiO₂ showing the Nd ppm range has remained generally constant over the 25 My history of the Los Frailes Complex and through variable SiO₂ content.

Symbols: Los Frailes Complex: squares- This study and Keller (2010), diamonds - Jiménez et al. (1997) and Luedke et al. (1997), triangles – Schneider (1985).

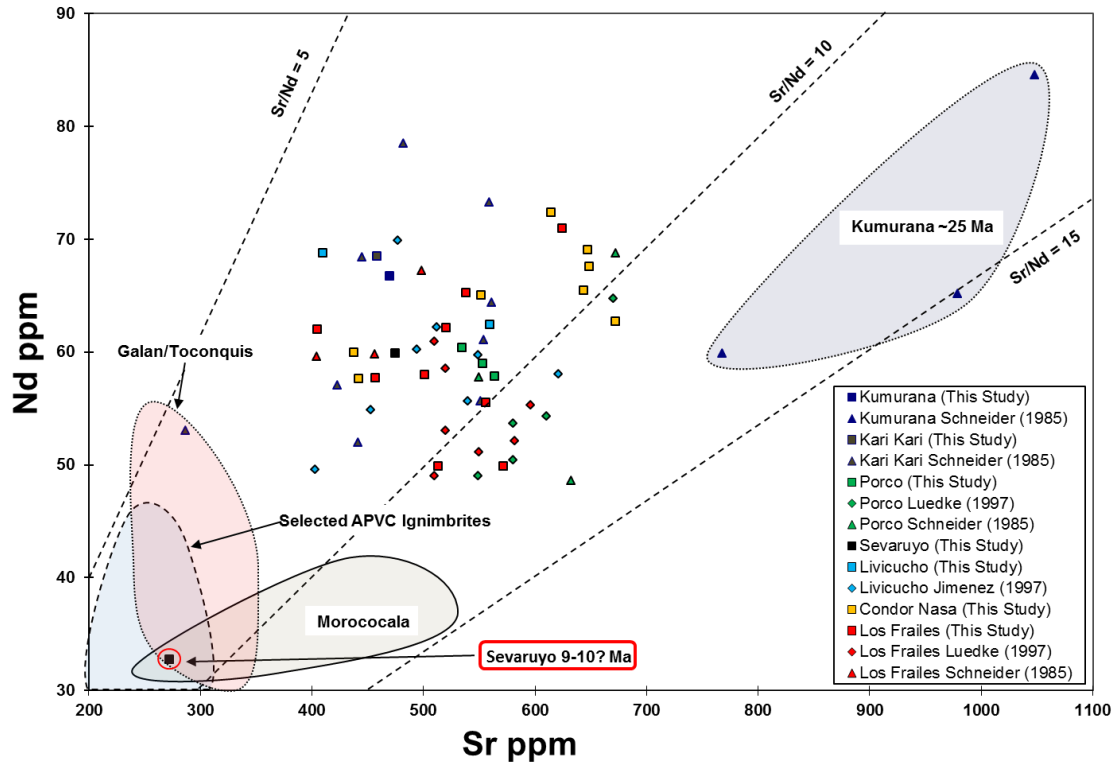


Figure 3.17

Plot of Nd ppm versus Sr ppm and resulting Sr/Nd ratio. Most Los Frailes Complex samples maintain a Sr/Nd ratio of 6-11. The higher Sr/Nd ratios seen in the Kumurana samples are due to their higher Sr content. The other Altiplano-Puna backarc ignimbrite fields show they are lower in Sr and Nd concentrations, but have roughly the same average Sr/Nd ratio range as the Los Frailes Complex. The Sevaruyo region sample PO-5, which is outlined in red, is the only Los Frailes Complex sample with concentrations like that of the other Altiplano-Puna backarc ignimbrites.

Symbols: Los Frailes Complex: squares- This study and Keller (2010), diamonds - Jiménez et al. (1997) and Luedke et al. (1997), triangles – Schneider (1985); Cerro Galán and APVC fields as compiled in Kay et al. (2010, 2011); Morococala field as compiled by Morgan et al. (1998).

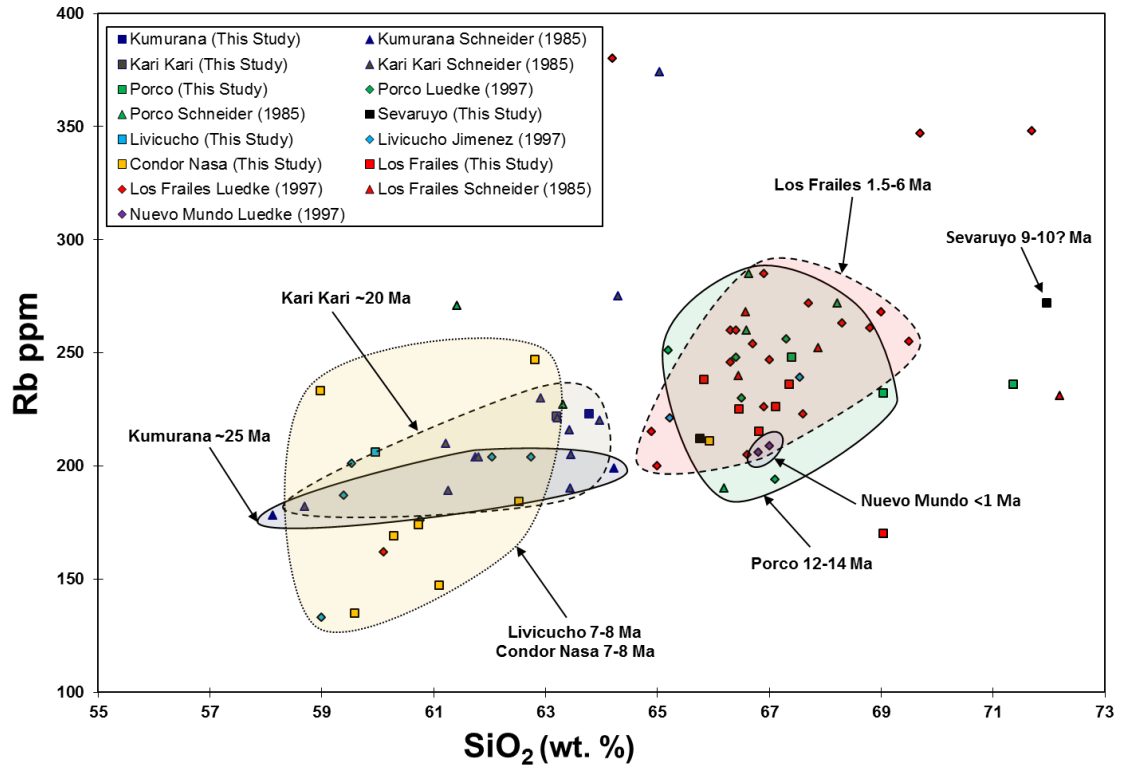


Figure 3.18

Plot of Rb ppm versus weight percent SiO₂ showing the Rb ppm range has remained generally constant over the 25 My history of the Los Frailes Complex and through variable SiO₂ content.

Symbols: Los Frailes Complex: squares- This study and Keller (2010), diamonds - Jiménez et al. (1997) and Luedke et al. (1997), triangles – Schneider (1985).

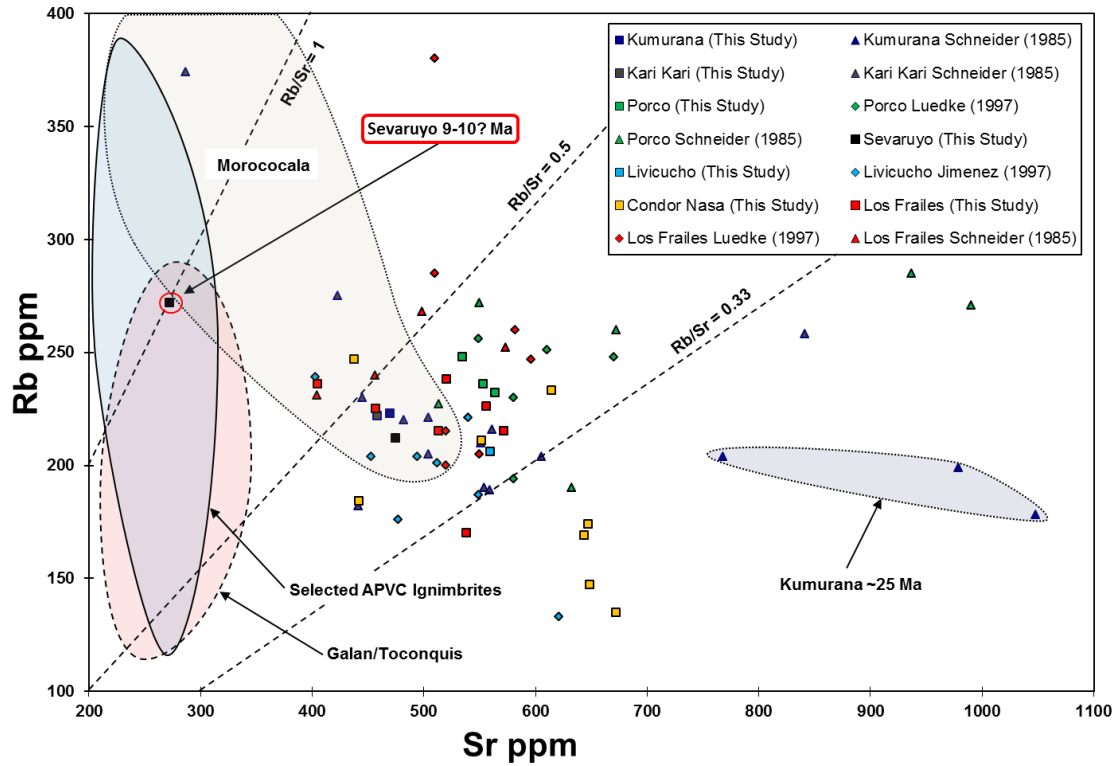


Figure 3.19

Plot of Rb ppm versus Sr ppm and resulting Rb/Sr ratios. Most Los Frailes Complex samples maintain an Rb/Sr ratio of 0.33-0.5 with some scatter and an average near 0.4. The lower Rb/Sr ratios seen in Kumurana samples are due to higher Sr content. The normal ranges of other Altiplano-Puna backarc ignimbrites are lower in Sr concentration, but have slightly higher Rb content than the Los Frailes Complex with an Rb/Sr average of >0.5. The Sevaruyo region sample (outlined in red) is the only Los Frailes Complex sample with concentrations like that of the other Altiplano-Puna backarc ignimbrites.

Symbols: Los Frailes Complex: squares- This study and Keller (2010), diamonds - Jiménez et al. (1997) and Luedke et al. (1997), triangles – Schneider (1985); Cerro Galán and APVC fields as compiled in Kay et al. (2010, 2011); Morococala field as compiled by Morgan et al. (1998).

Figure 3.18 exhibits overlapping Rb concentrations between 170-250 ppm for most Los Frailes Complex units. Only Condor Nasa seems to have a lower end-range with concentrations between 130-250 ppm Rb. The main Los Frailes ignimbrite has most values between 200-270 ppm Rb, but with some scatter. Sevaruyo sample PO-5, which has the lowest Sr concentration, also has the highest Rb concentration of 272 ppm and is the only new sample with $Rb/Sr \geq 1.0$ (see Figure 3.19).

Mineral Compositions

All Los Frailes Complex samples are crystal-rich welded ash tuffs with 30-50% phenocryst by volume. Like other CVZ backarc ignimbrites, plagioclase, quartz and biotite are the dominate minerals in all samples (e.g., Coira and Kay, 1993; de Silva and Gosnold, 2007; Morgan et al., 2008; Keller, 2010) with sanidine accounting for the remainder of the major minerals. Opaque and high birefringence accessory minerals are seen petrographically as both inclusions and free grains and are identified as ilmenite and zircon. Apatite and a REE phosphate (monazite) are also identified as accessory phases by electron microprobe. No cordierite or magnetite was seen in any of the samples examined.

Plagioclase

Plagioclase accounts for 40-60% of phenocrysts by area and exhibits a temporal trend of increasing anorthite values in the Porco (PT-1 and PT-3), Livicucho (PT-14) and Los Frailes ignimbrite (PT-11p and PT-16) samples as seen in Figure 3.20. See Table 3.1 for a representative analysis from each sample. Zoning is seen optically in most samples. The plagioclase from the higher silica Porco samples (69-71% SiO_2) is generally homogeneous with an average composition of (An_{29-34} , Ab_{61-65} , Or_{4-5}) with the highest anorthite values found on the crystal rims. Plagioclase from Livicucho (60% SiO_2) exhibits higher anorthite values (An_{36-47} , Ab_{49-60} , Or_{2-4}),

but with the reverse pattern of higher anorthite cores. Los Frailes samples (66-67% SiO₂) have the highest average anorthite values (An₃₉₋₄₄, Ab₅₃₋₅₇, Or₂₋₄) and, like the Livicucho sample, exhibits the highest anorthite values in the cores. Texturally, plagioclase appears to be the first silicate phase to crystallize in Livicucho samples PT-13 and PT-14 with no inclusions of other silicate phases observed in the cores. In other samples, plagioclase crystals have some inclusions of biotite as well as ilmenite and zircon in the cores.

Quartz

All samples analyzed exhibited quartz phenocrysts composed of nearly pure SiO₂ with generally large euhedral grains (some >3mm) and occasional undulatory extinction. Inclusions are common with plagioclase, biotite, sanidine, oxides and zircon found throughout indicating that quartz was a late-stage crystallizing phase as expected.

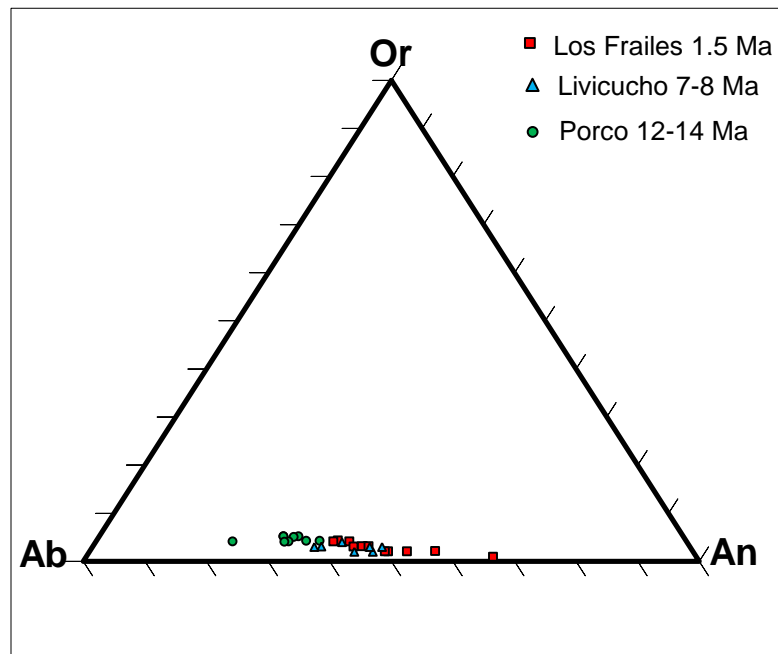
Sanidine

Sanidine accounts for around 10% of the phenocryst population by volume in all samples and shows little or no chemical variability between samples or between cores and rims. See Table 3.2 for a representative analysis for each sample. There is a slight temporal trend towards lower anorthite values decreasing from the Porco average of (An₀₋₁, Ab₂₁₋₂₃, Or₇₄₋₇₈) to the Livicucho average (An₁, Ab₁₇₋₂₁, Or₇₇₋₈₁) to the Los Frailes average (An₀₋₁, Ab₁₆₋₁₉, Or₇₉₋₈₃). Regular inclusions of plagioclase, biotite and zircon are present.

Table 3.1

Representative plagioclase electron microprobe analyses (cores and rims)										
Sample Unit	PT-1 Porco	PT-1 Porco	PT-3 Porco	PT-3 Porco	PT-14 Livch	PT-14 Livch	PT-11p Los Fr	PT-11p Los Fr	PT-16 Los Fr	PT-16 Los Fr
Core/Rim	core	rim	core	Rim	core	rim	core	rim	core	rim
SiO ₂	59.70	59.02	60.72	59.82	57.03	58.64	57.99	58.93	57.82	58.95
TiO ₂	0.03	0.00	0.04	0.00	0.07	0.00	0.00	0.00	0.00	0.00
Al ₂ O ₃	25.18	25.88	24.78	25.64	27.79	26.18	26.70	26.41	27.14	26.21
FeO	0.01	0.05	0.08	0.05	0.01	0.01	0.09	0.10	0.02	0.04
MnO	0.01	0.01	0.03	0.03	0.00	0.02	0.00	0.00	0.05	0.00
MgO	0.00	0.00	0.00	0.00	0.00	0.00	0.00	0.00	0.00	0.00
CaO	5.97	7.08	5.52	6.65	9.40	7.19	8.50	7.60	8.74	7.67
Na ₂ O	7.23	6.43	7.09	6.83	5.87	6.79	5.80	5.99	6.00	6.34
K ₂ O	0.81	0.72	0.93	0.85	0.34	0.52	0.06	0.68	0.49	0.64
Total	98.94	99.20	99.19	99.87	100.51	99.36	99.68	99.71	100.25	99.86
An (Ca)	29.9	36.2	27.9	33.3	45.9	36.1	43.6	39.1	43.3	38.5
Ab (Na)	64.9	59.6	66.7	61.5	52.1	60.8	53.2	56.5	53.6	57.3
Or (K)	5.2	4.2	5.4	5.2	2.0	3.1	3.2	4.4	3.1	4.2

In situ mineral analysis was completed at the Cornell University Center for Materials Research Electron Microprobe Laboratory by a JEOL 8900 in wavelength dispersive (WDS) mode with a beam diameter of 10 μm, accelerating voltage of 15 kV and an incident current of 2.00x10⁻⁸ amps. Smithsonian volcanic glass standards A-99, Juan de Fuca and Rhyolite glass along with natural mineral standards Lake City plagioclase, PX-1 clinopyroxene, and Kakanui hornblende were measured three times each at the beginning and end of each daily session. The deviation from known values was then used to produce a daily correction value for each oxide. Standards are presented in Appendix F.

**Figure 3.20**

Feldspar ternary diagram (Graham and Midgley, 2000) with plotted Los Frailes Complex plagioclase data. See text for discussion.

Symbols: red squares- main Los Frailes ignimbrite, green circles- Porco ignimbrite, blue triangles- Livicucho ignimbrite.

Biotite

Biotite occurs as euhedral phenocrysts up to 3mm in length and is the principal ferromagnesian mineral in all samples. No zoning is evident and broken or bent crystals are common. Biotite compositions are generally homogeneous and have little or no change between cores and rims, but exhibit some variation to higher Al and lower Fe, Mg and K. Inclusions of plagioclase, ilmenite, apatite and zircon are regularly seen. Plagioclase inclusions near several cores indicate biotite crystallization was later than or coeval with plagioclase. See Table 3.3 for a representative analysis for each sample.

Table 3.2

Representative sanidine electron microprobe analyses					
Sample Unit	PT-1 Porco	PT-3 Porco	PT-14 Livicucho	PT-11p Los Frailes	PT-16 Los Frailes
SiO ₂	63.78	65.68	65.24	65.08	65.30
TiO ₂	0.00	0.03	0.00	0.00	0.00
Al ₂ O ₃	18.86	19.30	19.12	19.20	18.98
FeO	0.00	0.03	0.05	0.06	0.01
MnO	0.03	0.02	0.00	0.00	0.01
MgO	0.00	0.00	0.00	0.00	0.00
CaO	0.11	0.22	0.16	0.14	0.10
Na ₂ O	2.42	2.24	2.23	1.93	2.03
K ₂ O	12.56	12.53	12.64	13.62	13.18
Total	97.76	100.06	99.44	100.03	99.61
An (Ca)	1.0	1.1	1.1	1.0	1.0
Ab (Na)	22.5	21.3	21.0	17.5	18.8
Or (K)	76.5	77.6	77.9	81.5	80.2

In situ mineral analysis was completed at the Cornell University Center for Materials Research Electron Microprobe Laboratory by a JEOL 8900 in wavelength dispersive (WDS) mode with a beam diameter of 10 μm , accelerating voltage of 15 kV and an incident current of 2.00×10^{-8} A. Specimens were cut and polished to 30 μm and coated with sputtered graphite carbon for microprobe analysis. Smithsonian volcanic glass standards A-99, Juan de Fuca and Rhyolite glass along with natural mineral standards Lake City plagioclase, PX-1 clinopyroxene, and Kakanui hornblende were measured three times each at the beginning and end of each daily session. The deviation from known values was then used to produce a daily correction value for each oxide. Standards are presented in Appendix F.

Accessory Minerals

An opaque mineral is seen optically in all samples and was identified as ilmenite by electron microprobe analysis. Ilmenite is the most common accessory

mineral and may be >1% of the phenocryst volume in the Porco PT-1 and all the Los Frailes ignimbrite samples. It is often texturally accompanied by other accessory minerals and has regular inclusions of apatite, monazite and some zircon. PT-1 and PT-14 from Porco Livicucho have Ti-rich ilmenite of 53-57 wt. % TiO₂ and 34-44 wt. % FeO. The Los Frailes unit samples (PT-11p and PT-16) have Fe-rich values with 34-36 wt. % TiO₂ and 62-64 wt. % FeO. Apatite and monazite are often observed associated with ilmenite, as well as seen as free grains and as inclusions in biotite cores. The high birefringence accessory mineral seen optically is zircon which is often associated or included within ilmenite. Zircon is also regularly observed as free grains in the groundmass as well as inclusions in all silicate phases indicating early crystallization. Although specifically sought, no magnetite or cordierite is evident in the samples examined (PT-1, PT-3, PT-11p, PT-12 and PT-16).

Table 3.3

Representative biotite electron microprobe analyses						
Sample Unit	PT-1 Porco	PT-3 Porco	PT-14 Livicucho	PT-8 Los Frailes	PT-11p Los Frailes	PT-16 Los Frailes
SiO ₂	35.70	35.83	36.17	36.81	35.79	35.51
TiO ₂	4.53	4.18	3.95	3.96	4.33	4.13
Al ₂ O ₃	16.91	17.51	18.10	18.59	17.64	16.75
FeO	20.50	21.83	19.07	18.47	19.43	18.57
MnO	0.09	0.12	0.14	0.13	0.13	0.11
MgO	9.99	9.59	10.14	8.91	10.71	9.70
CaO	0.00	0.02	0.03	0.09	0.01	0.01
Na ₂ O	0.59	0.47	0.26	0.32	0.34	0.29
K ₂ O	8.86	8.94	8.99	9.15	9.63	7.99
Total	97.17	98.51	96.86	96.43	98.02	93.08

In situ mineral analysis was completed at the Cornell University Center for Materials Research Electron Microprobe Laboratory by a JEOL 8900 in wavelength dispersive (WDS) mode with a beam diameter of 10 μm, accelerating voltage of 15 kV and an incident current of 2.00x10⁻⁸ A. Specimens were cut and polished to 30 μm and coated with sputtered graphite carbon for microprobe analysis. Smithsonian volcanic glass standards A-99, Juan de Fuca and Rhyolite glass along with natural mineral standards Lake City plagioclase, PX-1 clinopyroxene, and Kakanui hornblende were measured three times each at the beginning and end of each daily session. The deviation from known values was then used to produce a daily correction value for each oxide. Standards are presented in Appendix F.

Isotopic Results

Oxygen Isotopes

The calculated $\delta^{18}\text{O}_{\text{Magma}}$ values give an overall range of +9.43 to +10.79‰ for the Los Frailes Complex, as seen in Table 3.4 and Appendix D. The individual Los Frailes Complex units give the following $\delta^{18}\text{O}_{\text{Magma}}$ averages: Porco, +10.27‰; Sevaruyo, +10.53‰; Livicucho, +10.27‰; Condor Nasa, +9.52‰ and Los Frailes, +9.70‰. The resulting data exhibits a slight time dependent $\delta^{18}\text{O}_{\text{Magma}}$ decrease with the lowest values occurring in the younger Condor Nasa and Los Frailes samples. No clear correlation of $\delta^{18}\text{O}_{\text{Magma}}$ with other parameters is noted.

Strontium and Neodymium Isotopes

The $^{87}\text{Sr}/^{86}\text{Sr}$ and $^{143}\text{Nd}/^{144}\text{Nd}$ (ϵ_{Nd}) ratios depict a general progression of increasing isotopically evolved signature with time (Figure 3.21a). Samples from this study fall into two distinct fields with the four pre-12 Ma samples of Kumurana, Kari Kari and Porco showing less evolved isotopic character with $^{143}\text{Nd}/^{144}\text{Nd} = 0.512200$ - 0.512300 ($\epsilon_{\text{Nd}} = -6.59$ to -8.54) and $^{87}\text{Sr}/^{86}\text{Sr} = 0.71003$ - 0.71043 . Post-12 Ma samples of Sevaruyo, Livicucho, Condor Nasa and Los Frailes have a more evolved isotopic character of $^{143}\text{Nd}/^{144}\text{Nd} = 0.512140$ to 0.512200 ($\epsilon_{\text{Nd}} = -8.54$ to -9.71) and $^{87}\text{Sr}/^{86}\text{Sr} = 0.71140$ to 0.71267 . As in the elemental data, the Sevaruyo samples also have a large spread in isotopic values with PO-6 plotting near the Los Frailes ignimbrite field and PO-5 with more radiogenic values near the two Livicucho samples at $^{87}\text{Sr}/^{86}\text{Sr} \approx 0.71267$. See Appendix C for full analytical and standards results.

Figure 3.22 shows large variations in $^{87}\text{Sr}/^{86}\text{Sr}$ ratios between varying units at near equal wt. % SiO_2 and near equal Sr concentrations. Individual units have small $^{87}\text{Sr}/^{86}\text{Sr}$ ratio ranges with much larger comparative SiO_2 and Sr ppm ranges indicating that the isotopic character is being set prior to the processes which cause SiO_2 and Sr ppm variation.

Table 3.4

Sr, Nd and O isotopic analyses of Los Frailes Complex samples								
Sample	Unit	$^{87}\text{Sr}/^{86}\text{Sr}$	% S.E.	$^{143}\text{Nd}/^{144}\text{Nd}$	% S.E.	ϵ_{Nd}	$\delta^{18}\text{O}_{\text{Quartz}}\text{‰}$	$\delta^{18}\text{O}_{\text{Magma}}\text{‰}$
		Initial					Measured	Calculated
PT-1	Porco	0.70982	0.0005	0.512202	0.0017	-8.50	+10.45 ^a	+10.15
PT-3	Porco	0.70995 ^a	0.0006	0.512218	0.0022	-8.19	+10.68 ^a	+10.38
PT-4	Kumurana	0.70971 ^a	0.0009	0.512295	0.0013	-6.70	-	-
PT-5	Kari Kari	0.71004	0.0006	0.512260	0.0015	-7.38	-	-
PT-7	Condor Nasa	0.71148	0.0006	-	-	-	-	-
PT-8	Los Frailes	0.71147 ^a	0.0006	0.512146	0.0015	-9.60	+9.78	+9.48
PT-9	Los Frailes	0.71158	0.0008	0.512172	0.0015	-9.10	+9.73	+9.43
PT-10	Los Frailes	0.71132	0.0005	-	-	-	-	-
PT-11p	Los Frailes	0.71138	0.0006	0.512172	0.0016	-9.10	+10.45 ^a	+10.15
PT-12	Condor Nasa	0.71134	0.0009	0.512182	0.0023	-8.90	+9.82	+9.52
PT-13	Livicucho	0.71254	0.0008	-	-	-	-	-
PT-14	Livicucho	0.71238	0.0005	0.512163	0.0013	-9.27	+10.57 ^a	+10.27
PT-16	Los Frailes	0.71152	0.0006	0.512187 ^a	0.0019	-8.79	+10.04	+9.74
PO-2	Condor Nasa	0.71133	0.0005	0.512168	0.0011	-9.17	-	-
PO-5	Sevaruyo	0.71229	0.0009	0.512161	0.0020	-9.30	+11.09	+10.79
PO-6	Sevaruyo*	0.71154	0.0008	0.512200	0.0019	-8.54	+10.57	+10.27

Sr and Nd isotopic ratios were obtained on the TIMS at Cornell University and reflect measured values. Sr isotopic ratios were normalized to an $^{86}\text{Sr}/^{88}\text{Sr}$ value of 0.11940 and calculated to an initial ratio using $\lambda = 1.42 \times 10^{-11} \text{y}^{-1}$ and the assigned ages. The $^{87}\text{Sr}/^{86}\text{Sr}$ NBS 987 standard mean was measured at 0.71023 (n=27, from 10/2011 to 8/2012); and the $^{143}\text{Nd}/^{144}\text{Nd}$ Ames standard mean ratio was measured at 0.512167 (n=13, from 2/2012 to 5/2012). Reported $^{87}\text{Sr}/^{86}\text{Sr}$ are measured values while reported $^{143}\text{Nd}/^{144}\text{Nd}$ values are normalized to $^{143}\text{Nd}/^{144}\text{Nd}$ Ames = 0.512131 (-0.000036) which is also applied to the reported ϵ_{Nd} values (-0.70). ϵ_{Nd} is reported using a value of $^{143}\text{Nd}/^{144}\text{Nd}_{\text{CHUR}} = 0.512638$. Error for $^{87}\text{Sr}/^{86}\text{Sr}$ and $^{143}\text{Nd}/^{144}\text{Nd}$ are reported in percent standard error. See Appendix C for full analytical results. Oxygen isotopic ratios were obtained by laser fluorination on quartz grains at the University of Cape Town, South Africa. Measured values for unknowns were corrected to the average measured value for the internal standard of Monastery Garnet (MONGT, $\delta^{18}\text{O} = 5.38\text{‰}$ assuming a value of 5.80‰ for UWG-2). In run error (2σ) is estimated at $\pm 0.10\text{‰}$ (n=6, from 1/11/2013 to 1/18/2013). Following Chang (2007), the fractionation correction for quartz is about 0.3‰ for $\Delta_{\text{qtz-melt}}$ and therefore 0.3‰ was subtracted from $\delta^{18}\text{O}_{\text{quartz}}$ to produce $\delta^{18}\text{O}_{\text{magma}}$. See Appendix D for full analytical results.

^a Reported value is the average of two or more measurements.

* Sample may be from Los Frailes ignimbrite (see discussion at beginning of Chapter 3).

Figure 3.21

(a) Plot of $^{143}\text{Nd}/^{144}\text{Nd}$ (ϵ_{Nd}) versus $^{87}\text{Sr}/^{86}\text{Sr}$ for Los Frailes Complex data. Two distinct fields are seen with pre-12 Ma samples from Kumurana, Kari Kari and Porco having less enriched character, and the post-12 Ma samples of Sevaruyo, Livicucho, Condor Nasa and the Los Frailes ignimbrite with more enriched character. The increase in enriched character at 10-12 Ma is proposed to have been caused by a delamination event at that time which exposed enriched crust to melting and assimilation. (b) Plot of $^{143}\text{Nd}/^{144}\text{Nd}$ (ϵ_{Nd}) versus $^{87}\text{Sr}/^{86}\text{Sr}$ for comparative Puna backarc ignimbrites as well as plotted assumed mantle and calculated crustal end-members (see Chapter 5). Altiplano primitive lavas (purple diamonds) of <7 Ma are depicted with their associated SiO_2 values for reference. The Los Frailes Complex occupies a field of distinctly lower $^{143}\text{Nd}/^{144}\text{Nd}$ (ϵ_{Nd}) at a given $^{87}\text{Sr}/^{86}\text{Sr}$ when compared to APVC and Puna ignimbrites.

Symbols: Los Frailes Complex: squares- This study, diamonds – Davidson and de Silva (1995) and Hoke and Lamb (2007). APVC/Puna and individual ignimbrite fields as compiled in Kay et al. (2010, 2011).

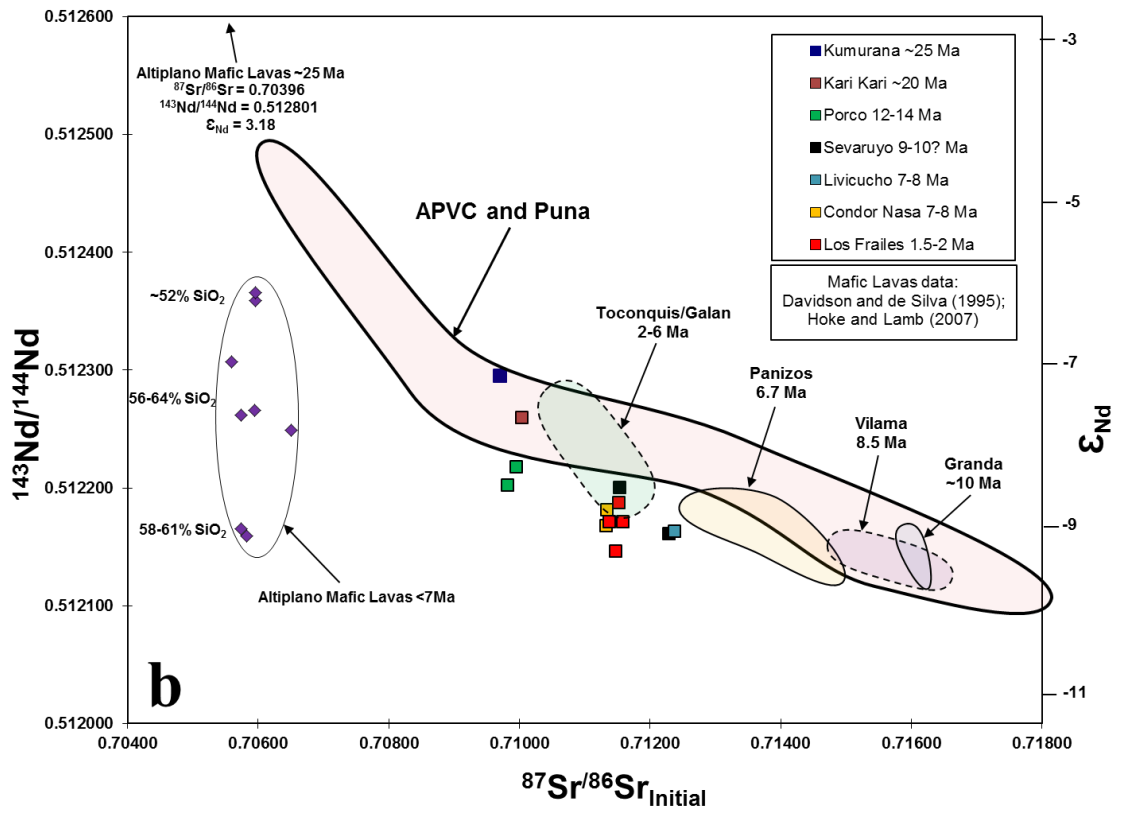
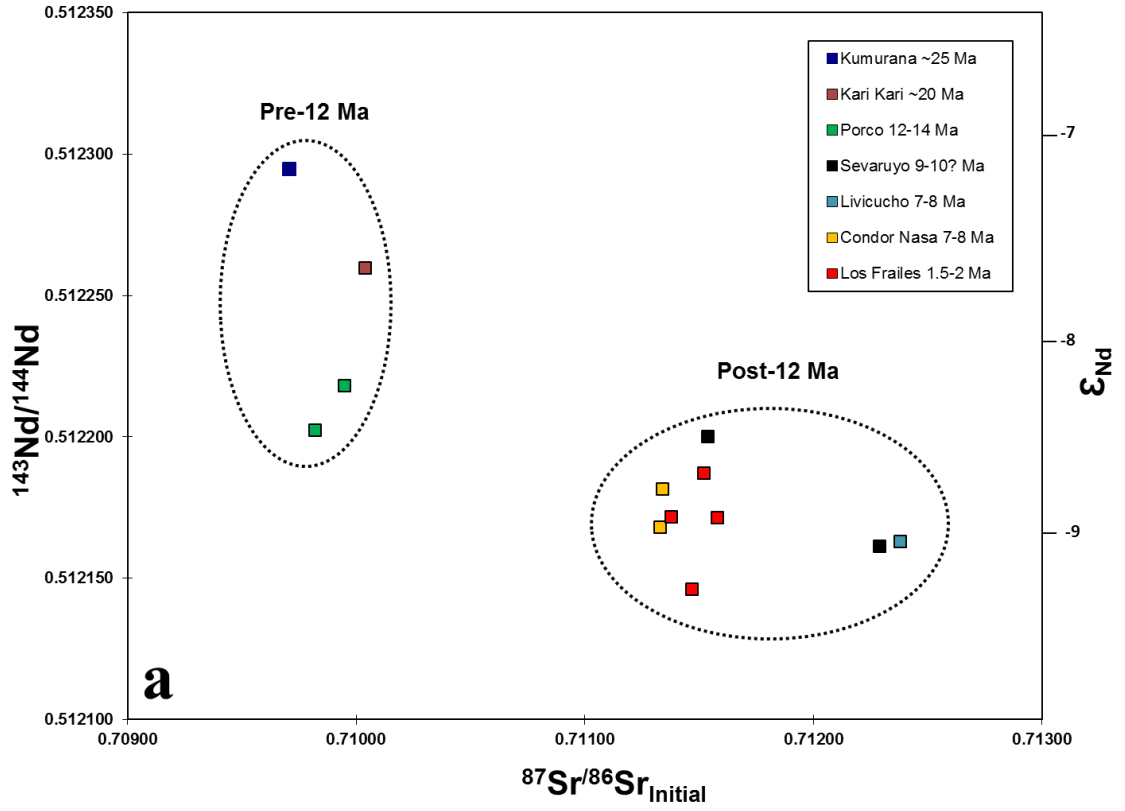
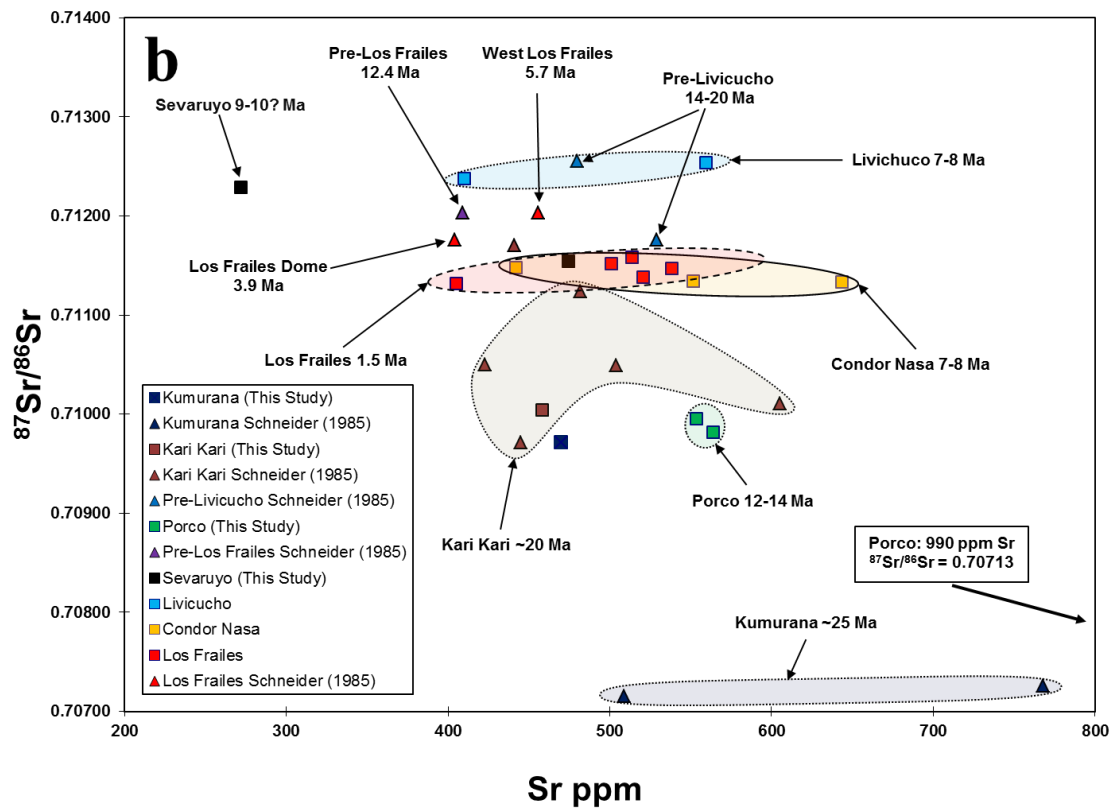
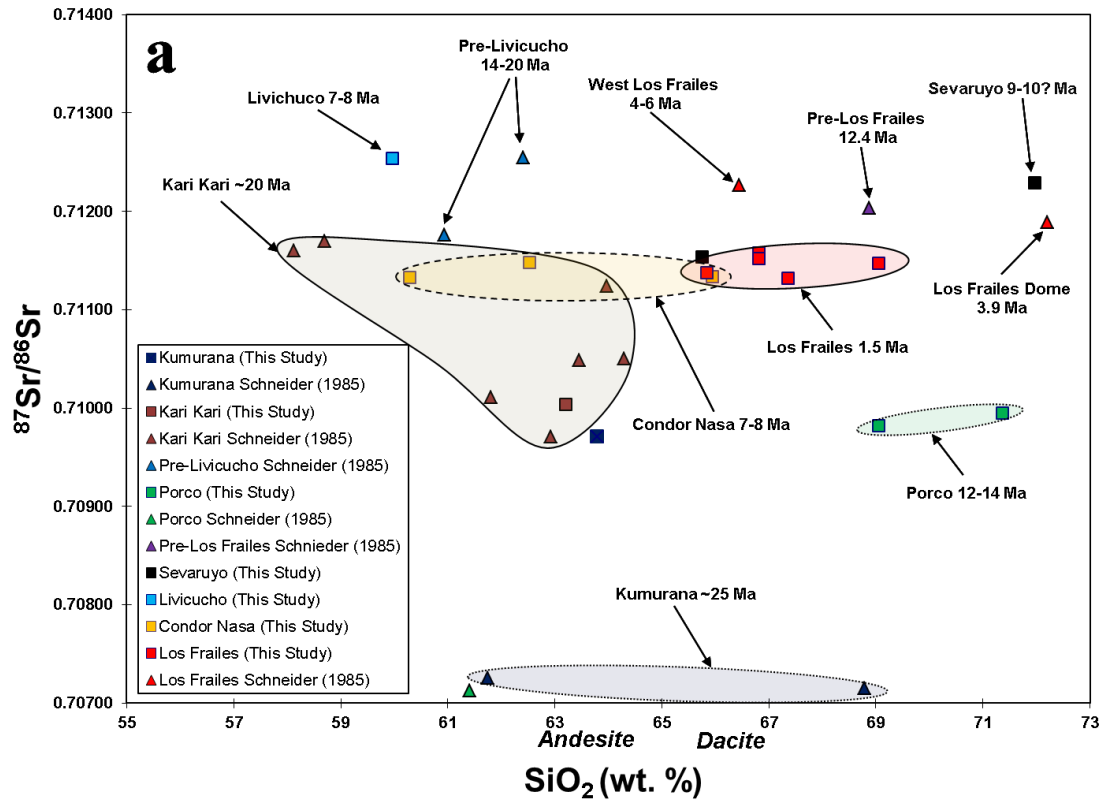


Figure 3.22

(a) Plot of $^{87}\text{Sr}/^{86}\text{Sr}$ versus weight percent SiO_2 . (b) Plot of $^{87}\text{Sr}/^{86}\text{Sr}$ versus Sr ppm. Both plots show large variation in $^{87}\text{Sr}/^{86}\text{Sr}$ between varying units at near equal SiO_2 and Sr ppm, but little change in $^{87}\text{Sr}/^{86}\text{Sr}$ within individual units with variable SiO_2 and Sr ppm (flat fields). This indicates that the isotopic character of magmas is being set prior to variation in SiO_2 and Sr ppm which occur due to fractionation in the middle crust. This is interpreted as crustal assimilation taking place only in the lower crust with fractionation, but no additional assimilation, occurring as the magmas transit to the surface.

Symbols: Los Frailes Complex: squares- This study, triangles – Schneider (1985).



Zircon Age Analysis

Little usable zircon age information was obtained due to the combination of low U content and the small average size of the zircons. While over 40 zircons from the Los Frailes ignimbrite samples PT-8, PT-10 and PT-15 were isolated, only a few survived chemical abrasion owing to their small size. Those that did were physically small and had very low U ppm which resulted in insufficient radiogenic Pb being collected relative to the lead blank (Pbc) to perform a good analysis. Additionally, the zircons are covered in a layer of volcanic glass that is difficult to remove and contain a large amount of common lead. As a result, radiogenic/common Pb ratios are extremely low and the precision is extremely poor by TIMS standards, even in the best cases. See Appendix E for detailed analytical results.

Although the results were disappointing, a few beneficial conclusions can be drawn from the zircon data. Los Frailes ignimbrite samples PT-10 and PT-15 contain an unusually high number of both antecrystic and xenocrystic zircons while PT-8 is zircon-poor. The discordant ages on zircons in PT-10 and PT-15 are likely due to mixing of autocrystic and xenocrystic domains where new zircon has overgrown an older inherited core. The xenocrysts have dates that ranged from 420 Ma for PT-15 z2 to 600 Ma for PT-15 z5 which indicates a Late Precambrian-Early Paleozoic age for their source consistent with what is known about the basement (e.g., Lucassen et al., 2001; Ramos, 2008). As zircon crystallization predates eruption, and in the absence of enough data to establish comprehensive zircon populations, all that can confidently be concluded about eruption dates is an upper limit of ≤ 1.9 Ma for PT-10 and ≤ 7.2 Ma for PT-15 which agrees with $^{40}\text{Ar}/^{39}\text{Ar}$ sanidine ages.

⁴⁰Ar/³⁹Ar Age Analysis

The two new ⁴⁰Ar/³⁹Ar sanidine dates obtained on chemically similar Los Frailes ignimbrite samples produced virtually identical ages with a weighted mean age of 1.520±0.014 Ma for PT-8 and 1.522±0.021 Ma for PT-11. See Appendix G for detailed analytical results.

Geothermometry and Geobarometry

The calculated zircon saturation temperatures for the PT series of samples all fall in the 800°-900°C range established by Keller (2010) for the Condor Nasa and Sevaruyo region samples. Table 3.6 lists zircon saturation temperatures ranging from 813°C in a Sevaruyo sample PO-5 to 895°C for the Kari Kari sample PT-5. The Porco and Los Frailes units have narrow ranges of 861°-875°C and 849°-858°C respectively while Condor Nasa samples have a wide range from 837° to 874°C. Two-feldspar thermometry temperatures calculated at 400 MPa and 1000 MPa (1 GPa) are also shown in Table 3.6. Two-feldspar temperatures for Sevaruyo samples PO-5 and PO-6 from Keller (2010) are included in Table 3.6. The calculated temperature variation with change in pressure is relatively small (~7°C per 100 MPa) and is nearly linear over the pressure range from 200 MPa to 1200 MPa (1.2 GPa). The plagioclase cores and rims give nearly identical values indicating little temperature change during plagioclase crystallization. The total overall temperature range is 675-755°C at 400 MPa. Two-feldspar temperatures are about 110-135°C below their paired zircon saturation temperature following the same general trend. Sevaruyo sample PO-5 shows the lowest two-feldspar temperature of 675°C while Porco samples PT-1 and PT-3 show the highest at 741°-747°C (no Condor Nasa samples were analyzed). The Los Frailes ignimbrite samples PT-11p and PT-16 have a small range of 720°-725°C which includes the Los Frailes-like Sevaruyo sample PO-6 (720°C).

Table 3.5**⁴⁰Ar/³⁹Ar sanidine age analyses**

Sample	Total Fusion Age (Ma)	2σ	Plateau Age (Ma)	2σ	n ^a	MSWD ^b	J ^c
<u>Los Frailes ignimbrite</u>							
PT-8	1.53	±0.02	1.520	±0.014	11/12	0.32	0.0012492
PT-11	1.52	±0.02	1.522	±0.021	10/10	0.32	0.0011160

⁴⁰Ar/³⁹Ar sanidine ages were obtained by irradiating samples and standards at the Oregon State University TRIGA-type reactor and fusing at the University of Wisconsin-Madison Rare Gas Geochronology Laboratory using a 25 Watt CO₂ laser. The gas was cleaned during and after the heating period with two SAES C50 getters operated at ~450°C and room temperature. Blanks were analyzed after every second laser fusion, and were less than 4×10⁻¹⁷, 3×10⁻¹⁹, 6×10⁻²⁰, and 2×10⁻¹⁹ moles for ⁴⁰Ar, ³⁹Ar, ³⁷Ar, ³⁶Ar, respectively. Ten to twenty mass discrimination measurements via automated analysis of air pipette tests were made prior to and following each incremental heating experiment and encompass the range of ⁴⁰Ar observed for the samples. Measured ⁴⁰Ar/³⁶Ar ratios of atmospheric argon were normalized to ⁴⁰Ar/³⁶Ar = 295.5 ± 0.5 and the discrimination was calculated using a linear law relationship. The 28.201 Ma Fish Canyon tuff sanidine (FCs) standard was used. Argon isotope analyses were done using a MAP 215–50 with ArArCalc software. Ages were calculated from the blank-, discrimination- and decay-corrected Ar isotope data after correction for interfering isotopes produced from potassium and calcium in the nuclear reactor. See Appendix G for a full analysis details.

^a The number of measurements used to calculate the weighted mean ages.

^b Mean square of weighted deviates; an F statistic that compares the variance within step ages with the variance about the age.

^c Combines the neutron fluence with the monitor age.

Table 3.6

Zircon saturation and two-feldspar geothermometry temperatures						
Sample	Unit	Zr Saturation (°C)	Two-spar (°C) at 400 MPa core	Two-spar (°C) at 1 GPa core	Two-spar (°C) at 400 MPa rim	Two-spar (°C) at 1 GPa rim
PT-1	Porco	871	741	784	738	781
PT-2	Porco	875	-	-	-	-
PT-3	Porco	861	747	789	755	797
PT-4	Kumurana	863	-	-	-	-
PT-5	Kari Kari	895	-	-	-	-
PT-6	Condor Nasa	856	-	-	-	-
PT-7	Condor Nasa	864	-	-	-	-
PT-8	Los Frailes	855	-	-	-	-
PT-9	Los Frailes	850	-	-	-	-
PT-9p	Los Frailes	858	-	-	-	-
PT-10	Los Frailes	850	-	-	-	-
PT-11	Los Frailes	849	-	-	-	-
PT-11p	Los Frailes	858	725	764	742	782
PT-12	Condor Nasa	857	-	-	-	-
PT-13	Livicucho	853	-	-	-	-
PT-14	Livicucho	-	707	749	715	756
PT-15	Condor Nasa	851	-	-	-	-
PT-16	Los Frailes	-	724	765	739	779
PT-16p	Los Frailes	-	-	-	-	-
PO-1	Condor Nasa	874 ^a	-	-	-	-
PO-2	Condor Nasa	871 ^a	-	-	-	-
PO-3	Condor Nasa	837 ^a	-	-	-	-
PO-4	Condor Nasa	848 ^a	-	-	-	-
PO-5	Sevaruyo	813 ^a	675 ^b	-	-	-
PO-6	Sevaruyo*	832 ^a	720 ^b	-	-	-

Zircon saturation thermometry uses the reported major and trace element data and equations of Watson and Harrison (1983). Two-feldspar thermometry is done by using the mineral data collected by microprobe analysis and calculated using the SOLV CALC program (Wen and Nekvasil, 1994) which uses the thermodynamic models of Nekvasil and Burnham (1987). Zircon saturation temperatures for PT-14, PT-16 and PT-16p are omitted due to lack of Zr concentration data for those samples.

^a Values are the same as those reported by Keller (2010).

^b Values reported by Keller (2010) using SOLV CALC program at 400 MPa.

* Sample may be from Los Frailes ignimbrite (see discussion at beginning of Chapter 3).

CHAPTER 4

DISCUSSION OF ANALYTICAL RESULTS

Samples collected by Schneider (1985) targeted, and were often from, alteration zones and minor units erupted prior to the large-volume ashflows of the Livicucho, Condor Nasa, and Los Frailes ignimbrites. Alteration and small volumes are thought to be responsible for several of these samples having significant geochemical differences from the main ignimbrites listed and the samples of other studies. Schneider (1985) samples considered in this study include 5 from Kumurana, 15 from Kari Kari, 7 from Porco, and 6 from the main Los Frailes ignimbrite with varying completeness of major element, trace element and isotopic data. Eight samples have been excluded due to their reported alteration or association with older low volume units not considered here.

Of the six Los Frailes ignimbrite samples from Schneider (1985), four (Fr-5, Fr-6, Fr-7 and Fr-9) are from domes and lava fields that are thought to be low volume pre-Los Frailes ignimbrite occurrences (2.0-3.9 Ma) while samples Fr-21 and Fr-22 are from the older (5-9 Ma) northwestern portion of the Los Frailes ignimbrite. These are included in most plots and labeled as “Los Frailes”, however, they are not direct samples from the main ~1.5 Ma Los Frailes ignimbrite and at times show significant variation from the samples of this study and those of Luedke et al. (1997). All 27 (20 Los Frailes, 5 Porco and 2 Nuevo Mundo) samples reported by Luedke et al. (1997) are included as well as all 8 Livicucho samples reported by Jiménez et al. (1997).

Major Elements

Major element data clearly reflect a large sedimentary component in the Los Frailes Complex, which is revealed in its high Al and low Na contents. The most striking feature is the highly peraluminous ($Al/(K+Na+Ca) > 1.0$) nature of the

complex. The $Al/(K+Na+Ca)$ versus weight percent SiO_2 (Figure 3.1a) shows the majority of samples fall in the $Al/(K+Na+Ca) = 1.1-1.3$ range. There may be a slight decreasing $Al/(K+Na+Ca)$ trend with time as ~20 Ma Kari Kari and 7-8 Ma Livicucho-Condor Nasa units have average values near ~1.2, the 1.5-3.5 Ma Los Frailes ignimbrite has an average between 1.1-1.2 and the youngest <1 Ma Nuevo Mundo values are ~1.1.

Peraluminosity is likely a product of assimilated sedimentary basement with high $Al/(K+Na+Ca)$ developed during deposition by the relative loss of K, Na, and Ca. Coranzuli, Panizos Vilama and Granada are the four northernmost APVC ignimbrites and sit to the north of a peraluminous-metaluminous border which splits the APVC and marks the change from an igneous-dominated lower crust in the south to a sedimentary-dominated lower crust in the north (Kay et al., 2010, 2011). This places the Los Frailes Complex firmly on the northern peraluminous side of the divide with the four peraluminous APVC centers to its south and the peraluminous Morococala ignimbrite to its north. The four APVC centers listed above are the most peraluminous ignimbrites found on the Puna plateau with other volcanic centers exhibiting generally intermediate to metaluminous values (Kay et al., 2010, 2011). Figure 3.1b depicts the selected Altiplano-Puna ignimbrite fields overlain on the Los Frailes Complex sample data. The four APVC centers have a range of $Al/(K+Na+Ca) = 1.0-1.3$ with a slightly lower average than the Los Frailes Complex. To the north, the central Altiplano ignimbrite Morococala has similar peraluminosity to the Los Frailes Complex with $Al/(K+Na+Ca) = 1.1-1.3$ (Morgan et al., 1998). On the southern Puna, the Cerro Galán center has an intermediate $Al/(K+Na+Ca)$ between 0.95-1.05 which is representative of the more igneous-dominated basement.

As noted by Kay et al. (2010), the aluminosity variability of the ignimbrites is also reflected in their Na_2O versus K_2O concentrations (Figure 3.2). The Los Frailes

Complex shows a clear Na-poor character, similar to the peraluminous APVC centers. Silica-rich (>64% SiO₂) Los Frailes Complex samples (red box in Figure 3.2) have the same low values of Na₂O = 2.3-3.1 as many of the more silica-poor samples indicating the Na₂O values are set early in magma evolution. These are similar Na₂O values to >64% SiO₂ filtered Coranzuli and slightly lower than more S-type (*sedimentary*) values at Vilama, Granada and Panizos (Kay et al., 2010). Morococala has higher Na₂O values of 3.0-3.5 which place it in the A-type (*anorogenic*) granitoid field. This is surprising, given the coherence of peraluminosity and low Na₂O seen in the Puna ignimbrites and mimicked in the Los Frailes Complex data. Cerro Galán also has an A-type signature with Na₂O = 3.0-4.0, which fits with its intermediate Al/(K+Na+Ca) character (Kay et al., 2011).

The Los Frailes Complex K₂O values (3.8-5.5) are higher than those seen in the four APVC ignimbrites (K₂O = 2.7-4.9) or at Morococala and Cerro Galán (K₂O = 4.0-5.0) (Morgan et al., 1998). When K₂O is set against SiO₂ in Figure 3.3, the high K₂O content of all but the Kumurana samples place them in the shoshonitic field with only a few high SiO₂ samples from Porco, Sevaruyo and the Los Frailes ignimbrite just below the shoshonitic/high-K boundary. The older Kumurana unit has distinctly lower K₂O values which plot in the high-K field.

While it shares many major elemental characteristics with both large and small ignimbrites on the Altiplano-Puna, the Los Frailes Complex is unique with its combination of high peraluminosity, high K₂O (shoshonitic), and moderate S-type signature. Based on these characteristics, the Los Frailes Complex displays a clear sedimentary component in all of its ignimbrites with slightly less sedimentary character in the older Kumurana unit.

Trace Elements

The depth at which assimilation of the crust and hybridization of the magmas occurs is reflected in the Los Frailes Complex trace element data by extremely steep negative REE patterns, high Sr concentration and variable HREE and HFSE depletion. Steep negative REE patterns combined with high Sr concentration point to crustal AFC processes in a high pressure environment with stable garnet and unstable plagioclase. Variable HREE and HFSE depletion indicate that rapid decreases in AFC zone depth have occurred periodically and are used here to identify large delamination events in the Los Frailes Complex history. Eu/Eu^* values indicate a middle crustal storage stage in which plagioclase fractionation imprints a negative Eu anomaly on the magma during its ascent.

Figure 3.4b is a plot of trace element concentrations from Kari Kari, Porco and the main Los Frailes units of the Los Frailes Complex with representative samples from the peraluminous APVC ignimbrites, Cerro Galán and Morococala. All comparative ignimbrites share the same negative REE slope reflecting LREE enrichment and HREE depletion but with reduced La/Sm, Sm/Yb and La/Yb ratios. Depletion of HFSE elements Nb, Ta and Ti is also clearly seen but with lower Nb/Ta and extreme Ti depletion at Morococala. Also of note are equally low (non-arc) Ba/La ratios but with reduced concentrations when compared to the Los Frailes Complex.

Rare Earth Elements

The Los Frailes Complex magmas occupy a field of LREE enrichment and extreme HREE depletion with a varying temporally dependent pattern (Figures 3.5). HREE depletion is quantified by an increasing Sm/Yb ratio while LREE enrichment is characterized by an increasing La/Sm ratio. When La/Sm versus Sm/Yb is plotted, these ratios form a pattern of REE slope change with shallow slopes plotting in the lower left and steep slopes in the upper right. In general, $Sm/Yb < 2$ indicates magma

that equilibrated with pyroxenes, Sm/Yb of 2-5 indicates amphiboles, and Sm/Yb >5 is likely a garnet-induced signature. Generally, Sm/Yb >5 requires an exceptionally thick crust of greater than 45-55 km with a pressure of ~15 kbar (1.5 GPa) in order to generate enough modal garnet in the crustal restite to produce the resulting steep HREE pattern in the magma (Indares et al., 2008). An increase in the La/Sm ratio represents an increase in amphibole presence which preferentially incorporates middle rare earth elements (MREE), represented by Sm. As amphibole is a lower pressure mineral compared to garnet, lower La/Sm is an indicator of equilibration of the magma at shallower levels of the middle or upper crust. La/Sm ratios are also sensitive to LREE enrichment of the magma, represented by La, which can occur during low percentage partial melting. Figure 3.8 shows no noteworthy trend of La concentration change with SiO₂ increase indicating that changes in the La/Sm and La/Yb ratios are not driven by SiO₂ sensitive accessory phases with high La affinities. Figure 3.6 shows no discernible effect of La concentration on the La/Yb ratio showing that the ratio is a reflection of changes in Yb rather than La concentration. Together, these elemental affinities dictate that movement from the lower-left to the upper-right in the La/Sm versus Sm/Yb field represents equilibration under higher pressure conditions which is interpreted as thickening of the continental crust below the Los Frailes Complex leading to garnet involvement in the AFC zone. Additionally, lower ratios for La/Sm, Sm/Yb or La/Yb can also be a signal of greater percentage melting which tends to flatten the REE pattern. Due to the relatively low 60-70% silica content of the samples, it is assessed that accessory phases, particularly zircon and monazite, have not played a significant role in altering the REE patterns or the La/Sm and Sm/Yb ratios. Figure 3.7a plots La/Yb ratios versus SiO₂ content and displays the more silicic Porco and Los Frailes units with the highest Sm/Yb ratios (>60). However, the moderate silica (64-68% SiO₂) Kumurana, Kari Kari, Livicucho and

Condor Nasa samples (red box in Figure 3.7a) have the same low Sm/Yb ratios as the lower silica (<64% SiO₂) samples from the same units. In addition, several of the highest silica Los Frailes and Sevaruyo samples have low La/Sm, Sm/Yb and La/Yb ratios. When only samples of intermediate silica content are considered (64-68% SiO₂), the La/Sm, Sm/Yb and La/Yb ratio patterns do not change appreciably, which indicates that variations in REE ratios are not SiO₂ driven. Similar patterns of near constant La/Yb ratios with variable SiO₂ are also seen in the APVC, Cerro Galán and Morococala fields shown in Figure 3.7b.

As Figure 3.5b and 3.7b illustrate, the high La/Yb and Sm/Yb ratios seen in the Porco, Los Frailes and Nuevo Mundo ignimbrites are far higher than those reported in the APVC, Puna or Morococala (Kay et al., 2010, 2011; Morgan et al., 1998). Most large volume APVC centers have Sm/Yb values of 2-4 with Coranzuli and Vilama showing the highest pressure signatures with ratios of 4-6 (Figure 3.5b). The small volume Granada center has slightly higher values with Sm/Yb of 5-7 and La/Sm of 4.5-6.5. The Cerro Galán field has similar values to Coranzuli and Vilama, which are high for APVC and Puna ignimbrites, but low compared to the Sm/Yb values of the Los Frailes Complex. Morococala has Sm/Yb = 5-8 and La/Sm = 4.5-6.5 with one sample as high as La/Sm = 10, which is nearly as high as in Porco samples, but without the correspondingly elevated Sm/Yb ratio.

As was first noted by Kay et al. (2010) and Keller (2010), the pattern of the Los Frailes Complex La/Sm versus Sm/Yb ratio data indicates that the southern Altiplano crust underwent two general thickening episodes with a dramatic thinning event between them at ~10 Ma (Figure 3.5a and 3.9a). The first thickening event begins with Kumurana at ~25 Ma and culminates in Porco samples at ~12 Ma with high La/Sm and extremely high Sm/Yb ratios. These are then followed by a dramatic decrease in Sm/Yb and La/Sm ratios with 9-10 Ma Sevaruyo and 7-8 Ma Livicucho

and Condor Nasa exhibiting the lowest La/Sm seen at the Los Frailes Complex. The second thickening event is seen as both the La/Sm and Sm/Yb values again increase from their lows at 7-8 Ma to higher values in the Los Frailes and Nuevo Mundo ignimbrite samples. The rapid decrease in La/Sm and especially Sm/Yb at 10-12 Ma, following the high ratios seen in the Porco field, is interpreted as delamination of the lithosphere and perhaps lower crust in response to the crustal thickening and density instability. After the loss of the lithospheric-mantle and possibly the lower mafic crust, there is again a steady increase in both Sm/Yb and La/Sm ratios. This is thought to show continuing crustal thickening in response to sustained crustal shortening and crustal flow after the dramatic loss of the lower lithosphere. The 1.5-6 Ma Los Frailes ignimbrite samples display the largest spread of values which may represent the competing processes of crustal thickening and periodic loss through delamination which continues to the present.

Figure 4.1, which distinguishes the ~1.5 and 4-6 Ma ages of the Los Frailes ignimbrite, depicts a possible second distinct delamination episode within the Los Frailes ignimbrite data at 2-4 Ma. The graph shows the individual unit average La/Sm, (Sm/Yb)/2, (La/Ta)/10 and (Ba/Ta)/100 ratios against age (Ma) and has been filtered to include only intermediate silica samples (~64-68% SiO₂) in order to avoid fractionation effects. Schneider (1985) samples Fr-21 and Fr-22, which are dated at 4.44-5.67 Ma, from the extreme northwestern portion of the Los Frailes meseta have high ratios and are followed by decreased ratios in the ~1.5 Ma Los Frailes samples. If a distinct delamination event occurred at 2-4 Ma, then the current absence of mantle-lithosphere (e.g., Beck and Zandt, 2002), as depicted in Figure 1.6, may be the direct result of that event which preceded the main volumetrically-dominant main Los Frailes ignimbrite emplacement at 1.5-3.5 Ma and the current (<1 Ma) volcanism at Nuevo Mundo.

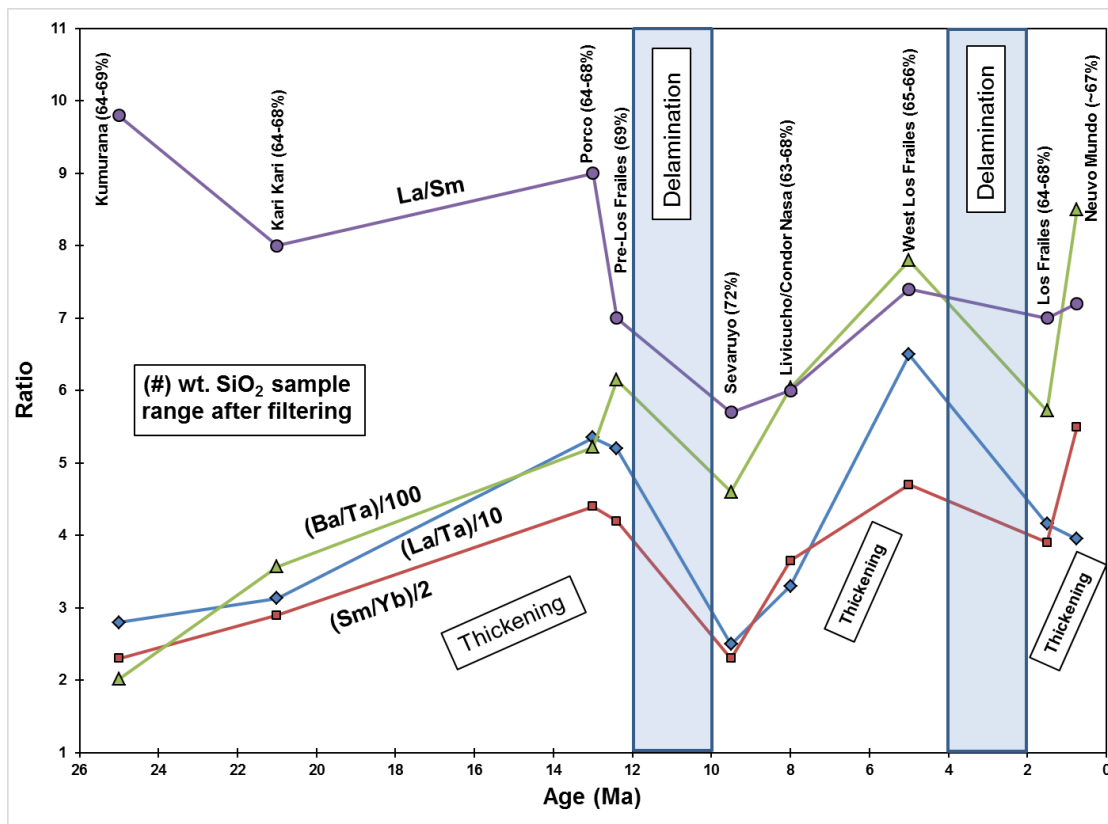


Figure 4.1

Graph of individual unit average La/Sm ppm ratios (purple circles and line), (Sm/Yb)/2 ppm ratios (blue diamonds and line), (La/Ta)/10 ppm ratios (red squares and line) and (Ba/Ta)/100 ppm ratios (green triangles and line) versus ignimbrite age (Ma). The individual unit samples have been filtered to include only intermediate SiO₂ samples (~64-68%) in order to avoid possible fractionation affects. The SiO₂ range of the samples included is listed in parentheses with the vertical unit label. The two proposed delamination events at 10-12 Ma and 2-4 Ma are highlighted in blue and labeled.

High Field Strength and Large-Ion Lithophile Elements

Large-ion lithophile elements (LILE) Ba, Cs, K, Rb and Sr can be used as indicators of hydrous fluid additions in the mantle, and as tracers of subduction products. In contrast, high field strength elements (HFSE) Nb, Hf, Ta and Zr have low aqueous solubilities and are relatively immobile during weathering and metamorphism. La is also an immobile element, but to a lesser degree than HFSEs. HFSE depletion is signaled by an increasing La/Ta ratio while LILE enrichment is shown by increasing Ba/Ta and Ba/La ratios. High LILE/HFSE (Ba/La) ratios are

observed in many subduction zone magmas and presumably reflect additional LILE-rich hydrous inputs to the mantle wedge source of those magmas. This makes the Ba/Ta versus La/Ta plot a potentially useful tool in determining the slab influence on mantle derived magmas. Ba/La and Ba/Ta ratios increase with greater involvement of Ba-rich pelagic sediment with values of Ba/La >20 and Ba/Ta >600 generally taken to indicate a subducted sediment-related arc signature. However, the Ba/La ratio is also sensitive to alkali-feldspar fractionation which makes the use of this system problematic when the magma must penetrate and may fractionate in thick crust such as in the Altiplano-Puna (Mamani et al., 2010). The Ba/Ta and La/Ta ratios are used here to track changes in crustal thickness while Ba/La shows changes in lower crust chemistry.

Figure 3.9a depicts Ba/Ta versus La/Ta as well as Ba/La ratios for the Los Frailes Complex and shows a bimodal distribution and systematic variation with time in the HFSE and LILE ratios. Ba/Ta and La/Ta ratios are generally driven by variations in Ta content with less variable Ba and La concentrations, which makes the Ba/La ratio a more sensitive tool to investigate LILE/HFSE chemistry in this case. The samples from the Los Frailes Complex, while generally plotting in the APVC range of Ba/La = 10-20, have a pre-12 Ma mean of about 12 and a distinct shift to a post-12 Ma mean of 17-18. Concurrently, there is a separate change in Ba/Ta versus La/Ta as both ratios increase steadily between 25 Ma and 12 Ma, rapidly decrease after 12 Ma, and then increase again from 10 Ma to the present. The young Nuevo Mundo center has the highest overall unit values of Ba/Ta = 829-870 and La/Ta \approx 55 with a Ba/La of \sim 16 (Luedke et al., 1997). Like the La/Sm and Sm/Yb patterns discussed above, high silica samples seem to display the highest Ba/Ta and La/Ta ratios as well. This pattern is again interrupted by the Sevaruyo sample PO-5 with 72% SiO₂ which has Ba/Ta, La/Ta and Ba/La ratios which plot with the low silica

Livicucho and Condor Nasa units (59-65% SiO₂). The Ba/Ta and La/Ta pattern of increasing and decreasing ratios mirror the temporal pattern seen in the La/Sm versus Sm/Yb plot (Figure 3.7a and 4.1) and therefore also point to a pressure-driven mechanism. High Ba/Ta and La/Ta ratios coincide with times believed to represent a thickened crust and low ratios occur prior to the initiation of major crustal thickening or following the proposed delamination events at 10-12 Ma and 2-4 Ma. The increase in Ba/La ratio seen at ~12 Ma at the Los Frailes Complex is interpreted as Ba/La enrichment of the mafic end-member or an increase in crustal fertility following the initiation of delamination when lithospheric-mantle and basal crustal materials are argued to have been lost. Taylor and McLennan (1995) report Archean crust Ba/La ratios range from 13-15 and a generalized lower crust Ba/La value of 13.6 which may represent values expected in the original Altiplano lower crust prior to 12 Ma. Metapelitic crustal material is expected to have a Ba/La ratios near 19 (Miller, 1985) and could represent current lower crustal values in areas of missing lithosphere. Delamination driven exposure of fertile Archean metapelitic crust following the loss of the depleted and refractory lithospheric-mantle and lower crust may explain the Ba/La ratio increase seen at that time.

Figure 3.9b illustrates that the APVC has a similar Ba/La of 10-20 but with much reduced La/Ta = 25-40 and Ba/Ta = 300-700 as compared to the Los Frailes Complex (Kay et al., 2010). This places them in the field of ratios occupied by Livicucho and Condor Nasa which have a slightly elevated Ba/La of about 17 but with intermediate Ba/Ta and La/Ta ratios. The Cerro Galán field has lower values with an average Ba/La ratio of 12-13, Ba/Ta of 100-400 and La/Ta of 15-30 which is described by Kay et al. (2011) as intraplate-like and is in the Kumurana and lower Kari Kari fields. Morococala has a wide range of moderate to extremely low Ba/Ta and La/Ta ratios caused by both low La and Ba and elevated Ta concentrations as

compared to the Los Frailes Complex. In contrast, Ba/La ratios are consistently 15-20 which is in the same range as post-12 Ma units of the Los Frailes Complex (Morgan et al., 1998).

The case for HFSE ratio changes being driven by accessory phase changes is supported by variable Nb, Ta and Ti depletion noted in Figure 3.4a and best depicted in Figure 3.10. The pattern of variable Nb and Ta concentrations is also present at Morococala, but not in the APVC or Puna ignimbrites, which have low and less variable Nb and Ta concentrations, and with the exception of Panizos, slightly lower Nb/Ta ratios as depicted in Figure 3.4b. Morococala has much higher Ta concentrations of 2-4 ppm which results in very low Nb/Ta ratios of 4-7. Previous to this study, only Luedke et al. (1997) has reported Ta concentration data on the Los Frailes Complex, and so PT-4 and PT-5 are the only data points for the Kumurana and Kari Kari centers. They show higher concentrations and near chondritic (19.9 ± 0.6) Nb/Ta ratios of 16.3 and 18.0 at Kumurana and Kari Kari while Livicucho and Condor Nasa also have high concentrations, but intermediate Nb/Ta ratios of 11-16. The lowest concentrations of both Nb and Ta as well as the lowest Nb/Ta ratios of 8-14 occur in the Porco, Sevaruyo, Los Frailes and Nuevo Mundo ignimbrites which are the most silicic units. The high-silica Sevaruyo sample PO-5 plots with other high-silica units and not with the low-silica, but temporally adjacent, Livicucho and Condor Nasa as it does with La/Sm versus Sm/Yb and Ba/Ta versus La/Ta (Figures 3.5a and 3.9a). This indicates that that Nb and Ta concentrations are more affected by silica-sensitive accessory phases than more pressure controlled Ba and La concentrations seem to indicate. Near chondritic ratios (19.9 ± 0.6) are uncommon in arc lavas and are attributed to contamination of the mantle by forearc subduction erosion (Goss and Kay, 2009). Rutile and low-Mg amphibole are the likely high pressure residual phases which fractionate Nb and Ta in mafic to intermediate lavas and are capable of

lowering both HFSE concentrations and the Nb/Ta ratio (Goss and Kay, 2009) (see discussion for Cerro Galán ignimbrites in Kat et al., 2011).

Europium Anomaly

Figure 3.11a shows the Los Frailes Complex has variable Eu/Eu* which ranges from near 1.0 in the Kumurana unit to 0.6 in Los Frailes ignimbrite samples showing the clear presence of plagioclase as a fractionating phase. Silica poor Kumurana has the overall highest Eu/Eu* ratios (smallest negative Eu anomaly) of 0.8-1.0 and overlays the upper half of the Kari Kari field which has values mostly from 0.7-0.9. Livicucho and Condor Nasa plot together and largely overlay the Kari Kari field with a range of 0.65-0.9. Porco ratios range from 0.65-0.75 with the Los Frailes ignimbrite exhibits the lowest Eu/Eu* ratios of 0.6-0.75 which also encompasses Nuevo Mundo. High silica Sevaruyo PO-5 (72% SiO₂) has Eu/Eu* = 0.64.

While lower Eu/Eu* values with increased silica are not unusual, the high silica units of the Los Frailes Complex, with the exception of the Sevaruyo region, all coincide with periods of proposed thickened crust and higher pressure assimilation. However, a plot of Eu/Eu* against Sm/Yb, Figure 3.12a shows no correlation of low Eu/Eu* values at times of thickened crust (high Sm/Yb ratios). This indicates that Eu/Eu* character is not being set in the assimilation region, and is instead generated later in the magma evolution at lower pressure. Greater plagioclase fractionation at lower pressures in the middle and upper crust is generally expected, and seems to be the source of Eu/Eu* ratio character in the Los Frailes Complex. An alternative explanation is that plagioclase loss is roughly equal at all times, and that the Eu anomaly is being controlled by variable fO₂ which would have to be greater during low-silica periods and lower during high-silica conditions. However, no mechanism for this has been described and so the volume of plagioclase removal, through a

variably thick middle to upper crust is the most likely cause of the range of Eu/Eu* values seen in the Los Frailes Complex magmas.

The Eu/Eu* values at the Los Frailes Complex are similar to those found in the APVC ignimbrites examined (Figures 3.11b and 3.12b). However, they are higher than the Eu/Eu* ratios of 0.45-0.65 found at Cerro Galán, which is on a 60 km thick crust, and is described by Kay et al. (2011) as indicating conditions that are not sufficiently oxidizing to reduce a substantial portion of Eu³⁺ to Eu²⁺. Los Frailes Complex Eu/Eu* ratios are also higher than the Eu/Eu* values of 0.35-0.55 reported by Morgan et al. (1998) at Morococala. This is expected, given that both Cerro Galán and Morococala have higher silica content as well as higher sanidine content, which also reduces Eu/Eu* ratios. Figure 3.11b show a clear Altiplano-Puna wide trend of decreasing Eu/Eu* with increased SiO₂ while Figure 3.12b shows a lack of correlation between Sm/Yb ratios and Eu/Eu* values. If the higher Eu/Eu* ratios of the Los Frailes Complex are due to a decrease in plagioclase fractionation as compared to Cerro Galán and Morococala, then the greater Sr concentrations at the Los Frailes Complex (400-650 ppm) compared to the Sr concentrations seen at Cerro Galán and Morococala (generally 250-350 ppm) may also be the result of decreased plagioclase removal. However, Sr enrichment is not seen in the four peraluminous APVC ignimbrites which have Sr concentrations comparable to Cerro Galán and Morococala but with higher Eu/Eu* ratios similar to the Los Frailes Complex. The mineralization of the pre-12 Ma Los Frailes Complex units and the lack of magnetite seen in thin section are consistent with a reduced crustal fractionating environment. Factors such as fO₂ and water pressure may play a significant role in determining the valence state of Eu (e.g., see parallel discussion in Kay et al., 2010). Therefore, the similar Eu/Eu* values found in the Los Frailes Complex and the peraluminous APVC ignimbrites

values cannot be exclusively used to imply an equal role for plagioclase in the middle crust of both regions.

Strontium, Rubidium and Neodymium

High Sr concentration is a temporally enduring hallmark of Los Frailes Complex volcanism which is unique among large Altiplano-Puna backarc ignimbrites. Figures 3.13, 3.14 and 3.15 show that variable Sm/Yb and Eu/Eu* ratios as well as SiO₂ content impart little change to the resulting Sr concentrations. With the exception of Kumurana, Sr content has remained consistent in the Los Frailes Complex at 400-650 ppm Sr since 20 Ma. The older ~25 Ma Kumurana unit alone deviates from the average range with Sr enrichment of 750-1050 ppm at 59-64% SiO₂, and also displays a pattern of Sr ppm decrease with decreasing Eu/Eu* ratios (see Figure 3.14). A lack of Sr concentration depletion in more evolved units is surprising given that Sr²⁺ is a mobile LILE element which plagioclase has a high affinity for in its Ca²⁺ divalent cation site. This indicates that plagioclase removal has not had a large effect on the resulting ignimbrite Sr concentrations, which may have resulted in the higher relative Sr ppm values. Only Sevaruyo PO-5 seems to show expected Sr depletion with 272 ppm at 72% SiO₂.

Figure 3.16 plots Nd ppm against SiO₂ and depicts Nd remaining relatively steady over time with most values between 50 and 70 ppm Nd. Kumurana has the highest unit average with a range of 60-85 ppm Nd. Similar to its Sr concentration, Sevaruyo PO-5 has a much lower concentration of 33 ppm Nd which is near the lowest values seen in the Los Frailes Complex. Like Sr concentrations, the Los Frailes Complex concentrations of 50-70 ppm Nd are also high compared to other Altiplano-Puna backarc ignimbrites, which have generally 30-50 ppm Nd. Figure 3.16 shows that Nd has not varied with SiO₂ which signals that accessory phases have not played a major role in REE depletion which can occur with higher SiO₂ content.

Figure 3.17 demonstrates that Sr and Nd concentrations in the Los Frailes Complex are proportionally enriched over other Altiplano-Puna backarc ignimbrites but maintain Sr/Nd \approx 10 (excluding Kumurana). The Kumurana Sr/Nd ratios of 13-15 are an exception, due mostly to their much higher Sr content.

The Rb concentrations of 160-280 ppm in the Los Frailes Complex (Figure 3.18) are nearly the same as other Altiplano-Puna backarc ignimbrites, which generally have 150-300 ppm Rb. As seen in Figure 3.19, this results in lower Rb/Sr ratios in the Los Frailes Complex as compared to other Altiplano-Puna backarc ignimbrites which may contribute to the lower $^{87}\text{Sr}/^{86}\text{Sr}$ ratios seen there. Rb concentrations and Rb/Sr ratios will be discussed further below.

Isotopic Compositions

Isotopic evidence indicates a crust-to-mantle mixing ratio of near 50:50 with assimilation of the crust occurring in a single region. New $\delta^{18}\text{O}$ data modeled with a metapelitic crustal end-member produces a crustal input range of 40-50%. AFC modeling using new $^{87}\text{Sr}/^{86}\text{Sr}$ and $^{143}\text{Nd}/^{144}\text{Nd}$ (ϵ_{Nd}) values also result in ~50% crustal input. In addition, constant $^{87}\text{Sr}/^{86}\text{Sr}$ values with changing SiO_2 and Sr concentrations support a single zone of assimilation followed by fractionation at middle and upper crustal levels. Temporal patterns in $^{87}\text{Sr}/^{86}\text{Sr}$ and $^{143}\text{Nd}/^{144}\text{Nd}$ (ϵ_{Nd}) ratio changes show a distinct increase in evolved character at 10-12 Ma, coeval with the delamination event as indicated by trace element ratios. Lead isotopic data is used to define the Los Frailes Complex basement compared to known central Andean crustal domains.

Table 4.1

Whole rock Sr and Pb isotopic data from Schneider (1985)							
Sample	Unit	Age (Ma)	⁸⁷ Sr/ ⁸⁶ Sr Initial	Sr ppm	²⁰⁶ Pb/ ²⁰⁴ Pb	²⁰⁷ Pb/ ²⁰⁴ Pb	²⁰⁸ Pb/ ²⁰⁴ Pb
As-4	Kari Kari	22	0.71124	482	18.725	15.669	39.008
As-52	Kari Kari	21	0.71049	510	18.866	15.697	39.216
As-57	Kari Kari	21	0.71011	605	18.926	15.686	39.252
As-69	Kari Kari	21	0.70971	445	18.711	15.664	39.028
As-70	Kari Kari	21	0.71160	440	18.652	15.684	38.970
As-71	Kari Kari	21	0.71170	441	-	-	-
As-144 ^a	Kari Kari	21	-	-	18.764	15.688	39.096
Fr-3	Pre-Frailes	12.42±0.79	0.71203	409	18.661	15.629	38.793
Fr-5	Frailes Dome	3.89±0.38	0.71189	404	-	-	-
Fr-13 ^a	Porco	10.56±0.30	-	937	18.263	15.624	38.320
Fr-14 ^a	Porco	11.52±0.42	0.70713	990	18.658	15.671	38.920
Fr-18	Pre-Livicucho	19.53±1.23	0.71255	480	19.051	15.849	39.386
Fr-19	Pre-Livicucho	14.09±0.55	0.71176	529	-	-	-
Fr-21	West Frailes	4.44-5.67	0.71227	456	18.580	15.660	38.850
KK-5-79	Kari Kari	21.95±0.92	0.71050	423	-	-	-
KK-10-81	Kari Kari	21	-	-	18.888	15.691	39.176
KK-11-79	Kumurana	25.25±0.90	0.70726	768	-	-	-
KK-12-79	Kumurana	26.13±1.22	0.70715	509	18.761	15.663	38.872

Those with (±) are K/Ar ages from Schneider (1985), those without are assigned ages based on location and composition.

^a Described by Schneider (1985) as “altered”, but included in this study.

Table 4.2

δ¹⁸O isotopic analyses of Los Frailes Complex samples						
Sample	Unit	δ ¹⁸ O _{Quartz} ‰ Measured	δ ¹⁸ O _{Magma} ‰ Calculated	δ ¹⁸ O _{Crust} ‰ 40:60 ^b	δ ¹⁸ O _{Crust} ‰ 50:50 ^b	δ ¹⁸ O _{Crust} ‰ 60:40 ^b
PT-1	Porco	+10.45 ^a	+10.15	+16.67	+14.49	+13.04
PT-3	Porco	+10.68 ^a	+10.38	+17.26	+14.96	+13.44
PT-8	Los Frailes	+9.78	+9.48	+15.01	+13.16	+11.94
PT-9	Los Frailes	+9.73	+9.43	+14.89	+13.07	+11.86
PT-11p	Los Frailes	+10.45 ^a	+10.15	+16.68	+14.50	+13.05
PT-12	Condor Nasa	+9.82	+9.52	+15.10	+13.24	+12.00
PT-14	Livicucho	+10.57 ^a	+10.27	+16.96	+14.73	+13.24
PT-16	Los Frailes	+10.04	+9.74	+15.65	+13.68	+12.37
PO-5	Sevaruyo	+11.09	+10.79	+18.28	+15.78	+14.12
PO-6	Sevaruyo*	+10.57	+10.27	+16.97	+14.73	+13.24

Oxygen isotopic ratios were obtained by laser fluorination on quartz grains at the University of Cape Town, South Africa. Measured values for unknowns were corrected to the average measured value for the internal standard of Monastery Garnet (MONGT, δ¹⁸O = 5.38‰ assuming a value of 5.80‰ for UWG-2). In run error (2σ) is estimated at ±0.10‰ (n=6, from 1/11/2013 to 1/18/2013). Following Chang (2007), the fractionation correction for quartz is about 0.3‰ for Δqtz-melt and therefore 0.3‰ was subtracted from δ¹⁸O_{quartz} to produce δ¹⁸O_{magma}. Calculations assumed that the mantle, crust and cumulates all have the same oxygen content.

^a Reported values are averages of two analyses.

^b δ¹⁸O values of crustal end-member given a mantle value of +5.80‰ (Bindeman, 2008) and the crust:mantle mixing ratio listed for each column.

* Sample may be from Los Frailes ignimbrite (see discussion at beginning of Chapter 3).

Previous isotopic work in the Los Frailes Complex includes 18 whole rock $^{87}\text{Sr}/^{86}\text{Sr}$ ratios and 19 whole rock $^{206}\text{Pb}/^{204}\text{Pb}$, $^{207}\text{Pb}/^{204}\text{Pb}$ and $^{208}\text{Pb}/^{204}\text{Pb}$ ratios reported by Schneider (1985). The samples considered here are shown in Table 4.1. Even when combined with new data (see Table 3.4), the resulting isotopic data set is not comprehensive and is incapable of capturing the full range of variations either geographically (7500-8500 km²) or temporally (~25 My).

Oxygen Isotopes

Crustal portions of 40-50% result in crustal $\delta^{18}\text{O}$ values that remain largely within the range of +14 to +20‰ expected in pelites (Miller, 1985) (Table 4.2). A 40% crustal input results in $\delta^{18}\text{O}_{\text{crust}}$ values of +14.89 to +18.28‰, 50% crust gives +13.07 to +15.78‰ and 60% crust shows sub-pelitic values of +11.86 to +14.12‰. The calculated crust-to-mantle mixing ratio of near 50:50, with a peraluminous pelitic crustal end-member, is comparable to the values reported for Vilama and Panizos using similar calculations by Kay et al. (2010).

Strontium and Neodymium Isotopes

Figure 3.20a shows two distinct isotopic fields in the Los Frailes Complex data, with the pre-12 Ma samples having less radiogenically evolved character ($^{143}\text{Nd}/^{144}\text{Nd} = 0.512200$ to 0.512300 , $\epsilon_{\text{Nd}} = -6.59$ to -8.54 , $^{87}\text{Sr}/^{86}\text{Sr} = 0.70715$ to 0.71170), and the post-12 Ma samples having greater radiogenically evolved character ($^{143}\text{Nd}/^{144}\text{Nd} = 0.512140$ to 0.512200 , $\epsilon_{\text{Nd}} = -8.54$ to -9.71 , $^{87}\text{Sr}/^{86}\text{Sr} = 0.71140$ to 0.71270). Additionally, the pre-12 Ma samples show a clear temporal progression of increasingly radiogenically evolved values internal to that data set. Kumurana samples KK-11-79 and KK-12-79 exhibit extremely low $^{87}\text{Sr}/^{86}\text{Sr} \approx 0.70720$ (Schneider, 1985) while Kumurana PT-4 has a $^{143}\text{Nd}/^{144}\text{Nd} = 0.512295$ ($\epsilon_{\text{Nd}} = -6.69$), but with a much higher $^{87}\text{Sr}/^{86}\text{Sr}$ ratio of 0.71018 which is near the middle of the Kari $^{87}\text{Sr}/^{86}\text{Sr}$ range of 0.70970 to 0.71170 . Kari Kari sample PT-5 has a similar $^{87}\text{Sr}/^{86}\text{Sr} =$

0.71043 to PT-4, but with a lower $^{143}\text{Nd}/^{144}\text{Nd} = 0.512260$ ($\epsilon_{\text{Nd}} = -7.37$). 12-14 Ma Porco samples PT-1 and PT-3 indicate even more evolved $^{143}\text{Nd}/^{144}\text{Nd} \approx 0.512210$ ($\epsilon_{\text{Nd}} \approx -8.35$) with $^{87}\text{Sr}/^{86}\text{Sr}$ at ~ 0.71010 . Porco sample Fr-14 has a much lower $^{87}\text{Sr}/^{86}\text{Sr} = 0.70713$ (Schneider, 1985), and is discussed in detail below.

While the post-12 Ma field is internally irregular, it fits the overall trend towards greater isotopically evolved character with time. Sevaruyo sample PO-5, with a uniquely high $\text{Rb}/\text{Sr} = 1.0$, has values similar to those of Livicucho samples PT-13 and PT-1. Collectively, these have the highest $^{87}\text{Sr}/^{86}\text{Sr} = 0.71267$ and lowest $^{143}\text{Nd}/^{144}\text{Nd} = 0.512161$ ($\epsilon_{\text{Nd}} = -9.30$) values in the Los Frailes Complex. The 7-8 Ma Condor Nasa, ~ 1.5 Ma Los Frailes ignimbrite and Sevaruyo PO-6 samples occupy a field centered at $^{87}\text{Sr}/^{86}\text{Sr} = 0.71150$ and $^{143}\text{Nd}/^{144}\text{Nd} = 0.512180$ ($\epsilon_{\text{Nd}} = -8.93$).

The above described temporal trend of increasing isotopically evolved values can also be interpreted as a spatial pattern. From Kumurana, Kari Kari and Porco in the southeast to Livicucho and Sevaruyo in the northwest, there is a trend of increasing isotopically evolved character across the Los Frailes Complex. Schneider (1985) samples Fr-3, Fr-18 and Fr-19 were reported with ^{40}K - ^{40}Ar biotite ages of 12.4 ± 0.8 , 19.5 ± 1.2 Ma and 14.1 ± 0.6 Ma respectively and have relatively high $^{87}\text{Sr}/^{86}\text{Sr}$ values of 0.71203, 0.71255 and 0.71176. While the domes and units from which these samples were collected are not well described and thought to be minor, their $^{87}\text{Sr}/^{86}\text{Sr}$ ratios do not fit with the previously described temporal pattern of isotopic evolution. This may be due to alteration or greater crustal contamination of small volume melts or may be caused by heterogeneity of the underlying crust. The three samples are described by Schneider (1985) as “Pre-Frailes eruptives”, but Fr-18 and Fr-19 are referred to in this study as “Pre-Livicucho” based on location. Although both Fr-18 and Fr-19 are described as altered, they are considered here as their $^{87}\text{Sr}/^{86}\text{Sr}$ ratios are close to 7-8 Ma Livicucho sample values. Fr-3 is from the extreme western side of the main Los

Frailes ignimbrite in older pyroclastic rocks and is labeled “pre-Los Frailes”. Fr-18 has $^{87}\text{Sr}/^{86}\text{Sr}$ ratio and Sr concentration values in the field of 7-8 Ma Livicucho samples PT-13 and PT-14 while Fr-3 and Fr-19 are closer to Condor Nasa and Los Frailes ignimbrite values (see Figure 3.21). With over 130 km separating the Kumurana and Sevaruyo centers, the potential for crustal isotopic heterogeneities is a possibility and may become recognizable with increased sample density. However, due to the condition of the samples and the size of the units from which they were collected, the temporal trend is considered more likely.

Porco sample Fr-14 exhibits the lowest whole rock $^{87}\text{Sr}/^{86}\text{Sr}$ reported in the Los Frailes Complex. This sample, with its low $^{87}\text{Sr}/^{86}\text{Sr}$ ratio, Sr ppm = 990, Rb/Sr = 0.27, SiO₂ = 61.4% and Eu/Eu* = 0.81 (Schneider, 1985), infers that the mantle isotopic character had not changed appreciably since similar values were seen in Kumurana samples KK-12-79 and particularly KK-11-79 ($^{87}\text{Sr}/^{86}\text{Sr}$ = 0.70726, Sr ppm = 768, Rb/Sr = 0.27, SiO₂ = 61.7%, Eu/Eu* = 0.79; Schneider, 1985). These primitive values are surprising given its ^{40}K - ^{40}Ar biotite age of 11.52±0.42 Ma, which is ~14 My after Oligocene-Miocene magmatism had restarted and much crustal thickening had occurred in the southern Altiplano (e.g., Gubbels et al., 1993; Husson and Sempere, 2003). Like other Porco samples, Fr-14 has high La/Sm = 10.40 and Sm/Yb = 8.41 (Schneider, 1985) which indicates equilibration beneath an extremely thick crust. The low SiO₂ and Eu/Eu* values combined with high Sr concentration indicates that plagioclase fractionation was suppressed or played a relatively minor role and could indicate that middle crustal storage and evolution was brief or bypassed by some magma batches during this period.

One of the most consistent patterns of the isotopic data is near constant $^{87}\text{Sr}/^{86}\text{Sr}$ ratios with variable SiO₂ and Sr concentration within individual units (Figure 3.22). Large variation in $^{87}\text{Sr}/^{86}\text{Sr}$ ratios between units at equal SiO₂ or equal Sr

concentration is also common. This pattern is also seen in APVC and Puna volcanic rocks (e.g., Aitcheson and Forrest, 1994; Davidson and de Silva, 1992; Kay et al., 2010). This indicates that once the $^{87}\text{Sr}/^{86}\text{Sr}$ ratio of the magma is achieved in the lower crust through assimilation, there is little or no further assimilation during ascent. Magma SiO_2 and Sr concentration evolution is driven by fractionation, particularly of plagioclase. The largest SiO_2 and Sr ppm variations occur at Condor Nasa which shows 60-66% SiO_2 and 440-640 ppm Sr at $^{87}\text{Sr}/^{86}\text{Sr} \approx 0.71150$ and in Kumurana samples from Schneider (1985) with 61-69% SiO_2 , 510-770 ppm Sr at $^{87}\text{Sr}/^{86}\text{Sr} \approx 0.71260$. Kari Kari is the only significant Los Frailes Complex unit which has a minor deviation in $^{87}\text{Sr}/^{86}\text{Sr}$ ratios (0.70971 to 0.71170). Although some $^{87}\text{Sr}/^{86}\text{Sr}$ ratio variation exists, there is no pattern of increasing ratios with increasing SiO_2 or decreasing Sr concentration which would be expected if continued crustal assimilation had caused the $^{87}\text{Sr}/^{86}\text{Sr}$ ratio variation. Instead the Kari Kari field shows variable $^{87}\text{Sr}/^{86}\text{Sr}$ values at dispersed SiO_2 and Sr ppm values. This can be explained either by the Kari Kari unit being made up of several individual batches of magma with independent $^{87}\text{Sr}/^{86}\text{Sr}$ values, or a single batch of poorly mixed magma with several separate assimilation histories. The concentration of study and thorough sampling conducted by Schneider (1985) likely captured these differences if they are present. $^{87}\text{Sr}/^{86}\text{Sr}$ ratio variation may also exist within sub-units of the main Los Frailes ignimbrite, however, the four samples presented here are from a relatively small geographic area of the northeastern Los Frailes meseta with similar age, chemistry and magmatic batch history (see Figure 1.3).

On a regional scale, Figure 3.21b shows that the Los Frailes Complex occupies a field of distinctly lower $^{143}\text{Nd}/^{144}\text{Nd}$ (ϵ_{Nd}) ratios at a given $^{87}\text{Sr}/^{86}\text{Sr}$ ratio compared to APVC and Puna ignimbrites. While the Los Frailes Complex $^{87}\text{Sr}/^{86}\text{Sr}$ ratios cover the lower half of the APVC and Puna $^{87}\text{Sr}/^{86}\text{Sr}$ ratio range, it is well below the

$^{87}\text{Sr}/^{86}\text{Sr}$ values of the three northern APVC volcanoes; Granada, Panizos and Vilama, but has similar Nd isotopic values. The pattern of lower $^{143}\text{Nd}/^{144}\text{Nd}$ (ϵ_{Nd}) values at a given $^{87}\text{Sr}/^{86}\text{Sr}$ ratio was noted in Altiplano mafic lavas when compared to Puna mafic lavas by Kay et al. (2010) and may be reflected in the isotopic signature of the adjacent ignimbrites. These lower $^{143}\text{Nd}/^{144}\text{Nd}$ (ϵ_{Nd}) values can be explained by either the mafic lavas directly representing the mantle-derived end-member and imparting their isotopic signature on the resulting ignimbrites, or by the mafic lavas being contaminated in a similar manner to the ignimbrites by low-percentage crustal assimilation. Unlike Puna ignimbrites, the Los Frailes Complex has a significant range of $^{143}\text{Nd}/^{144}\text{Nd}$ ratios from 0.512140 to 0.512300 ($\epsilon_{\text{Nd}} = -6.59$ to -9.71) and breaks from the pattern of normally flat $^{143}\text{Nd}/^{144}\text{Nd}$ (ϵ_{Nd}) ratio fields at $^{87}\text{Sr}/^{86}\text{Sr} > 0.70800$ (Kay et al., 2010). Compared to the 2-6 Ma Cerro Galán ignimbrite in the southern Puna, the 0-25 Ma Los Frailes Complex field overlays it but with greater range in both $^{87}\text{Sr}/^{86}\text{Sr}$ and $^{143}\text{Nd}/^{144}\text{Nd}$ (ϵ_{Nd}) ratios which may display greater temporal changes in the mantle and crust. No systematic isotopic variation is seen in the limited Los Frailes Complex data between the large and small volume ignimbrite units as is noted in the southern Puna by Schurr et al. (2007) and in the northern Puna by Kay et al. (2010).

Lead Isotopes

Lead isotopic data is used by several researchers to define the crustal domains of the central Andean basement (e.g., Lucassen et al., 2001, 2002; Wörner et al., 1992; Aitchison et al., 1995; Mamani et al., 2008, 2010). The 13 Schneider (1985) samples considered here are listed in Table 4.1 and plotted in Figures 4.2a and 4.2b. Only one sample (4.44-5.67 Ma aged Fr-21 from West Los Frailes) is post-10 to 12 Ma, which is argued by Husson and Sempere (2003) to be the onset of optimal deep crustal flow conditions in the Altiplano. Crustal flow from the east to the west would cause the

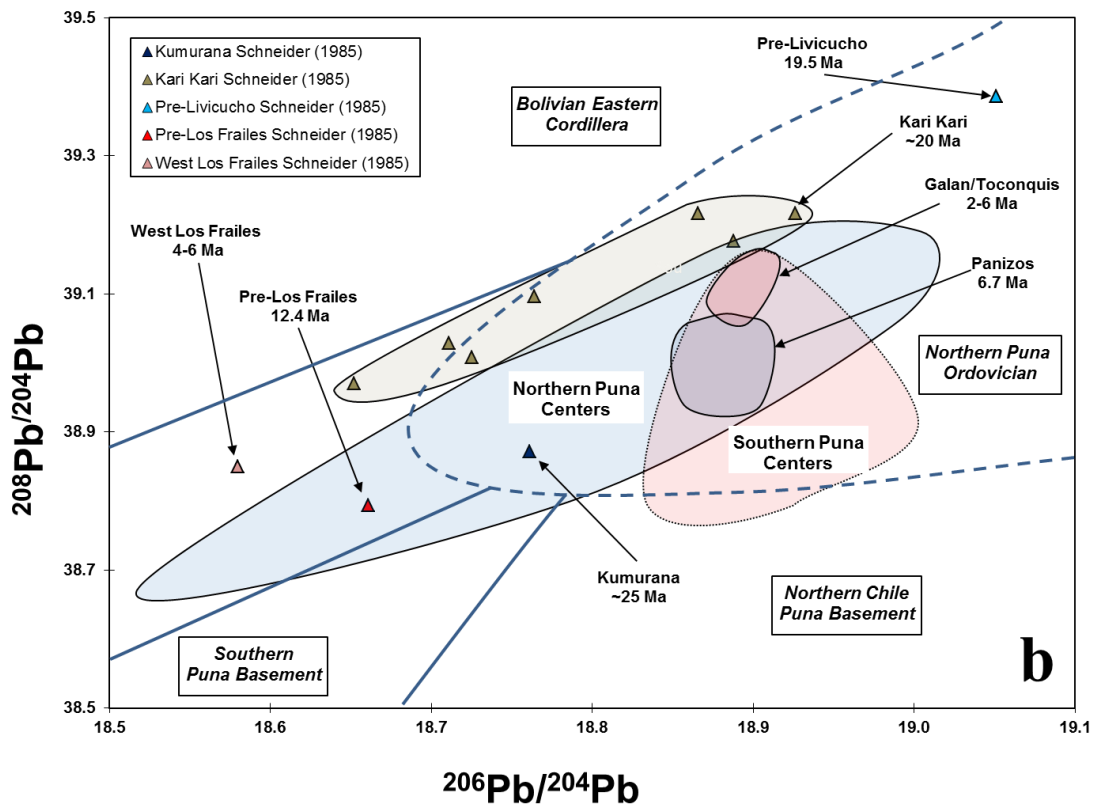
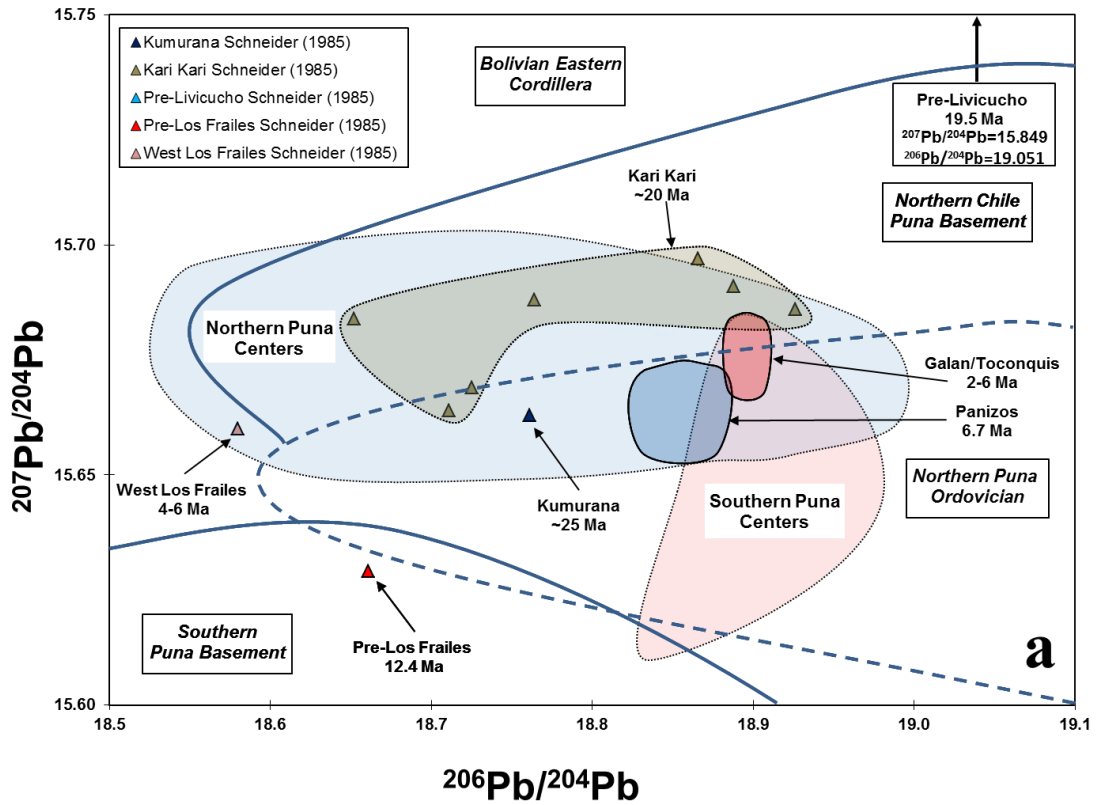
westward movement of basement derived Pb isotopic signatures as well as cause diffusion of the boundaries (Mamani et al., 2008).

Figure 4.2 depicts the fields for the northern Chile Puna basement, northern Puna Ordovician rocks, Bolivian Eastern Cordillera and southern Puna basement based on Lucassen et al. (2001, 2002). Overlaid are the fields for southern Puna volcanic centers and northern Puna volcanic centers as well as the Cerro Galán and Panizos ignimbrite fields (Kay et al., 2010; Ort et al., 1996). The Los Frailes Complex samples predominately plot with the northern Puna volcanic centers which reflect similar basement compositions compared to the more mafic southern Puna basement. This generally agrees with the trend of similar peraluminosity values in the Los Frailes Complex and northern APVC centers (see Figure 3.1b). While the Kari Kari samples plot with the northern Puna centers in the northern Puna Ordovician field in $^{206}\text{Pb}/^{204}\text{Pb}$ versus $^{207}\text{Pb}/^{204}\text{Pb}$ space, they have higher $^{208}\text{Pb}/^{204}\text{Pb}$ ratios than the northern Puna centers which places them on the border with the Bolivian Eastern Cordillera field. This indicates that although the Los Frailes Complex basement is similar to that found in the northern Puna, it has differences which are expressed in the higher $^{208}\text{Pb}/^{204}\text{Pb}$ ratios.

Figure 4.2

(a) Plot of $^{207}\text{Pb}/^{204}\text{Pb}$ versus $^{206}\text{Pb}/^{204}\text{Pb}$ ratios. (b) Plot of $^{208}\text{Pb}/^{204}\text{Pb}$ versus $^{206}\text{Pb}/^{204}\text{Pb}$ ratios. These depict the Los Frailes Complex basement similarities to the northern Puna centers (light blue) as compared with the southern Puna centers (light red). The Cerro Galán (dark red) and Panizos (dark blue) ignimbrite fields are also included for reference. The fields for the northern Chile Puna basement, northern Puna Ordovician rocks, Bolivian Eastern Cordillera and southern Puna basement are based on Lucassen et al. (2001, 2002) and outlined in heavy solid blue and dashed blue lines with boxed labels.

Symbols: Los Frailes Complex: triangles – Schneider (1985); Northern Puna centers, southern Puna centers, Galán and Panizos fields as compiled in Kay et al. (2010, 2011) and Ort et al. (1996).



Mineralogy

Plagioclase is the most abundant mineral phase in all Los Frailes Complex ignimbrites accounting for 40-60% of the volume of the phenocryst population. However, the observed ignimbrite Eu/Eu* ratios seem higher than would be expected for rampant plagioclase fractionation. This situation is not unique and is also seen in the APVC (Kay et al., 2010) as discussed above (Figure 3.11b). At Panizos, in the APVC, high Eu/Eu* ratios and unzoned plagioclase are attributed by Ort et al. (1996) to high crystal content and incomplete mixing prior to magma reaching pre-eruptive crustal levels. While limited plagioclase zoning is seen in Los Frailes Complex samples examined in this study, only 5-10% of plagioclase phenocrysts display optical indications of zoning.

Like the Morococala cordierite–biotite bearing rhyolite tuffs unit, ilmenite is the only oxide phase found in the examined Los Frailes Complex samples. Morgan et al. (1998) attributes this lack of magnetite in the rhyolite tuffs unit and ilmenite presence in all three Morococala units to reducing conditions imposed by a graphite-bearing sedimentary source. Compositional changes in ilmenite and magnetite (when present) in the quartz-latitude tuff unit indicate progressive increases in its pre-eruptive fO_2 conditions (Morgan et al., 1998). These findings at Morococala generally parallel those proposed here for reducing conditions in the Los Frailes Complex crust.

Geochronology

As has been noted by several researchers (Charlier et al., 2007; Hora et al., 2010) using $^{40}\text{Ar}/^{39}\text{Ar}$ sanidine and $^{40}\text{Ar}/^{39}\text{Ar}$ biotite ages, biotite consistently shows 0.2-0.6 older ages than sanidine from the same unit. Kay et al. (2011) specifically investigated the variation in ages at Cerro Galán in the southern Puna and found biotite ages that were 0.4-0.56 Ma older than paired sanidine ages. As biotite is thought to preserve inherited argon in structural traps (Hora et al., 2010) and has a

complex behavior in silicic melts, its precise behavior during crystallization is hard to predict. Thus, with sanidine crystallization occurring after biotite near the end of the magma cooling history, the $^{40}\text{Ar}/^{39}\text{Ar}$ sanidine ages are considered a more accurate eruption dating tool.

Table 4.3

25 Samples collected on 2009 and 2010 reconnaissance trips and assigned ages

Sample	Unit	Type	Age (Ma)	Latitude	Longitude	Elevation
PT-1	Porco	Ashflow Tuff	12-14 ^d	S 19.71020	W 65.87138	3916 m
PT-2	Porco	Ashflow Tuff	12-14 ^d	S 19.71020	W 65.87138	3916 m
PT-3	Porco	Inter-Caldera Tuff	12-14 ^d	S 19.80210	W 65.97706	4080 m
PT-4	Kumurana	Intrusive	~25 ^d	S 19.77537	W 65.67075	4586 m
PT-5	Kari Kari	Ashflow Tuff	20-22 ^d	S 19.36375	W 65.70851	4361 m
PT-6	Condor Nasa	Ashflow Tuff	7-8 ^e	S 19.36858	W 66.00847	4042 m
PT-7	Condor Nasa	Ashflow Tuff	7-8 ^e	S 19.35165	W 66.04090	3890 m
PT-8	Los Frailes	Ashflow Tuff	1.52 ±0.01 ^a	S 19.44460	W 66.11150	3943 m
PT-9	Los Frailes	Ashflow Tuff	~1.5 ^a	S 19.38651	W 66.07663	3889 m
PT-9p	Los Frailes	Pumice	~1.5 ^a	S 19.38651	W 66.07663	3889 m
PT-10	Los Frailes	Pumice	~1.5 ^a	S 19.38712	W 66.07063	3824 m
PT-11	Los Frailes	Ashflow Tuff	1.52 ±0.02 ^a	S 19.38523	W 66.06510	3720 m
PT-11p	Los Frailes	Pumice	1.52 ±0.02 ^a	S 19.38523	W 66.06510	3720 m
PT-12	Condor Nasa	Ashflow Tuff	7-8 ^e	S 19.35593	W 66.04590	3762 m
PT-13	Livicucho	Ashflow Tuff	7-8 ^f	S 19.02840	W 66.16620	4077 m
PT-14	Livicucho	Ashflow Tuff	7-8 ^f	S 19.13400	W 66.37816	4107 m
PT-15	Condor Nasa	Ashflow Tuff	~7 ^b	S 19.34906	W 65.91299	3757 m
PT-16	Los Frailes	Ashflow Tuff	1.5 ^a	S 19.60108	W 65.89838	3589 m
PT-16p	Los Frailes	Silicic Lava	1.5 ^a	S 19.60108	W 65.89838	3589 m
PO-1	Condor Nasa	Ashflow Tuff	7-8 ^e	S 19.3637	W 65.9355	3600 m
PO-2	Condor Nasa	Ashflow Tuff	7-8 ^e	S 19.3637	W 65.9355	3600 m
PO-3	Condor Nasa	Ashflow Tuff	7-8 ^e	S 19.3687	W 65.9637	3819 m
PO-4	Condor Nasa	Ashflow Tuff	7-8 ^e	S 19.3687	W 65.9637	3819 m
PO-5	Sevaruyo	Ashflow Tuff	9-10 ^c	S 19.1733	W 66.7811	3721 m
PO-6	Sevaruyo*	Ashflow Tuff	9-10 ^c	S 19.1733	W 66.7811	3721 m

Sample locations and type as reported in Keller (2010).

^a Based on new $^{40}\text{Ar}/^{39}\text{Ar}$ sanidine ages reported in this study.

^b Based on new zircon ages reported in this study.

^c Based on $^{40}\text{Ar}/^{39}\text{Ar}$ biotite ages from Barke et al. (2007).

^d Based on $^{40}\text{K}/^{40}\text{Ar}$ biotite ages from Schneider (1985).

^e Based on $^{40}\text{K}/^{40}\text{Ar}$ biotite ages from Kennan et al. (1995).

^f Based on $^{40}\text{K}/^{40}\text{Ar}$ biotite ages from Jiménez et al. (1997).

* Sample may be from Los Frailes ignimbrite (see discussion at beginning of Chapter 3).

Table 4.3 lists the age assignments for the 25 samples from this study. Los Frailes pumice sample PT-11p is assigned the 1.522±0.021 Ma age based on its collection from the same location and unit as the $^{40}\text{Ar}/^{39}\text{Ar}$ sanidine dated PT-11 sample. Similarly, PT-9, PT-9p and PT-10 were collected from the main Los Frailes

unit close to PT-11 and PT-11p and are nearly chemically identical including $^{87}\text{Sr}/^{86}\text{Sr}$ ratios of ~ 0.7114 from PT-10 and PT-11p. PT-16 and PT-16p are also chemically matched to the other Los Frailes ignimbrite samples with PT-16 sharing an $^{87}\text{Sr}/^{86}\text{Sr}$ value of ~ 0.7115 with PT-9 and assigned an age of 1.5 Ma. These are younger ages than the previously used 2.24 ± 0.09 based on the Barke et al. (2007) reported $^{40}\text{Ar}/^{39}\text{Ar}$ biotite age of sample G1 (19.377°S 66.056°W) as well as the associated sample PM15 (19.578°S 65.942°W) from the same study. Due to the discussed difference in sanidine versus biotite ages, the lower $^{40}\text{Ar}/^{39}\text{Ar}$ sanidine ages are not unexpected, but the ~ 0.75 My difference is probably too large to attribute purely to the dating techniques.

The zircon eruption dates for Los Frailes sample PT-10 of ≤ 1.9 Ma and for Condor Nasa sample PT-15 of ≤ 7.2 Ma are both in line with expectations. These dates support the 1.5 Ma age assigned to PT-10 and restricts the PT-15 age to ~ 7 Ma instead of the more general 7-8 Ma used for Condor Nasa samples based on $^{40}\text{K}/^{40}\text{Ar}$ biotite ages reported by Kennan et al. (1995). The remaining 15 samples from this study have been assigned ages based on their chemical signatures and physical proximities to the reported dated samples of studies listed in Table 4.3.

The two new $^{40}\text{Ar}/^{39}\text{Ar}$ sanidine dates obtained from Los Frailes ignimbrite samples PT-8 and PT-11 support the Barke et al. (2007) assertion that the main Los Frailes ignimbrite has a lower end age of ~ 1.5 Ma. The previous age of the northeastern portion of the main Los Frailes ignimbrite was placed at 2.24 ± 0.09 Ma based on sample G1 of Barke et al. (2007) as described above. The ~ 1.5 Ma ages of this study are now the youngest obtained on the main Los Frailes ignimbrite and exceed the previous lower end limit of 1.86 ± 0.09 Ma which was based on the $^{40}\text{Ar}/^{39}\text{Ar}$ biotite age of Los Frailes ignimbrite sample YURb ($S19.741$ $W66.381$) (Barke et al., 2007). The chemical similarities between the 8 Los Frailes ignimbrite

samples of this study collected on the northeast side of the meseta and the 20 reported by Luedke et al. (1997) collected about 50 km away on the southern side are interpreted to indicate it is a single unit. This places the age of the central and eastern portion of the main Los Frailes meseta at 1.5-3.5 Ma. The 3.5 Ma upper limit is set by the Schneider (1985) sample Fr-5 from an exposed dome, partially covered by the main Los Frailes ignimbrite, which has a $^{40}\text{K}/^{39}\text{Ar}$ biotite age of 3.86 ± 0.38 Ma and adjusted to 3.5 Ma accounting for the biotite versus sanidine age discussion above. This moves the main eruptive volume of the Los Frailes Complex firmly into the Pliocene-Pleistocene from its previous Miocene assignment. As no new data are available in the western and northwestern portions of the main Los Frailes meseta, they are assessed to be 9-16 Ma and 5-9 Ma respectively; in agreement with the ages proposed by Barke et al. (2007).

Geothermometry and Geobarometry

The 110°-135°C higher zircon temperatures as compared to two-feldspar temperatures are consistent with zircon crystallization prior to plagioclase. This is supported by observed zircon inclusions in all silica minerals including plagioclase cores. This same arrangement is seen in the PO series of samples as described by Keller (2010). These temperature ranges are proposed to have existed in pre-eruption magma chambers in the middle or upper crust. The high crystal percentage and large phenocryst size indicate that slow cooling occurred in the magma storage chambers prior to eruption.

Although no cordierite is observed in this study, it is reported in the older and lower SiO₂ Condor Nasa sample PO-2 by Keller (2010). Luedke et al. (1997) also reported wide-spread but scarce cordierite in southern Los Frailes Meseta samples and Morgan et al. (1998) reported it to be common at Morococala to the north. While cordierite is expected in highly peraluminous rocks, it has not been definitively

established if the crystals found are magmatic or inherited xenoliths from a meta-sedimentary basement (Luedke et al., 1997). If the cordierite is magmatic, as is consistent with the pseudosection for PO-2 (Keller, 2010), it would indicate equilibrium at low pressures of <450 MPa which corresponds to very shallow upper crustal depths of <14 km given the equilibrium assemblages reported. These pressures and depths generally agree with the geophysical evidence of a 14-20 km deep partial melt zone beneath the Los Frailes Complex detected by the receiver function study of Beck and Zandt (2002) discussed in Chapter 1 and depicted in Figure 1.6.

CHAPTER 5

MODELING

AFC Models

The creation of erupted silicic magmas on the Altiplano-Puna involves contributions from both a mantle-derived mafic source and a crustal-derived felsic source. Opinions have differed on the ratio of the contributing sources with arguments made for crustal proportions ranging from 0 to 100%. One line of thought uses a mafic end-member as a means to move mantle heat into contact with the crust which drives melting and delivery of a pure crustal magma to the surface. The other view holds that mafic magmas undergo fractional crystallization in the crust which transforms them into silicic magmas which continue their upward movement to the surface. Intermediary models have large volumes of mafic mantle material entering the crust where it heats, melts, and assimilates silicic rocks while simultaneously undergoing fractional crystallization before transport to the surface. While each of these models works to the first order, geochemical evidence in the form of $\delta^{18}\text{O}_{\text{Quartz}}$ paired with Sr isotopic and concentration data can be used to point to a mixture of mantle and crustal sources contributing to the resulting hybrid chemical and isotopic values seen in Altiplano-Puna ignimbrites. Nd isotopic and concentration data are also used as an additional constraint on possible models, but do not help appreciably in the initial identification of end-member magma sources.

Dacitic Altiplano ignimbrites have consistently high values of $\delta^{18}\text{O}_{\text{Quartz}}$ of +9.7‰ to +11.1‰ (see Table 4.2) which indicate a large (40-60%) crustal component in their genesis when considering a mantle value of +5.8‰ (following Kay et al., 1999, 2010, 2011; Kay, 2006; Bindeman, 2008). However, the uppermost crust is too radiogenic and highly concentrated in Sr (Lucassen et al., 2001) to reconcile with the

associated low $^{87}\text{Sr}/^{86}\text{Sr}$ ratio values measured in the Los Frailes Complex ignimbrites when given the 40-60% crustal component required by the $\delta^{18}\text{O}$ data. Therefore, the crustal assimilates must be from the middle or lower crust with either less radiogenic $^{87}\text{Sr}/^{86}\text{Sr}$ ratios, lower Sr concentrations or a composite thereof. Similar combinations of $\delta^{18}\text{O}$, $^{87}\text{Sr}/^{86}\text{Sr}$ ratio values and elemental concentrations are seen to the south in studies on APVC and Puna ignimbrites (e.g., Francis et al., 1989; Caffè et al., 2002, Kay et al. 2010, 2011) which have concluded similarly that the crustal end-member is located in the lower crust. As $^{143}\text{Nd}/^{144}\text{Nd}$ (ϵNd) ratio zoning within the crust is expected to be much smaller than $^{87}\text{Sr}/^{86}\text{Sr}$ ratios, $^{143}\text{Nd}/^{144}\text{Nd}$ (ϵNd) ratio values are not considered a limiting factor when selecting the depth for the crustal end-member (Davidson and de Silva, 1995).

The primary problem with determining the crust-to-mantle ratio of the resulting dacitic ignimbrites is the lack of direct samples from either the lower crust or the underlying mantle. This lack of knowledge of end-member chemistry is partially alleviated by the existence of low volume Miocene mafic flows along the western and central Altiplano. These near primitive lavas can be used to predict the character of the mantle-derived mafic partial melts and serve as a mafic end-member proxy for AFC models. The most isotopically primitive samples reported by Davidson and de Silva (1995) and Hoke and Lamb (2007) were used to represent the mafic end-member in this study. In addition to their $^{87}\text{Sr}/^{86}\text{Sr}$ and $^{143}\text{Nd}/^{144}\text{Nd}$ (ϵNd) ratios, their wt. % SiO_2 and wt. % MgO as well as Cr and Ni concentrations are considered when determining an appropriate mafic end-member to represent mantle-derived mafic end-member melts.

As the Los Frailes ignimbrites show an isotopic shift in $^{87}\text{Sr}/^{86}\text{Sr}$ and $^{143}\text{Nd}/^{144}\text{Nd}$ (ϵNd) ratios between pre- and post-12 Ma samples, two sets of AFC models were considered. The pre-12 Ma values represent the Kari Kari ignimbrite

while the post-12 Ma represents the more voluminous main Los Frailes ignimbrite. With ~20 My separating the two eruptions, during which the subducting Nazca Plate steepened and subduction-related contamination of the underlying asthenospheric wedge may have occurred, each model is assigned separate mafic end-member values. These values are determined by examination of available mafic lava samples of corresponding ages. The pre-12 Ma mafic end-member is assigned values of $\delta^{18}\text{O} = +5.8\text{‰}$, $^{87}\text{Sr}/^{86}\text{Sr} = 0.7040$, 500-900 ppm Sr, $^{143}\text{Nd}/^{144}\text{Nd} = 0.51280$ ($\epsilon_{\text{Nd}} = +3.16$) and 30 ppm Nd which is based on samples Gu-3, Luk-1 (Hoke and Lamb, 2007) and BC9016a (Davidson and de Silva, 1995) (see Table 5.1). Luk-1 and BC9016a are from the primitive alkali basalt Chiar Kkollu sill located to the west of the Los Frailes Complex (see Figure 1.2) which is dated at 22-26 Ma, near the time of the 20-22 Ma Kari Kari emplacement. It is the most Neogene mafic volcanic flow ($\text{SiO}_2 = 44\text{-}45$ wt. %, $\text{MgO} = 9.26\text{-}14.87\%$, 387-825 ppm Cr) collected on the Altiplano-Puna. The Chiar Kkollu sample is free from petrographic evidence of contamination and is taken to represent an unmodified basaltic mantle melt composition prior to Miocene crustal shortening (Davidson and de Silva, 1992, 1995). The Sr concentration of the mafic end-member was lowered from the Chiar Kkollu values as Sr is an incompatible element and expected to concentrate in small percentage melts such as the small volume Chiar Kkollu sill. In higher percentage melts, such as those expected in large volume events like the Kari Kari and Los Frailes ignimbrite eruptions, the Sr concentration would be diluted as additional depleted rock is melted and incorporated. The $\delta^{18}\text{O}$ value of the mafic end-member was set at +5.8‰ following Bindeman (2008) and Kay et al. (2010). The $^{143}\text{Nd}/^{144}\text{Nd}$ ratio value is set to 0.51280 ($\epsilon_{\text{Nd}} = +3.16$) which is that of sample BC9016. The Nd concentration is set at 30 ppm Nd, which is slightly below that in the basalt samples (40-46 ppm Nd). The reduction in

concentration is again due to REEs being fairly incompatible elements which, like Sr, are enriched in small percentage melts.

Post-12 Ma mafic end-member values used are based on samples CCO-1, 7/91-19 and Maar-1 (Hoke and Lamb, 2007) which are placed at 5.0-7.0 Ma as well as sample BC9012 (Davidson and de Silva, 1995). These samples are taken as representing the state of the mantle during the 1.5-3.5 Ma Los Frailes ignimbrite emplacement (see Table 5.1). Unlike the Chiar Kkollu values used for the pre-12 Ma mafic end-member, no uncontaminated lavas have been reported in the post-12 Ma mafic record as is evidenced by the more evolved character of the samples used ($\text{SiO}_2 = 51\text{-}54$ wt. %, $\text{MgO} = 5.69\text{-}9.06\%$, $175\text{-}727$ ppm Cr). With more uncertainty and fewer constraints, the post-12 Ma mafic end-member is assigned values of $\delta^{18}\text{O} = +5.8\text{‰}$, $^{87}\text{Sr}/^{86}\text{Sr} = 0.7055$, $500\text{-}950$ ppm Sr, $^{143}\text{Nd}/^{144}\text{Nd} = 0.51260$ ($\epsilon_{\text{Nd}} = -0.74$) and $25\text{-}30$ ppm Nd considering the samples listed above. Sr concentration was not reduced as in the pre-12 Ma values as it was judged that the more evolved nature of the mafic samples on which the mafic end-member is based incurred some Sr removal during plagioclase fractionation. That Sr loss could approximately cancel the concentrating effects of small percentage melts and makes a major mafic end-member Sr concentration correction unnecessary. The $^{143}\text{Nd}/^{144}\text{Nd} = 0.51260$ ($\epsilon_{\text{Nd}} = -0.74$) value is set based on sample BC9012 ($^{143}\text{Nd}/^{144}\text{Nd} = 0.512405$, $\epsilon_{\text{Nd}} = -4.55$) taking into account noted crustal contamination. A Nd concentration of $25\text{-}30$ ppm is based on the range seen in basaltic samples ($24\text{-}42$ ppm Nd), and is set near the lower end of the range owing to the effects of incompatible elemental enrichment.

Table 5.1**Selected Altiplano volcanic samples for mafic end-members**

Center	Chiar Kkollu	Chiar Kkollu	Guallatire	Ollague Region	Salar de Empexa	Chullunquiani Nekhe Kkata
Sample	Luk-1 ^a	BC9016 ^b	Gu-3 ^a	BC9012 ^b	7/91-19 ^a	Maar-1 ^a
Age (Ma)	25.2 ± 0.9	22.51 ± 0.45	25.9 ± 0.8	<7	3.31 ± 0.25	<0.128
SiO ₂	44.66	44.85	44.36	53.59	53.68	52.85
TiO ₂	2.38	2.26	0.92	0.96	1.69	1.44
Al ₂ O ₃	13.72	14.09	11.52	15.58	16.49	15.88
Fe ₂ O ₃	3.76	11.38	9.76	9.29	3.06	8.60
FeO	6.99	-	-	-	4.89	-
MnO	0.18	0.18	0.18	0.16	0.11	0.15
MgO	9.39	9.26	14.87	8.37	5.69	7.02
CaO	12.16	12.17	10.13	6.86	7.45	8.23
Na ₂ O	3.06	3.05	4.53	3.10	4.15	3.54
K ₂ O	1.32	1.31	1.78	1.79	1.95	2.32
P ₂ O ₅	0.73	0.77	0.58	0.27	0.56	0.42
LOI	1.85	0.70	1.70	0.03	0.61	0.07
Total	100.20	100.02	100.33	100.00	100.33	100.52
La	49.70	47.50	47.50	22.9	37.10	34.30
Ce	96.00	91.2	99.00	48.5	81.00	70.00
Pr	11.50	-	12.20	-	10.10	8.40
Nd	46.40	40.1	46.40	23.9	42.20	32.90
Sm	8.76	8.5	7.91	5.25	8.38	6.13
Eu	2.87	2.72	2.02	1.38	2.33	96.00
Gd	8.37	6.24	6.24	-	6.47	5.99
Tb	1.03	1.01	0.76	0.83	0.78	0.87
Dy	5.72	-	4.19	-	4.02	4.63
Ho	0.98	-	0.74	-	0.63	0.87
Er	2.32	-	1.95	-	1.48	2.16
Tm	0.31	-	0.27	-	0.24	0.29
Yb	2.06	2	1.81	2.67	1.29	2.06
Lu	0.27	0.28	0.27	0.39	0.18	0.27
Y	25	28	19	18	-	23
Rb	20	23	46	49	-	55
Sr	876	936	1516	716	977	776
Ba	624	226	835	343	907	887
Cs	-	-	-	-	-	-
Pb	-	9	7	8	-	9
U	1.65	1.3	0.78	1.9	0.67	1.71
Th	5.77	4.8	3.82	4	3.18	7.60
Nb	60	55	15	139	24	32
Ta	3.47	2.97	1.16	0.55	1.28	3.05
Zr	186	202	163	139	-	206
Hf	5.49	4.7	3.92	0.55	-	6.19
Sc	-	29.9	26.0	28	-	22.00
Cr	387	433	825	354	175	257
Ni	119	129	423	82	69	92
⁸⁷ Sr/ ⁸⁶ Sr	0.703960	0.704052	-	0.705781	0.705550	0.705961
¹⁴³ Nd/ ¹⁴⁴ Nd	-	0.512801	-	0.512405	-	-
ε _{Nd}	-	+3.18	-	-4.55	-	-
²⁰⁶ Pb/ ²⁰⁴ Pb	-	18.52	-	-	-	-
²⁰⁷ Pb/ ²⁰⁴ Pb	-	15.63	-	-	-	-
²⁰⁸ Pb/ ²⁰⁴ Pb	-	38.67	-	-	-	-

^a Data from Hoke and Lamb (2007).^b Data from Davidson and de Silva (1995).

Based on the $\delta^{18}\text{O}$ values discussed above, the crust-to-mantle magma mixing ratio of the Los Frailes Complex ignimbrites is constrained to 40-50% crustal input. (see Table 3.4). With near equal inputs from crustal and mafic end-member sources, the combination of ignimbrite $^{87}\text{Sr}/^{86}\text{Sr}$ ratio values, peraluminous composition and interpreted silicic nature of the southern Altiplano lower crust as determined geophysically (Beck et al., 1996; Myers et al., 1998; Swenson et al., 2000; Beck and Zandt, 2002; Yuan et al., 2002; McGlashan et al., 2008), an appropriate crustal end-member source is Paleozoic metapelites. At the base of the modern southern Altiplano crust, at depth of near 65 km, a pressure of ~20 kbar (2.0 GPa) is expected. Under these conditions, pelitic sedimentary rocks would experience some H_2O loss during high pressure and temperature metamorphism resulting in metapelitic basement rocks in the eclogite facies.

Using P-T pseudosections, constructed using THERMOCALC 3.26 (Powell and Holland, 1988), by Indares et al. (2008) for aluminous bulk compositions similar to possible Altiplano metapelitic lower crust (H_2O : 2.15-2.20, SiO_2 : 64.59-67.24, Al_2O_3 : 10.78-13.31, CaO : 1.19-1.87, MgO : 4.69-5.58, FeO 7.58-8.36, K_2O : 2.52-2.77, Na_2O : 1.79-1.83, TiO_2 : 0.69-0.71, O : 0.01, X_{Fe} : 0.58-0.64 in mol. %), a mineral assemblage can be calculated. At P-T parameters near ~20 kbar (2.0 GPa) and ~940°C (maximums for the pseudosections), the resulting Na_2O , CaO , K_2O , FeO , MgO , Al_2O_3 , SiO_2 , H_2O , TiO_2 and O (NCKFMASHTO) system assemblage consists primarily of garnet + quartz + K-feldspar + melt with minor amounts of kyanite + rutile (Indares et al., 2008). At lower pressures near 16-17 kbar (1.6-1.7 GPa), plagioclase becomes stable whereas lower temperatures of ~850°-880°C allow plagioclase, biotite and ilmenite to be added to the assemblage. At ~20 kbar (2.0 GPa) and ~940°C, the melt accounts for 8-10 mol. % of the assemblage. This melt is produced mostly through the loss of muscovite and biotite (Indares et al., 2008) and

represents the crustal end-member melt in the AFC models below. In equilibrium with the melt, the remaining Fe and Mg is incorporated in an almandine-rich garnet phase, which makes up ~35 mol. % of the assemblage. A grossular content of ~6-10% of the garnet incorporates the remaining Ca while the spessartine content of the observed rocks is <3% of the garnet and so the pseudosection assemblage is assumed to be Mn-free (Indares et al., 2008). The K-feldspar phase houses the remaining K and Na and, together with quartz, accounts for ~55 mol. % of the assemblage. Kyanite and rutile are minor mol. % phases in the assemblage with rutile incorporating Ti.

Pelites, such as shales or argillites, have a distinct composition which is established through the process of chemical weathering during deposition. Ca and particularly Na are removed, whereas Al is slightly enriched in the near-surface environment resulting in a strongly peraluminous composition with ≤ 3 wt. % CaO and ≤ 2 wt. % Na₂O (e.g., Miller 1985). In a similar process, the concentration of highly soluble Sr drops to the range of 50-300 ppm which is greatly dependent on the incorporation of associated carbonates. While Sr is removed, the Rb is retained by the sheet silicates and remains high; about 100-200 ppm (Miller 1985). This results in high Rb/Sr ratios, usually ≥ 0.5 , which are much higher than in average crust. Nd evolution in the crust will have a continental signature, but no specific pelitic signature (Miller 1985), and is given a ¹⁴³Nd/¹⁴⁴Nd ratio value of 0.51190 to 0.5121 ($\epsilon_{\text{Nd}} = -10.49$ to -14.40) (Caffe et al., 2002; Lucassen et al., 2007). REEs, including Nd, show little change in their abundance even during fine grained weathering of crystalline rock and should have concentrations near that of the constituent sediments. Crustal end-member Nd concentrations are assigned a range of 20-40 ppm Nd for models in this study given average continental concentrations of 10-25 ppm Nd (Rudnick and Gao, 2004), Archean crust concentrations of 15-20 ppm Nd (Rudnick and Fountain, 1995; Taylor and McLennan, 1995, 2009) and Proterozoic-Phanerozoic shale

concentrations as high as 40 ppm Nd (Condie, 1993). Due to the low temperature formation of clay minerals in equilibrium with meteoric water, pelitic rocks have high $\delta^{18}\text{O}$ values of +14 to +20‰ (Miller, 1985). See Table 5.3 for a full description of the crustal end-member parameters used. Using a metapelitic rock as a crustal end-member is a similar conclusion to that reached by Kay et al. (2010) for the Panizos and Vilama centers in the APVC, which are also peraluminous and have similar $\delta^{18}\text{O}$ with slightly higher $^{87}\text{Sr}/^{86}\text{Sr}$ ratios compared to the Los Frailes Complex (see Table 1.2). The basement of the northern Puna, which is described in equivalent terms and with comparable Sr and Nd isotopic and concentration values by Caffè et al. (2002), is considered to be comparable to that in the southern and central Altiplano. While $\delta^{18}\text{O}$ and $^{87}\text{Sr}/^{86}\text{Sr}$ ratio values in the Los Frailes Complex are similar to the APVC, the 450-550 ppm Sr is much higher in Los Frailes ignimbrites compared to 200-350 ppm Sr in the APVC and 260-350 ppm Sr at Cerro Galán. This Sr concentration difference may be caused by fractionating plagioclase playing a smaller role in the middle crust below the Los Frailes Complex or a higher initial mafic end-member Sr concentration which results in AFC models distinct from those of the APVC and Puna (Ort et al., 1996; Caffè et al., 2002; Kay et al., 2010).

The AFC calculations used in this study are described in Aitchison and Forrest (1994) and are derived from the differential equations of DePaolo (1981). See Table 5.2 for equations and definitions of variables. The three equations (5, 6 and 7) describe simultaneous assimilation of country rock and removal of mass through fractional crystallization of an evolving magma with complete mixing as it undergoes transport in the crust. This model was chosen based on the uncertainty of the end-member compositions and the need to constrain those values. As discussed in Kay et al. (2010) regarding APVC calculations, the mass balance AFC model of Aitchison and Forrest (1994) with a constant value of r is also preferred in the case of the Los

Frailas Complex over the Energy Constrained (EC)-AFC model of Spera and Bohrsen (2001).

Table 5.2

Aitchison and Forrest (1994) AFC equations derived from DePaolo (1981) equations

ρ in terms excluding C_m and F :

$$\rho = \frac{r}{r-1} \left\{ \left[1 + \frac{\lambda(r+D-1)}{r\gamma} \right]^{(r-1)/(r+D-1)} - 1 \right\} \quad \text{for } r+D \neq 1, \quad r \neq 1 \quad (5)$$

ρ in terms of element concentrations only:

$$\rho = \left(\frac{r}{r-1} \right) \left\{ \left[\frac{C_m^o(r+D-1) - rC_a}{C_m(r+D-1) - rC_a} \right]^{(r-1)/(r+D-1)} - 1 \right\} \quad (6)$$

ρ in terms excluding C_a :

$$\rho = \left(\frac{r}{r-1} \right) \left\{ \left[\frac{C_m^o (\epsilon_a - \epsilon_m^o)}{C_m (\epsilon_a - \epsilon_m)} \right]^{(r-1)/(r+D-1)} - 1 \right\} \quad (7)$$

$\rho = M_a/M_m^o$	Crust/magma ratio in non-recharge situations
M_m	Mass of magma remaining (including neutrally buoyant crystals)
M_m^o	Mass of original magma
M_a	Mass of crust assimilated
$F = M_m/M_m^o$	Fraction of magma remaining in non-recharge situations
r	(rate of assimilation of crust) / (rate of fractional crystallization)
D (Kd _{xx})	Bulk distribution coefficient of the element
C_m	Element concentration in the contaminated magma
ϵ_m	Isotopic ratio in the contaminated magma
C_a	Element concentration in wall-rock melt
ϵ_a	Isotopic ratio in the wall-rock melt
C_m^o	Element concentration in the original magma
ϵ_m^o	Isotopic ratio in the original magma
$\lambda = (\epsilon_m^o - \epsilon_m) / (\epsilon_m - \epsilon_a)$	
$\gamma = C_a / C_m^o$	

An AFC without magma recharge model is used to solve for the crust/magma ratio (ρ), which is the mass of the crustal end-member over the mass of the mafic end-member. This can be expressed in terms of the fraction of magma remaining (F), and the rate of assimilation of the crust over the rate of fractional crystallization (r) (see Table 5.2). The resulting three equations (5, 6 and 7) by Aitchison and Forrest (1994) are used to evaluate the two end-member compositions, crust-to-mantle mixing ratio, and percent fractionation for both pre- and post-12 Ma Los Frailes ignimbrite compositions (see Table 5.3). The equations are calculated in parallel for both the Sr and Nd isotopic systems while holding ρ and r equal in both sets of equations and F within a range of 0.2-0.6. This method produces only models which are valid for both element systems. $\delta^{18}\text{O}$ values are used to constrain the value of ρ which is held near 0.5 (50:50 crust to mafic inputs) in keeping with the end-member controls discussed above. As plagioclase incorporates Sr^{2+} , its presence or absence is the largest control on bulk Kd_{Sr} values, which are set using the anticipated stability of plagioclase at varying depths. Kd_{Nd} values are harder to constrain as in addition to the relatively predictable pyroxene and amphibole phases, Nd^{3+} can be preferentially incorporated into several accessory minerals with extreme Kd_{Nd} values and variable stability such as apatite, zircon, rutile and titanite (sphene) (Luhr and Carmichael, 1980; Fujimaki, 1986).

In the method of Kay et al. (2010), the procedure used to solve the equations is to first use equation 5 to calculate a minimum value for r without a constraint on F , which along with the contaminated magma concentration (C_m) is not used in the equation. Based on the extremely steep REE patterns and very high Sr content of the Los Frailes Complex, a Kd_{Sr} near 0.10 and Kd_{Nd} near 0.25 are used to represent conditions in the lower crust, where garnet is stable but plagioclase is not and where most melting and assimilation of crust occurs (e.g., Bea et al., 1994; Dunn and Sen,

1994; Hauri et al., 1994; Ort et al., 1996). As the Sr and Nd isotopically evolved signature is attributed to crustal end-member contamination of a depleted mafic end-member from the mantle, the enrichment must take place prior to or during the differentiation, which elevates Sr and Nd concentrations. The elevation of Sr concentration is doubtful at shallower crustal levels where Sr incorporating plagioclase is a fractionating phase and so the majority of crustal assimilation and the resulting isotopic enrichment of the mixture is limited to the lower crust (Aitchison and Forrest, 1994). Crustal assimilation prior to the onset of plagioclase fractionation is supported by flat $^{87}\text{Sr}/^{86}\text{Sr}$ ratios versus SiO_2 and Sr ppm trends (Figures 3.22a and 3.22b), as they show that $^{87}\text{Sr}/^{86}\text{Sr}$ ratios are not altered during plagioclase driven fractionation. This type of pattern is also seen and interpreted similarly in the APVC (e.g., Kay et al., 2010) and elsewhere (e.g., Aitchison and Forest, 1994). However, it should be noted that the higher Sr concentrations in the Los Frailes ignimbrites would make the effects of continued crustal assimilation on the $^{87}\text{Sr}/^{86}\text{Sr}$ ratio values harder to detect.

Using the r value (0.50-0.63) determined by equation 5, equation 6 is then used to find the value of F . The values of K_{dSr} and K_{dNd} are adjusted, and the equation now includes elemental concentration in the contaminated magma (C_m) and is dominated by the elemental concentration values and excludes the isotopic ratios (ϵ_a , ϵ_m and ϵ_m°). Here, $K_{\text{dSr}} = 0.50-0.70$ and $K_{\text{dNd}} = 0.70-0.80$ are used to represent conditions in the middle crust where plagioclase is stable and fractionation is occurring (Dunn and Sen, 1994; Hauri et al. 1994; Shimizu, 1980). This is appropriate considering the moderately negative Eu anomalies ($\text{Eu}/\text{Eu}^* = 0.60-0.90$) in the Los Frailes ignimbrites. Here the benefit of having multiple isotopic systems to constrain the model becomes obvious. Using only one system, such as Sr in Kay et al. (2010), a wide range of F

values can be produced (0.20-0.80) by simply raising or lowering the $K_{d_{Sr}}$ value within a relatively narrow window of reasonable values (~0.5-1.0).

With the additional constraint of the Nd system to consider, the permissible range of F values that satisfy both systems is reduced, even with the less certain $K_{d_{Nd}}$ values. As equation 6 is largely controlled by the elemental concentration values (C_a , C_m , and C_m°), the high Sr concentrations in the Los Frailes Complex ignimbrites cause the $K_{d_{Sr}}$ in equation 6 and 7 to decrease and the F to increase relative to solutions found by Kay et al. (2010) using the same AFC equations for the APVC volcanoes which have slightly higher $^{87}\text{Sr}/^{86}\text{Sr}$ ratios (see Table 1.2). The reduced $K_{d_{Sr}}$ values represent a lower affinity of the fractionating phases for Sr, and therefore could signal a lesser role for plagioclase in the fractionating region as compared to the APVC and Puna systems. In addition, lower $K_{d_{Sr}}$ values in equation 6 are complemented by increased F values, which imply a smaller fraction of absolute mass removal from the magma at the middle crustal level. A reduction in plagioclase removal does not appear to be supported, however, by the Los Frailes Complex Eu/Eu* ratios compared to the peraluminous APVC centers (Figure 3.11).

An alternate explanation for the $K_{d_{Sr}}$ discrepancy is that the calculated $K_{d_{Sr}}$ values for equation 6 are too low due to the accompanying mafic end-member Sr concentration having been set too low. Solution 4 (see Table 5.3) for each system has higher Sr concentration for the mafic end-member, which raises the corresponding $K_{d_{Sr}}$ to 0.7. This $K_{d_{Sr}}$ value is commensurate with the APVC ignimbrite models, but requires an accompanying increase in crustal end-member Sr concentration or $^{87}\text{Sr}/^{86}\text{Sr}$ ratios to maintain the isotopic balance. Assuming metapelitic crustal assimilates, an increased crustal $^{87}\text{Sr}/^{86}\text{Sr}$ ratio is favored over an increased crustal Sr concentration if evidence for a mafic end-member enriched in Sr concentration becomes persuasive and balancing becomes necessary. Both of these modifications

Table 5.3

AFC models using $^{87}\text{Sr}/^{86}\text{Sr}$, Sr ppm, $^{143}\text{Nd}/^{144}\text{Nd}$, Nd ppm and $\delta^{18}\text{O}$									
Ignimbrite	Whole	Whole	Whole	Whole	Calculated Magma $\delta^{18}\text{O}\%$	Calculated values	Aitchison and Forrest (1994) equations		
	rock $^{87}\text{Sr}/$ ^{86}Sr	rock Sr ppm	rock $^{143}\text{Nd}/$ ^{144}Nd	rock Nd ppm			Eqn 5	Eqn 6	Eqn 7
Kari Kari	0.7105	450	0.51226	57	+10.4-10.7				
Mafic 1	0.7040	500	0.51280	30	+5.8				
Crust 1	0.7350	130	0.51190	35	+14.8-15.3	Sr bulk D	0.10	0.66	0.575
						Nd bulk D	0.25	0.75	0.56
						% crust =	47	47	47
						r =	0.5	0.5	0.5
						F =	-	0.36-0.41	0.30-0.39
Mafic 2	0.7040	550	0.51280	30	+5.8				
Crust 2	0.7400	100	0.51190	35	+14.5-15.0	Sr bulk D	0.10	0.60	0.54
						Nd bulk D	0.20	0.65	0.50
						% crust =	50	50	50
						r =	0.60	0.60	0.60
						F =	-	0.50-0.51	0.46-0.48
Mafic 3	0.7040	800	0.51280	30	+5.8				
Crust 3	0.7500	128	0.51190	40	+14.7-15.2	Sr bulk D	0.10	0.77	0.70
						Nd bulk D	0.20	0.69	0.52
						% crust =	48	48	48
						r =	0.60	0.60	0.60
						F =	-	0.54-0.57	0.50-0.57
Mafic 4	0.7040	900	0.51280	30	+5.8				
Crust 4	0.7400	160	0.51190	30	+14.5-15.0	Sr bulk D	0.10	0.70	0.59
						Nd bulk D	0.20	0.75	0.53
						% crust	50	50	50
						r =	0.50	0.50	0.50
						F =	-	0.32-0.37	0.23-0.33
Frailes	0.7115	550	0.512175	45	+9.4-10.2				
Mafic 1	0.7055	500	0.51260	25	+5.8				
Crust 1	0.7300	130	0.51190	25	+13.0-14.6	Sr bulk D	0.10	0.564	0.492
						Nd bulk D	0.23	0.59	0.46
						% crust	51	51	51
						r =	0.55	0.55	0.55
						F =	-	0.34-0.40	0.29-0.38
Mafic 2	0.7055	500	0.51260	25	+5.8				
Crust 2	0.7400	115	0.51190	35	+14.0-16.0	Sr bulk D	0.10	0.485	0.446
						Nd bulk D	0.29	0.53	0.445
						% crust	46	46	46
						r =	0.60	0.60	0.60
						F =	-	0.52-0.56	0.49-0.55
Mafic 3	0.7055	650	0.51260	25	+5.8				
Crust 3	0.7500	95	0.51190	30	+13.1-14.7	Sr bulk D	0.07	0.45	0.50
						Nd bulk D	0.24	0.49	0.41
						% crust	50	50	50
						r =	0.63	0.63	0.63
						F =	-	0.51-0.57	0.48-0.57
Mafic 4	0.7055	950	0.51260	30	+5.8				
Crust 4	0.7400	160	0.51190	32	+13.1-14.7	Sr bulk D	0.11	0.70	0.60
						Nd bulk D	0.22	0.74	0.53
						% crust	50	50	50
						r =	0.51	0.51	0.51
						F =	-	0.35-0.38	0.27-0.35

come with problematic ramifications for the Rb concentration and Sr/Rb ratio discussed below. As such, an explanation of a slightly lower K_{dSr} reflecting decreased plagioclase fractionation remains viable as well as preferable based on the AFC models. However, no clear cause for reduced plagioclase fractionation is known and Eu/Eu* inconsistencies may still be explained by differences in fO_2 and water pressure.

With the value of F now established (0.23-0.57) by equation 6 and using the r value set by equation 5, equation 7 is used to determine another set of K_{dSr} , K_{dNd} and F values. These K_{dSr} and K_{dNd} values are intermediate between those used in equations 5 and 6 and represent an average if assimilation and fractionation had occurred continuously throughout the crust rather than the more bimodal system of assimilation dominating in the lower crust followed by fractionation dominating in the mid-crust represented by equations 5 and 6. Based upon the flat $^{87}Sr/^{86}Sr$ ratios versus Sr ppm and $^{87}Sr/^{86}Sr$ ratios versus SiO_2 , continuous assimilation is not an appreciable factor in the character of the Los Frailes Complex ignimbrites, and therefore the solutions from equation 7 are not considered representative here.

Table 5.3 contains a selection of the best fitting AFC model results for both the Kari Kari and Los Frailes ignimbrites. These selections show non-unique solutions to equations 5, 6 and 7 for the given mafic and crustal end-members and list the values used for each variable. The Kari Kari and Los Frailes ignimbrite models show very similar crustal end-member results which indicate that melting and assimilation of the lower crust occurred in a region with parameters of $^{87}Sr/^{86}Sr = 0.7030-0.7500$, 95-160 ppm Sr, $^{143}Nd/^{144}Nd = 0.51190$ ($\epsilon_{Nd} = -14.40$), 25-40 ppm Nd and $\delta^{18}O = +13.0$ to $+16.0\%$. These values are consistent with the published metapelitic values stated above and can be produced through radiogenic isotope calculations. As the southern Altiplano plateau basement considered to have a thick Lower Paleozoic (Ordovician to

Devonian) sequence of Archean derived sediments deposited on the western margin of the Brazilian Shield (Schneider, 1985; Caffè et al., 2002; Lucassen et al., 2007), a 500 Ma age is used for the metapelite and 2700 Ma is used as the mean age for the Brazilian Shield cratonic crust from which it was likely derived (Cordani et al., 1988; Cordani and Sato, 1999; Sail et al., 1999). The Rb concentration at deposition is set at 50-100 ppm Rb given a bulk Archean crustal composition of 30-50 ppm Rb and 200-300 ppm Sr (Rudnick and Fountain 1995; Taylor and McLennan, 1995, 2009) and allowing for minor Rb concentration enrichment due to incorporation of non-Archean sediments during deposition with an expected pelitic Rb/Sr ratio of 0.5-1.0 (Miller, 1985). This range of Rb concentrations combined with a 100 ppm Sr, as calculated by the AFC models, produces a present day $^{87}\text{Sr}/^{86}\text{Sr}$ ratio of 0.7300 to 0.7400 which is consistent with the isotopic character of the AFC calculated crustal end-member using $^{87}\text{Rb} \rightarrow ^{87}\text{Sr}$ $\lambda = 1.396 \times 10^{-11} \text{y}^{-1}$ (Rotenberg et al., 2012) and bulk earth/solar system initial $^{87}\text{Sr}/^{86}\text{Sr}$ of 0.699 at 4.55 Ga (Papanastassiou et al., 1970). Allowing for a greater absolute Rb concentration of 100-200 ppm Rb as documented in pelites (Miller, 1985) and the North American Shale Composite (NASC) (Condie, 1993), which may occur during alteration, the Rb/Sr ratio can reach as high as 2.0 and produce $^{87}\text{Sr}/^{86}\text{Sr}$ ratio values in excess of 0.7650.

The AFC model values calculated for the Los Frailes Complex broadly match the values found by Kay et al. (2010) using only the Sr system for the Coranzuli, Panizos and Vilama APVC volcanoes with the deviations in K_{dSr} and F discussed above. The lower K_{dSr} (0.45-0.564) and higher F values (0.33-0.57) in the main Los Frailes ignimbrite are explained by its high 550 ppm Sr as compared to Kari Kari at 450 ppm Sr and the APVC values of 280-340 ppm Sr (Kay et al., 2010). Caffè et al. (2002) reported a calculated K_{dSr} as low as 0.57 for a northern Puna peraluminous

Figure 5.1

Plots of (a) Sr ppm versus $^{87}\text{Sr}/^{86}\text{Sr}$ ratios and (b) $\delta^{18}\text{O}_{\text{magma}}$ in ‰ versus $^{87}\text{Sr}/^{86}\text{Sr}$ ratios for representative measured values of the Kari Kari (brown circle) and Los Frailes (red circle) ignimbrites. The modeled values from Table 5.3 (brown and red diamonds) with proposed metapelite crustal contaminant field (solid black line) are also depicted. Comparative Puna ignimbrites (colored-coded circles) and possible crustal end-member fields (dashed color-coded fields): Vilama and Panizos (blue); Coranzuli (purple) and Cerro Galán (green) as proposed by Kay et al. (2010, 2011). Labels with letters and numbers by the diamonds indicate the modeled ignimbrite (KK- Kari Kari, LF- Los Frailes) and the crustal percentage from Table 5.3, which were determined using the AFC equations of Aitchison and Forrest (1994) following the procedure discussed in the text at the Sr concentrations and $^{87}\text{Sr}/^{86}\text{Sr}$ ratios plotted in (a). Where there is more than one label next to a diamond the single diamond represents multiple solutions for independent AFC models for both KK and LF. The mantle-derived end-member magma used for the modeling is given an $^{87}\text{Sr}/^{86}\text{Sr}$ ratio = 0.7040-0.7055, Sr ppm = 500-950 and $\delta^{18}\text{O} = 5.8\text{‰}$. Modeled $\delta^{18}\text{O}_{\text{magma}}$ values plotted in (b) were calculated from the fractionation corrected $\delta^{18}\text{O}_{\text{quartz}}$ values (Table 3.4) at the percentage of crustal contaminant (number in label) listed in Table 5.3.

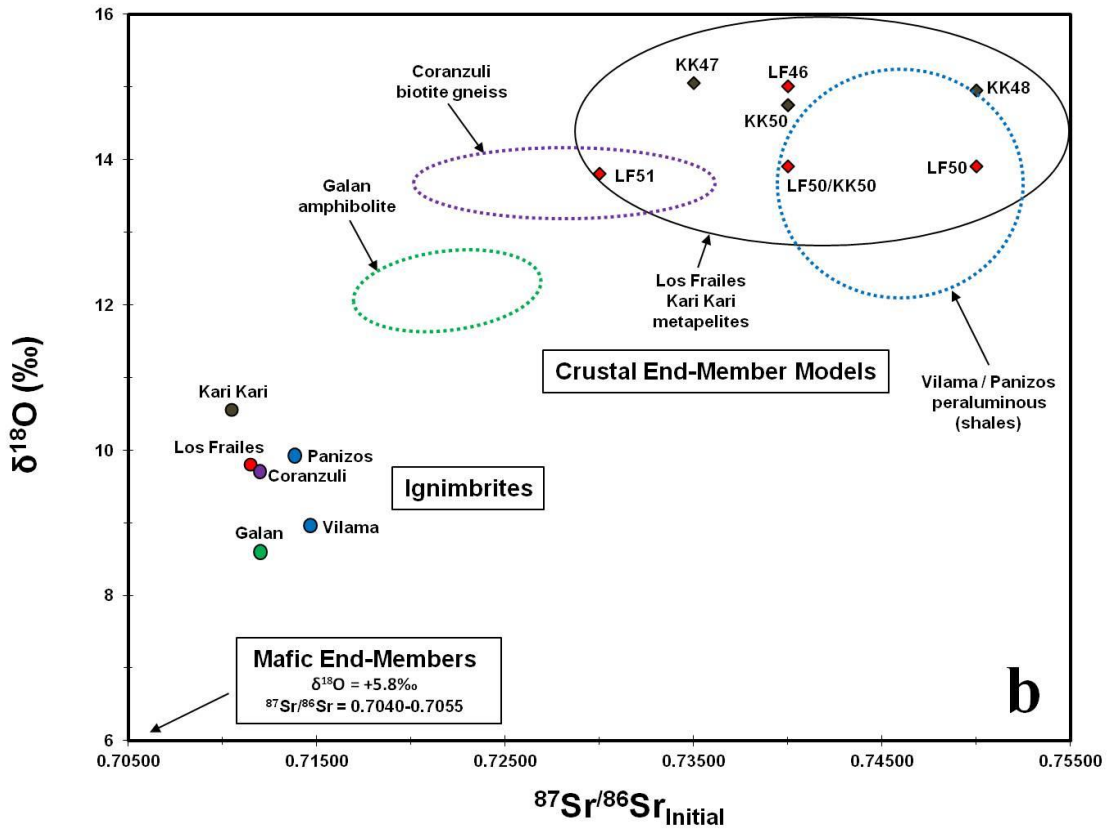
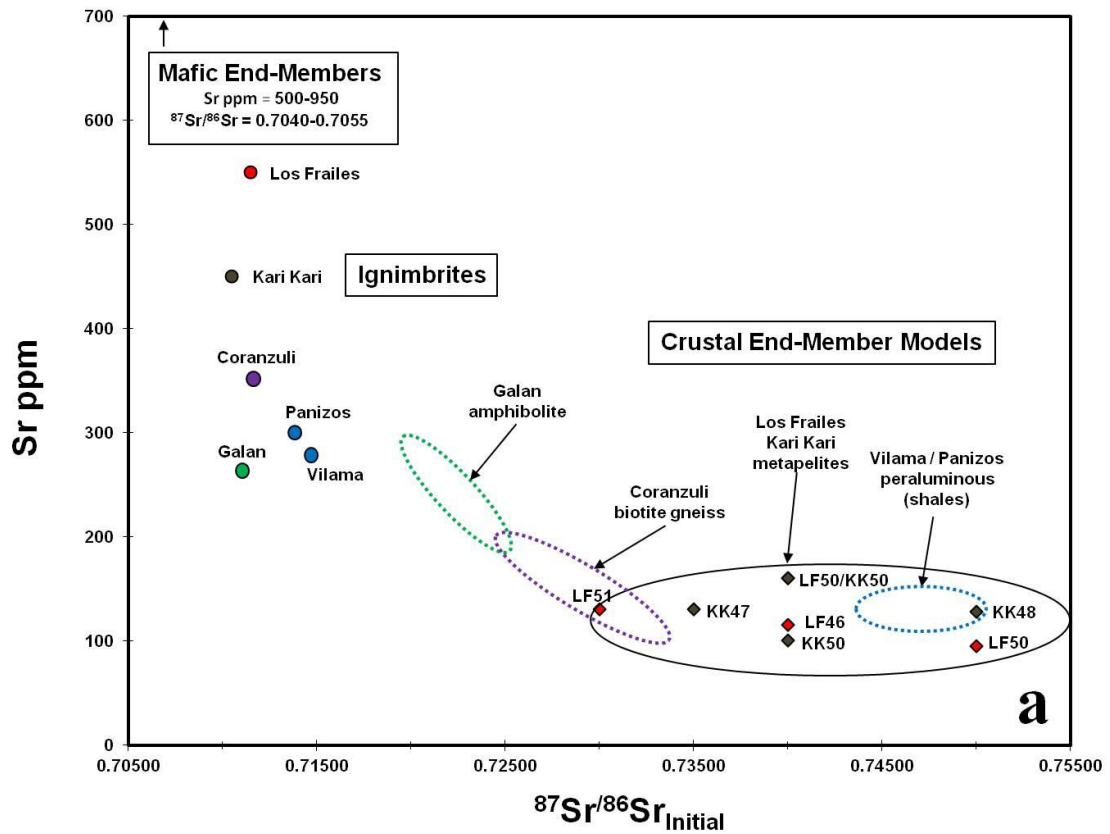
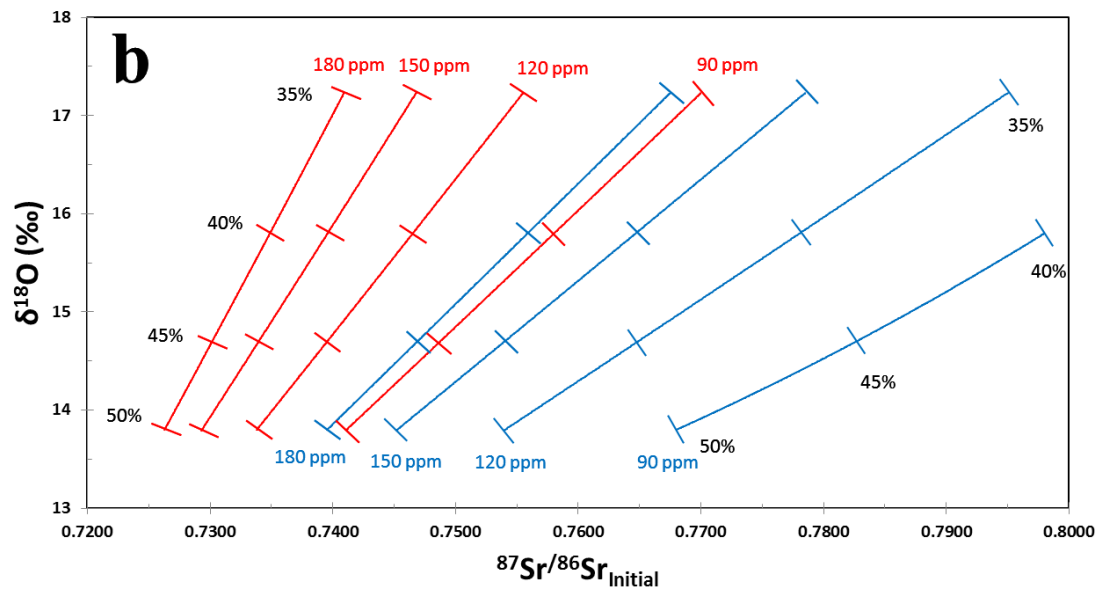
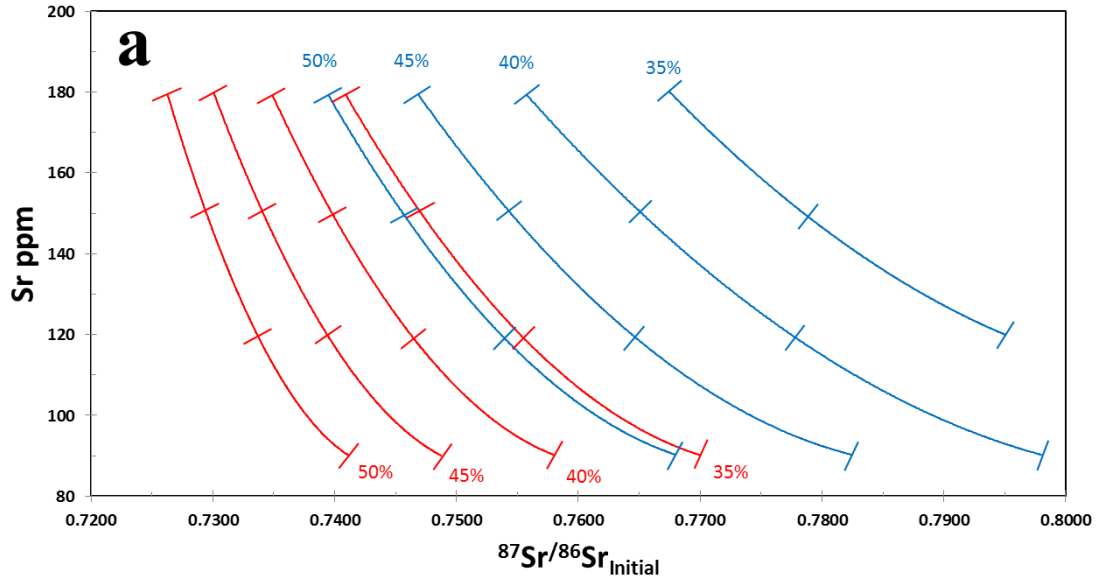


Figure 5.2

Plots of (a) Sr ppm versus $^{87}\text{Sr}/^{86}\text{Sr}$ ratios and (b) $\delta^{18}\text{O}_{\text{magma}}$ in ‰ versus $^{87}\text{Sr}/^{86}\text{Sr}$ ratios with AFC curves for various Los Frailes ignimbrite crustal end-member compositions using the equations of Aitchison and Forrest (1994). (a) Curves represent equal percent of crustal end-member contribution to the resulting Los Frailes ignimbrite with the tick marks showing variable Sr ppm in the crustal end-member. (b) Curves represent equal Sr ppm with the tick marks showing varied % of crustal end-member contribution to the ignimbrite. The modeled values use a mantle-derived end-member containing $\delta^{18}\text{O} = +5.8\text{‰}$, $^{87}\text{Sr}/^{86}\text{Sr}$ ratio = 0.7055 and Sr ppm = 500 (red curves) or Sr ppm = 950 (blue curves). The Los Frailes ignimbrite values used are $\delta^{18}\text{O} = +9.8\text{‰}$, $^{87}\text{Sr}/^{86}\text{Sr}$ ratio = 0.7115 and Sr ppm = 550. All models use $r = 0.6$, $K_{\text{dSr}} = 0.1$ (Eqn 5), $K_{\text{dSr}} = 0.42$ to 0.8 (Eqn 6), $K_{\text{dSr}} = 0.4$ to 0.8 (Eqn 7) and $F = 0.3$ to 0.7 .



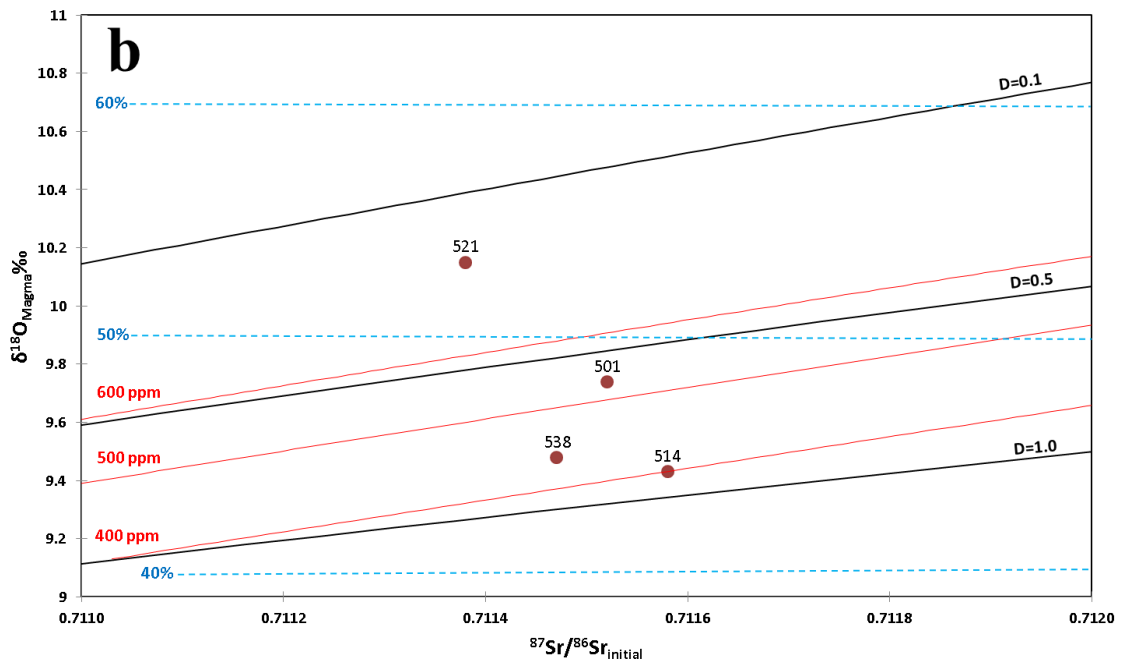
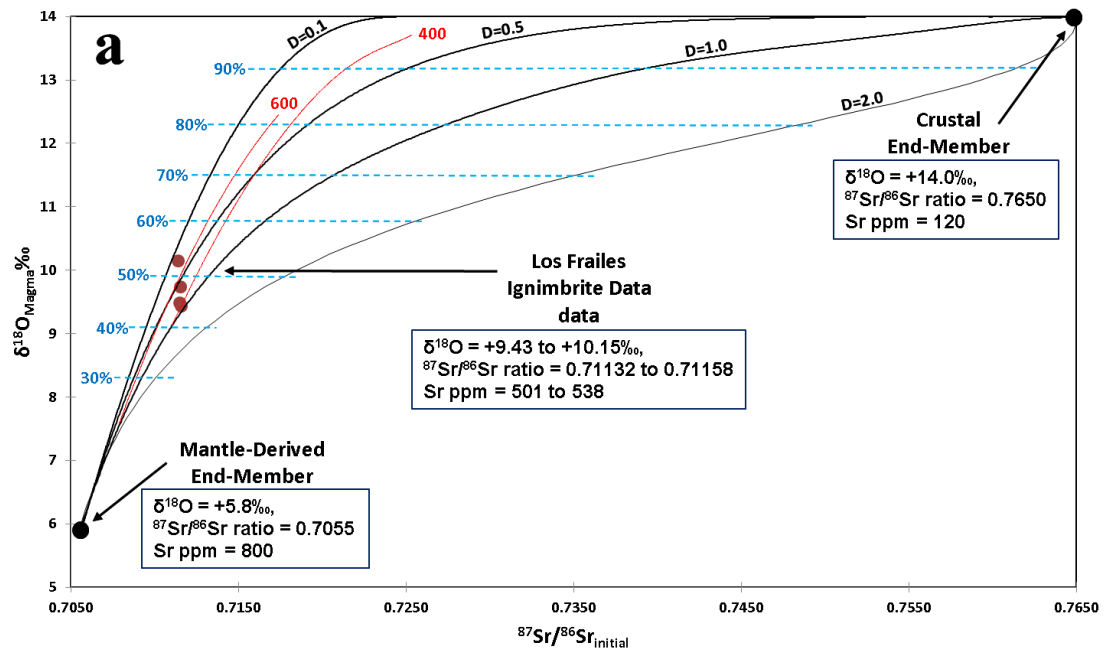
dacite with 543-686 ppm Sr, $r = 0.6$ and $F = 0.5$. These are comparable to the Los Frailes ignimbrite values and indicate a similar need to lower the Kd_{Sr} in order to produce the high Sr concentrations in the product magma. The Kari Kari ignimbrite Sr concentrations are intermediate between those of the Los Frailes ignimbrite and APVC ignimbrites. This results in intermediate values for Kd_{Sr} which overlap the lower end of the APVC Kd_{Sr} range. The AFC model values reported for Cerro Galán by Kay et al. (2010, 2011) have even higher equation 6 middle crustal Kd_{Sr} values of 0.77 to 1.07, which accompany the lowest ignimbrite and highest crustal end-member Sr concentration as well as the lowest $\delta^{18}O$ values discussed here.

The Los Frailes Complex crustal end-member values stated above overlap the $\delta^{18}O$ and Sr ppm versus $^{87}Sr/^{86}Sr$ ratio (see Figures 5.1 and 5.2) fields of crustal end-members values for the Panizos and Vilama ignimbrites proposed by Kay et al. (2010). Kay et al. (2010) used 48-52% crustal input and a peraluminous shale crustal end-member with 125-150 ppm Sr, $^{87}Sr/^{86}Sr = 0.745$ to 0.7500 and $\delta^{18}O = +12.5$ to $+14.8\text{‰}$ to model those crustal end-members. Given the similar isotopic and concentration values (except Sr concentration) of these ignimbrites with the Los Frailes Complex, the similarity in crustal end-member conclusion is not unexpected. The Los Frailes Complex crustal end-member values, like those of the Panizos and Vilama ignimbrites with 50-54% crustal input at $^{87}Sr/^{86}Sr = 0.730$, can be solved using values which extend into the field of biotite gneiss (Kay et al., 2010) and which the Coranzuli crustal end-member solutions occupy. Taking into account only Sr values, this appears to be a viable option for the Los Frailes Complex, but becomes less likely when considered with the reported low $^{143}Nd/^{144}Nd = 0.5115$ ($\epsilon_{Nd} = -22.20$) and low $\delta^{18}O = +7.5$ to $+12.6\text{‰}$ for the 1.9 Ga aged northern Chilean Charcani gneiss basement rock (James, 1982; Martignole and Martelat, 2003).

Figure 5.3 shows AFC curves produced following the calculations of Taylor (1980) using the $\delta^{18}\text{O}$ and $^{87}\text{Sr}/^{86}\text{Sr}$ ratio systems and overlaid on the four Los Frailes ignimbrite data points. The best fit mantle-derived and crustal end-members generally agree with the expected ranges of $\delta^{18}\text{O}$, $^{87}\text{Sr}/^{86}\text{Sr}$ ratio and Sr ppm found using the equations of Aitcheson and Forrest (1994). The K_{dSr} (D) values here are similar to K_{dSr} values found using equation 7 above and represent a system average if assimilation and fractionation had occurred continuously.

Figure 5.3

Plot of $\delta^{18}\text{O}_{\text{magma}}$ versus $^{87}\text{Sr}/^{86}\text{Sr}$ ratios with AFC curves for Los Frailes ignimbrites following Taylor (1980). (a) Black solid curves show variation with changing solid/liquid partition coefficient (D), blue dashed lines are percent crustal end-member contribution to the resulting Los Frailes ignimbrite, red solid curves show equal Sr ppm concentrations in the resulting ignimbrite, and solid maroon dots are Los Frailes ignimbrite data points. (b) Is a plot of the enlarged Los Frailes ignimbrite data field with labels showing the measured Sr ppm for each data point. The D values here represent an average value for the system, which are roughly equal to those found using Aitcheson and Forrest (1994) equation 7 above. The best fit model is shown with a mantle-derived end-member containing $\delta^{18}\text{O} = +5.8\text{‰}$, $^{87}\text{Sr}/^{86}\text{Sr}$ ratio = 0.7055 and Sr ppm = 800. The crustal end-member uses $\delta^{18}\text{O} = +14.0\text{‰}$, $^{87}\text{Sr}/^{86}\text{Sr}$ ratio = 0.7650 and Sr ppm = 120. Due to the high temperature thought to exist at the base of the thickened crust, $R = 0.7$ (mass ratio of material assimilated to material crystallized) is used.



Magma Evolution and Ignimbrite Genesis Model

As seen in Figure 5.4, a three tier magma evolution is proposed to explain the Los Frailes Complex geochemical data presented here in the context of existing geophysical and structural data and models of the Altiplano-Puna backarc region. Similar three tier models of magma evolution in the crust have been proposed by Kay et al. (2010) for the Cerro Galán ignimbrites, by Kay et al. (2011) for a general APVC ignimbrite model and by Keller (2010) for the Los Frailes Complex. Figure 5.4 shows a current cross-section of the southern Altiplano crust and mantle over the steepening subducted Nazca plate at 19° to 20°S. The thicknesses and locations of the crust, mantle-lithosphere and partial melt zones are based on the work of Myers et al. (1998), Polet et al. (2000), Yuan et al. (2000, 2002) and Beck and Zandt (2002). The model for magma evolution at various crustal levels is based on the geochemical evidence.

Reinitiation of magmatism at 19° to 20°S latitude may have been triggered at ~25 Ma by the opening of the mantle wedge and inflow of hot asthenosphere. These conditions occurred as the subducted Nazca plate steepened following the southward passage of the flat slab geometry (see Figure 1.4; James and Sacks, 1988). At that time, the southern Altiplano crustal thickness is estimated to have been ~30-35 km (James and Sacks, 1988) with continuous contractional crustal thickening occurring throughout the Neogene (e.g., Gubbels et al., 1993; Husson and Sempere, 2003). Associated with this resumption of magmatism may have been the detachment of hydrated and weakened mantle lithosphere and possibly mafic lower crust (Hoke and Lamb, 2007).

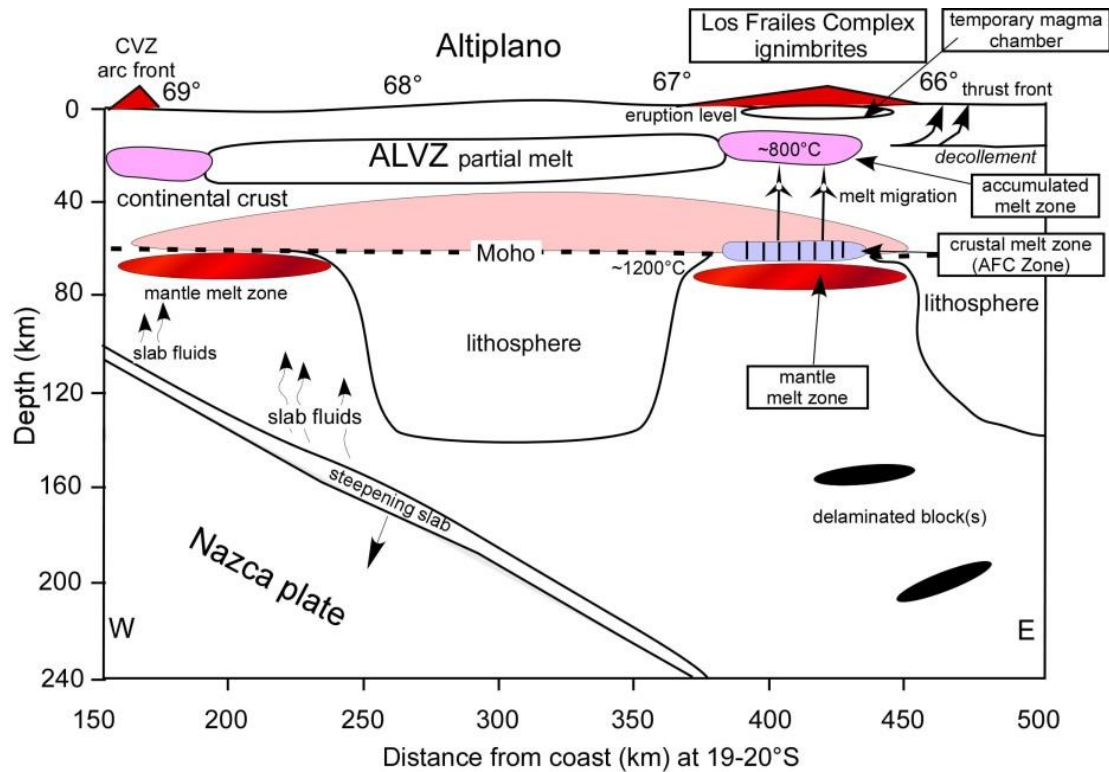


Figure 5.4

Model of the Los Frailes Complex magmatic system at 19° to 20°S with evolution at three crustal levels based on geochemical and geophysical evidence and the proposed models of Kay et al. (2010, 2011) and by Keller (2010). Geophysical framework is from Myers et al. (1998), Polet et al. (2000), Yuan et al. (2000; 2002) and Beck and Zandt (2002). The model depicts decompression mantle melting producing basaltic composition magmas that infiltrate the base of the crust. An AFC zone is established with crustal melting which mixes with the basaltic magma. The hybridized melts then rise and accumulate in a middle crustal mush zone near 15-20 km. Fractionation continues in the partial melt zone before the melts are transferred to a transient upper crustal magma chamber near 4-8 km. Release from middle crustal partial melt zones could be associated with compressional deformation or in response to additional delamination produced melts from below. See text for full description.

The model proposes that basaltic magmas are produced by wet adiabatic decompression melting which takes place in the upwelling part of the mantle wedge. Based on the chemistry of the mafic lavas discussed above, these basaltic melts can include some contamination from a source or sources such as delaminated lithospheric material, subduction-erosion products, or subcontinental lithospheric mantle (SCLM) associated with the intrusion of the Brazilian Shield from the east (e.g., Isacks, 1988;

Polet et al., 2000; Beck and Zandt, 2002). These enriched basaltic melts rise and collect near the Moho and intrude the crustal base where they establish an AFC zone.

The AFC zone in the lower crust is the first tier and is the region in which mantle-derived mafic end-member magmas intrude, melt and assimilate the crust. The crustal thickness influences the depth of the AFC zone and the melted crust imparts a geochemical signature on the resulting hybrid magma. This crustal signature is influenced by the minerals stable at the pressure where the hybridization occurs. The process of crustal thickening with potential deep crustal flow (Isacks, 1988; Husson and Sempere, 2003; Gerbault et al., 2005) transports and replenishes upper crustal pelitic material to the AFC zone depth. A thick pelitic crust subjected to high pressure conditions in the AFC zone results in a metapelitic crustal end-member with a major assemblage of garnet + quartz + K-feldspar + melt along with minor kyanite + rutile ± plagioclase ± biotite ± ilmenite (Indares et al., 2008). The large HREE affinity in garnet imparts the distinctive high Sm/Yb ratio in the rising hybridized melt which is best seen in Figures 3.5a and 4.1.

The high pressure phases of rutile, and possibly low-Mg amphibole and/or ilmenite are also present in the AFC zone restite which fractionates Nb and Ta in the mafic to intermediate lavas (Goss and Kay, 2009). This generates the Ba/Ta and La/Ta ratios in the magma which generally increase and decrease with the La/Sm and Sm/Yb ratios (see Figures 3.9a and 4.1). The peraluminous nature of the Los Frailes Complex ignimbrites, seen in elevated Al/(K+Na+Ca) ratios, is imparted by the metapelitic crust which itself has raised Al/(K+Na+Ca) ratios (see Figure 3.1). Shoshonitic and S-type values are also transferred with the metapelitic melts which have elevated K₂O and depressed Na₂O values (see Figures 3.2 and 3.3). Assimilation of crustal material is confined primarily to the AFC zone where the temperatures are high. The majority of crustal assimilation takes place in these high temperature

regions at the base of the crust and results in magma batches with small $^{87}\text{Sr}/^{86}\text{Sr}$ ratio ranges which are depicted in Figures 3.22a and 3.22b. The high pressure at the base of thickened crust suppresses plagioclase stability and reduces its role in determining differentiation trends. This combined with low percentage melting of replenishing crust allows elevated Sr concentrations to develop in the melts. The rising hybridized melts leave a garnet bearing restite assemblage in the lower crust which is gravitationally unstable and sets the stage for further delamination which can occur piecemeal or in irregular larger events.

As the melts are removed from the AFC zone and rise, they cool and continue to fractionate, but no longer have the heat available for large volume assimilation of the country rock. As pressure decreases in response to reduced depth, plagioclase stability and fractionation increases. This causes the geochemical signatures of plagioclase fractionation in the melt to be superimposed on those of deeper AFC zone fractionation. Plagioclase removal decreases the magma Sr concentration while increasing silica content leading to the SiO_2 and Sr concentration variability seen in Figures 3.22a and 3.22b. With adequately reducing conditions (low $f\text{O}_2$), negative Eu anomalies develop as Eu^{2+} is incorporated and removed with the plagioclase (see Figure 3.11 a).

As the rising hybrid melts reach neutral buoyancy in the middle crust, they pool near 15-20 km forming a mush zone, which is inferred from seismic studies by Yuan et al. (2000) and Beck and Zandt (2002). These partial melts continue to cool and fractionate with minimal assimilation of the middle or upper crust with temperatures near $\sim 800^\circ\text{C}$. Triggers such as regional contraction, structural changes or increased melt production from below, perhaps in response to larger delamination events, forces the low density melt from the mush zone which then moves upward into temporary upper crustal magma chambers near 4-8 km (Kay et al., 2010, 2011). The

upper crustal magma chambers are the location of rapid heat loss and crystallization, which can include cordierite (Luedke et al., 1997; Keller, 2010), but little fractionation, resulting in high crystal content at eruption. Following the partial evacuation of the upper crustal magma chambers, the remaining melt quickly cools and solidifies making the exhausted magma chamber hard or impossible to detect post-eruption.

CHAPTER 6

CONCLUSIONS

The age of the main Los Frailes ignimbrite is confidently established at 1.5-3.5 Ma based on the two new $^{40}\text{Ar}/^{39}\text{Ar}$ sanidine ages and zircon age analysis. These ages are similar to $^{40}\text{Ar}/^{39}\text{Ar}$ biotite ages in Barke et al. (2007) and represent a major readjustment of the previous age estimate of 5-8 Ma (Schneider, 1985). The young age of the volumetrically dominant Los Frailes ignimbrite allows correlation of this large emplacement event with existing seismic anomalies at the same location. The current low velocity (V_p and V_s) region in the mantle, interpreted as a gap in the mantle-lithosphere, below the Los Frailes Complex (Myers et al., 1998; Polet et al., 2000; Beck and Zandt, 2002), is potentially related to the 1.5-3.5 Ma event, the effects of which are still ongoing. This agrees with the $^3\text{He}/^4\text{He}$ emissions study of Hoke and Lamb (2007) which suggests recent mantle melting and crustal intrusion throughout the Altiplano region.

Using new $\delta^{18}\text{O}_{\text{Quartz}}$ data and the AFC model equations of Aitchison and Forrest (1994) which incorporate $^{87}\text{Sr}/^{86}\text{Sr}$ ratios, $^{143}\text{Nd}/^{144}\text{Nd}$ (ϵ_{Nd}) ratios and concentration data, the crustal contribution to the magmas is assessed to be near 50% of the erupted ignimbrite volume. This crustal input value is consistent with the values found by Kay et al. (2010, 2011) in the APVC ignimbrites and at Cerro Galán in the southern Puna and likely involves intrusion of mantle derived basaltic melts into the crust. With an enriched mantle-end member having $\delta^{18}\text{O} = +5.8\text{‰}$, $^{87}\text{Sr}/^{86}\text{Sr} = 0.7055$, 500-950 ppm Sr, $^{143}\text{Nd}/^{144}\text{Nd} = 0.51260$ ($\epsilon_{\text{Nd}} = -0.74$) and 25-30 ppm Nd based on mafic lava samples, the crustal end-member is calculated to contain $\delta^{18}\text{O} = +13.0$ to $+16.0\text{‰}$, $^{87}\text{Sr}/^{86}\text{Sr} = 0.7030$ to 0.7500 , 95-160 ppm Sr, $^{143}\text{Nd}/^{144}\text{Nd} = 0.51190$ ($\epsilon_{\text{Nd}} = -14.4$) and 25-40 ppm Nd. The peraluminous character of the ignimbrites with

the associated isotopic values and trace element concentrations strongly suggest a metapelitic crustal source.

Coherent temporal trends in La/Sm, Sm/Yb, La/Ta and Ba/Ta ratios track the effects of crustal thickening and episodic delamination at the depth of the Moho and resulting AFC zone location. A general pattern of crustal thickening is inferred from steepening HREE ratios since 25 Ma which corresponds with the current models of Altiplano crustal thickening primarily in response to crustal shortening (e.g., Elger et al., 2005). Breaking the trend of otherwise steady HREE ratio increase are two distinct ratio decreases which are proposed to correlate with two discrete delamination events. With the loss of the lithosphere and basal crust, the AFC zone is argued to have decreased in depth to the bottom of the newly exposed lower crust. These decreases occur at 10-12 Ma and 2-4 Ma prior to major eruptions of the Livicucho and Condor Nasa ignimbrites at 7-8 Ma and the main Los Frailes ignimbrite at 1.5-3.5 Ma. A 10-12 Ma delamination event is supported by a corresponding shift to the east of Altiplano brittle deformation after 10 Ma (e.g., Gubbels et al., 1993) and the isotopic enrichment in Los Frailes Complex volcanic rocks at 10-12 Ma demonstrated here. The enriched isotopic signature is thought to be a response to an increased radiogenic composition of the crust being exposed and assimilated. A 2-4 Ma delamination is supported by temporal correlation with the emplacement of the large Los Frailes ignimbrite with the now established age of 1.5-3.5 Ma.

A three tier magma evolution, in the style proposed by Kay et al. (2010, 2011) and Keller (2010), for the Los Frailes Complex is well supported by the geochemical and geophysical evidence. Mantle melting produces basaltic magmas which may include some contamination by delaminated lithospheric material, subduction-erosion products, or SCLM which collect near the Moho and intrude the base of the crust. Crustal thickness variations influence the depth of the resulting AFC zone which

imparts geochemical signatures on the resulting hybrid magma through pressure-dependent mineral phase stability and low percentage melting. A metapelitic assemblage and garnet restite impart the distinctive HREE patterns and peraluminous character on the rising hybridized melt. Assimilation of the crust is largely confined to the AFC zone in the hot lower crust where high pressure suppresses plagioclase stability and allows elevated Sr concentrations to develop. The rising hybridized melts leave a gravitationally unstable restite which encourages further delamination. As the melts rise, plagioclase stability and fractionation increases with reduced pressure leading to increased SiO₂, decreased Sr concentration and negative Eu anomalies. Melts pool near 15-20 km and form a mush zone where cooling and fractionation continues at temperatures near ~800°C. Regional contractions and structural changes or delamination driven melt production from below push the mush zone melts into temporary upper crustal magma chambers near 4-8 km. Rapid heat loss and crystallization ensue resulting in high crystal content, including cordierite. Emplacement of the ignimbrites occurs from these shallow storage chambers which cool quickly and solidify after depletion.

APPENDIX A
NEODYMIUM SEPARATION PROCEDURE

The following procedures were developed to separate Nd cuts from previously collected REE fractions using Eichrom LN Resin 100-150 micron columns (ion exchange chromatography). The procedures were adapted from the method reported by Pin et al. (1996) and outlined on the Eichrom website at (http://www.eichrom.com/products/info/LN_resin.cfm). Column calibration procedures and times are as follows:

- 1) If the column is new, drain by breaking off the bottom plastic plug and removing cap. Collect to waste. (10 minutes)
- 2) Condition Column: Fill the reservoir (~3.5 ml) with 0.23N QD HCL and allow it to drain. Collect to waste. (10 minutes)
- 3) Repeat step one again.
- 4) Load Sample: Dissolve REE sample in 0.2 ml of 0.23N QD HCL using low heat on a hot plate for five minutes to aid dissolution. Using pipette, place 0.2 ml of dissolved sample in the top of the column. Wait one minute.
- 5) Collect Samples: Add 1.0 ml of 0.23N QD HCL to the column reservoir. Collect in a labeled 45 ml beaker. (3 minutes)
- 6) Repeat step four 14-23 more times. (45-75 minutes)
- 7) Flush the column and store in a beaker following the directions below.
- 8) Add 24 ml of 2% HNO₃ to each 1.0 ml collected sample.
- 9) Load samples and analyze in ICP-MS looking for counts of Ce140, Pr141, Nd144, Nd146, Sm147, and Sm149.
- 10) Analysis: The samples should show that Ce140 peaks at 8-9 ml (± 1) and Pr141 peaks at 11 ml (± 1). The Nd144 and Nd146 peaks should be at 13 ml (\pm

1). The Sm147 and Sm149 may not show peaks, but should show increasing trends to the right or a peak at greater than 20 ml.

Based on two calibration data sets, optimum collection of Nd was determined to be from 10 to 18 ml. This was based on the desire to maximize Nd144 and Nd146 collection while minimizing Ce140, Sm147 and Sm149. Nd fraction separation procedures and times are as follows:

- 1) Condition Column: Fill the reservoir (~3.5 ml) with 0.23N QD HCL and allow it to drain. Collect to waste. (10 minutes)
- 2) Repeat step one again.
- 3) Load Sample: Dissolve REE sample in 0.2 ml of 0.23N QD HCL using low heat on a hot plate for five minutes to aid dissolution. Using pipette, place 0.2 ml of dissolved sample in the top of the column. Wait one minute.
- 4) Add 1.0 ml of 0.23N QD HCL to the column reservoir. Collect in waste HCL beaker. (3 minutes)
- 5) Add 9.0 ml of 0.23N QD HCL to the column reservoir (this will have to be done in three steps as the reservoir only holds about 3.5 ml). Collect in waste HCL beaker. (30 minutes)
- 6) Collect Sample: Add 8.0 ml of 0.23N QD HCL to the column reservoir. Collect in a labeled beaker. (25 minutes)
- 7) Flush Column: Fill the reservoir (~3.5 ml) with 6.0N QD HCL. Collect in waste HCL beaker. (10 minutes)
- 8) Repeat step seven twice more.
- 9) Fill the reservoir (~3.5 ml) with 0.23N QD HCL. Collect in waste HCL beaker. (10 minutes)

- 10) Column Storage: Fill the reservoir (~3.5 ml) with 0.23N QD HCL then replace the column cap. The goal is to ensure that the white LN resin remains immersed in acid and does not dry out.
- 11) Place the capped column in storage container (45 ml beaker) and fill with 0.23N QD HCL to a level that submerges the white LN resin (about 25 ml).
- 12) Documentation: Document in order to track the number of uses of a particular column and to determine how many samples the column can be used before recalibration or disposal is required.
- 13) The 8.0 ml sample should then be placed on a hot plate at low heat and allowed to dry.

APPENDIX B
MAJOR AND TRACE ELEMENT DATA

Major and trace element data for PT and PO series samples					
Center Sample	Porco PT-1	Porco PT-2	Porco PT-3	Kumurana PT-4	Kari Kari PT-5
SiO ₂	69.05	67.40	71.37	63.79	63.20
TiO ₂	0.74	0.76	0.71	0.57	0.56
Al ₂ O ₃	16.43	16.21	16.08	18.50	18.85
Fe ₂ O ₃	3.39	3.07	3.19	4.33	4.05
FeO	3.05	2.77	2.87	3.90	3.64
MnO	0.02	0.02	0.02	0.06	0.05
MgO	1.12	1.06	1.06	1.06	1.03
CaO	1.94	1.64	2.43	3.45	3.67
Na ₂ O	2.64	2.72	2.97	2.72	2.89
K ₂ O	5.09	5.29	4.80	5.00	4.81
P ₂ O ₅	0.23	0.12	0.32	0.30	0.29
LOI	1.36	1.28	1.14	1.15	0.77
Total	101.67	99.28	103.76	100.48	99.77
La	83.8	84.5	93.2	87.3	85.6
Ce	164.4	158.6	165.7	170.6	173.1
Pr	-	-	-	-	-
Nd	57.8	60.4	59.0	66.7	68.5
Sm	9.6	9.3	10.2	12.3	12.6
Eu	1.63	1.50	1.66	2.07	2.24
Gd	-	-	-	-	-
Tb	0.79	0.45	0.68	1.28	1.08
Dy	-	-	-	-	-
Ho	-	-	-	-	-
Er	-	-	-	-	-
Tm	-	-	-	-	-
Yb	1.09	0.84	0.96	2.76	2.63
Lu	0.150	0.115	0.131	0.358	0.337
Y	12	6	10	27	31
Rb	232	248	236	223	222
Sr	564	535	554	470	458
Ba	1047	1154	1153	1015	1133
Cs	11.6	13.1	21.2	18.5	12.3
Pb	-	-	-	-	-
U	7.4	5.5	7.6	4.2	6.7
Th	25.1	24.1	23.8	26.4	26.1
Nb	24	25	23	38	39
Ta	1.73	1.74	1.59	2.33	2.18
Zr	258	266	253	293	410
Hf	6.1	6.2	6.0	8.2	8.3
Sc	5.2	5.3	4.9	7.3	7.6
Cr	13	13	12	21	21
Ni	3.0	4.3	-	4.8	8.2
Co	5	5	5	6	24

Major and trace element data for PT and PO series samples

Center Sample	Condor Nasa PT-6	Condor Nasa PT-7	Los Frailes PT-8	Los Frailes PT-9	Los Frailes PT-9p
SiO ₂	60.73	62.53	69.05	66.82	66.47
TiO ₂	1.27	1.12	0.64	0.65	0.72
Al ₂ O ₃	17.69	16.75	16.35	15.85	16.17
Fe ₂ O ₃	5.60	5.25	3.03	2.98	3.26
FeO	5.04	4.73	2.72	2.68	2.93
MnO	0.05	0.02	0.04	0.04	0.08
MgO	2.05	2.33	1.19	1.20	1.28
CaO	4.32	2.98	2.70	2.60	2.55
Na ₂ O	2.43	2.94	2.81	2.71	2.66
K ₂ O	4.47	4.88	4.81	4.93	4.97
P ₂ O ₅	0.49	0.43	0.30	0.30	0.31
LOI	0.88	1.47	0.49	0.90	1.22
Total	99.43	100.17	101.11	98.66	99.36
La	74.0	54.9	74.6	66.3	73.5
Ce	150.5	108.6	152.7	136.3	154.8
Pr	-	-	-	-	-
Nd	69.0	57.6	65.2	49.9	57.7
Sm	12.6	10.7	11.5	9.7	10.7
Eu	2.37	1.95	1.84	1.67	1.72
Gd	-	-	-	-	-
Tb	1.08	0.96	0.83	0.78	0.78
Dy	-	-	-	-	-
Ho	-	-	-	-	-
Er	-	-	-	-	-
Tm	-	-	-	-	-
Yb	2.08	1.84	1.42	1.41	1.53
Lu	0.270	0.242	0.173	0.178	0.198
Y	27	24	16	15	16
Rb	174	184	170	215	225
Sr	648	442	538	514	457
Ba	1252	1067	1223	1118	1120
Cs	9.0	6.6	2.7	7.6	8.5
Pb	-	-	-	-	-
U	4.3	5.1	5.9	6.4	8.0
Th	17.8	15.8	25.0	22.6	25.6
Nb	32	29	20	21	22
Ta	2.14	2.11	1.57	1.77	1.76
Zr	332	312	248	247	261
Hf	7.3	6.7	6.4	6.2	6.8
Sc	22.3	11.7	6.5	6.3	7.1
Cr	22	10	9	9	10
Ni	14.8	7.6	6.7	5.2	4.9
Co	8	8	3	3	4

Major and trace element data for PT and PO series samples

Center Sample	Los Frailes PT-10	Los Frailes PT-11	Los Frailes PT-11p	Condor Nasa PT-12	Livicucho PT-13
SiO ₂	67.36	67.12	65.84	65.94	59.96
TiO ₂	0.68	0.69	0.67	0.72	1.38
Al ₂ O ₃	15.36	15.94	15.83	16.54	18.04
Fe ₂ O ₃	3.34	3.31	3.10	3.2940	5.87
FeO	3.01	2.98	2.79	2.96	5.28
MnO	0.05	0.03	0.04	0.04	0.07
MgO	1.28	1.28	1.48	1.38	2.42
CaO	2.49	2.63	2.51	2.75	4.26
Na ₂ O	2.59	2.97	2.54	2.71	2.44
K ₂ O	4.91	5.04	4.82	4.83	4.32
P ₂ O ₅	0.33	0.34	0.30	0.34	0.43
LOI	1.15	0.38	1.71	1.04	1.03
Total	99.20	99.39	98.53	99.26	99.63
La	67.8	65.0	73.1	75.3	65.9
Ce	144.5	137.9	158.3	167.4	142.2
Pr	-	-	-	-	-
Nd	62.0	55.5	62.2	65.0	62.4
Sm	11.0	10.2	11.2	11.5	11.9
Eu	1.52	1.83	1.83	1.99	2.55
Gd	-	-	-	-	-
Tb	-	0.93	0.92	0.89	1.22
Dy	-	-	-	-	-
Ho	-	-	-	-	-
Er	-	-	-	-	-
Tm	-	-	-	-	-
Yb	1.50	1.38	1.40	1.44	2.01
Lu	0.189	0.178	0.193	0.181	0.268
Y	14	14	14	15	29
Rb	236	226	238	211	206
Sr	405	556	521	552	559
Ba	842	1223	1035	1159	1318
Cs	9.5	5.8	9.8	10.7	5.9
Pb	-	-	-	-	-
U	9.4	8.3	10.3	8.1	7.2
Th	23.6	22.3	25.5	26.7	17.8
Nb	21	21	21	20	28
Ta	1.81	1.61	1.71	1.83	2.18
Zr	243	250	262	262	314
Hf	6.4	6.7	6.7	6.9	7.5
Sc	7.3	7.0	7.0	7.2	14.68
Cr	10	10	10	10	21.1
Ni	1.2	7.8	3.1	6.0	15.3
Co	4	4	3	3	5

Major and trace element data for PT and PO series samples

Center Sample	Livicucho PT-14	Condor Nasa PT-15	Los Frailes PT-16	Los Frailes PT-16p	Condor Nasa PO-1
SiO ₂	-	59.59	66.82	68.02	58.98
TiO ₂	-	1.37	0.69	0.63	1.27
Al ₂ O ₃	-	18.14	16.07	15.23	18.39
Fe ₂ O ₃	-	5.74	3.25	3.05	-
FeO	3.79	5.17	2.93	2.74	5.90
MnO	-	0.05	0.04	0.03	0.08
MgO	-	2.47	1.32	1.24	2.46
CaO	-	4.42	2.63	1.95	4.00
Na ₂ O	3.91	2.17	2.82	3.84	1.69
K ₂ O	-	3.84	5.02	4.40	4.04
P ₂ O ₅	-	0.44	0.32	0.37	0.50
LOI	-	-	-	-	2.91
Total	7.70	97.65	98.66	98.44	100.21
La	90.2	70.9	66.6	94.9	80.1
Ce	112.1	154.4	146.3	190.7	173
Pr	-	-	-	-	-
Nd	68.8	62.7	58.0	70.9	72.3
Sm	13.4	11.6	10.5	12.8	13.2
Eu	1.88	2.62	1.67	1.87	2.74
Gd	-	-	-	-	-
Tb	0.94	1.15	0.70	0.87	1.053
Dy	-	-	-	-	-
Ho	-	-	-	-	-
Er	-	-	-	-	-
Tm	-	-	-	-	-
Yb	1.75	1.98	1.27	1.27	2.47
Lu	0.217	0.255	0.16	0.158	0.308
Y	-	27	-	-	28
Rb	-	135	-	-	233
Sr	410	672	501	625	614
Ba	1114	1269	1098	993	1140
Cs	5.6	3.8	8.7	7.7	23.2
Pb	-	-	-	-	-
U	11.0	4.0	7.9	13.6	5.7
Th	13.8	17.5	23.7	30.6	19.8
Nb	-	34	-	-	33
Ta	1.56	2.10	1.66	3.06	2.34
Zr	-	336	-	-	342
Hf	5.3	7.6	6.1	6.3	8.2
Sc	11.2	13.8	6.7	5.5	13.9
Cr	16	25	10	9	23
Ni	8.2	13.0	-	2.7	8.0
Co	5	10	3	2	8

Major and trace element data for PT and PO series samples

Center Sample	Condor Nasa PO-2	Condor Nasa PO-3	Condor Nasa PO-4	Sevaruyo PO-5	Sevaruyo* PO-6
SiO ₂	60.29	61.11	62.82	71.97	65.76
TiO ₂	1.30	1.30	1.01	0.34	0.78
Al ₂ O ₃	18.19	18.24	17.82	14.84	16.82
Fe ₂ O ₃	-	-	-	-	-
FeO	5.30	5.40	3.19	1.92	3.41
MnO	0.06	0.06	0.03	0.02	0.04
MgO	2.43	2.36	1.26	0.64	1.12
CaO	4.23	4.18	2.49	1.69	3.22
Na ₂ O	2.02	2.36	2.31	2.66	2.94
K ₂ O	4.37	4.50	5.75	4.82	4.93
P ₂ O ₅	0.51	0.51	0.45	0.21	0.39
LOI	1.50	0.68	3.13	1.31	0.86
Total	100.20	100.69	100.25	100.42	100.26
La	74.9	75.0	65.2	38.7	67.9
Ce	163	159	138	85	147
Pr	-	-	-	-	-
Nd	65.4	67.6	59.9	32.8	59.9
Sm	11.7	12.4	10.9	6.8	10.8
Eu	2.77	2.67	2.22	1.04	2.07
Gd	-	-	-	-	-
Tb	0.975	0.969	0.838	0.450	0.582
Dy	-	-	-	-	-
Ho	-	-	-	-	-
Er	-	-	-	-	-
Tm	-	-	-	-	-
Yb	1.99	2.14	1.74	1.34	1.54
Lu	0.259	0.273	0.221	0.174	0.187
Y	27	23	17	10	15
Rb	169	147	247	272	212
Sr	644	649	438	272	475
Ba	1160	1258	1102	761	1259
Cs	7.8	5.5	11.1	9.5	12.4
Pb	-	-	-	-	-
U	3.8	4.4	5.4	7.0	7.6
Th	18.1	18.0	16.7	15.4	20.0
Nb	33	30	29	14	20
Ta	2.08	2.23	2.35	1.65	1.93
Zr	358	254	227	140	221
Hf	7.4	8.0	7.0	3.8	6.2
Sc	13.8	14.1	9.5	4.8	7.2
Cr	24	23	14	10	8
Ni	18.0	18.9	11.2	4.4	6.2
Co	8	9	3	3	5

* Sample may be from Los Frailes ignimbrite (discussion at beginning of Chapter 3).

APPENDIX C

STROTIUM AND NEODYNIUM ISOTOPIC DATA AND ERROR ANALYSES

Sample	Date	Grand Mean (After Rejection)		Total Accepted	Total Run	Notes
		87/86n	% Sd Err			
PT-1	1-Feb-12	0.71003	0.0005	142	150	
PT-3	5-May-11	0.71017	0.0019	143	150	
PT-3	23-Jan-12	0.71017	0.0006	210	225	1300 ppm Rb
PT-3	24-Jan-12	0.71017	0.0006	144	150	
PT-4	23-Jan-12	0.71018	0.0007	143	150	7700 ppm Rb
PT-4	23-Jan-12	0.71018	0.0011	136	150	1100 ppm Rb
PT-4	23-Jan-12	0.71020	0.0010	138	150	500 ppm Rb
PT-4	24-Jan-12	0.71015	0.0011	172	180	Fractionated, some blocks with high Rb
PT-5	20-Jan-12	0.71043	0.0006	141	150	
PT-7	5-May-11	0.71160	0.0006	146	150	
PT-8	5-May-11	0.71149	0.0005	143	150	
PT-8	26-Jan-12	0.71149	0.0006	143	150	
PT-9	27-Jan-12	0.71156	0.0010	143	150	Fractionated, early blocks have high Rb
PT-9	8-Feb-12	0.71153	0.0032	149	150	8700 ppm Rb, high error
PT-9	19-Feb-12	0.71160	0.0008	137	150	1200 ppm Rb
PT-10	5-May-11	0.71136	0.0005	143	150	
PT-11p	31-Jan-12	0.71141	0.0006	135	150	
PT-12	31-Jan-12	0.71146	0.0014	136	150	High error
PT-12	7-Feb-12	0.71145	0.0009	158	165	
PT-13	5-May-11	0.71267	0.0008	142	150	
PT-14	23-Jan-12	0.71257	0.0005	144	150	
PT-16	24-Jan-12	0.71155	0.0006	228	240	Early blocks are fractionated, but no effect on 87/86
PO-2	27-Jan-12	0.71140	0.0005	145	150	
PO-5	2-Feb-12	0.71269	0.0004	362	375	2400 ppm Rb
PO-5	3-Feb-12	0.71267	0.0009	143	150	200 ppm Rb
N-987	5-May-11	0.71025	0.0012	144	150	
N-987	5-May-11	0.71023	0.0014	144	150	High error
N-987	26-Jan-12	0.71025	0.0007	142	150	
N-987	18-Feb-12	0.71025	0.0005	140	150	1000 ppm Rb
N-987	19-Feb-12	0.71024	0.0007	141	150	
N-987	20-Feb-12	0.71025	0.0009	138	150	

Sample	Date	Grand Mean (After Rejection)			
		143/144 Exp	%SdErr	Total Accepted	Total Run
PT-1	6-Mar-12	0.512238	0.0017	142	150
PT-3	5-Mar-12	0.512254	0.0022	141	150
PT-4	2-Apr-12	0.512331	0.0013	214	225
PT-5	4-Apr-12	0.512296	0.0015	143	150
PT-8	30-Apr-12	0.512182	0.0015	216	225
PT-9	10-Apr-12	0.512208	0.0015	259	270
PT-11p	25-Feb-12	0.512208	0.0016	145	150
PT-12	28-Feb-12	0.512218	0.0023	130	135
PT-14	2-Apr-12	0.512199	0.0013	215	225
PT-16	5-Apr-12	0.512235	0.0019	145	150
PT-16	11-Apr-12	0.512214	0.0020	141	150
PT-16	12-Apr-12	0.512221	0.0017	145	150
PO-2	28-Feb-12	0.512204	0.0011	145	150
PO-5	29-Feb-12	0.512197	0.0020	115	120
PO-6	28-Feb-12	0.512236	0.0019	144	150
Ames STD 1	24-Feb-12	0.512187	0.0018	143	150
Ames STD 2	24-Feb-12	0.512157	0.0014	145	150
Ames STD 3	25-Feb-12	0.512194	0.0016	144	150
Ames STD 4	4-Mar-12	0.512165	0.0021	144	150
Ames STD 5	4-Mar-12	0.512171	0.0011	145	150
Ames STD 6	6-Mar-12	0.512153	0.0011	145	150
Ames STD 7	7-Mar-12	0.512183	0.0015	144	150
Ames STD 7	7-Mar-12	0.512147	0.0013	145	150
Ames STD 8	26-Mar-12	0.512170	0.0013	144	150
Ames STD 9	9-Apr-12	0.512203	0.0014	145	150
Ames STD 10	27-Apr-12	0.512162	0.0018	144	150
Ames STD 11	1-May-12	0.512141	0.0009	158	165
Ames STD 12	1-May-12	0.512137	0.0010	145	150

APPENDIX D
OXYGEN ISOTOPIC DATA AND ERROR ANALYSIS

New laser line run #1 (2013)

Jan 11th 2013

sample	wt. (g)	P inlet	mb/mg	d33	d34	$\delta^{17}\text{O}$ norm	$\delta^{17}\text{O}$ norm	$\delta^{18}\text{O}$ norm	$\delta^{18}\text{O}$ norm
Mon gt	2.45	10.8	4.41	-2.91	-6.382	3.64	3.64	6.18	6.18
Mon gt	2.03	8.3	4.09	-3.06	-6.410	3.49	3.49	6.15	6.15
PO5 qz	3.03	17.5	5.78	0.03	-0.755	6.60	6.60	11.88	11.88
PO6 qz	2.06	12.0	5.83	-0.32	-1.274	6.25	6.25	11.35	11.35
PT16 qz	2.85	Grain jumped out							
PT1 qz*	3.33	19.9	5.98	-0.35	-1.306	6.22	6.22	11.32	11.32
PT12 qz	2.64	Grain jumped out							
PT11P qz	2.83	16.7	5.90	-0.45	-1.545	6.12	6.12	11.08	11.08
PT8 qz	2.86	Grain jumped out							
PT9 qz	2.77	9.2	3.32	-1.37	-2.096	5.19	5.19	10.52	10.52
Mon gt ave								6.16	
Mon gt diff								0.78	
Error (2 sigma)								0.02835	

New laser line run #3 (2013)

Jan 18th 2013

sample	wt. (g)	P inlet	mb/mg	d33	d34	$\delta^{17}\text{O}$ norm	$\delta^{17}\text{O}$ norm	$\delta^{18}\text{O}$ norm	$\delta^{18}\text{O}$ norm
Mon gt	2.31	10.9	4.72	-3.12	-6.524	3.43	1.12	6.03	3.72
Mon gt	2.35	11.0	4.68	-3.15	-6.446	3.40	1.09	6.11	3.80
PT3 qz	2.39	5.9	2.47	-0.17	-1.230	6.40	4.09	11.39	9.08
PT3 qz	3.19	19.5	6.11	-0.42	-1.268	6.15	3.84	11.36	9.05
PT14 qz	3.58	20.6	5.75	-0.54	-1.498	6.03	3.72	11.12	8.81
PT14 qz	3.19	18.9	5.92	-0.47	-1.230	6.10	3.79	11.39	9.08
Mon gt ave								6.07	
Mon gt diff								0.69	
Error (2 sigma)								0.0790	

APPENDIX E

ZIRCON ISOTOPIC DATA AND ERROR ANALYSIS

PT-8	206Pb/238U	$\pm 2\sigma$	207Pb/235U	$\pm 2\sigma$	207Pb/ 206Pb	$\pm 2\sigma$	Corr.	%	Th/U
Fraction	^a	abs	^a	abs	^a	abs	Coef.	disc ^b	^c
Zircon (no CL)									
z2	11.9	2.2	18.9	6.2	1037	510	0.655	98.85	0.8

PT-10	206Pb/238U	$\pm 2\sigma$	207Pb/235U	$\pm 2\sigma$	207Pb/ 206Pb	$\pm 2\sigma$	Corr.	%	Th/U
Fraction	^a	abs	^a	abs	^a	abs	Coef.	disc ^b	^c
Zircon (no CL)									
z3	12.054	0.013	12.28	0.14	57	26	0.596	78.85	0.15
L zircon									
L z2	2.220	0.11	3.6	1.7	1043	880	0.781	99.79	0.41
L z4	1.868	0.035	2.15	0.55	330	540	0.783	99.43	0.21
L z6	5.423	0.031	5.97	0.48	231	180	0.782	97.66	0.36

PT-15	206Pb/238U	$\pm 2\sigma$	207Pb/235U	$\pm 2\sigma$	207Pb/ 206Pb	$\pm 2\sigma$	Corr.	%	Th/U
Fraction	^a	abs	^a	abs	^a	abs	Coef.	disc ^b	^c
Zircon (no CL)									
z1	57.5	2.5	102	35	1337	630	0.78	95.7	0.34
z2	419.82	0.67	423.9	6.6	446	40	0.725	5.84	0.77
z3	8.52	0.13	10.1	2	410	420	0.781	97.92	0.13
z4	7.89	0.59	14.9	9.1	1368	1100	0.78	99.42	0.58
L zircon									
L z2	7.095	0.097	7.7	1.5	214	430	0.78	96.69	0.28
L z3	7.139	0.012	7.26	0.17	49	53	0.722	85.41	0.53
L z5	598.91	0.44	681.8	2.9	966	11	0.631	37.99	0.46
L z6	7.200	0.11	8.5	1.7	402	410	0.78	98.21	0.43

Pb* (pg) ^d	Pbc (pg) ^e	Pb*/ Pbc ^f	206Pb/ 204Pb ^g	206Pb/ 238U ^h	$\pm 2\sigma$ %	207Pb/ 235U ^h	$\pm 2\sigma$ %	207Pb/ 206Pb ^h	$\pm 2\sigma$ %
3.54	12.81	0	33	0.00184	19	0.188	33	0.074	25

Pb* (pg) ^d	Pbc (pg) ^e	Pb*/ Pbc ^f	206Pb/ 204Pb ^g	206Pb/ 238U ^h	$\pm 2\sigma$ %	207Pb/ 235U ^h	$\pm 2\sigma$ %	207Pb/ 206Pb ^h	$\pm 2\sigma$ %
40	4.71	8	579	0.001872	0.11	0.01217	1.2	0.04715	1.1
0.571	3.95	0	27	0.000344	4.9	0.0035	47	0.074	43
0.333	0.95	0	41	0.00029	1.9	0.00212	25	0.053	24
0.822	0.67	1	94	0.000842	0.57	0.00598	8.1	0.0508	7.6

Pb* (pg) ^d	Pbc (pg) ^e	Pb*/ Pbc ^f	206Pb/ 204Pb ^g	206Pb/ 238U ^h	$\pm 2\sigma$ %	207Pb/ 235U ^h	$\pm 2\sigma$ %	207Pb/ 206Pb ^h	$\pm 2\sigma$ %
6.37	39.32	0	28	0.00895	4.3	0.106	36	0.086	32
160	31.29	5	302	0.06729	0.17	0.5181	1.9	0.0558	1.8
5.39	12.9	0	46	0.001323	1.5	0.1	20	0.055	19
1.74	17.68	0	24	0.001225	7.5	0.0147	62	0.087	56
0.951	1.95	0	49	0.001101	1.4	0.0077	20	0.0504	18
3.79	0.8	5	299	0.001108	0.17	0.00718	2.3	0.047	2.2
46.6	3.79	12	750	0.097358	0.077	0.9571	0.58	0.0713	0.54
0.839	1.81	0	46	0.001118	1.5	0.0084	20	0.055	18

a Isotopic dates calculated using the decay constants

$$A_{238} = 1.55125E-10 \text{ and } A_{235} = 9.8485E-10 \text{ (Jaffey et al.1971).}$$

b % discordance = $100 - (100 * (206\text{Pb}/238\text{U date}) / (207\text{Pb}/206\text{Pb date}))$.

c Th contents calculated from radiogenic 208Pb and the 207Pb/206Pb date of the sample, assuming concordance between U-Th and Pb systems.

d Total mass of radiogenic Pb.

e Total mass of common Pb.

f Ratio of radiogenic Pb (including 208Pb) to common Pb.

g Measured ratio corrected for fractionation and spike contribution only.

h Measured ratios corrected for fractionation, tracer and blank.

APPENDIX F

MICROPROBE DATA AND ERROR ANALYSIS

Standards used to produce daily correction values for each oxide						
Standard	A99	PX-1	LCP	JDF	KH	RG
SiO ₂	50.94	53.94	51.25	50.81	40.38	76.72
TiO ₂	4.06	0.26	0.05	1.86	4.72	0.13
Al ₂ O ₃	12.49	0.66	30.91	14.07	14.90	12.07
FeO	13.32	2.93	0.46	11.83	10.93	1.24
MnO	0.15	0.07	0.01	0.22	0.09	0.04
MgO	5.08	16.93	0.14	6.72	12.81	0.00
CaO	9.30	24.55	13.64	11.13	10.31	0.50
Na ₂ O	2.66	0.24	3.45	2.63	2.61	3.76
K ₂ O	0.82	0.00	0.18	0.19	2.05	4.89
Total	98.82	99.58	100.09	99.46	98.80	99.35

Smithsonian standards A-99 and Juan de Fuca glass (JDF) along with natural mineral standards Lake City plagioclase (LCP), PX-1 clinopyroxene, Kakanui hornblende (KH) and rhyolite glass (RG) were measured three times each at the beginning and end of each daily session. The deviation from known values was then used to produce a daily correction value for each oxide.

Plagioclase electron microprobe analyses									
Sample	PT1-4	PT1-4	PT1-4	PT1-4	PT1-4	PT1-4	PT1-5	PT1-5	PT1-5
Unit	Porco	Porco	Porco	Porco	Porco	Porco	Porco	Porco	Porco
Core/Rim	1 core	2 core	3 core	4 rim	5 rim	6 rim	1 core	2 core	3 core
SiO ₂	59.85	59.68	59.53	59.02	58.89	58.91	59.70	59.72	59.41
TiO ₂	0.01	0.04	0.05	0.00	0.00	0.00	0.03	0.08	0.03
Al ₂ O ₃	24.89	24.79	25.21	25.88	25.31	25.27	25.18	25.52	25.22
FeO	0.06	0.00	0.10	0.05	0.06	0.17	0.01	0.10	0.12
MnO	0.03	0.01	0.01	0.01	0.00	0.01	0.01	0.02	0.02
MgO	0.01	0.00	0.00	0.00	0.00	0.00	0.00	0.00	0.02
CaO	6.38	6.44	6.62	7.08	6.45	6.19	5.97	6.32	6.35
Na ₂ O	6.90	6.83	6.67	6.43	7.06	7.03	7.23	7.10	6.85
K ₂ O	0.83	0.81	0.77	0.72	0.85	0.82	0.81	0.77	0.77
Total	98.95	98.60	98.96	99.20	98.61	98.40	98.94	99.62	98.78
An (Ca)	32.29	32.29	34.04	36.17	31.63	30.93	29.90	31.25	32.63
Ab (Na)	62.50	62.50	61.70	59.57	63.27	63.92	64.95	64.58	63.16
Or (K)	5.21	5.21	4.26	4.26	5.10	5.15	5.15	4.17	4.21

Sample	PT1-5	PT1-5	PT1-5	PT3-5	PT3-5	PT3-5	PT3-5	PT3-5	PT3-5
Unit	Porco	Porco	Porco	Porco	Porco	Porco	Porco	Porco	Porco
Core/Rim	4 rim	5 rim	6 rim	1 core	2 core	3 core	4 rim	5 rim	6 rim
SiO ₂	59.71	59.03	58.75	60.72	60.81	60.00	59.27	59.82	57.82
TiO ₂	0.00	0.00	0.00	0.04	0.02	0.00	0.00	0.00	0.05
Al ₂ O ₃	24.62	25.82	25.18	24.78	25.39	27.47	24.29	25.64	27.54
FeO	0.09	0.00	0.03	0.08	0.03	0.03	0.07	0.05	0.21
MnO	0.02	0.02	0.00	0.03	0.05	0.00	0.00	0.03	0.00
MgO	0.00	0.01	0.00	0.00	0.00	0.01	0.00	0.00	0.01
CaO	5.91	6.90	6.73	5.52	6.49	6.38	6.25	6.65	8.74
Na ₂ O	7.22	6.75	6.92	7.09	6.76	6.68	7.04	6.83	5.84
K ₂ O	0.88	0.76	0.79	0.93	0.72	0.64	0.89	0.85	0.51
Total	98.44	99.29	98.40	99.19	100.28	101.21	97.81	99.87	100.72
An (Ca)	29.90	34.38	33.33	27.96	33.33	32.97	31.63	33.33	44.21
Ab (Na)	64.95	61.46	61.62	66.67	62.37	62.64	63.27	61.46	52.63
Or (K)	5.15	4.17	5.05	5.38	4.30	4.40	5.10	5.21	3.16

Plagioclase electron microprobe analyses

Sample	PT3-5	PT3-6	PT3-6						
Unit	Porco								
Core/Rim	7 core	8 core	9 core	10 rim	11 rim	12 rim	13 rim	1 core	2 core
SiO ₂	61.66	61.49	61.17	61.22	61.44	61.33	61.19	61.09	60.61
TiO ₂	0.01	0.00	0.01	0.02	0.00	0.00	0.03	0.00	0.07
Al ₂ O ₃	24.58	23.15	25.68	25.22	25.15	25.22	25.10	25.02	24.91
FeO	0.00	0.14	0.06	0.00	0.13	0.03	0.10	0.02	0.03
MnO	0.00	0.00	0.00	0.01	0.02	0.00	0.00	0.00	0.00
MgO	0.00	0.03	0.00	0.00	0.00	0.00	0.00	0.00	0.00
CaO	5.93	4.35	6.60	6.54	6.38	6.41	6.42	6.45	6.51
Na ₂ O	7.38	7.97	7.07	7.23	7.27	7.31	7.05	7.34	7.18
K ₂ O	0.83	0.65	0.68	0.76	0.81	0.78	0.71	0.75	0.72
Total	100.37	97.79	101.27	101.00	101.19	101.07	100.60	100.66	100.03
An (Ca)	29.2	22.1	32.6	32.0	30.9	31.3	31.9	31.6	32.0
Ab (Na)	65.6	73.7	63.2	63.9	63.9	64.6	63.8	64.3	63.9
Or (K)	5.2	4.2	4.2	4.1	5.2	4.2	4.3	4.1	4.1

Sample	PT3-6	PT3-6	PT3-6	PT11p-7	PT11p-7	PT11p-7	PT11p-6	PT11p-6
Unit	Porco	Porco	Porco	Frailes	Frailes	Frailes	Frailes	Frailes
Core/Rim	3 rim	4 rim	5 rim	1 core	2 rim	3 rim	1 core	2 rim
SiO ₂	60.85	60.89	60.83	57.99	58.46	58.58	58.62	58.49
TiO ₂	0.03	0.00	0.00	0.00	0.00	0.00	0.00	0.03
Al ₂ O ₃	25.04	25.07	25.12	26.70	27.52	27.28	27.30	26.47
FeO	0.09	0.05	0.02	0.09	0.05	0.12	0.02	0.02
MnO	0.00	0.01	0.00	0.00	0.01	0.01	0.00	0.01
MgO	0.01	0.00	0.00	0.00	0.01	0.01	0.01	0.01
CaO	6.55	6.55	6.21	8.50	8.76	8.64	8.56	8.20
Na ₂ O	7.22	7.04	7.44	5.80	5.80	5.81	5.81	6.00
K ₂ O	0.74	0.77	0.76	0.60	0.53	0.52	0.57	0.62
Total	100.54	100.39	100.39	99.68	101.13	100.96	100.89	99.86
An (Ca)	32.0	32.3	30.6	43.62	43.62	43.62	43.62	41.05
Ab (Na)	63.9	63.5	65.3	53.19	53.19	53.19	53.19	54.74
Or (K)	4.1	4.2	4.1	3.19	3.19	3.19	3.19	4.21

Sample	PT11p-6						
Unit	Frailes						
Core/Rim	3 rim	4 rim	5 core	6 core	7 core	8 core	9 rim
SiO ₂	57.85	58.93	58.36	58.38	58.77	58.06	58.52
TiO ₂	0.02	0.00	0.00	0.02	0.01	0.03	0.00
Al ₂ O ₃	27.45	26.41	26.95	26.69	26.53	27.05	27.00
FeO	0.09	0.10	0.08	0.12	0.14	0.13	0.09
MnO	0.00	0.00	0.03	0.02	0.01	0.01	0.02
MgO	0.00	0.00	0.00	0.00	0.00	0.00	0.01
CaO	8.89	7.60	8.59	8.57	8.30	8.79	8.75
Na ₂ O	5.66	5.99	6.12	6.26	6.23	5.99	6.31
K ₂ O	0.55	0.68	0.54	0.56	0.58	0.55	0.53
Total	100.49	99.71	100.68	100.62	100.57	100.60	101.21
An (Ca)	44.68	39.13	42.3	41.8	41.2	43.3	42.4
Ab (Na)	52.13	56.52	54.6	55.1	55.7	53.6	54.5
Or (K)	3.19	4.35	3.1	3.1	3.1	3.1	3.0

Plagioclase electron microprobe analyses								
Sample	PT11p-6	PT11p-6	PT11p-6	PT11p-6	PT14-2	PT14-2	PT14-2	PT14-2
Unit	Frailles	Frailles	Frailles	Frailles	Livic	Livic	Livic	Livic
Core/Rim	10 rim	11 rim	12 rim	13 rim	1 core	2 core	3 core	4 rim
SiO ₂	59.00	59.05	58.42	58.99	59.16	57.03	58.36	57.06
TiO ₂	0.03	0.00	0.00	0.03	0.00	0.07	0.00	0.00
Al ₂ O ₃	26.81	26.52	26.63	25.95	26.15	27.79	26.32	27.61
FeO	0.07	0.05	0.11	0.10	0.08	0.01	0.04	0.03
MnO	0.00	0.02	0.03	0.00	0.03	0.00	0.00	0.03
MgO	0.01	0.00	0.00	0.01	0.00	0.00	0.01	0.00
CaO	8.11	8.05	8.23	7.50	7.63	9.40	7.50	8.80
Na ₂ O	6.46	6.41	6.41	6.92	6.72	5.87	6.68	6.05
K ₂ O	0.57	0.60	0.57	0.62	0.49	0.34	0.48	0.39
Total	101.07	100.70	100.39	100.11	100.25	100.51	99.38	99.98
An (Ca)	39.6	39.6	40.2	36.0	37.11	45.92	37.11	43.30
Ab (Na)	57.3	57.3	56.7	60.0	59.79	52.04	59.79	54.64
Or (K)	3.1	3.1	3.1	4.0	3.09	2.04	3.09	2.06

Sample	PT14-2	PT14-2	PT14-2	PT14-2	PT16-2	PT16-2	PT16-2	PT16-3
Unit	Livic	Livic	Livic	Livic	Frailles	Frailles	Frailles	Frailles
Core/Rim	5 rim	6 core	7 rim	8 rim	1 core	2 rim	3 rim	1 core
SiO ₂	58.64	56.79	57.15	58.17	57.82	58.95	59.02	55.43
TiO ₂	0.00	0.00	0.04	0.03	0.00	0.00	0.01	0.00
Al ₂ O ₃	26.18	27.88	27.35	26.19	27.14	26.21	25.64	26.67
FeO	0.01	0.14	0.03	0.07	0.02	0.04	0.13	0.09
MnO	0.02	0.00	0.00	0.00	0.05	0.00	0.02	0.00
MgO	0.00	0.00	0.00	0.00	0.00	0.00	0.00	0.00
CaO	7.19	9.61	9.01	7.87	8.74	7.67	7.53	8.44
Na ₂ O	6.79	5.59	5.69	6.20	6.00	6.34	6.41	5.72
K ₂ O	0.52	0.45	0.50	0.65	0.49	0.64	0.62	0.47
Total	99.36	100.45	99.77	99.18	100.25	99.86	99.38	96.82
An (Ca)	36.08	47.42	45.26	39.58	43.30	38.54	37.50	43.75
Ab (Na)	60.82	49.48	51.58	56.25	53.61	57.29	58.33	53.13
Or (K)	3.09	3.09	3.16	4.17	3.09	4.17	4.17	3.13

Sample	PT16-3							
Unit	Frailles							
Core/Rim	2 rim	3 rim	4 rim	5 core	6 rim	7 core	8 core	8 core
SiO ₂	56.95	55.79	54.76	52.01	54.16	58.01	57.60	57.60
TiO ₂	0.02	0.00	0.00	0.01	0.02	0.02	0.00	0.00
Al ₂ O ₃	25.54	25.95	26.77	31.09	28.86	26.97	27.67	27.67
FeO	0.03	0.03	0.05	0.09	0.12	0.00	0.05	0.05
MnO	0.00	0.00	0.02	0.00	0.00	0.01	0.01	0.01
MgO	0.00	0.00	0.00	0.02	0.04	0.00	0.00	0.00
CaO	7.60	7.89	8.67	12.85	10.36	8.62	9.40	9.40
Na ₂ O	6.18	5.90	5.47	3.51	4.33	6.09	5.78	5.78
K ₂ O	0.56	0.51	0.43	0.20	0.30	0.51	0.44	0.44
Total	96.88	96.07	96.16	99.79	98.19	100.22	100.95	100.95
An (Ca)	39.58	41.05	45.26	65.96	56.04	42.3	45.9	45.9
Ab (Na)	57.29	55.79	51.58	32.98	41.76	54.6	51.0	51.0
Or (K)	3.13	3.16	3.16	1.06	2.20	3.1	3.1	3.1

Plagioclase electron microprobe analyses

Sample	PT16-3	PT16-3	PT16-3	PT16-3	PT16-3	PT16-3	PT16-3.2	PT16-3.2
Unit	Frailles							
Core/Rim	9 core	10 core	11 core	12 core	13 core	14 core	1 core	2 rim
SiO ₂	58.20	57.08	58.67	58.69	57.89	60.80	57.18	56.78
TiO ₂	0.01	0.00	0.04	0.00	0.00	0.00	0.00	0.00
Al ₂ O ₃	27.07	27.94	27.20	26.79	27.18	25.49	26.61	26.89
FeO	0.05	0.04	0.09	0.07	0.12	0.08	0.03	0.01
MnO	0.02	0.01	0.00	0.01	0.00	0.00	0.01	0.03
MgO	0.00	0.01	0.00	0.01	0.00	0.00	0.01	0.00
CaO	8.73	9.65	8.60	8.54	8.96	6.72	8.13	8.69
Na ₂ O	6.06	5.58	6.04	5.92	5.92	6.88	6.15	5.79
K ₂ O	0.53	0.41	0.51	0.56	0.49	0.79	0.45	0.41
Total	100.67	100.71	101.15	100.58	100.56	100.75	98.56	98.59
An (Ca)	43.3	47.9	42.7	43.2	44.3	33.7	41.24	44.21
Ab (Na)	53.6	50.0	54.2	53.7	52.6	62.1	55.67	53.68
Or (K)	3.1	2.1	3.1	3.2	3.1	4.2	3.09	2.11

Sample	PT16-3.2	PT16-3.2
Unit	Frailles	Frailles
Core/Rim	3 core	4 rim
SiO ₂	54.38	54.94
TiO ₂	0.06	0.00
Al ₂ O ₃	28.55	27.77
FeO	0.05	0.08
MnO	0.01	0.01
MgO	0.00	0.00
CaO	10.25	9.56
Na ₂ O	5.03	5.38
K ₂ O	0.31	0.34
Total	98.64	98.08
An (Ca)	51.55	48.45
Ab (Na)	46.39	49.48
Or (K)	2.06	2.06

Biotite electron microprobe analyses

Sample	PT1-3	PT1-3	PT1-3	PT1-3	PT1-3	PT1-3	PT1-6	PT1-6	PT1-6
Unit	Porco	Porco	Porco	Porco	Porco	Porco	Porco	Porco	Porco
Core/Rim	1 core	2 core	3 core	4 rim	5 rim	6 rim	1 core	2 core	3 core
SiO ₂	35.58	35.70	35.67	36.46	36.07	36.20	35.93	35.76	35.88
TiO ₂	4.37	4.53	4.42	4.42	4.64	4.47	4.14	4.49	4.41
Al ₂ O ₃	17.12	16.91	17.39	17.21	17.35	17.13	17.51	17.31	17.77
FeO	20.88	20.50	20.87	20.75	21.05	20.44	19.98	20.78	21.32
MnO	0.14	0.09	0.10	0.09	0.10	0.11	0.09	0.14	0.09
MgO	9.83	9.99	9.76	9.44	9.67	9.40	9.33	9.39	9.75
CaO	0.00	0.00	0.00	0.01	0.00	0.05	0.03	0.04	0.04
Na ₂ O	0.53	0.59	0.50	0.63	0.65	0.60	0.43	0.41	0.43
K ₂ O	8.81	8.86	8.62	8.62	8.64	8.55	8.45	8.62	8.85
Total	97.25	97.17	97.33	97.62	98.18	96.94	95.88	96.94	98.54

Biotite electron microprobe analyses									
Sample	PT1-6	PT1-6	PT3-4	PT3-4	PT3-4	PT3-4	PT3-4	PT3-4	PT3-4
Unit	Porco	Porco	Porco	Porco	Porco	Porco	Porco	Porco	Porco
Core/Rim	4 rim	5 rim	1 core	2 core	3 core	4 rim	5 rim	6 rim	7 rim
SiO ₂	36.40	36.17	35.83	35.51	36.05	36.06	35.61	36.43	36.31
TiO ₂	4.39	4.41	4.18	4.06	4.38	4.13	4.83	4.24	4.58
Al ₂ O ₃	17.66	17.56	17.51	17.54	17.50	17.37	17.55	17.52	17.23
FeO	19.70	19.79	21.83	21.63	21.78	20.66	21.75	20.22	18.53
MnO	0.10	0.10	0.12	0.12	0.08	0.12	0.12	0.13	0.08
MgO	9.21	9.05	9.59	9.71	9.80	11.03	9.74	10.73	11.42
CaO	0.07	0.10	0.02	0.03	0.03	0.07	0.04	0.02	0.04
Na ₂ O	0.44	0.47	0.47	0.44	0.51	0.45	0.45	0.45	0.47
K ₂ O	8.38	8.35	8.94	8.47	8.89	8.57	8.53	8.92	8.93
Total	96.34	96.00	98.51	97.52	99.00	98.47	98.63	98.66	97.60

Sample	PT3-4.2	PT3-4.2	PT3-4.2	PT3-4.2	PT3-4.2	PT3-4.2	PT3-5	PT3-5	PT3-5
Unit	Porco	Porco	Porco	Porco	Porco	Porco	Porco	Porco	Porco
Core/Rim	1 core	2 core	3 core	4 rim	5 rim	6 rim	1 core	2 core	3 core
SiO ₂	36.25	35.84	35.85	36.19	34.86	35.41	35.79	36.41	36.13
TiO ₂	4.26	4.14	4.28	4.10	4.14	4.14	4.35	4.44	4.30
Al ₂ O ₃	17.87	17.79	17.79	17.56	17.36	17.39	17.25	17.57	17.44
FeO	21.67	22.47	22.24	21.55	23.12	24.51	22.13	21.49	22.31
MnO	0.11	0.11	0.10	0.09	0.11	0.14	0.09	0.13	0.14
MgO	9.80	9.74	9.85	9.64	10.13	9.18	9.70	9.83	9.82
CaO	0.02	0.03	0.02	0.01	0.03	0.01	0.01	0.05	0.03
Na ₂ O	0.46	0.48	0.46	0.44	0.44	0.46	0.46	0.48	0.45
K ₂ O	9.01	8.72	8.73	8.78	8.59	8.56	8.94	8.99	8.66
Total	99.45	99.31	99.33	98.37	98.78	99.80	98.71	99.38	99.27

Sample	PT3-5	PT3-5	PT3-5	PT8-2	PT8-2	PT11p-1	PT11p-1	PT11p-1
Unit	Porco	Porco	Porco	Frailles	Frailles	Frailles	Frailles	Frailles
Core/Rim	4 rim	5 rim	6 rim	1 rim	2 rim	1 core	2 rim	3 rim
SiO ₂	35.91	36.41	36.05	35.66	36.81	35.79	36.05	36.99
TiO ₂	4.32	4.36	4.53	3.80	3.96	4.33	4.46	4.26
Al ₂ O ₃	17.54	17.68	17.61	18.02	18.59	17.64	17.62	17.85
FeO	21.67	21.72	20.32	19.12	18.47	19.43	19.48	18.80
MnO	0.11	0.11	0.12	0.09	0.13	0.13	0.14	0.12
MgO	10.14	9.51	10.47	9.49	8.91	10.71	10.69	10.34
CaO	0.09	0.00	0.04	0.08	0.09	0.01	0.03	0.00
Na ₂ O	0.44	0.44	0.44	0.25	0.32	0.34	0.31	0.30
K ₂ O	8.48	8.79	8.79	9.23	9.15	9.63	9.60	9.70
Total	98.69	99.02	98.36	95.74	96.43	98.02	98.38	98.35

Biotite electron microprobe analyses									
Sample	PT11p-5	PT11p-5	PT11p-5	PT11p-5.2	PT11p-5.2	PT11p-5.2	PT11p-7	PT11p-7	
Unit	Frailes	Frailes	Frailes	Frailes	Frailes	Frailes	Frailes	Frailes	
Core/Rim	1 core	2 rim	3 rim	1 core	2 rim	3 rim	1 core	2 rim	
SiO ₂	34.91	35.72	35.72	35.52	36.52	35.92	35.41	35.48	
TiO ₂	3.91	4.23	4.22	4.00	3.76	4.04	4.09	4.09	
Al ₂ O ₃	17.14	17.20	17.46	17.31	17.92	17.23	17.29	17.49	
FeO	19.35	19.20	19.63	19.32	18.99	19.91	20.03	19.89	
MnO	0.14	0.17	0.16	0.18	0.14	0.18	0.15	0.18	
MgO	9.90	9.95	10.18	10.23	9.94	10.43	10.28	10.04	
CaO	0.06	0.06	0.06	0.03	0.12	0.05	0.01	0.05	
Na ₂ O	0.32	0.26	0.27	0.31	0.30	0.33	0.33	0.31	
K ₂ O	9.10	9.29	9.41	8.77	8.65	8.72	9.43	9.30	
Total	94.83	96.08	97.10	95.68	96.34	96.80	97.02	96.83	
Sample	PT11p-7	PT11p-7	PT11p-7	PT11p-7	PT14-1	PT14-1	PT14-1	PT14-1	
Unit	Frailes	Frailes	Frailes	Frailes	Livicuc	Livicuc	Livicuc	Livicuc	
Core/Rim	3 rim	4 core	5 rim	6 rim	1 core	2 core	3 core	4 core	
SiO ₂	35.77	35.41	35.48	35.77	33.74	33.40	21.30	30.01	
TiO ₂	4.04	4.09	4.09	4.04	4.61	4.63	2.97	3.96	
Al ₂ O ₃	17.67	17.29	17.49	17.67	27.69	23.27	52.43	29.58	
FeO	20.12	20.03	19.89	20.12	15.73	17.65	9.95	16.46	
MnO	0.13	0.15	0.18	0.13	0.10	0.12	0.08	0.11	
MgO	10.06	10.28	10.04	10.06	9.25	9.80	5.98	8.09	
CaO	0.02	0.01	0.05	0.02	0.25	0.14	0.33	0.17	
Na ₂ O	0.26	0.33	0.31	0.26	0.47	0.37	0.32	0.29	
K ₂ O	9.37	9.43	9.30	9.37	7.40	7.73	4.47	7.57	
Total	97.46	97.02	96.83	97.46	99.24	97.12	97.82	96.24	
Sample	PT14-3	PT14-3	PT14-4	PT14-4	PT14-4	PT14-3	PT16-4	PT16-4	PT16-4
Unit	Livicuc	Livicuc	Livicuc	Livicuc	Livicuc	Livicuc	Frailes	Frailes	Frailes
Core/Rim	1 core	2 rim	3 rim	1 core	2 rim	3 rim	1 core	2 rim	3 rim
SiO ₂	35.85	36.21	35.15	35.79	36.17	35.83	35.36	35.47	35.14
TiO ₂	4.06	4.05	4.17	4.21	3.95	4.17	3.46	3.53	3.61
Al ₂ O ₃	17.61	18.01	17.08	17.47	18.10	17.63	17.30	17.53	17.02
FeO	18.53	18.15	18.71	19.34	19.07	20.35	17.72	16.79	17.07
MnO	0.14	0.17	0.13	0.16	0.14	0.17	0.16	0.12	0.15
MgO	10.05	9.78	9.81	10.16	10.14	10.58	10.05	9.50	9.78
CaO	0.03	0.07	0.08	0.01	0.03	0.02	0.00	0.09	0.05
Na ₂ O	0.25	0.28	0.20	0.30	0.26	0.26	0.32	0.32	0.31
K ₂ O	8.69	8.90	8.76	8.88	8.99	9.00	8.64	8.29	8.64
Total	95.21	95.63	94.09	96.31	96.86	98.02	93.01	91.64	91.77

Biotite electron microprobe analyses						
Sample	PT16-5	PT16-5	PT16-5	PT16-5.2	PT16-5.2	PT16-5.2
Unit	Frailes	Frailes	Frailes	Frailes	Frailes	Frailes
Core/Rim	1 core	2 rim	3 rim	4 core	5 rim	6 rim
SiO ₂	34.83	34.59	34.82	35.96	35.62	35.51
TiO ₂	3.67	3.56	3.82	3.79	3.87	4.13
Al ₂ O ₃	17.59	17.56	17.79	17.05	16.89	16.75
FeO	17.46	17.31	17.48	17.94	18.38	18.57
MnO	0.17	0.12	0.16	0.13	0.15	0.11
MgO	9.88	9.59	9.55	9.34	9.90	9.70
CaO	0.04	0.05	0.09	0.05	0.03	0.01
Na ₂ O	0.25	0.31	0.32	0.30	0.36	0.29
K ₂ O	8.70	8.53	8.44	8.03	8.22	7.99
Total	92.59	91.63	92.46	92.60	93.43	93.08

Sanidine electron microprobe analyses									
Sample	PT1-1	PT1-1	PT1-1	PT1-1	PT1-1	PT1-1	PT1-1	PT1-1	PT1-1
Unit	Porco	Porco	Porco	Porco	Porco	Porco	Porco	Porco	Porco
Core/Rim	1 core	2 core	3 rim	4 core	5 rim	6 rim	7 rim	8 core	9 core
SiO ₂	63.78	62.73	62.64	63.78	62.32	62.59	62.97	66.13	66.14
TiO ₂	0.00	0.03	0.05	0.00	0.03	0.05	0.04	0.00	0.00
Al ₂ O ₃	18.86	18.95	18.93	18.86	18.76	19.21	18.84	18.88	19.03
FeO	0.00	0.09	0.11	0.00	0.10	0.00	0.08	0.04	0.07
MnO	0.03	0.00	0.01	0.03	0.00	0.05	0.08	0.01	0.01
MgO	0.00	0.00	0.00	0.00	0.00	0.00	0.00	0.00	0.00
CaO	0.11	0.18	0.10	0.11	0.17	0.10	0.14	0.15	0.13
Na ₂ O	2.42	2.45	2.47	2.42	2.70	2.43	2.39	2.47	2.50
K ₂ O	12.56	12.67	12.58	12.56	12.25	12.75	12.71	12.31	12.25
Total	97.76	97.10	96.89	97.76	96.33	97.19	97.24	100.00	100.12
An (Ca)	1.02	1.01	0.00	1.02	1.00	1.00	1.01	1.06	1.06
Ab (Na)	22.45	22.22	23.23	22.45	25.00	22.00	22.22	23.40	23.40
Or (K)	76.53	76.77	76.77	76.53	74.00	77.00	76.77	75.53	75.53

Sample	PT1-1	PT1-2	PT1-2	PT1-2	PT1-2	PT1-2	PT1-2	PT1-4	PT1-4
Unit	Porco	Porco	Porco	Porco	Porco	Porco	Porco	Porco	Porco
Core/Rim	10 rim	1 core	2 core	3 core	4 rim	5 rim	6 rim	1 core	2 core
SiO ₂	65.68	63.88	63.80	64.19	63.68	63.98	64.98	63.88	63.80
TiO ₂	0.00	0.02	0.05	0.01	0.00	0.00	0.00	0.02	0.05
Al ₂ O ₃	19.14	19.26	19.10	18.80	18.77	18.74	19.45	19.26	19.10
FeO	0.04	0.00	0.10	0.00	0.21	0.05	0.11	0.00	0.10
MnO	0.00	0.00	0.01	0.00	0.00	0.00	0.01	0.00	0.01
MgO	0.00	0.00	0.00	0.00	0.00	0.00	0.00	0.00	0.00
CaO	0.11	0.18	0.19	0.12	0.06	0.19	0.10	0.18	0.19
Na ₂ O	2.48	2.35	2.41	2.31	2.56	2.41	2.50	2.35	2.41
K ₂ O	12.32	12.96	12.92	12.98	12.71	12.81	12.57	12.96	12.92
Total	99.77	98.66	98.57	98.42	97.99	98.18	99.71	98.66	98.57
An (Ca)	1.05	1.01	1.00	1.01	0.00	1.01	0.00	1.01	1.00
Ab (Na)	23.16	21.21	22.00	21.21	23.23	22.22	23.16	21.21	22.00
Or (K)	75.79	77.78	77.00	77.78	76.77	76.77	76.84	77.78	77.00

Sanidine electron microprobe analyses

Sample	PT1-4	PT1-4	PT1-4	PT1-4	PT3-7	PT3-7	PT3-7	PT3-7	PT3-7
Unit	Porco	Porco	Porco	Porco	Porco	Porco	Porco	Porco	Porco
Core/Rim	3 core	4 rim	5 rim	6 core	1 core	2 core	3 core	4 rim	5 rim
SiO ₂	64.19	63.68	63.98	64.98	65.79	65.62	65.86	65.68	65.54
TiO ₂	0.01	0.00	0.00	0.00	0.05	0.00	0.02	0.03	0.00
Al ₂ O ₃	18.80	18.77	18.74	19.45	19.22	19.06	19.43	19.30	19.39
FeO	0.00	0.21	0.05	0.11	0.04	0.08	0.00	0.03	0.00
MnO	0.00	0.00	0.00	0.01	0.00	0.00	0.00	0.02	0.01
MgO	0.00	0.00	0.00	0.00	0.00	0.00	0.00	0.00	0.00
CaO	0.12	0.06	0.19	0.10	0.17	0.17	0.21	0.22	0.21
Na ₂ O	2.31	2.56	2.41	2.50	2.32	2.28	2.34	2.24	2.22
K ₂ O	12.98	12.71	12.81	12.57	12.56	12.55	12.47	12.53	12.71
Total	98.42	97.99	98.18	99.71	100.15	99.77	100.33	100.06	100.08
An (Ca)	1.01	0.00	1.01	0.00	1.1	1.1	1.1	1.1	1.1
Ab (Na)	21.21	23.23	22.22	23.16	21.3	21.3	22.3	21.3	21.1
Or (K)	77.78	76.77	76.77	76.84	77.7	77.7	76.6	77.7	77.9

Sample	PT3-7	PT11p-3	PT11p-3	PT11p-3	PT11p-5	PT11p-5	PT11p-5	PT14-2
Unit	Porco	Frailles	Frailles	Frailles	Frailles	Frailles	Frailles	Livicu
Core/Rim	6 rim	1 core	2 rim	3 rim	1 core	2 rim	3 rim	1 core
SiO ₂	65.69	65.77	65.75	65.08	65.69	65.51	65.30	65.24
TiO ₂	0.00	0.04	0.00	0.00	0.00	0.02	0.05	0.03
Al ₂ O ₃	19.25	19.39	19.10	19.20	19.26	18.96	19.01	18.82
FeO	0.07	0.04	0.05	0.06	0.10	0.02	0.01	0.00
MnO	0.02	0.00	0.02	0.00	0.02	0.00	0.00	0.00
MgO	0.00	0.00	0.00	0.00	0.00	0.00	0.00	0.00
CaO	0.22	0.14	0.09	0.14	0.15	0.14	0.15	0.12
Na ₂ O	2.21	1.83	1.85	1.93	1.80	2.04	1.88	2.00
K ₂ O	12.61	13.72	13.79	13.62	13.67	13.50	13.74	13.06
Total	100.07	100.94	100.65	100.03	100.69	100.19	100.14	99.26
An (Ca)	1.1	1.04	0.00	1.03	1.04	1.02	1.02	1.05
Ab (Na)	20.4	16.67	16.67	17.53	16.67	18.37	17.35	18.95
Or (K)	78.5	82.29	83.33	81.44	82.29	80.61	81.63	80.00

Sample	PT14-2	PT14-2	PT14-3	PT14-3	PT14-3	PT16-1	PT16-1	PT16-1	PT16-2
Unit	Livicu	Livicu	Livicu	Livicu	Livicu	Frailles	Frailles	Frailles	Frailles
Core/Rim	2 rim	3 rim	1 core	2 rim	3 rim	1 core	2 rim	3 core	1 core
SiO ₂	65.07	65.24	64.16	64.57	65.09	65.30	64.85	63.71	63.13
TiO ₂	0.00	0.00	0.00	0.00	0.01	0.00	0.00	0.03	0.03
Al ₂ O ₃	19.01	19.12	19.03	18.66	18.99	18.98	19.23	19.16	18.79
FeO	0.07	0.05	0.03	0.00	0.02	0.01	0.04	0.10	0.04
MnO	0.00	0.00	0.00	0.01	0.01	0.01	0.00	0.00	0.00
MgO	0.00	0.00	0.00	0.00	0.00	0.00	0.00	0.00	0.00
CaO	0.15	0.16	0.10	0.11	0.10	0.10	0.12	0.13	0.17
Na ₂ O	2.01	2.23	2.11	1.89	1.93	2.03	2.18	2.04	1.96
K ₂ O	12.82	12.64	12.98	13.13	13.20	13.18	13.07	12.78	12.28
Total	99.13	99.44	98.41	98.38	99.35	99.61	99.49	97.96	96.41
An (Ca)	1.06	1.05	1.03	1.04	1.05	1.04	1.03	1.05	1.08
Ab (Na)	19.15	21.05	19.59	17.71	17.89	18.75	19.59	18.95	19.35
Or (K)	79.79	77.89	79.38	81.25	81.05	80.21	79.38	80.00	79.57

Sanidine electron microprobe analyses

Sample	PT16-2	PT16-6	PT16-6
Unit	Frailes	Frailes	Frailes
Core/Rim	2 rim	1 core	2 rim
SiO ₂	63.13	63.60	63.55
TiO ₂	0.06	0.05	0.00
Al ₂ O ₃	18.58	18.91	18.91
FeO	0.09	0.02	0.07
MnO	0.00	0.04	0.00
MgO	0.00	0.00	0.00
CaO	0.19	0.12	0.14
Na ₂ O	2.01	1.95	2.02
K ₂ O	12.04	12.79	12.52
Total	96.11	97.48	97.22
An (Ca)	1.09	1.05	1.1
Ab (Na)	19.57	18.95	19.1
Or (K)	79.35	80.00	79.8

Ilmenite electron microprobe analyses

Sample	PT1-1	PT1-1	PT1-1	PT11p-1	PT11p-1	PT11p-1	PT11p-1	PT11p-1
Unit	Porco	Porco	Porco	Frailes	Frailes	Frailes	Frailes	Frailes
Core/Rim	1 core	2 rim	3 rim	1 core	2 rim	3 core	4 core	5 core
SiO ₂	0.14	0.19	0.20	0.01	0.06	0.05	0.04	0.01
TiO ₂	56.37	57.27	56.24	36.08	35.70	36.05	35.87	35.73
Al ₂ O ₃	0.12	0.12	0.13	0.39	0.41	0.44	0.42	0.40
FeO	37.26	34.58	35.03	62.78	61.86	61.87	62.23	63.32
MnO	0.64	0.68	0.69	0.46	0.42	0.40	0.46	0.42
MgO	0.41	0.63	0.38	0.76	0.78	0.70	0.73	0.71
CaO	0.00	0.03	0.03	0.00	0.00	0.00	0.00	0.00
Na ₂ O	0.06	0.02	0.01	0.00	0.00	0.00	0.01	0.00
K ₂ O	0.00	0.01	0.00	0.00	0.01	0.00	0.00	0.00
Total	95.00	93.52	92.71	100.48	99.24	99.51	99.75	100.60

Sample	PT11p-1	PT14-1	PT14-1	PT14-1	PT16-1	PT16-1	PT16-2	PT16-2
Unit	Frailes	Livcuc	Livcuc	Livcuc	Frailes	Frailes	Frailes	Frailes
Core/Rim	6 rim	1 core	2 core	3 core	1 core	2 rim	1 core	2 rim
SiO ₂	0.10	0.02	0.11	0.07	0.00	0.00	0.05	0.07
TiO ₂	35.97	53.10	54.52	53.95	36.16	36.35	34.54	34.85
Al ₂ O ₃	0.42	0.44	0.69	0.41	0.41	0.45	0.47	0.40
FeO	62.06	44.85	43.03	40.68	62.17	61.58	63.30	63.62
MnO	0.39	0.61	0.55	1.23	0.61	0.63	0.47	0.52
MgO	0.72	2.18	1.96	2.20	0.86	0.88	0.73	0.75
CaO	0.00	0.00	0.00	0.00	0.00	0.00	0.00	0.00
Na ₂ O	0.02	0.00	0.00	0.00	0.00	0.03	0.00	0.00
K ₂ O	0.01	0.00	0.03	0.00	0.00	0.00	0.00	0.01
Total	99.69	101.20	100.87	98.53	100.21	99.93	99.55	100.23

Ilmenite electron microprobe analyses

Sample	PT16-3	PT16-3	PT16-3	PT16-3
Unit	Frailes	Frailes	Frailes	Frailes
Core/Rim	1 core	2 core	3 rim	4 rim
SiO ₂	0.02	0.03	0.00	0.00
TiO ₂	35.64	35.58	35.74	35.72
Al ₂ O ₃	0.41	0.38	0.42	0.43
FeO	62.72	62.51	63.11	62.31
MnO	0.50	0.51	0.52	0.51
MgO	0.75	0.71	0.77	0.77
CaO	0.00	0.00	0.00	0.00
Na ₂ O	0.03	0.01	0.05	0.00
K ₂ O	0.00	0.00	0.00	0.00
Total	100.06	99.72	100.61	99.74

APPENDIX G

^{40}Ar - ^{39}Ar DATA AND ERROR ANALYSIS

Sample: PT8

File	Laser power (%)	^{40}Ar (moles)	^{40}Ar (Volts)	$\pm 1\sigma_{40}$ (Volts)	^{39}Ar (Volts)	$\pm 1\sigma_{39}$ (Volts)	^{38}Ar (Volts)	$\pm 1\sigma_{38}$ (Volts)
BI7586	40	8.657E-16	0.146686	0.000198	0.204244	0.000254	0.002404	0.000066
BI7587	40	1.208E-15	0.204601	0.000245	0.216373	0.000275	0.002591	0.000030
BI7589	40	1.168E-15	0.197969	0.000229	0.251807	0.000324	0.002895	0.000057
BI7590	40	9.963E-16	0.168807	0.000347	0.187690	0.000203	0.002146	0.000045
BI7592	40	6.679E-16	0.113172	0.000181	0.149779	0.000242	0.001653	0.000061
BI7593	40	1.077E-15	0.182541	0.000163	0.221981	0.000242	0.002705	0.000050
BI7617	40	7.790E-16	0.131989	0.000482	0.175042	0.000349	0.002136	0.000076
BI7618	40	4.698E-16	0.079595	0.000457	0.093069	0.000255	0.001142	0.000034
BI7620	40	5.336E-16	0.090407	0.000536	0.125157	0.000315	0.001502	0.000066
BI7621	40	1.278E-15	0.216495	0.000481	0.258838	0.000331	0.002980	0.000045
BI7623	40	2.030E-15	0.343893	0.000523	0.484830	0.000500	0.005856	0.000068
BI7624	40	1.950E-15	0.330453	0.000540	0.429908	0.000484	0.005183	0.000115

Sample: PT11

BI7595	40	6.694E-16	0.113416	0.000285	0.134720	0.000429	0.001648	0.000049
BI7596	40	5.560E-16	0.094198	0.000295	0.114631	0.000260	0.001323	0.000060
BI7598	40	5.183E-16	0.087823	0.000299	0.103315	0.000229	0.001227	0.000036
BI7599	40	8.158E-16	0.138230	0.000344	0.140377	0.000262		0.000029
BI7601	40	6.591E-16	0.111681	0.000333	0.115571	0.000280	0.001224	0.000037
BI7602	40	6.559E-16	0.111128	0.000307	0.137439	0.000213	0.001634	0.000066
BI7626	40	9.627E-16	0.163109	0.000600	0.186625	0.000546	0.002271	0.000032
BI7627	40	7.208E-16	0.122133	0.000556	0.113543	0.000312	0.001354	0.000049
BI7629	40	8.453E-16	0.143228	0.000509	0.153628	0.000205	0.001886	0.000052
BI7630	40	8.192E-16	0.138799	0.000523	0.170087	0.000225	0.002072	0.000044

The values in this table represent blank, discrimination, and decay (^{37}Ar and ^{39}Ar) corrected values.

Atmospheric argon ratios

$^{40}\text{Ar}/^{36}\text{Ar}$	295.5 ± 0.5	Steiger & Jäger (1977)
$^{38}\text{Ar}/^{36}\text{Ar}$	0.1880 ± 0.0003	Nier (1950)

Interfering isotope production ratios

$(^{40}\text{Ar}/^{39}\text{Ar})_{\text{K}}$	$(5.4 \pm 1.4) \times 10^{-4}$	Jicha & Brown (2013)
$(^{38}\text{Ar}/^{39}\text{Ar})_{\text{K}}$	$(1.210 \pm 0.002) \times 10^{-2}$	Jicha & Brown (2013)
$(^{39}\text{Ar}/^{37}\text{Ar})_{\text{Ca}}$	$(6.95 \pm 0.09) \times 10^{-4}$	Renne et al. (2013)
$(^{38}\text{Ar}/^{37}\text{Ar})_{\text{Ca}}$	$(1.96 \pm 0.08) \times 10^{-5}$	Renne et al. (2013)
$(^{36}\text{Ar}/^{37}\text{Ar})_{\text{Ca}}$	$(2.65 \pm 0.022) \times 10^{-4}$	Renne et al. (2013)

³⁷ Ar (Volts)	± 1σ ₃₇ (Volts)	³⁶ Ar (Volts)	± 1σ ₃₆ (Volts)	% ⁴⁰ Ar*	⁴⁰ Ar*/ ³⁹ Ar _K	± 2σ	Age ± 2σ (ka) (ka)	K/Ca	Comment
0.011182	0.000349	0.000038	0.000010	92.93	0.667421	0.02926	1526 ± 67	7.85	
0.003022	0.000225	0.000149	0.000010	78.60	0.743278	0.02710	1699 ± 62	30.79	xenocryst
0.003119	0.000175	0.000104	0.000010	84.47	0.664120	0.02284	1518 ± 52	34.71	
0.002273	0.000192	0.000150	0.000010	73.77	0.663485	0.03066	1517 ± 70	35.51	
0.001013	0.000155	0.000040	0.000010	89.51	0.676334	0.03891	1546 ± 89	63.58	
0.003718	0.000210	0.000114	0.000010	81.69	0.671800	0.02650	1536 ± 61	25.67	
0.002068	0.000162	0.000061	0.000008	86.29	0.650650	0.02917	1487 ± 67	36.40	
0.000760	0.000160	0.000062	0.000009	76.90	0.657658	0.05581	1503 ± 128	52.69	
0.001984	0.000162	0.000022	0.000008	92.94	0.671375	0.04036	1535 ± 92	27.12	
0.001397	0.000171	0.000160	0.000009	78.14	0.653556	0.02090	1494 ± 48	79.66	
0.003785	0.000216	0.000071	0.000009	93.88	0.665928	0.01107	1522 ± 25	55.07	
0.004169	0.000164	0.000147	0.000009	86.85	0.667604	0.01224	1526 ± 28	44.34	
MSWD = 0.32				weighted mean (11 of 12):		1520 ± 14			
0.001224	0.000129	0.000038	0.000007	90.00	0.757714	0.03252	1547 ± 66	47.32	
0.001186	0.000147	0.000022	0.000007	93.23	0.766089	0.03664	1564 ± 75	41.54	
0.000820	0.000128	0.000036	0.000007	87.74	0.745813	0.04095	1523 ± 84	54.15	
0.000838	0.000147	0.000113	0.000008	75.75	0.745936	0.03325	1523 ± 68	72.07	
0.000653	0.000148	0.000092	0.000008	75.64	0.730979	0.03942	1493 ± 80	76.16	
0.001712	0.000165	0.000032	0.000007	91.50	0.739869	0.03056	1511 ± 62	34.51	
0.001265	0.000180	0.000083	0.000008	84.91	0.742117	0.02587	1515 ± 53	63.43	
0.001042	0.000170	0.000125	0.000007	69.77	0.750511	0.03907	1533 ± 80	46.85	
0.001496	0.000170	0.000102	0.000008	79.08	0.737300	0.03241	1506 ± 66	44.15	
0.005160	0.000211	0.000042	0.000008	91.19	0.744205	0.02743	1520 ± 56	14.17	
MSWD = 0.32				weighted mean (10 of 10):		1522 ± 21			

Decay constants

λ_{40Ar}	(0.580 ± 0.014) × 10 ⁻¹⁰ a ⁻¹	Min et al. (2000)			
λ_{B^-}	(4.884 ± 0.099) × 10 ⁻¹⁰ a ⁻¹	Min et al. (2000)			
³⁹ Ar	(2.58 ± 0.03) × 10 ⁻³ a ⁻¹	Stoener et al. (1965)			
³⁷ Ar	(5.4300 ± 0.0063) × 10 ⁻² a ⁻¹	Renne & Norman (2001)			
³⁶ Cl λ_B	(2.35 ± 0.02) × 10 ⁻⁶ a ⁻¹	Endt (1998)			
PT8	J-value: 0.0012492 ± 0.000001 (1σ)	D/amu: 1.00720 ± 0.00050 (1σ)			
PT11	J-value: 0.0011160 ± 0.000001 (1σ)	D/amu: 1.00720 ± 0.00050 (1σ)			

REFERENCES

- Asch, G., Schurr, B., Bohm, M., Yuan, X., Haerland, C., Heit, B., Kind, R., Woelbern, I., Bataille, K., Comte, D., Pardo, M., Viramonte, J., Rietbrock, A., Geisse, P., 2006, Seismological studies of the Central and Southern Andes, in Oncken, O., et al., eds., *The Andes-Active Subduction Orogeny*; Berlin, Springer-Verlag, *Frontiers in Earth Sciences*, v. 1, p. 439-451.
- Aitchison, S.J. and Forrest, A.H., 1994, Quantification of crustal contamination in open magmatic systems, *Journal of Petrology*, v. 35, p. 461-488.
- Aitchison, S.J., Harmon, R.S., Moorbath, S., Schneider, A., Soler, P., Soria-Escalante, E., Steele, G., Swainbank, I., 1995. Pb isotopes define basement domains of the Altiplano, central Andes. *Geology*, v. 23, p. 555-558.
- Allmendinger, R.W., Jordan, T.E., Kay, S.M., Isacks, B.L., 1997, The evolution of the Altiplano-Puna Plateau of the Central Andes, *Annual Reviews of Earth and Planetary Sciences*, v. 25, p. 139-174.
- ANCORP Working Group, 2003, Seismic imaging of a convergent continental margin and plateau in the central Andes (Andean Continental Research Project 1996 ANCORP'96), *Journal of Geophysical Research*, v. 108, p. 2328.
- Babeyko, A. Yu, Sobolev, S. V., Trumbull, R. B, Oncken, O., Lavier, L.L., 2002, Numerical models of crustal scale convection and partial melting beneath the Altiplano-Puna plateau. *Earth Planetary Science Letters*, v. 199, p. 373-388.
- Baker, M.C.W and Francis, P.W., 1978, Upper Cenozoic volcanism in the Central Andes, ages and volumes, *Earth and Planetary Science Letters*, v. 41, p. 175-187.
- Barazangi, M., Isacks, B., 1976, Spatial distribution of earthquakes and subduction of the Nazca Plate beneath South America, *Geology*, v. 4, p. 686-692.
- Barke, R., Lamb, S., 2006, Late Cenozoic uplift of the Eastern Cordillera, Bolivian Andes, *Earth and Planetary Science Letters*, v. 249, p. 350-367.
- Barke, R, Lamb, S., MacNiocaill, C., 2007, Late Cenozoic bending of the Bolivian Andes: New paleomagnetic and kinematic constraints, *Journal of Geophysical Research*, v. 12, B01101, doi:10.1029/2006JB004372.
- Barnes, J. B., Ehlers, T.A., 2009, End member models for Andean Plateau uplift. *Earth Science Reviews*, v. 97, p. 117-144.

- Bea, F., Pereira, M.D. and Stroh, A., 1994, Mineral/leucosome trace-element partitioning in a peraluminous migmatite (a laser ablation-ICP-MS study), *Chemical Geology*, v. 117, p. 291-312.
- Beck, S., Zandt, G., Myers, S., Wallace, T., Silver, P., Drake, L., 1996, Crustal thickness variations in the central Andes: *Geology*, v. 24, p. 407–410.
- Beck, S., Zandt, G., 2002, The nature of orogenic crust in the central Andes, *Journal of Geophysical Research*, v. 107, No. B10, 2230, doi:10.1029/2000JB000124.
- Bevis, M., Kendrick, E., Smalley, R., Brooks, B., Allmendinger, R., Isacks, B., 2001, On the strength of interplate coupling and the rate of backarc convergence in the Central Andes: an analysis of the interseismic velocity field. *Geochem. Geophys. Geosyst.* 2 Paper 2001GC000198.
- Bianchi, M., Heit, B., Jakovlev, A., Yuan, X., Kay, S.M., Sandvol, E., Alonso, R.N., Coira, B.L., Brown, L.D., Kind, R. and Comte, D., 2013, Teleseismic tomography of the southern Puna plateau in Argentina and adjacent regions. *Tectonophysics*, v. 586, p. 65-83.
- Bindeman, I., 2008, Oxygen Isotopes in Mantle and Crustal Magmas as Revealed by Single Crystal Analysis, *Reviews in Mineralogy and Geochemistry*, v. 69, p. 445-478.
- Caffe, P.J., Trumbull, R.B., Coira, B.L., Romer, R.L., 2002, Petrogenesis of early Neogene magmatism in the northern Puna; implications for magma genesis and crustal processes in the Central Andean plateau, *Journal of Petrology*, v. 43, p. 907-942.
- Cahill, T.A., and Isacks, B.L., 1992, Seismicity and shape of the subducted Nazca plate: *Journal of Geophysical Research*, v. 97, p. 17,503–17,529.
- Chang, Y.H., 2007, O-Isotopes as tracer for assimilation processes in different magmatic regimes (El Misti, S. Peru and Tapacca, N. Chile), *Diplom Thesis*, 51 pp, Gottingen.
- Chappell, B.W. and White, A.J.R., 1974, Two contrasting granite types, *Pac. Ged.* v. 8, p. 173-174.
- Charlier, B.L.A., Bachmann, O., Davidson, J.P., Dugan, M.A., Morgan, D.J., 2007, The upper crustal evolution of a large silicic magma body: evidence from crystal-scale Rb/Sr isotopic heterogeneities in the Fish Canyon magmatic system, *Colorado Journal of Petrology*, v. 48, p. 1875-1894.

- Coira, B., Kay, S.M., Viramonte, J., 1993, Upper Cenozoic magmatic evolution of the Argentine Puna - A model for changing subduction geometry: *International Geology Review*, v. 35, p. 677-720.
- Coira, B., Kay, S.M., 1993, Implications of Quaternary volcanism at Cerro Tuzgle for crustal and mantle evolution of the Puna plateau, central Andes, *Contributions to Mineralogy and Petrology*, v. 113, p. 40-58.
- Condie, K.C., 1993, Chemical composition and evolution of the upper continental crust: contrasting results from surface samples and shales, *Chemical Geology*, v. 104, p. 1-37.
- Cordani, U.G., Sato, K., 1999, Crustal evolution of the South American Platform, based on Nd isotopic systematics on granitoid rocks. *Episodes*, v. 22, p. 167-173.
- Cordani, U.G., Teixeira, W., Tassinari, C.C.G., Kawashita, K., Sato, K., 1988, The Growth of the Brazilian Shield, *Episodes*, v. 11, p. 163-167.
- Cunningham, C.G., Zartman, R.E., McKee, E.H., Rye, R.O., Naeser, C.W., Sanjines V., O., Ericksen, G.E., Tavera V., F. 1996, The age and thermal history of Cerro Rico de Potosi, Bolivia, *Mineral Deposita* v. 31, p. 374-385.
- Davidson, J. P., de Silva, S. L., 1992, Volcanic rocks from the Bolivian Altiplano: insights into crustal structure, contamination, and magma genesis in the Central Andes, *Geology*, v. 20, p. 1127-1130.
- Davidson, J. P., de Silva, S. L., 1995, Late Cenozoic magmatism of the Bolivian Altiplano, *Contributions to Mineralogy and Petrology*, v. 119, p. 387-408.
- DeMets, C., Gordon, R.G., Argus, D.F., and Stein, S., 1990, Current plate motions, *Geophysical Journal International*, v. 101, p. 425-478.
- DePaolo, D.J., 1981, Trace element and isotopic effects of combined wallrock assimilation and fractional crystallization: *Earth and Planetary Science Letters*, v. 53, p. 189-202.
- de Silva, S.L., 1989, The Altiplano-Puna Volcanic Complex of the Central Andes, *Geology*, v.17, p. 1102-1106.
- de Silva, S.L., Francis, P.W., 1991, *Volcanoes of the Central Andes*, Springer-Verlag, ISBN 3 540 53706 6, 216 pp.

- de Silva, S.L., Gosnold, W.D., 2007, Episodic construction of batholiths: Insights from the spatiotemporal development of an ignimbrite flare-up, *Journal of Volcanology and Geothermal Research*, v. 167, p. 320-325.
- Dunn, T. and Sen, C., 1994, Mineral/Matrix Partition-Coefficients for Ortho-Pyroxene, Plagioclase, and Olivine in Basaltic to Andesitic Systems - a Combined Analytical and Experimental-Study, *Geochimica et Cosmochimica Acta*, v. 58(2), p. 717-733.
- Elger, K., Oncken, O., Glodny, J., 2005, Plateau-style accumulation of deformation: southern Altiplano: *Tectonics*, v. 24, p. TC4020, doi: 10.1029/2004TC001675.
- Endt, P.M., 1998, Supplement to energy levels of A=21-44 nuclei (VII), *Nuclear Physics A*, v. 633, p. 1-220.
- Evernden, J.F., Kriz, S.J., Cherroni, C., 1977, Potassium-argon ages of some Bolivian rocks, *Economic Geology* 72, 1042-1061.
- Francis, P.W., Baker, M.C.W., Halls, C., 1981, The Kari Kari caldera, Bolivia, and the Cerro Rico stock, *Journal of Volcanology and Geothermal Research*, v. 10, p. 113–124.
- Francis, P.W., Sparks, R.S.J., Hawkesworth, C.J., Thorpe, R. S., Pyle, D. M., Tait, S. R., Mantovani, M. S., McDermott, R., 1989. Petrology and geochemistry of volcanic rocks of the Cerro Galán caldera, northwest Argentina, *Geological Magazine*, v. 126, p. 515-547.
- Francis, P.W., Hawkesworth, C.J., 1994, Late Cenozoic rates of magmatic activity in the Central Andes and their relationships to continental crust formation and thickening, *Journal of the Geological Society of London*, v. 151, p. 845-854.
- Fujimaki, H., 1986, Partition-Coefficients of Hf, Zr, and Ree between Zircon, Apatite, and Liquid, *Contributions to Mineralogy and Petrology*, v. 94, p. 42-45.
- Gans, C., Beck, S., Zandt, G., Gilbert, H., Alvarado, P., Anderson, M., and Linkimer, L., 2011, Continental and oceanic crustal structure of the Pampean flat slab region, western Argentina, using receiver function analysis: New high-resolution results, *Geophys. J. Int.*, v. 186, p. 45-58.
- Garziona, C.N., Molnar, P., Libarkin, J.C., MacFadden, B.C., 2006, Rapid late Miocene rise of the Bolivian Altiplano: Evidence for removal of mantle lithosphere, *Earth and Planetary Science Letters*, v. 241, p. 543– 556.

- Gerbault, M., Martinod, J., Herail, G., 2005, Possibly orogeny-parallel lower crustal flow and thickening in the central Andes, *Tectonophysics*, v. 399, p. 59-72.
- Ghosh, P., Garziona, C.N., Eiler, J.M., 2006, Rapid uplift of the Altiplano revealed in ^{13}C – ^{18}O bonds in paleosol carbonates: *Science*, v. 311, p. 511–515, doi: 10.1126/science.1119365.
- Goss, A. and Kay, S.M., 2009, Extreme high field strength element (HFSE) depletion and near-chondritic Nb/Ta ratios in central Andean adakite-like lavas ($\sim 27^\circ$ S, $\sim 68^\circ$ W), *Earth and Planetary Science Letters*, v. 270, 97-109.
- Graham, D.J. and Midgley, N.G., 2000, Graphical representation of particle shape using triangular diagrams: an Excel spreadsheet method, *Earth Surface Processes and Landforms*, v. 25(13), p. 1473-1477.
- Grant, N.J., Halls, C., Alvilá Salinas, W., Snelling, N.J., 1979, K-Ar ages of igneous rocks and mineralization in part of the Bolivian tin belt, *Economic Geology*, v. 74, p. 838–851.
- Gubbels, T.L., Isacks, B.L., Farrar, E., 1993, High level surfaces, plateau uplift, and foreland development, Central Bolivian Andes: *Geology*, v. 21, p. 695–698.
- Harris, C., Vogeli, J., 2010, Oxygen Isotope Composition of Garnet in the Peninsula Granite, Cape Granite Suite, South Africa: Constraints on Melting and Emplacement Mechanisms, *Geological Society of South Africa*, v. 113, p.401-412.
- Heit, B.S., Koulakov, I., Asch, G., Yuan, X., Kind, R., Alcocer-Rodriguez, I., Tawackoli, S., Wilke, W., 2008, More constraints to determine the seismic structure beneath the Central Andes at 21°S using teleseismic tomography analysis, *Journal of South American Earth Sciences*, v. 25, p. 22–36.
- Hoke, L., Lamb, S., 2007, Cenozoic behind-arc volcanism in the Bolivian Andes, South America: implications for mantle melt generation and lithospheric structure, *Journal of the Geological Society of London*, v. 164, p. 705-814.
- Hora, J.M, Singer, B.S., Jicha, B.R., Beard, B.L., Johnson, C.M., deSilva, S., Salisbury, M. J., 2010, Volcanic biotite-sanidine $^{40}\text{Ar}/^{39}\text{Ar}$ age discordances reflect Ar partitioning and pre-eruption closure in biotite. *Geology*, v. 38, p. 923-926.
- Husson, L., Sempere, T., 2003, Thickening the Altiplano crust by gravity-driven crustal channel flow, *Geophysical Research Letters*, v. 30: doi 10.1029/2002GL016877.

- Hauri, E.H., Wagner, T.P. and Grove, T.L., 1994, Experimental and natural partitioning of Th, U, Pb and other trace elements between garnet, clinopyroxene and basaltic melts. *Chemical Geology*, v. 117, p. 149-166.
- Indares, A., White, R.W., Powell, R., 2008, Phase equilibria modelling of kyanite-bearing anatectic paragneiss from the central Grenville Province. *Journal of Metamorphic Geology*, v. 26, p. 815-836.
- Isacks, B.L., 1988. Uplift of the Central Andean plateau and bending of the Bolivian orocline. *Journal of Geophysical Research*, v. 93, p. 3211-3231.
- Jaffey, A.H., Flynn, K.F., Glendenin, L.E., Bentley, W.C., and Essling, A.M., 1971, Precision measurements of half-lives and specific activities of ^{235}U and ^{238}U , *Physical Review C*, v. 4, p. 1889-1906.
- James, D.E., 1982, A combined O, Sr, Nd and Pb isotopic and trace element study of crustal contamination in central Andean lavas, I. Local geochemical variations, *Earth Planet Science Letter*, v. 57, p. 47-62.
- James, D.E., Sacks, I., S., 1999, Cenozoic formation of the central Andes: A geophysical perspective. In Skinner, B., ed., *Geology and ore deposits of the central Andes*, Society of Economic Geology Special Publication 7, p. 1-25.
- Jicha, B.R., Brown, F.H., 2013, An age on the Korath Range and the viability of $^{40}\text{Ar}/^{39}\text{Ar}$ dating of kaersutite in Late Pleistocene volcanics, Ethiopia, *Quaternary Geochronology*, <http://dx.doi.org/10.1016/j.quageo.2013.3.007>.
- Jiménez, N., Arando, G., Almendras, O., 1997, Estructura, evolución y petrología del complejo volcánico de Livicucho, norte de la meseta de los Frailes, *Boletín del Servicio Nacional de Geología y Minería* 23, 37-59.
- Jiménez, N., Santiváñez, R., Ramírez, V., 2005, Estudio de los volcanes potencialmente activos: Informe de la primera fase. Instituto de Investigaciones Geológicas y del Medio Ambiente (IGEMA), Facultad de Ciencias Geológicas, Universidad Mayor de San Andrés. Informe interno.
- Kay, R.W., Kay, S.M., 1993, Delamination and delamination magmatism, *Tectonophysics*, v. 219, pp. 177-189.
- Kay, S. M., 2006, Chemical and isotopic evidence for modification of the Central Andean arc mantle by crust removed by forearc subduction erosion. *Geochimica Cosmochimica Acta*, v. 170, A385.
- Kay, S.M., Coira, B., 2009, Shallowing and steepening subduction zones, continental lithosphere loss, magmatism and crustal flow under the Central Andean

- Altiplano-Puna Plateau. In Kay, S.M., Ramos, V.A., Dickinson, W.M. (editors), *Backbone of the Americas: Shallow Subduction, Plateau and Ridge and Terrane Collisions*, Geological Society of America Memoir 204, p. 229-260.
- Kay, S.M., Coira, B.L., Caffè, P.J., Chen, C-H, 2010, Regional chemical diversity, crustal and mantle sources and evolution of the Neogene Puna plateau ignimbrites of the Central Andes, *Journal of Volcanology and Geothermal Research*, v.198, p. 81-111.
- Kay, S. M., Coira, B., Viramonte, J., 1994, Young mafic back-arc volcanic rocks as indicators of continental lithospheric delamination beneath the Argentine Puna plateau, Central Andes, *Journal of Geophysical Research*, v. 99, p. 24323-24339.
- Kay, S.M., Coira, B., Wörner, G., Kay, R.W., Singer, B.S., 2011, Geochemical, isotopic and single crystal $^{40}\text{Ar}/^{39}\text{Ar}$ age constraints on the evolution of the Cerro Galán ignimbrites, *Bulletin of Volcanology*, DOI 10.1007/s00445-010-0410-7.
- Kay, S.M., Mpodozis, C., Coira, B.L., 1999, Magmatism, tectonism and mineral deposits of the central Andes (22°-33°S latitude). In Skinner, B.J. (ed.), *Geology and ore deposits of the central Andes*, Soc Economic Geol Special Pub 7:27-59.
- Keller, C.B., 2010, Chemical constraints on the origin of the Frailes Volcanic Complex in the Central Andean Altiplano Plateau, Bolivia, Bachelor of Science thesis, Cornell University, Ithaca, NY, 49 pp.
- Kennan, L., Lamb, S. H., Rundle, C., 1995, K-Ar dates from the Altiplano and Cordillera Oriental of Bolivia: Implications for Cenozoic stratigraphy and tectonics, *Journal of South American Earth Science*, v. 8, p. 163– 186.
- Koeppen, R.P., Smith, R.L., Kunk, M.L., Flores, A.M., Luedke, R.G., Sutter, J.F., 1987, The Morococala volcanics: highly peraluminous rhyolite ash flow magmatism in the Cordillera Oriental, Bolivia: *Geological Society of America Abstracts with Programs*, v. 19, pp. 731.
- Kuiper, K. F., Deino, A., Hilgen, F. J., Krijgsman, W., Renne, P. R., and Wijbrans, J. R., 2008, Synchronizing rock clocks of earth history. *Science*, v. 320, p. 500-505.
- Loiselle, M.C., Wones, D.R., 1979, Characteristics and origin of anorogenic granites, *Geological Society of America Abstracts with Programs* 11, v. 7, p. 468.

- Lucassen, F., Becchio, R., Harmon, R., Kasemann, S., Franz, G., Trumbull, R., Wilke, H.-G., Romer, R.L., Dulski, P., 2001. Composition and density model of the continental crust in an active continental margin — the Central Andes between 18° and 27°S. *Tectonophysics* v. 341, p. 195–223.
- Lucassen, F., Escayola, M., Franz, G., Romer, R.L., Koch, K., 2002. Lead evolution of the Pre-Mesozoic crust in the Central Andes (18°-27°): progressive homogenization of Pb, *Chemical Geology*, v. 186, p. 183-297.
- Lucassen, F., Franz, G., Romer, R.L., Schultz, F., Dulski, P., Wemmer, K., 2007. Pre-Cenozoic intra-plate magmatism along the Central Andes (17°-34°S): Composition of the mantle at an active margin, *Lithos*, v.99, p. 312-338.
- Luedke, R.G, Ericksen, G.E., Urquidi B., Tavera V., F., Smith, R.L., Cunningham, C.G., 1997, Geochemistry of peraluminous volcanic rocks along the southern margin of the Los Frailes volcanic field, central Bolivian tin belt, *Boletín del Servicio Nacional de Geología y Minería* v. 23, p. 14-36.
- Luhr, J.F. and Carmichael, I.S.E., 1980, The Colima volcanic complex, Mexico. I: post-caldera andesites from Volcan Colima, *Contributions to Mineralogy and Petrology*, v. 71, p. 343-372.
- Mamani, M., Tassara, A., Wörner, G., 2008, Composition and structural control of crustal domains in the central Andes, *Geochemistry Geophysics Geosystems*, v. 9-3, p. 1-13.
- Mamani, M., Wörner, G., Sempere, T., 2010, Geochemical variations in igneous rocks of the Central Andean orocline (13°S to 18°S): Tracing crustal thickening and magma generation through time and space, *Geological Society of America Bulletin*, v. 122, p. 162-182.
- Martignole, J. and Martelat, J.E., 2003, Regional-scale Grenvillian-age UHT metamorphism in the Mollendo-Camana block (basement of the Peruvian Andes), *Metamorphic Geology*, v. 21, p. 99-120.
- McBride, S.L., Robertson, R.C.R., Clark, A.H., Farrar, E., 1983. Magmatic and metallogenic episodes in the northern tin belt, Cordillera Real, Bolivia. *Geologische Rundschau* 72 (2), 685–713.
- McGlashan, N., Brown, L.D., Kay, S.M., 2008, Crustal thicknesses in the Central Andes from teleseismically recorded depth phase precursors, *Geophysical Journal International*, v. 175, p. 1013–1022.

- McQuarrie, N., 2002, The kinematic history of the central Andean fold-thrust belt, Bolivia: Implications for building a high plateau, *Geological Society of America Bulletin*, v. 114, p. 950–963.
- McQuarrie, N., B. K. Horton, G. Zandt, S. Beck, P.G. DeCelles, 2005, Lithospheric evolution of the Andean fold-thrust belt, Bolivia, and the origin of the central Andean plateau, *Tectonophysics*, v. 399, p. 15–37.
- Miller, C., 1985, Are Strongly Peraluminous Magmas Derived from Pelitic Sedimentary Sources?, *The Journal of Geology*, v. 93, p. 673–689.
- Min K., Mundil R., Renne P. R. and Ludwig K. R., 2000, A test for systematic errors in $^{40}\text{Ar}/^{39}\text{Ar}$ geochronology through comparison with U–Pb analysis of a 1.1 Ga rhyolite. *Geochim. Cosmochim. Acta*, v. 64(1), p. 73–98.
- Molnar, P., Garzzone, C. 2007, Bounds on the viscosity coefficient of continental lithosphere from removal of mantle lithosphere beneath the Altiplano and Eastern Cordillera, *Tectonics*, v. 26, TC2013, doi: 10.1029/2006TC001964.
- Morgan IV, G.B., London, D., Luedke, R., 1998, Petrochemistry of Late Miocene peraluminous silicic volcanic rocks from the Morococala field, Bolivia, *Journal of Petrology*, v. 39, p. 601–632.
- Myers, S. C., Beck, S., Zandt, G., Wallace, T., 1998, Lithospheric-scale structure across the Bolivian Andes from tomographic images of velocity and attenuation for P and S waves, *Journal of Geophysical Research*, v 103, p. 21,233–21,252.
- Nekvasil, H., Burnham, C.W., 1987, The calculated individual effects of pressure and water content on phase equilibria in the granite system, in Mysen, Ed., *Magmatic processes: Physicochemical principles*, Geochemical Society Special Publication, v. 1, p. 433–445.
- Nier, A.O., 1950, A redetermination of the relative abundances of the isotopes of carbon, nitrogen, oxygen, argon, and potassium, *Phys. Review*, v. 77, p. 789–793.
- Nur, A., Ben-Avraham, Z., 1981, Volcanic gaps and the consumption of aseismic ridges in South America, In: Kulm, L. (Ed.), *Nazca Plate: Crustal Formation and Andean Convergence*. Geological Society of America, p. 729–740.
- Oncken, O., Hindle, D., Kley, J., Elger, K., Victor, P., Schemmann, K., 2006, Deformation of the Central Andean upper plate system – facts, fiction, and constraints for plateau models. In: Oncken, O. and 7 others, eds., *The Andes –*

- Active Subduction Orogeny, *Frontiers in Earth Sciences*, p. 3-28, Springer-Verlag, Berlin.
- Ort, M., Coira, B., Mazzoni, M., 1996, Generation of a crust-mantle magma mixture: magma sources and contamination at Cerro Panizos, Central Andes. *Contributions to Mineralogy and Petrology*, v. 123, p. 308-322.
- Papanastassiou, D.A., Wasserburg, 1969, Initial strontium isotopic abundances and the resolution of small time differences in the formation of planetary objects, *Earth Planetary Science, Letters*, v.5, p. 361.
- Pardo, M., Comte, D., Monfret, T., 2002, Seismotectonic and stress distribution in the central Chile subduction zone, *Journal of South American Earth Sciences*, v. 15, p. 11-22.
- Parrish, R.R, Noble, S.R, 2003, Zircon U-Th-Pb Geochronology by Isotope Dilution – Thermal Ionization Mass Spectrometry (ID-TIMS). *Reviews in Mineralogy and Geochemistry*, v. 53, p. 183-213.
- Pilger, R.H., 1981, Plate reconstructions, aseismic ridges, and low-angle subduction beneath the Andes, *Geological Society of America Bulletin*, v. 92, p. 448-456.
- Pin, C. and Zalduegui, J.S., 1996, Sequential Separation of Rare-earth Elements, Thorium and Uranium by Miniaturized Extraction Chromatography: Application to Isotopic Analyses of Silicate Rocks, *Analytica Chimica Acta*, v. 339, p. 79–89.
- Powell, R., Holland, R.J.B., 1988, An internally consistent dataset with uncertainties and correlations; 3, Applications to Geobarometry, worked examples and a computer program, *Journal of Metamorphic Geology*, v.6, p. 173-204.
- Polet, J., Silver, P., Zandt, G., Ruppert, S., Bock, G., Kind, R., Reudloff, A., Asch, G., Beck, S., Wallace, T., 2000, Shear wave anisotropy beneath the Andes from the BANJO, SEDA, and PISCO experiments, *Journal of Geophysical Research*, v. 105, p. 6287–6304.
- Ramos, V.A., 2008. The basement of the Central Andes: the Arequipa and related terranes. *Annual Review Earth and Planetary Sciences* 36, 289–324.
- Ramos, V.A., Folguera, A., 2009, Andean flat-slab subduction through time, *The Geological Society of London, Special Publications*, v. 327, p. 31-54.
- Renne, P.R., Farley, K.A., Becker, T.A., Sharp, W.D., 2001, Terrestrial cosmogenic argon, *Earth Planet Science Letters*, v. 188, p. 435-440.

- Renne, P.R., Deino, A.L., Hilgen, F.J., Kuiper, K.F., Mark, D.F., Mitchell, W.S., Morgan, L.E., Mundil, R., Smit, J., 2013, Time scales of critical events around the Cretaceous-Paleogene boundary, *Science*, v. 339, p. 684-687.
- Rice, C.M., Steele, G.B., Barfod, D.N., Boyce, A.J., Pringle, M.S., 2005, Duration of magmatic, hydrothermal and supergene activity at Cerro Rico de Potosi, Bolivia, *Economic Geology*, v. 100, pp. 1647–1656.
- Rotenberg E., Davis D.W., Amelin Y., Ghosh S., Bergquist B.A., 2012, Determination of the decay-constant of ^{87}Rb by laboratory accumulation of ^{87}Sr . *Geochim. Cosmochim. Acta*, v. 85, p. 41-57.
- Rudnick, R.L. and Fountain, D.M., 1995, Nature and composition of the continental crust -- a lower crustal perspective. *Reviews in Geophysics*, v. 33, p. 267-309.
- Rudnick, R.L., Gao, S., 2004, Composition of the Continental Crust, In Rudnick, R. (Ed.), *Treatise on Geochemistry (Vol. 3): The Crust*, p. 1-64.
- Sail, A.N., Dall'Agnol, R., Ferreira, V.P., Nardi, L.V.S., Pimentel, M.M., and Wiedemann, C.M., 1999, Precambrian granitic magmatism in Brazil, *Episodes*, v. 22, p. 191-198.
- Schneider, A., 1985, Eruptive processes, mineralization and isotopic evolution of the Los Frailes KariKari region, Bolivia, PhD Thesis, Imperial College of Science and Technology, University of London, 295 pp.
- Schneider, A., Halls, C., 1985, Chronology of eruptive processes and mineralization of the Frailes Karikari volcanic field, Eastern Cordillera, Bolivia: *Comunicaciones, Departamento de Geología, Universidad de Chile*, v. 35, pp. 217-224.
- Schneider, A., 1987, Eruptive processes, mineralization and isotopic evolution of the Los Frailes, Kari Kari region, Bolivia. *Revista Geología de Chile*, v. 30, p.27-33.
- Schnurr, W.B., Trumbull, R.B., Clavero, J, Hahne, K., Siebel, W., Gardeweg, M., 2007, Twenty-five million years of silicic volcanism in the southern central volcanic zone of the Andes: Geochemistry and magma genesis of ignimbrites from 25° to 27°S, 67° to 72°W, *Journal of Volcanology and Geothermal Research*, v. 266, p. 27-46.
- Schurr, B., Rietbrock, A., Asch, G., Kind, R., Oncken, O., 2006, Evidence for lithospheric detachment in the central Andes from local earthquake tomography: *Tectonophysics*, v. 415, p. 203–223, doi: 10.1016/j.tecto.2005.12.007.

- Shimizu, H., 1980, Experimental study on rare-earth element partitioning in minerals formed at 20 and 30kb for basaltic systems, *Geochemical Journal*, v. 14(4), p. 185-202.
- Soler, M.M., 2005, Caldera Vilama (Mioceno Superior): Su estratigrafía, evolución magmática y relación con eventos ignimbríticos tempranos, Puna Argentina – Altiplano Boliviano, Ph.D. Thesis, Univ. Nacional de Salta, Salta, Argentina.
- Soler, M.M, Caffè, P., Coira, B., Onofre, A.T., Kay, S. M., 2007, Geology of the Vilama caldera: correlations and a new interpretation of a large scale explosive event in the Central Andean plateau during the Upper Miocene, *Journal of Volcanology and Geothermal Research*, v. 164, p. 27-53.
- Sparks, R.S.J., Francis, P.W., Hamer, R.D., Pankhurst, R.J., O'Callaghan, L.L., Thorpe, R.S., Page, R.S., 1985, Ignimbrites of the Cerro Galán Caldera, NW Argentina. *Journal of Volcanology and Geothermal Research*, v. 24, p. 205-248.
- Spera, F.J., Bohron, W.A., 2001, Energy-Constrained Open-System Magma Processes I: General Model and Energy-Constrained Assimilation-Fractional Crystallization (EC-AFC) Formation, *Journal of Petrology*, v. 42, p. 999-1018.
- Steiger, R.H., Jäger, E., 1977, Subcommittee on geochronology: convention on the use of decay constants in geo- and cosmochemistry. *Earth Planet. Sci. Lett.*, v. 36, p. 359–362.
- Stoener, R.W., Schaeffer, O.A., Katcoff, S., 1965, Half-lives of argon-37, argon-39 and argon-42, *Science*, v. 148, p. 1325-1328.
- Sun, S.S. and McDonough, W.F., 1989, Chemical and isotopic systematics of oceanic basalts: implications for mantle composition and processes, *Geological Society*, v. 42, p. 313-345.
- Swenson, J.L., Beck, S.L., Zandt, G., 2000, Crustal structure of the Altiplano from broadband regional waveform modeling; implications for the composition of thick continental crust, *Journal of Geophysical Research*, v 105, p. 607-621.
- Taylor, H.P., 1980, The effects of assimilation of country rocks by magmas on $^{18}\text{O}/^{16}\text{O}$ and $^{87}\text{Sr}/^{86}\text{Sr}$ systematics in igneous rocks, *Earth and Planetary Science Letters*, v. 47, p. 243-254.
- Taylor, S.R. and McLennan, S.M., 1995, The geochemical evolution of the continental crust. *Reviews in Geophysics*, v. 33, p. 241-265.

- Taylor, S.R. and McLennan, S.M., 2009, Planetary Crusts; Their compositions, origin and evolution. Cambridge Planetary Science.
- Trumbull, R.B., Riller, U., Oncken, O., Scheuber, E., Munier, K., Hongn, F., 2006, The time-space distribution of Cenozoic arc volcanism in the Central Andes: a new data compilation and some tectonic considerations. In: Oncken, O., et al. (Ed.), The Andes-Active Subduction Orogeny.: Frontiers in Earth Science Series, 1. Springer-Verlag, Berlin, p. 29-43.
- Watson, B.E., Harrison, M.T., 1983, Zircon saturation revisited: temperature and composition effects in a variety of crustal magma types, Earth and Planetary Science Letters, v. 64, p. 295-304.
- Wen, S., Nekvasil, H., 1994, SOLVCALC: An interactive graphics program package for calculating the ternary feldspar solvus and for two-feldspar geothermometry, Computers and Geoscience, v. 20, p. 1025-1040.
- White, A.J.R., 1979, Sources of granite magmas, Geological Society of America Abstracts with Programs 11, v. 7, p. 539.
- White, W.M., Duncan, R.A., 1996, Geochemistry and geochronology of the Society Islands: New evidence for deep mantle recycling, *in* Basu, A., and Hart, S., eds., Earth Processes: Reading the Isotopic Code, v. 95, AGU Geophysical Monograph, p. 183-206.
- Wörner, G., Moorbath, S., Harmon, R.S., 1992, Andean Cenozoic volcanics reflect basement isotopic domains, Geology, v. 20, p. 1103-1106.
- Yáñez, G.; Ranero, C.; von Huene, R.; Díaz, J. 2001. Magnetic anomaly interpretation across the southern Central Andes (32°-33.5°S): the role of the Juan Fernández ridge in the late Tertiary evolution of the margin. Journal of Geophysical Research, Vol. 106, p. 6325-6345.
- Yuan, X., Sobolev, S., Kind, R., Oncken, O., Bock, G. and others, 2000, Subduction and collision processes in the central Andes constrained by converted seismic phases, Nature, v. 408, p. 958-961
- Yuan, X., Sobolev, S. V. and Kind, R., 2002, Moho topography in the central Andes and its geodynamic implications: Earth and Planetary Science Letters, v. 199, p. 389-402.

Zandt, G. M., Leidig, J., Chmielowski, J., Baumont, D. and Yuan, X., 2003, Seismic detection and characterization of the Altiplano-Puna magma body, Central Andes, *Pure and Applied Geophysics*, v. 160, p. 789-807.

Zartman R.E., Cunningham, C.G., 1995, U-Pb zircon dating of the 13.8-Ma dacite volcanic dome at Cerro Rico de Potosi, Bolivia, *Earth and Planetary Science Letters*, v.133, p. 227-237.